PREDICTION OF DAMAGE TO STRUCTURE RESULTING FROM RECIRCULATION OF PARTICLES FROM A MAGNETOPLASMA SPACECRAFT ENGINE

A Dissertation

by

MICHAEL WILLIAM MARTIN

Submitted to the Office of Graduate and Professional Studies of
Texas A&M University
in partial fulfillment of the requirements for the degree of

DOCTOR OF PHILOSOPHY

Chair of Committee,	Thomas Lalk
Co-Chair of Committee,	David Staack
Committee Members,	Gerald Morrison
	Sharath Girimaji
Head of Department,	Andreas Polycarpou

December 2014

Major Subject: Mechanical Engineering

ABSTRACT

A magnetoplasma spacecraft engine, such as the Variable Area Specific Inpulse Magnetoplasma Rocket (VASIMR®), uses magnetic fields and a magnetic nozzle to constrict and accelerate plasma to produce thrust. Most of the ejected plasma particles are expected to detach from the magnetic field lines and escape to provide thrust but some particles may not and could impact the spacecraft structure resulting in surface erosion and electrical charging. The plasma plume for a magnetoplasma engine was modeled computationally and scaled to determine what percentage of particles remained in the magnetic field and the kinetic energy of all impacting particles. Factors such as average particle velocity at the engine exit, magnetic field strength, and plume density distribution (i.e. width) were varied in a full factorial experiment to ascertain the effects of each factor and the important inter-relationships. The results are presented for a generic magnetoplasma engine and for the specific VASIMR® case.

Detachment was found to be occurring with 99.42% of particles escaping under the worst conditions and only 0.0172% of particles impacting structure. It was determined that three things led to an increase in the number of impacting particles on spacecraft structure: a stronger magnetic field, a lower exit velocity of particles into the plume, and a wider plume. In addition, there was an "erosion zone" where an increasing particle exit velocity led to more erosion until the number of impacting particles was negligible and erosion dropped significantly.

For the specific case under nominal conditions, the erosion rate was 1.386 nm/month of engine operating time on aluminum and 0.611 nm/month on silicon. The electrical charging on spacecraft surfaces was found to be -27.85 V DC, which can be mitigated with current plasma contactor technology or some variant. Therefore, magnetoplasma spacecraft engines can be shown to cause minimal erosion and electrical charging and should be capable of operating safely with current technology by varying the three parameters previously mentioned.

DEDICATION

This dissertation is dedicated to my wife (Carrie Martin), my mother (Anne Martin), my brother (Steven Martin), and Carrie's parents (Robert and BJ Stokes) who have stood behind me and helped me most when I felt defeated.

ACKNOWLEDGEMENTS

I want to thank my Co-Chairs, Dr. Thomas Lalk and Dr. David Staack, for their great help in the formation and completion of this dissertation. The use of the PEDL lab equipment and computers has made this research possible.

I also want to thank Dr. Gerald Morrison and Dr. Sharath Girimaji for agreeing to be on my dissertation committee and giving me advice from time to time. I appreciate your help. Thanks goes to Dr. Michael Schuller for his help as well.

Thank you to Dr. Chris Olsen, Dr. Jared Squire, Dr. Tim Glover, and everyone else who, while working at the Ad Astra company, educated me about the experimental data. I am especially grateful to Dr. Franklin Chang-Díaz, CEO of Ad Astra. I greatly appreciate the help given to me by Dr. Edgar Bering of the University of Houston.

Further thanks go to Carrie Martin, Anne Martin, and Steven Martin for their encouragement. You've inspired me.

Help has been tendered by my lab mates: Will Pollard, Robert Geiger, Ping Xiao, Dani Wakim , Pingjia Ming, Frans Ebersohn, and Cliff Tsai. Thanks to Jeff Polasek for letting me use the lcat mini-cluster.

NOMENCLATURE

A	Cross Sectional Area of the Coil
$\boldsymbol{A_m}$	Magnetic Vector Potential
$\boldsymbol{B}$	Magnetic Field
e	Electric Charge
$\boldsymbol{e}_{\text{coil}}$	Electrical Vector of the Coil
$\boldsymbol{E}$	Electric Field
$\boldsymbol{F}$	Force
$\boldsymbol{H}$	Magnetic Field Strength
I	Electrical Current
ICH	Ion Cyclotron Heating
ICRF	Ion Cyclotron Radio Frequency
ISS	International Space Station
ITAR	International Traffic in Arms Regulations
$\boldsymbol{J}$	Current Density
MHD	Magnetohydrodynamics
m_I	Ion Mass
m_E	Electron Mass
N	Number of Turns in an Electrical Coil
r	Radius from the Engine Centerline
RF	Radio Frequency

t	Time
V	Velocity
$\mathbf{V}$	Electric Potential
V_x	Velocity in the x direction
V_y	Velocity in the y direction
V_z	Velocity in the z direction
V_{mag}	Velocity magnitude
VASIMR®	VAriable Specific Impulse Magnetoplasma Rocket
x	Component of the Radial Direction
y	Component of the Radial Direction
z	Component of the Axial Direction along the Centerline
Z	Charge Number

TABLE OF CONTENTS

Page

LIST OF FIGURES

Page

LIST OF TABLES

Page

1. INTRODUCTION

Sending spacecraft to other planets in our solar system has always been an expensive undertaking. This is partly because of the inability to provide long-lasting acceleration to the spacecraft. Since the 1950's, chemical propulsion, where chemical reactions release energy, has been the primary method to launch spacecraft into and out of Earth orbit. Although chemical propulsion, such as LH/LOX rocket engines, can provide significant acceleration to spacecraft, it can only do so for a very short time (on the order of minutes) before propellant is exhausted. As such, interplanetary spacecraft have generally had to rely on chemical propulsion to give a strong push in the beginning of the mission and then coast to the destination. Using creative orbital mechanics such as the Hohmann Transfer, the range and speed of these spacecraft can be extended after their propellant is gone but only to a point.

However, starting in the 1990's, electric propulsion, where propulsion is generated through the use of electricity, began to be utilized in long range probes such as NASA's Deep Space One (launched in 1998) and Dawn (launched in 2007). It allowed these spacecraft to continuously generate thrust throughout the mission to achieve record-breaking speeds. These were ion engines, specifically, but a new type of electric propulsion called magnetoplasma engines is now being developed. Magnetoplasma engines are defined here as utilizing a magnetic nozzle to accelerate and eject plasma particles in order to generate thrust. To better understand how magnetoplasma engines work, an explanation of what plasma, nozzles, and various plasma-based engines are will be given in the next section.

1.1 Research Motivation

Before any plasma spacecraft engine can be tested in space, the potential effects the engine will have on spacecraft structure need to be determined. Specifically, how the exhaust plume will interact with the large metallic surfaces, solar arrays, and optics needs to be considered. Mission managers working for any number of government or commercial entities need to feel confident that choosing a magnetoplasma engine is safe and beneficial to the mission. If any of the ionized particles ejected by the magnetoplasma engine remain magnetized (i.e. follow magnetic field lines), the particles might impact an assortment of spacecraft surfaces and cause erosion of those surfaces or electrical charging of the structure. Therefore, the motivation of this research is to advance the current state of this technology by providing a model that predicts what amount of erosion and electrical charging might be expected on spacecraft surfaces during engine firings at maximum thrust conditions, using experimental data as a starting point. This is important because damage to orbiting spacecraft, no matter how minimal, is extremely difficult to repair because replacement parts may need to be launched from Earth at a current rate of $10,000 per pound. Erosion of the solar panels may lead to reduced electrical power generation for the spacecraft. Erosion of optical surfaces may lead to equipment failure.

1.2 Research Relevance

While all literature on this subject will be shown (in Section 2) to have used fluid models and continuum physics to describe plume dynamics, either in part or wholly, this research used particle kinetic theory only to describe plasma flow because the plume

fringe from experimental data was rarified (i.e. has a Knudsen number that is much greater than 1, as calculated in Appendix H). The ability to model millions of individual ionized particles in a complex magnetic field is a new capability due to advances in computer technology. Until now, researchers had to treat the exhaust plume as a fluid because the modeling of individual particle trajectories was too time consuming, even though the assumption of continuum is not valid beyond the engine throat. For the ions in particular, which have large mean free paths and large gyro radii, continuum physics does not apply. In the plume at 0.3 m downstream of the engine, the ion Knudsen number is around 117, which means that the individual particles no longer act collectively and fluid dynamic equations are not valid. This location is where much of the experimental data used in this research was taken by Ad Astra. Advances in computational power and software now make it feasible to simulate the trajectory of many particles within a reasonable amount of time.

1.3 Research Objective

The objective of this research is to predict the structural damage due to the erosion and electrical charging on the surface of a spacecraft operating a magnetoplasma engine caused by recirculating particles and how engine operational parameters affect the amount of damage. To make a realistic determination, this research will quantify the amount of erosion and electrical charging to an aluminum or silicon surface due to impacting particles entering the engine backfield during different engine configurations for a generic magnetoplasma engine. The backfield is defined as being the area adjacent to the magnetoplasma engine, along the sides and back of the engine (the left side of

Figure 1). These results can be used to predict and mitigate any damage to spacecraft surfaces caused by recirculating particles from a magnetoplasma spacecraft engine. The necessary steps to meet this objective are listed in Section 3.

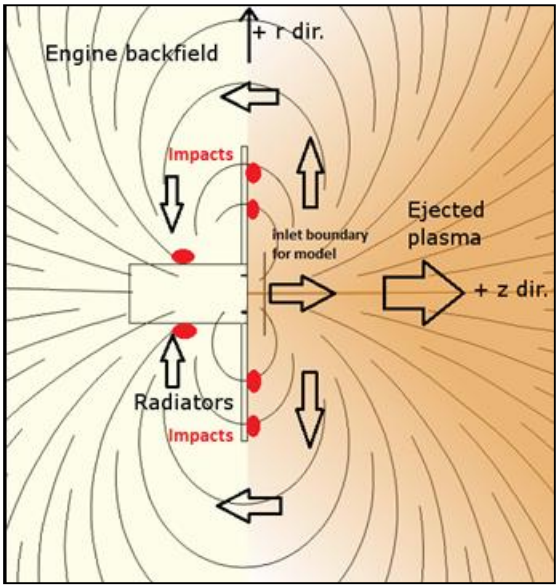

Figure 1. Schematic showing recirculating plasma particles impacting structure.

1.4 Dissertation Overview

This section lays out how the rest of the document is organized. Section 2 presents a literature survey where an overview of plasma, nozzles, and magnetic nozzles is given. Research concerning the VASIMR® engine will also be explored as the experimental data used by this research came from the VX-200 engine. Finally, how particles are expected to detach from magnetic field lines and how plasma may interact with the spacecraft will also be presented in Section 2.

Section 3 has the need analysis that was used to determine what was needed to meet the research objective and how to attain it. The assumptions and constraints of the overall research are mentioned. Section 4 documents how the simulation model was developed, its limitations, and its validation. Section 5 presents the trajectory, electrical charging, and erosion rate results from the simulation model as well their limitations. The baseline run will be presented first with its validation information, and then the remaining runs will be explained in comparison to the baseline. Finally, Section 6 summarizes the findings stated throughout this document, lists possible avenues to improve the model, and how these results can be used in the development of plasma spacecraft engines in the future. A distinction will be made between results that are unique to the VX-200 and those that can be generalized to any magnetoplasma engine.

2. BACKGROUND

2.1 Introduction

In order to understand what needed to be done in this research, a firm understanding of what has come before is necessary. Specifically, we need to know the mechanisms by which the ejected ions from a plasma spacecraft engine will detach from the engine's magnetic field, how any trapped ions will interact with the spacecraft, and what amount of electrical charging and erosion should be expected from ion impacts. To understand the mechanism of ion detachment, magnetic nozzles and ion detachment from this type of nozzle have been studied for about 30 years and will be discussed in this section. To understand how the mechanism relates to the magnetoplasma engine, the VASIMR® engine needs to be explained. Various versions of VASIMR® have been in development since 1999. To relate how the plasma plume from a magnetoplasma engine might affect the attached spacecraft, we need to look at the plasma environment of a spaceship-analog such as the International Space Station (ISS), which also happens to be the proposed test facility for magnetoplasma engines. The plasma environment around the ISS has been under study since 2000 and the results from numerous sample experiments serve to put the results of this research into context. The plasma environment interaction includes erosion as well as electrical charging on spacecraft surfaces due to the plasma. The following sections explain the research done in magnetic nozzles, the VASIMR® engine, ion detachment from magnetic nozzles, and the plasma plume interaction with a spacecraft.

2.2 Plasma

Plasma occurs naturally throughout the universe and constitutes almost all of the visible matter therein. It is often referred to as the fourth state of matter, after solids, liquids, and gases. Examples of plasma in the natural world are lightning, fluorescent light bulbs, and the Sun. Gas is converted into plasma when electrons within the gas disconnect from atoms, forming a collection of ionized particles (ions and free electrons) and neutral particles. This process can happen either through the gas achieving a sufficiently high temperature (kinetic transfer), exposure to radiation (photoionization), or exposure to a strong electrical field (field ionization)[1]. After a gas becomes plasma, it is susceptible to electric and magnetic fields via the Lorentz force and conducts electricity readily. The ions move toward negatively-charged surfaces and away from positively-charged surfaces. Conversely, electrons move toward positively-charged surfaces and away from negative ones. The ions and electrons both rotate around magnetic field lines and follow the lines longitudinally. Thus, plasma can be constricted and guided by magnetic field lines, which serves as the basis of magnetic nozzles used in magnetoplasma engines. A magnetic nozzle is similar to a conventional rocket nozzle but utilizes magnetic field lines instead of physical walls to constrict and accelerate plasma in order to generate thrust. A plasma consists of electrons, ions, or neutral particles. Generally, it is the impact of ions on a surface that creates the most erosion, as electrons are very low mass and neutral particles do not recirculate. Therefore, in this document, the words “particle” and “ion” are used interchangeably.

2.3 Nozzles

A conventional rocket nozzle, known as a de Laval nozzle after its creator, Gustaf de Laval, consists of a convergent and divergent section and uses a throat to accelerate fluid flow to sonic velocity[2]. The divergent section further accelerates flow to supersonic velocities and converts exhaust gas pressure into directed thrust (Figure 2). The physical walls of the nozzle are in contact with high temperature exhaust gases, which limits the maximum thrust possible. This limitation is due to the fact that as the exhaust gas temperature rises, the possibility that the nozzle will melt and fail during engine operation becomes more likely. Magnetic nozzles, on the other hand, can be utilized for higher temperature flow because the magnetic field lines mostly keep the plasma from physically contacting any of the engine surfaces. Thus, magnetic nozzles allow for higher efficiency rocket engines. Electromagnetic engines can have exhaust gases in the form of plasma with a temperature over 100,000 K. This temperature is much higher than the melting point of any viable engine material (and many times hotter than the surface of the Sun). Magnetic nozzles make magnetoplasma engines feasible.

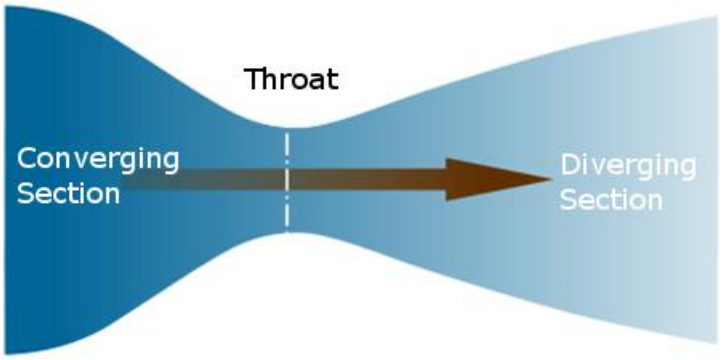

Figure 2. Diagram of a De Laval nozzle. Flow enters from the left, reaching Mach 1 at the throat, and expands outward to the right in order to provide thrust.

The use of magnetic nozzles, however, has led to the question of whether ionized particles detach from the magnetic field lines after being ejected. The answer to this question is vital to the practicality of magnetoplasma engines. If a subset of these particles fails to detach, then those particles can follow the field lines back to the spacecraft and impact upon spacecraft surfaces. These impacts could result in degraded performance or a shortened lifespan for the impacted equipment.

2.4 Magnetic Nozzles

Much research has been done on the acceleration of plasma particles caused by a divergent magnetic nozzle, which magnetoplasma engines use to convert magnetic pressure into vehicle thrust. The magnetic nozzle was investigated to determine the point at which ejected particles detach from the magnetic field[3]. In the 1950s, studies

of the solar wind led to the proposition that plasma detaches from a magnetic field when the flow velocity exceeds the local Alfvén velocity[4]. Alfvénic waves propagate along the external magnetic field through plasma at a constant rate known as the Alfvén velocity. Once plasma has left the engine's nozzle, any particles that have achieved Alfvénic velocity or faster are predicted to detach from the engine's magnetic field lines and provide horizontal thrust[5]. Current research with the VASIMR® VX-200 indicates that almost all of the plasma particles escape the magnetic field[6].

Ahedo and Merino took one dimensional nozzle models and developed a two dimensional, collisionless, two fluid magnetohydrodynamic (MHD) model[7]. Winglee et al. showed that for super-Alfvénic flow from a high power helicon thruster nozzle, the magnetic field is insufficient to pull the plasma back to the thruster[8]. Therefore, these plasma particles will detach from the field lines and escape as thrust.

However, some particles are traveling at sub-Alfvénic velocity and will follow the field lines into the engine's backfield. If the plasma density decreases near the nozzle wall of a magnetoplasma engine, there may exist a thin sub-Alfvénic boundary layer[9]. The sub-Alfvénic layer may not be able to detach[9]. Not only could a sub-Alfvénic layer exist, but plasma particles that are initiated far from the engine's centerline axis may become trapped by the field and eventually collide with the spacecraft[10].

Particles with sub-Alfvénic velocities do not have sufficient kinetic energy to detach from the magnetic field lines and will follow these field lines into the engine backfield, where the particles may collide with spacecraft structure.

2.5 Engines using Magnetic Nozzles

As magnetic nozzles are a relatively new development in rocket propulsion, there are only a few engines utilizing this type of nozzle to focus and accelerate ejected plasma. None of the engines have flown in space yet. Examples of engines that use magnetic nozzles include the High Power Helicon (HPH) thrusters, Helicon Double Layer Thruster, Magnetoplasma Dynamic (MPD) thrusters, and the Variable Specific Impulse Magnetoplasma Rocket (VASIMR®). HPH thrusters generate helicon waves to heat a plasma without the use of a cathode[8]. The plasma is confined and accelerated by use of a magnetic field and nozzle. Similarly, the Helicon Double Layer Thruster generates helicon waves and current-free double layers in radio frequency plasmas, along with a magnetic nozzle, to accelerate ions to supersonic speeds[11]. MPD thrusters have cathodes and use the Lorentz force, which is made up of both the electrical and magnetic force on point charges within the plasma, to focus and accelerate the plasma[12].

Lastly, the VASIMR® engine is a relatively new type of magnetoplasma engine that accelerates a radio-frequency (RF) generated plasma to high velocities, producing thrust of about 5.8 N for the VX-200 version[6, 13, 14]. VASIMR® was invented by Dr. Franklin Chang-Díaz. It uses a magnetic nozzle, which serves to channel and accelerate the plasma. As all magnetic field lines form closed loops, the ejected plasma must then detach from the magnetic field lines in order to provide thrust.

The VASIMR® engine consists of three major subsystems: the plasma generator stage, the RF booster stage, and the magnetic nozzle stage (Figure 3)[15]. In the plasma

generator stage, gas is ionized forming plasma through a collisional process using radio frequency (RF) waves launched by a helicon antenna. In the RF booster stage, an ion cyclotron radio frequency (ICRF) antenna energizes the ions before reaching the magnetic nozzle. In the magnetic nozzle stage, the plasma is accelerated to provide thrust. The ejected plasma must then detach from the magnetic field lines. Superconducting magnet coils surround the plasma during the three stages limiting damage to the engine walls. The only inputs for the VASIMR® engine are electrical power, coolant for the electronics, and argon gas (or deuterium, hydrogen, krypton) as propellant.

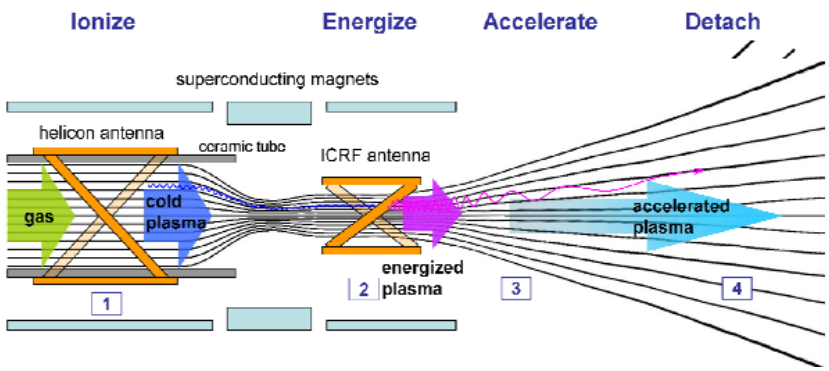

Figure 3. Diagram of the VASIMR® engine.[16] **The helicon antenna generates the plasma and the ICRF antenna adds kinetic energy to the plasma.**

The VX-200 device is an experimental version of VASIMR® which has a maximum power level of 200 kW as input to the RF antennas. It was built and is currently being tested at the Ad Astra Rocket company facility in Houston, TX. A flight

version of the VX-200, called VF-200, may be installed and test-fired on the International Space Station (ISS) in the future (Figure 4).

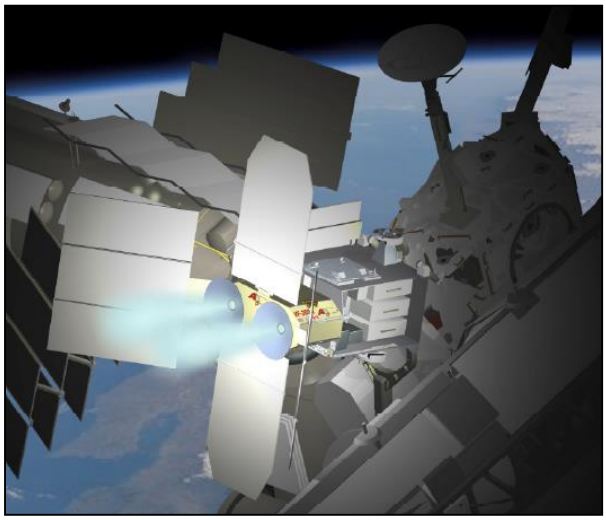

Figure 4. Illustration of the VASIMR® VF-200 engine installed and firing at the ISS.[17]

2.6 VASIMR® Research

Investigators such as Chang-Diaz[13], Glover[18], Squire[16] et al. from the Ad Astra Rocket Company, Bering[15] from the University of Houston, Longmier[19] from the University of Michigan, and Bengtson[20] from the University of Texas at Austin conducted research on the VASIMR® VX-200 engine. Their research focused on the helicon source, the exhaust plume, and the confining supercooled electromagnetic rings.

Their research can be broken down into a) updates on the development and testing of the VX-10[21], VX-25[22], VX-50[23], VX-100[19], and VX-200[16, 24] engines, b) exhaust plume structure and diagnostic methods, and c) VASIMR®'s

suitability for use as propulsion for interplanetary missions. Updates have been reported steadily over a decade of testing and development at Ad Astra's Houston location. These results include thruster efficiency improvements and ionization cost reductions. Exhaust plume structure has been analyzed to show the current density profile and force on a graphite target[25].

Olsen et al. made careful measurements of the VX-200 in 2013 to find that the "frozen-in flow" theory, where the plasma is expected to stretch the magnetic field lines, was not occurring[26]. There was no observed difference in magnetic field lines when the plasma was present and not present. Olsen also did not observe predominant magnetization of the ions radially farther away from the plume centerline where the magnetic field lines curve. However, measured data did show that ions could become trapped in areas in high magnetic field regions, where the magnetic field lines have high curvature, and when ions had lower velocities. Olsen et al. concluded that electrons are more tightly bound in stronger magnetic fields and ions are temporarily trapped as the field lines expand. However, as the ions get farther from the engine, the magnetic field weakens, the ions escape, and electrons are pulled from following the magnetic field lines in pursuit of the fleeing ions. The plume was effectively detached about 2 m downstream of the nozzle throat (or roughly 1.4 m from the engine exit). This paper is very relevant to the research presented here as plasma detachment is the question with magnetic nozzles.

Loss of adiabaticity was the detachment theory that was most consistent with the experimental data from the VX-200[26]. The data also showed that, due to large

differences in collision frequency between electrons and ions, any collisions between ions and neutrals can be ignored.

Whether to treat the plasma as a continuous fluid or as a group of individual particles was determined using experimental data from Bering[6]. The Knudsen number for the measured plume was calculated using a current density gradient from Literature so that

$$Kn = \frac{L_{mfp}}{Q}\left|\frac{dQ}{dz}\right| \tag{2-1}$$

where L_{mfp} = the mean free path distance between particle collisions (m)

Q = the current density of the plasma (A/m^2)

z = axial distance from the engine exit (m)

The mean free path was found to be 7.06 m, which means that ejected particles do not collide with another particle until over 7 m downstream of the engine exit. Therefore, the plasma can be considered collisionless within the immediate (< 7 m) area downstream of the engine. The Knudsen number is gradient- and length-scale based as shown in dQ/dz. The Knudsen number's value at the VX-200's maximum power setting (i.e. ICH full) using the ion temperature is 117 and using the electron temperature is 3.27. Both Knudsen numbers are above 1 indicating that the assumption of a continuous fluid is not correct. Therefore, treating the plasma as a group of individual particles is required.

2.7 Particle Detachment from Magnetic Fields

Several papers have been written to describe detachment of particles from magnetic field lines of a magnetic nozzle[9, 13]. Plasma detachment from a magnetic nozzle is possible even when using an ideal MHD simulation[9]. As the ratio of dynamic pressure to magnetic pressure approaches unity at the magnetic nozzle, the plasma will be able to detach from the magnetic field due to sufficient energy[3].

There are five types of plasma detachment[4]:

a. Kinetic detachment
b. Loss of Adiabaticity detachment
c. Resistive detachment
d. Recombination detachment
e. Electron inertia detachment

Kinetic detachment happens when the plasma particles attain super-Alfvénic velocity and detach from the magnetic field lines. The ratio of plasma kinetic energy to the energy in the magnetic field will increase along the magnetic nozzle until the ratio between kinetic energy and magnetic field energy reaches unity at which point the plasma is theorized to detach from the magnetic field[4]. This ratio can be written as the square of the ratio of plasma velocity to the Alfvén velocity, V_A:

$$\beta = \frac{\rho u^2/2}{B^2/(2\mu_0)} = \left(\frac{u}{B/\sqrt{\mu_0\rho}}\right)^2 = \left(\frac{u}{v_A}\right)^2 \text{[4]} \quad (2\text{-}2)$$

where $v_A = \frac{B}{\sqrt{\mu_0\rho}}$ (2-3)

ρ = density (kg/m^3)

u = velocity (m/s)

B = magnetic field (T or N/Am)

μ_0 = permeability of free space or magnetic constant (N/A^2)

This research could determine if Kinetic detachment is occurring as a form of model validation.

Loss of Adiabaticity detachment results when the magnetic field has a strong spatial gradient[4]. In this theory, ions may detach from the magnetic field lines but the electrons may not, so the ions will either not totally detach (to maintain quasi-neutrality) or will pull the electrons with them (to maintain quasi-neutrality). Olsen et al. stated that loss of adiabaticity was the theory most consistent with the VX-200 experimental data[26]. The limits of the model chosen for this research are such that the plasma particles lose adiabaticity at the limit and beyond so that detachment is assumed.

Resistive detachment is caused by a sufficiently resistive plasma, which supports collisionally driven plasma transport transverse to the magnetic field[4]. Resistive detachment relies on ion collisions, but Olsen et al. found that ion and neutral collisions could be ignored due to VX-200 experimental data[26]. As such, resistive detachment will not be addressed in this research.

Recombination detachment is not considered a viable form because the ions and electrons do not recombine within the residence time of the engine. The recombination rates are generally too low within the nozzle area.[9] Recombination detachment will not be addressed in this research.

Electron inertia detachment is proposed to occur because electrons have finite mass and can inhibit the flow of azimuthal currents in the nozzle leading to collisionless detachment. However, this effect is extremely minimal and will not be considered in this research. It can represent a lower limit of possible particle detachment [4].

These detachment mechanisms can further be characterized as collisional, collisionless, or magnetic reconnection detachment[27]. Resistive and recombination detachments are considered collisional detachment. Kinetic and Loss of Adiabaticity detachments are forms of collisionless detachment. Magnetic reconnection detachment results in magnetic "islands" where ejected plasma tears the magnetic field lines and causes them to reconnect. As the magnetic field was not found to be stretched during VX-200 testing[28], no magnetic reconnection detachment is assumed here.

2.7.1 Detachment Methods Used in this Research

As previously mentioned, the only two detachment methods used in this research are Kinetic detachment, where particles exceeding the local Alfvénic velocity detach, and Loss of Adiabaticity detachment, where the magnetic field changes or drops off faster than a particle can react to it. These detachment methods are particle-based and do not require the assumption of a continuous fluid because the engine plume is too rarefied as discussed in Section 2.6 VASIMR® Research. The engine plume is also assumed to be collisionless (as mentioned in Section 2.6 VASIMR® Research), and Kinetic and Loss of Adiabaticity are collisionless detachment methods.

2.8 Plasma Plume – Spacecraft Interaction

2.8.1 Plasma Environment around a Spacecraft

Research has been done on plasma ejection from the Plasma Contactor Unit (PCU) onboard the ISS and the effect the Earth's magnetic field has on this plume[29]. It was found that an ejected low density plume from the PCU (Figure 5) had an enormous effect on the distribution of electric currents and potentials between ISS surface elements. No attempt was made to determine the effect of the plume on surface erosion. For example, it was determined that the geomagnetic field around the ISS ensured that the high-voltage areas of the solar arrays were bombarded by a maximum number of electrical charges from the PCU when the plume angle was equal to the sunlit-angle of the solar arrays[29].

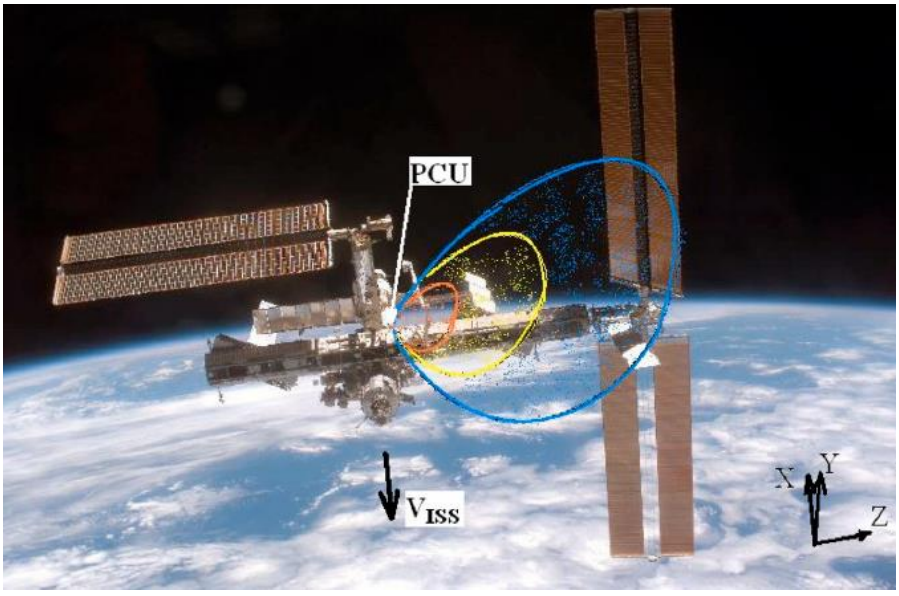

Figure 5. Illustration of "plasma bridge" or plume from PCU aboard of the ISS[29]**. The orange, yellow, and blue ellipses indicate different plasma densities and the boundary of ejected plasma from an ISS plasma contactor unit (PCU).**

Another finding was that the electrical current in the PCU was amplified when the PCU magnetic field lines crossed conductive parts of the solar arrays, leading to a "plasma bridge" process where electrons in the plume followed field lines into the solar arrays[29].

Both of these findings are relevant to this research because it verifies that electrical charging to the ISS was occurring due to ejected plasma into a magnetic field. This process is likely to occur with operation of any magnetoplasma spacecraft engine installed on the ISS.

2.8.2 Erosion due to Plasma Impingement

As particles impact a surface, some amount of surface particles are eroded and ejected. Experimental rates of erosion by plasmas have been documented by many sources. Behrish et al. did numerous physical experiments to determine what effect ions have on metallic surfaces at different energy levels [30]. An example of this research for argon gas ions on an aluminum surface can be seen in Figure 6. As the argon ion kinetic energy increases, the amount of aluminum particles eroded from the aluminum surface also increases. Aluminum was chosen as a surface material to determine an erosion rate because it is used on the exterior of the ISS in its Micro-meteoroid and orbital Debris Protection System (MDPS) and would thus likely be used on future spacecraft as well. Silicon was chosen as the other surface material to determine an erosion rate on the solar array panels which generate the electrical power for various spacecraft.

The sputtered atom yield from plasma particle impacts onto a surface can be written as[30]

$$Y(E_0) = qS_N^{KrC} \frac{\left(\frac{E_0}{E_{th}} - 1\right)^{\mu}}{\lambda + \left(\frac{E_0}{E_{th}} - 1\right)^{\mu}} \tag{2-4}$$

where E_0 = kinetic energy of impacting particle (eV)

Y = sputtering yield (particles eroded)

E_{th} = threshold energy (eV)

S_n^{KrC} = nuclear stopping power

λ, q, μ = experimental fitting parameters

The nuclear stopping power is defined as

$$S_N^{KrC} = \frac{0.5\ln(1+1.2288\varepsilon)}{\varepsilon+0.1728\sqrt{\varepsilon}+0.008\varepsilon^{0.1504}} \tag{2-5}$$

where ε = the reduced energy

Experimentally-determined erosion rates for energy dependent sputter yield of argon ions on aluminum was taken by W. Eckstein and R. Behrisch and used to determine the curve fit for erosion rate in Figure 6 below[30]. The experimental data was taken using a vacuum chamber at ambient temperature which is not exactly same as what would be encountered in outer space. For instance, temperatures on the ISS range between 250°F in sunlight and -250° F in shadow.

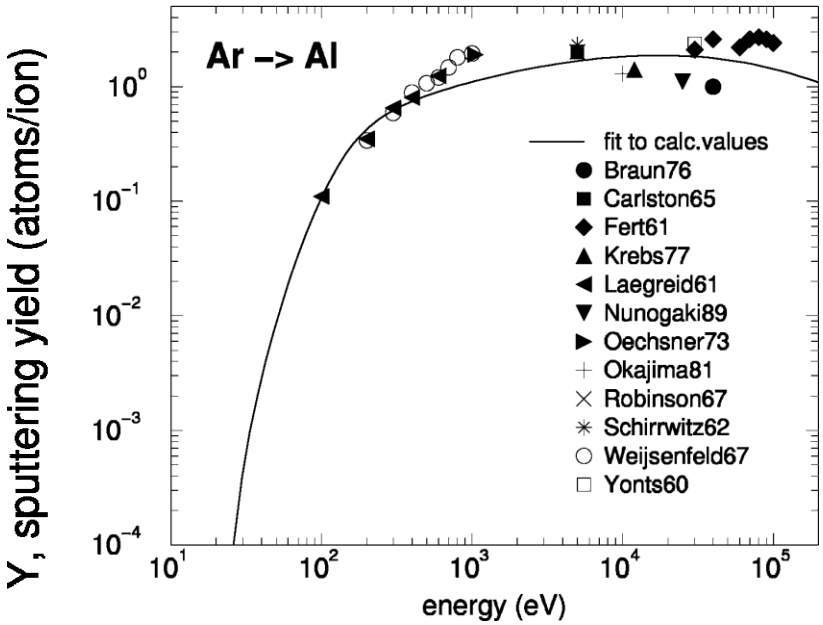

Figure 6. Energy dependence of sputtering yields of Al for bombardment at normal incidence with argon[30]**.**

Similarly, W. Eckstein and R. Behrisch plotted all available erosion data for argon ions impacting silicon surfaces and then added a curve fit as shown in Figure 7.

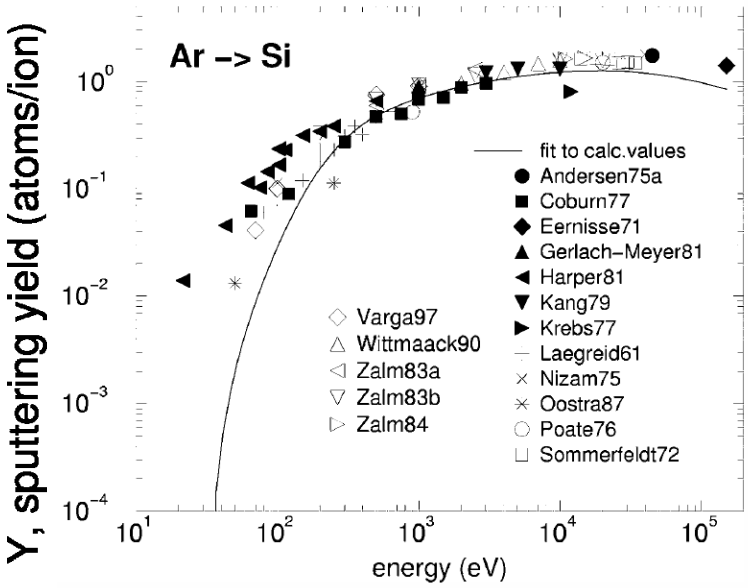

Figure 7. Energy dependence of sputtering yields of Si for bombardment at normal incidence with argon[30]**.**

In the following section, the necessary steps to perform this research are laid out in the form of a Need Analysis. Specifically, the individual components of the research are listed and how the components were implemented.

3. NEED ANALYSIS

3.1 Introduction

In the previous section, a firm understanding of magnetic nozzles, the VASIMR® engine, ion detachment from magnetic nozzles, and the plasma plume interaction with a spacecraft was presented. In this section, the necessary steps to determine the plasma environment around a magnetoplasma engine in space are presented in the form of a Need Analysis.

3.2 What Needs To Be Done

The following methods could be used to determine the amount of trapped or recirculating ions as a percentage of all ejected ions, the amount of electrical charging caused by impacting ions, and the amount of erosion on aluminum and silicon surfaces of a plasma spacecraft engine:

1. Launch a magnetoplasma engine to the ISS, test the engine, and observe and record the erosion and electrical charging in real time.
2. Test a magnetoplasma engine on Earth in a much larger vacuum chamber, such as Chamber A at the NASA Johnson Space Center, and observe and record the erosion and electrical charging in real time.
3. Simulate a magnetoplasma spacecraft engine plume in a supercomputer to estimate the erosion and electrical charging, using experimental data to validate the model.

Launching a magnetoplasma engine is a very complicated and expensive task to obtain the erosion and electrical charging data. Even using the Falcon 9 Heavy rocket being developed by SpaceX, the cost of launching a pound of payload to low Earth orbit will be about $1000 with the cost of launching any foreseeable magnetoplasma engine being over $1 million. The cost is beyond the means of this researcher and does not include the additional cost of the engine itself. Therefore, testing a magnetoplasma engine in space to determine erosion and electrical charging rates is not feasible at this time, but may become so after an engine is eventually launched and installed at the ISS.

Using a larger vacuum chamber to test a magnetoplasma engine is also problematic because although very large vacuum chambers do exist, the chambers are expensive to operate and cannot maintain a strong vacuum after the engine begins ejecting particles. For instance, the Chamber A vacuum chamber, located at the NASA Johnson Space Center, in Houston, TX, has a diameter of 65 ft, which is certainly large enough to allow particles to recirculate. It can provide a vacuum environment of around 1×10^{-6} torr (1.93×10^{-8} psia) but cannot handle engine outgassing of greater than 3×10^{5} liters/sec which leads to back pressure in the chamber. Back pressure leads to particle trajectories being interrupted by neutrals that existed in the chamber before the engine was operational and invalidating the erosion and electrical charging data. Transporting a magnetoplasma engine to NASA JSC would be cost-prohibitive as would building a fully equipped larger vacuum chamber at the Ad Astra facilities. Therefore, testing a magnetoplamsa engine in a larger vacuum chamber is not feasible.

Lastly, simulating a magnetoplasma engine plume with a supercomputer could provide the erosion and electrical charging data that is wanted. There are a few reasons why a simulated numerical model of a magnetoplasma engine plume would be advantageous over testing an actual engine either at the ISS or in a larger vacuum chamber. The cost is considerably less to use the supercomputers at Texas A&M, a perfect vacuum can be created which is not effected by any engine outgassing, and many changes can be done to the model to test different factors that may change the engine plume properties. Therefore, a simulated computer model of a magnetoplasma engine plume was chosen to determine the erosion and electrical charging caused by recirculating particles.

To develop a numerical model for this research to be accurate, it must be able to provide:

1. A simulation of the a magnetoplasma engine plume
2. A simulation of the immediate space environment around the a magnetoplasma engine
3. A simulation of the magnetoplasma engine's magnetic field
4. A simulation of the engine surfaces including radiator panels

In the next section, the development of the numerical model is explored in greater detail and the specifics are explained in Section 4.

3.3 Implementation (How to Meet the Objective)

A simulation of a magnetoplasma engine's plume and backfield environment was created to determine the quantity and kinetic energy of recirculating particles. The top-

level functions of the simulation are: 1.) provide a means to determine which particles impact structure, and 2.) provide a means to determine damage, including charge buildup, to structure and sub-systems resulting from the impacts. The full Functional Decomposition can be found in Appendix C at the end of this dissertation.

1.) Determining which particles impact structure will require knowledge of which particles are trapped by the engine's magnetic field and follow the field lines into the engine backfield and which trajectories actually intersect with structure or a sub-system (such as a solar panel or docked spacecraft at the ISS). This requires information on:
    a. Which particles recirculate along magnetic field lines
    b. The initial conditions at the engine exit (plume)
    c. Particle velocity distribution in the backfield

2.) Determining damage to structure and sub-systems caused by impacts from returning plasma particles trapped by the magnetic field lines will require knowledge of the energy distribution in the backfield to determine the erosion rate, charge build-up, and deposition due to particle impacts.

The functional decomposition was used to track research progress. Here is how each component was addressed:

1.0 Provide a means to determine which particles impact structure.

1.1 Provide a means to determine particle trajectories in the backfield

1.1.1 *Determine which particles recirculate along B field lines.* As continuum physics was determined to not be applicable in the plume region, no detachment methods were assumed. Therefore, all particles followed the magnetic field lines. However, particles that had not entered the backfield within the 30 m sphere were assumed to have "escaped" to provide thrust.

1.1.2 *Initial flow conditions at the engine exit*.

1.1.2.1 *Magnetic field at exit.* The magnetic field was modeled in a commercial finite element analysis software called COMSOL Multiphysics® using experimental data. Due to International Traffic in Arms Regulations (ITAR) restrictions, the exact field strength at the engine exit was not provided but was determined by the COMSOL model.

1.1.2.2 *Particle velocity vector distribution at exit.* The velocity distribution of the ions and electrons was taken from literature at z = 0.3 m and is discussed in section 4.3.2.

1.1.2.2.1 *Particle angle at exit.* Particle angle was assumed to match the magnetic field line angle at the particle's location with respect to the plume centerline.

1.1.2.2.2 *Particle speed at exit.* Particle speed is derived from experimental data.

1.1.2.3 *Particle charge distribution at exit.* The charge distribution was assumed to be quasi-neutral with an equal number of ions and electrons.

1.1.3 *Particle velocity vector distribution in backfield*

1.1.3.1 *Particle angle.* The location of every particle was tracked by the numerical model. The particle angle comes from the distance travelled between time steps.

1.1.3.2 *Particle speed.* The speed of every particle was tracked by the COMSOL model.

1.2 Provide a means to determine which particle trajectories impact structure.

1.2.1 *Particle trajectories in the backfield.* The numerical model tracked all particle trajectories that entered the backfield.

1.2.2 *Spacecraft / Engine dimensions.* The dimensions for the magnetoplasma spacecraft engine were chosen to be similar to the VX-200 and were derived from published photos or diagrams in literature from the Ad Astra Rocket Company.

1.2.3 *Engine location in spacecraft.* The ISS was not modeled due to the enormous processing load this would have added to the numerical model.

Instead, particles impacting a representative engine housing and radiator panels were modeled.

2.0 Provide a means to determine damage to structure.

2.1 Provide a means to determine particle trajectories in the backfield that impact structure. The numerical model tracked all particle trajectories, including ones that entered the engine backfield and impacted the engine housing or radiator panels.

2.2 Provide a means to determine energy distribution in the backfield

2.2.1 *Particle charge distribution.* The number of ions was tracked by the numerical model over the entire timescale. The number of impacting ions was used to determine the electric field on the spacecraft surface.

2.2.2 *Particle kinetic energy.* The kinetic energy of every particle was tracked by the numerical model over the entire timescale. The ions had a mass equivalent to an argon atom (6.633×10^{-26} kg).

2.3 Provide a means to determine erosion rate due to particle impacts

2.3.1 *Particle velocity of impacting particles*. The numerical model was used to keep track of what particles entered the engine backfield and impacted the engine housing or radiator panels and their impact velocity.

2.3.2 *Structure surface conditions*. The surface was assumed to be aluminum and smooth. The erosion rate was determined by using Behrisch's Sputtering Yield data[30] and the kinetic energy of impacting particles from the numerical model.

2.4 Provide a means to determine charge build-up due to particle impacts

2.4.1 *Particle trajectories that impact structure*. The numerical model was used to determine which particles entered the engine backfield and impacted the engine housing or radiator panels.

2.4.2 *Particle charge*. The ions are positively charged.

2.4.3 *Structure charge*. The charge of impacting particles on structure was recorded. Charge was assumed transferred to the structure.

In this section, a need analysis was presented with what steps are required to successfully determine the plasma environment around a magnetoplasma spacecraft engine in space and the effect that environment will have on spacecraft surfaces. The next section will present how the determination was carried out.

4. MODEL

4.1 Introduction

In the previous section, the necessary steps to determine the plasma environment around a plasma spacecraft engine in space were presented in the form of a Need Analysis. In this section, the actual methods used to achieve this determination are listed. Specifically, the determination was made using a three dimensional computer simulation because a 3-D numerical model is the only method available to determine particle trajectories due the size of the zero pressure volume required was larger than any current vacuum chamber. Furthermore, the need for a perfect vacuum in order to ensure that ejected particles would not interact with ambient particles was also a consideration, and this perfect vacuum can only be achieved inside a numerical model, except for high Earth orbit itself. Outside of actually flying a magnetoplasma engine in outer space, a computer simulation is the most accurate way of predicting the plume – spacecraft interaction.

The commercial finite element analysis software package, COMSOL Multiphysics®, was chosen to do the simulation so that a high degree of accuracy could be obtained within a reasonable timeframe. The software consists of many modules, of which the AC/DC and Particle Tracing modules were used for this research. The components of this module employed for this research were a) magnetic field simulation for multi-turn coils and b) charged particle tracing. Simple problems, such as Hagen-Poiseuille flow and Hartmann flow, with known results were simulated using the Multiphysics® software to validate its accuracy with fluids (in Appendix A and B,

respectively). It was not possible to validate the accuracy of the particle tracing module beyond verifying that particles do deflect in a magnetic field.

The numerical model and particle tracing software module were used to simulate the trajectory of ions and electrons to determine the resulting electric field. However, as electrons make up less than 0.01% of the total mass ejected per second and their average kinetic energy is below the threshold energy needed to cause erosion, they contribute nothing to the total erosion rate. Therefore, the erosion rate was calculated from the ions only. The entire process is explained in more detail in Section 5.5.

The tools used in this research were:

- A PC running 64-bit Windows 7 Professional with an Intel® Core2 Quad CPU Q6600 @ 2.40 GHz
    - COMSOL Multiphysics®, version 4.3.0.233
    - MATLAB®, version 7.12.0.635 (R2011a), 64-bit
    - MS Excel®
- EoS, a 3168-core IBM (iDataPlex) Linux cluster, at the Texas A&M Supercomputer Facility
- KAT Mini-cluster in the Texas A&M Chemical Engineering department

4.2 Assumptions

1. The plume is assumed to be 100% ionized. No neutrals were included in the model to provide a worst case scenario, as collisions with neutrals would lower the average kinetic energy of impacting particles and lower the erosion rate. However, impacts with neutrals may lead to more ions remaining trapped in the magnetic field.

2. All particles are assumed to be magnetized at the model inlet, z = 0.3 m downstream of the engine exit, and are following the magnetic field lines at the start of the simulation.
3. The magnetic field lines are not altered by movement of particles within the plasma plume to simplify the model because Olsen[28] did not find any field line stretching. This research does not simulate "magnetic islands".
4. Any ions that reach the 30 m limit in the computer model are assumed to have escaped the engine's magnetic field and will not return because the magnetic field strength at 30 m is negligible. This assumption comes from the Loss of Adiabaticity detachment method.
5. The plume was assumed to be collisionless because analysis of a magnetic nozzle can be made with a collisionless, quasi-neutral plasma[10]. Collisions enhance plasma detachment, so the worst case conditions can be obtained by using a collisionless plasma for the model[10]. The Debye length was found to be 3.8×10^{-8} m at maximum argon mass flow rate, which is so small that only a negligible amount of particles "see" each other. The mean free path was found to be about 7 m, so particles will be away from the magnetic nozzle before any particle is expected to impact another. Therefore, because the Debye length is so small and the mean free path large, the assumption of collisionless plasma is valid.
6. The plasma was assumed to be in quasi-equilibrium with a Maxwellian distribution of particle kinetic energies so that a temperature exists.

7. The angle in which particles impact the aluminum surface has a negligible effect to the total erosion rate. The difference between the average impact angle, 23.91°, and a 90° impact is less than 0.029%, according to Behrisch[30]. This calculation can be found in Appendix I. Therefore, impact angle was not used in determining the erosion rate.
8. Density distribution of all particles is assumed to be the same for all velocities. This is discussed more in section 4.3.2.
9. Velocity distribution of all particles is assumed to be the same from r = 0 m to r = 0.7 m at z = 0.3 m. This is discussed more in section 4.3.2.

4.3 Solution Approach

4.3.1 Introduction of the Solution

A magnetoplasma engine transforms gas (such as argon) into plasma and ejects it. In order to model the argon ions being ejected, the following must be known: electric field strength, magnetic field strength, argon mass flow rate, density distribution profile, and the velocity distribution profile. The electron and ion density were assumed to be the same for a quasi-neutral plasma. Experimental data from the VX-200 (given at z = 0.3 m downstream of the thruster exit) was utilized for the particle density and energy distribution functions of the ions as an inlet condition. The particles were subjected to magnetic and electric forces and their equations of motion were integrated over time to determine the particles' Lagrangian trajectories.

4.3.1.1 Full Factorial Experiment

Three factors were explored using the numerical model with 2 variations (high and low). These factors were 1.) the plasma's velocity profile at high and mid-power to the ICH antenna, 2.) the magnetic field strength with high and low current to the coils, and 3.) the density profile with narrow or wide distribution around the plume centerline. The factors were chosen because they were believed to be the most important in governing whether a particle recirculates into the backfield and impacts the spacecraft structure or not. By using a full factorial experiment, the manipulation of more than one of these independent variables can be done in the same experiment. The variables A, B, and C are assigned as follows:

A_{high} (+1) = Velocity distribution with ICH/RF = 6 ($\bar{V}$ = 29.7 km/s, FWHM = 23 km/s)

A_{low} (-1) = Velocity distribution with ICH/RF ≈ 3 ($\bar{V}$ = 24.4 km/s, FWHM = 10 km/s)

B_{high} (+1) = Magnetic field strength with I = 140 A

B_{low} (-1) = Magnetic field strength with I = 70 A

C_{high} (+1) = Density distribution with P_{ICH} = 100 kW (ICH/RF≈ 3, $\bar{r}$ = ±0.205 m)

C_{low} (-1) = 20% wider density distribution with P_{ICH} = 100 kW (ICH/RF≈ 3, $\bar{r}$ = ±0.25 m)

These 3 factors were varied over 8 runs of the numerical model in the configuration found in Table 1.

Table 1. Full Factorial Experiment configuration for each run

Run	A	B	C	AxB	BxC	AxC
1	-1	-1	-1	1	1	1
2	1	-1	-1	-1	1	-1
3	1	1	-1	1	-1	-1
4	1	1	1	1	1	1
5	-1	1	1	-1	1	-1
6	-1	-1	1	1	-1	-1
7	-1	1	-1	-1	-1	1
8	1	-1	1	-1	-1	1

Other factors that could have been explored are magnetic field geometry due to placement of the three magnetic coils, mass flow rate of argon, and the use of krypton and other gases. These were not considered here but are included in Section 6.7 Recommendations for Future Work.

4.3.2 Trajectory Model

The trajectory model was created within the COMSOL Multiphysics® software as shown in Figure 8. The software has been used extensively to model complex phenomena of interest to researchers. A quick survey of literature online finds that over 5,000 peer-reviewed published articles have been written that used COMSOL Multiphysics® to develop either all or in part of the data discussed in the research paper.

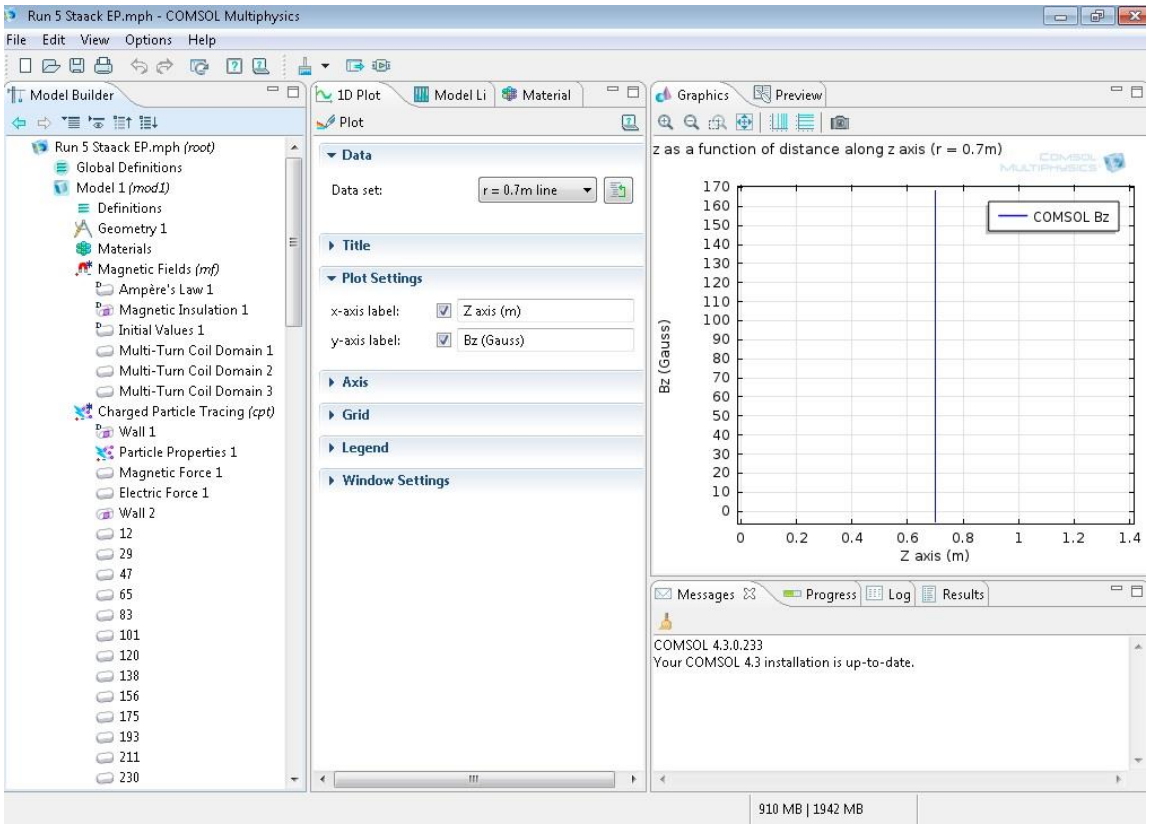

Figure 8. COMSOL Multiphysics® software running the magnetoplasma engine model.

4.3.2.1 Boundary & Initial Conditions

4.3.2.1.1 Magnetic field

The magnetic field in the numerical model was calculated using 3 solenoid coils with several geometric and operating parameters of the solenoid chosen to have the calculated field match several dozen experimental determined data points in the far field plume provided by the Ad Astra Rocket Company. Comparisons of the magnetic field in the z direction for the numerical model and from VX-200 data along the z axis (r = 0 m) are shown in Figure 9 and Figure 10. The numerical model generated B_z (red dotted line)

match the VX-200 experimental B_z data (blue solid line) with an average error for B_z = 3.83%. Figure 11 plots B_r along the z axis with an average error for B_r = 7.64%.

The numerical model generated magnetic field very closely matches both the radial and axial field dependence of the VX-200, but, due to ITAR restrictions, this model makes no attempt to match the more complicated magnetic structure of the VX-200 or the field inside of the thruster. Although this research uses a magnetic geometry similar to the one from the VASIMR® engine, the results are relevant to all magnetoplasma spacecraft engines.

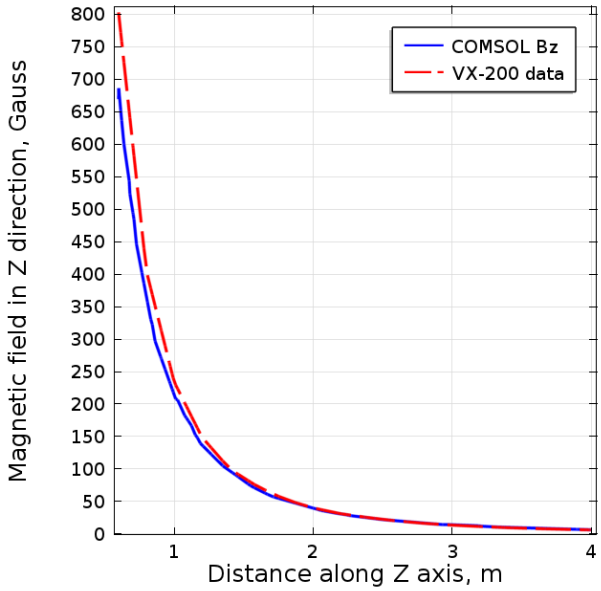

Figure 9. Magnetic field, B_z, from the numerical model at r = 0 m (centerline) compared to VX-200 data.

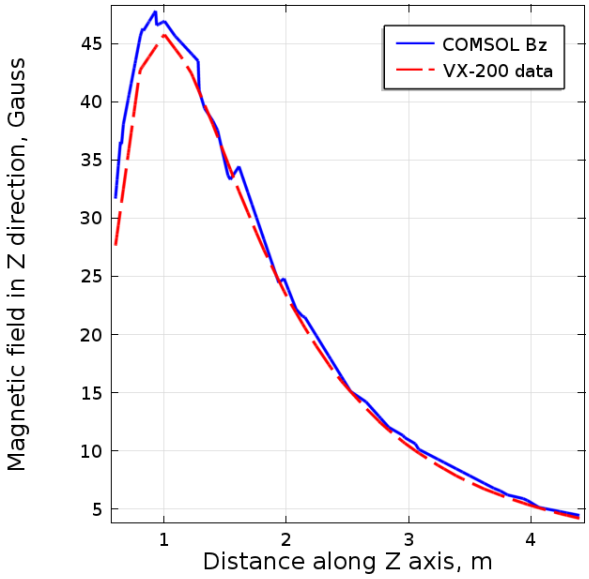

Figure 10. Magnetic field, B_z, from the numerical model at r = 1 m compared to VX-200 data.

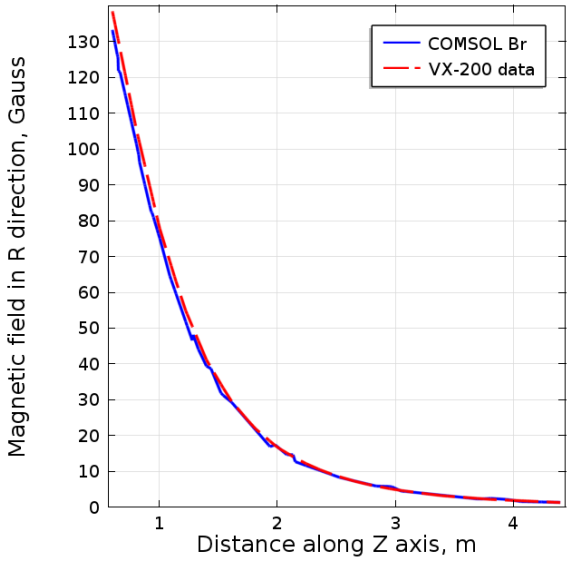

Figure 11. Magnetic field, B_r, from the numerical model at r = 1 m compared to VX-200 data.

4.3.2.1.2 Electric field

An electric field exists in the exhaust plume because the ions and electrons, having significantly different masses, leave the plume at different rates. To create as accurate a model as possible, the plume's electric field needs to be taken into consideration. This was done by comparing experimental data from Ad Astra with the ion densities simulated by the numerical model.

The experimental data provided the electric potential (in Volts) in the r and z directions, and the electric field (in V/m) was mathematically derived from this data. The result in the z direction is shown in Figure 12. These values are only averages because the instrumentation used by Ad Astra recorded fluctuations of as much as ±4 V. Even so, it is apparent that the electric field in the z direction is strong nearest to the engine and then quickly subsides. Beyond z = 4 m downstream of the engine, it is essentially zero.

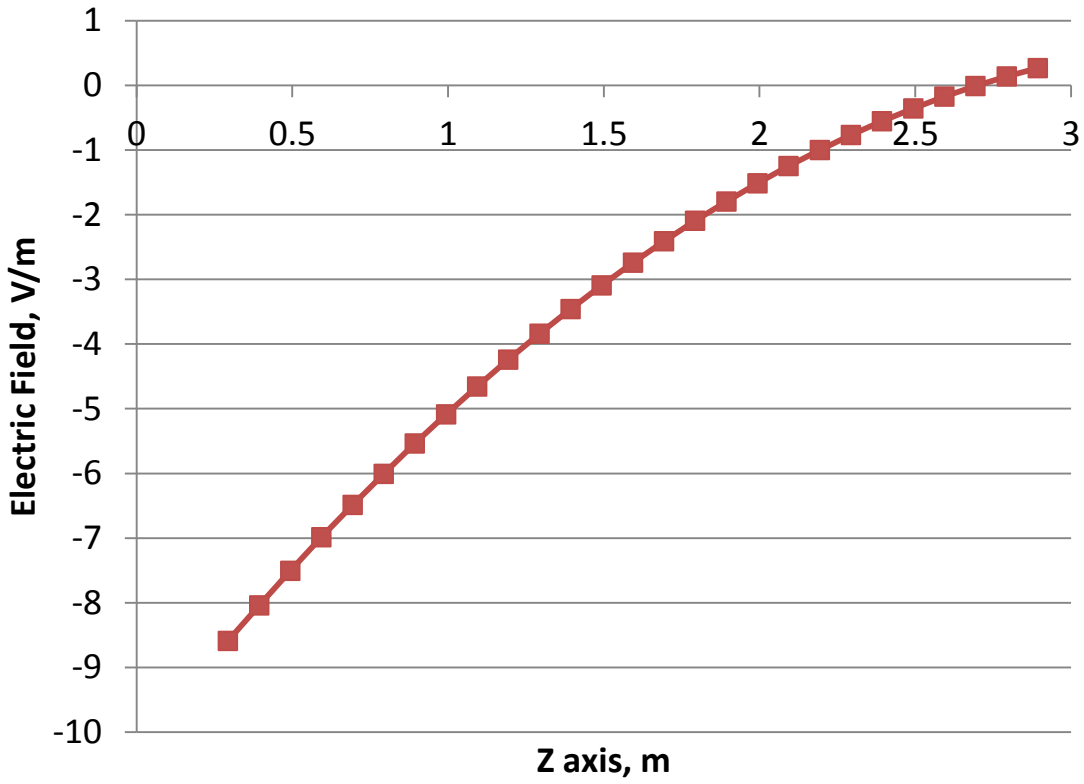

Figure 12. Electric field (in the z direction) derived from the VX-200 electric potential data provided by the Ad Astra Rocket Company.

The electric field in the r direction (Figure 13) does not have a symmetric pattern as would be expected on either side of the plume centerline (r = 0 m). This non-symmetry may be due to biasing with the instrument used or from an interaction between the grounded walls of the vacuum chamber in which the VX-200 was tested. Regardless, the electric field in the r and z direction was included in multiple numerical models to determine the effect it has on ions impacting the engine housing or radiator panels and the resultant erosion rate.

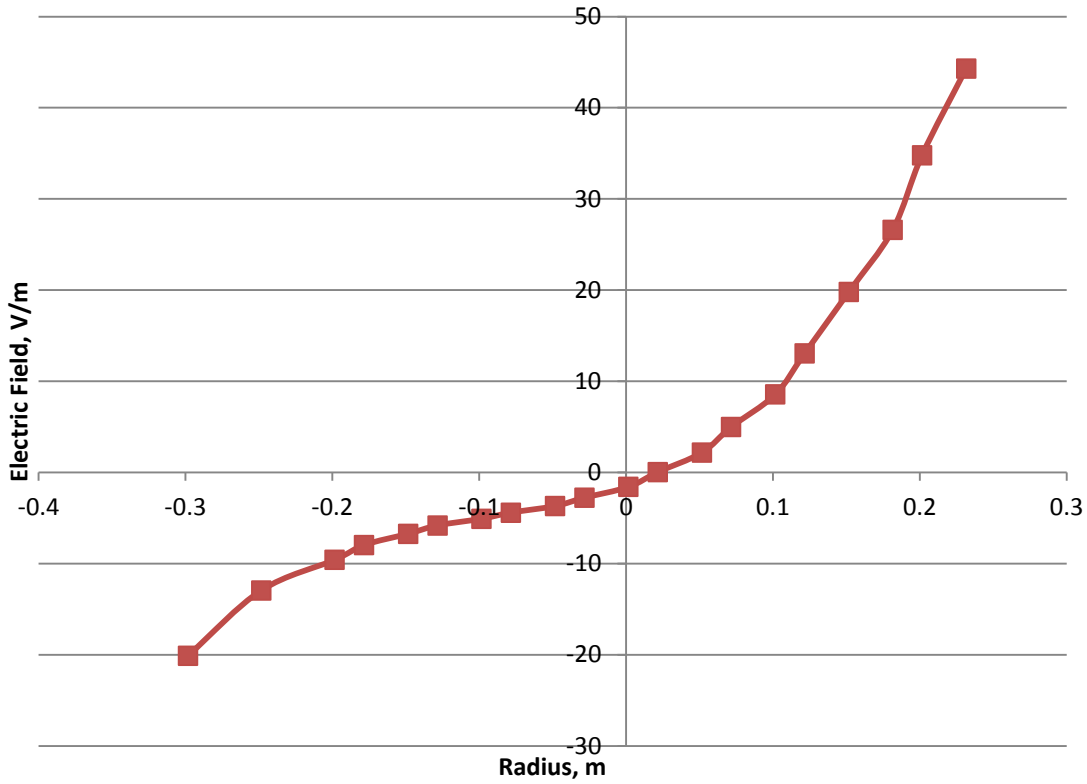

Figure 13. Electric field (in the r direction) derived from the VX-200 electric potential data provided by the Ad Astra Rocket Company.

It was determined that the electric field only led to a 7% increase in the number of ions impacting the engine housing and radiator panels and a 7% increase in the erosion rate. The difference is illustrated in Figure 14 where the green bar, representing the percentage of ions impacting, is nearly identical for 4 different electric field conditions.

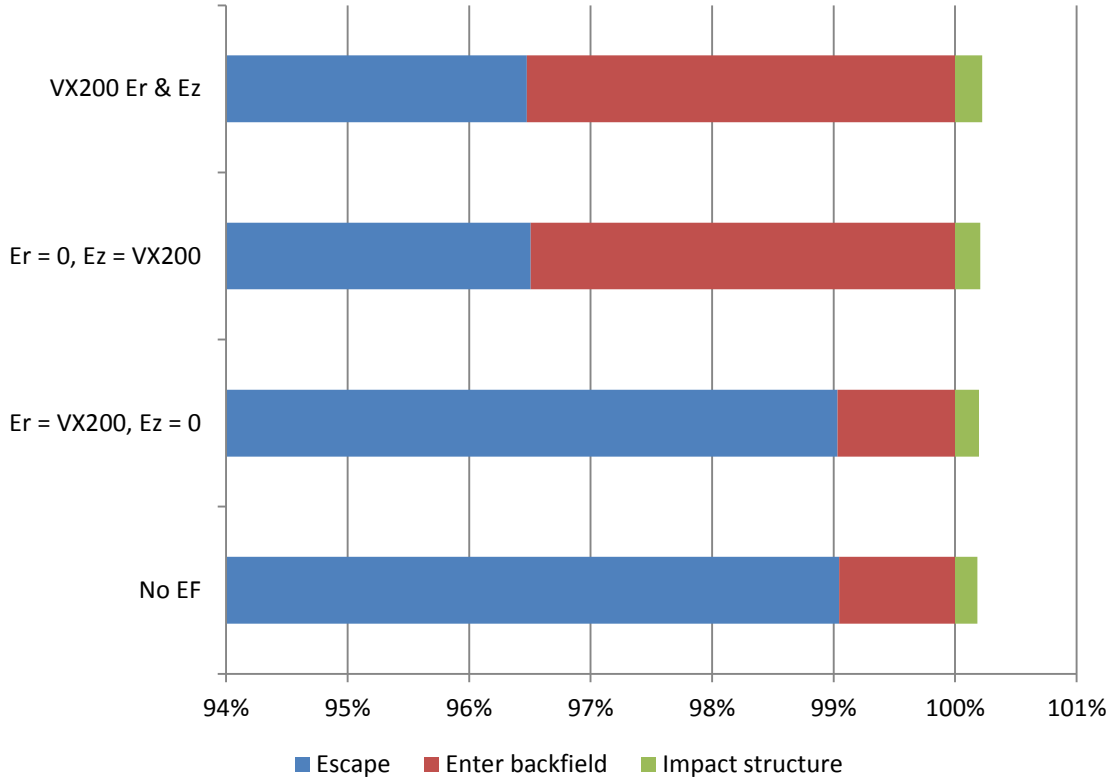

Figure 14. Effect of electric field on ion recirculation.

4.3.2.1.3 Plume density profile

Data on the VX-200's operating conditions, such as mass flow rate of argon gas (150 mg/s), come from papers published by the Ad Astra Rocket Company[31]. The ion flow rate was determined to be 2.26 x 10^{21} ions/s from the published maximum argon mass flow rate of 150 mg/s. The density distribution of ions ejected by the VX-200 was determined from the plume ion flux graph (Figure 15) taken at z = 0.3 m downstream of the engine throat at medium RF power (Figure 16) by Bering et al.[6]. There was a difference in opinion from the experimenters on the location of the Langmuir probe,

which was either z = 0.2 m or 0.3 m from the engine exit and wall. A sensitivity analysis was done to find that the error caused by using the wrong location was only 5.52%.

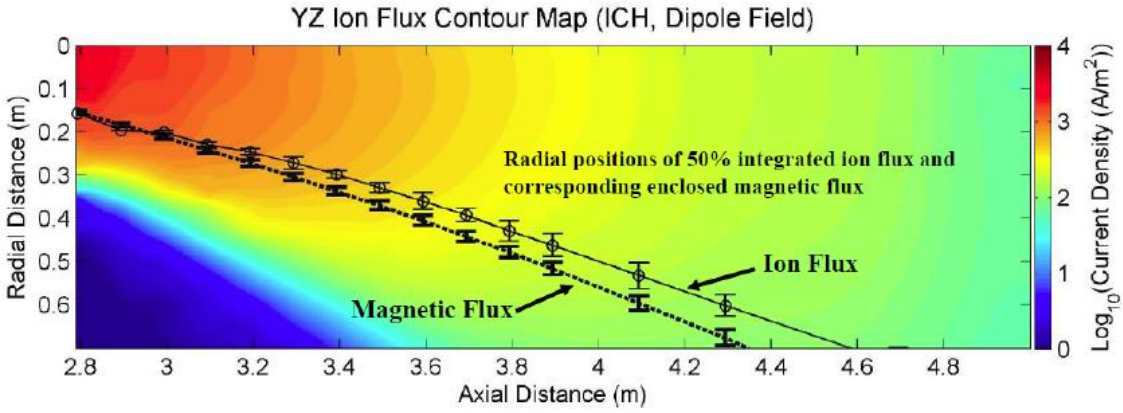

Figure 15. Experimental ion flux contour map from the VX-200[6]**.**

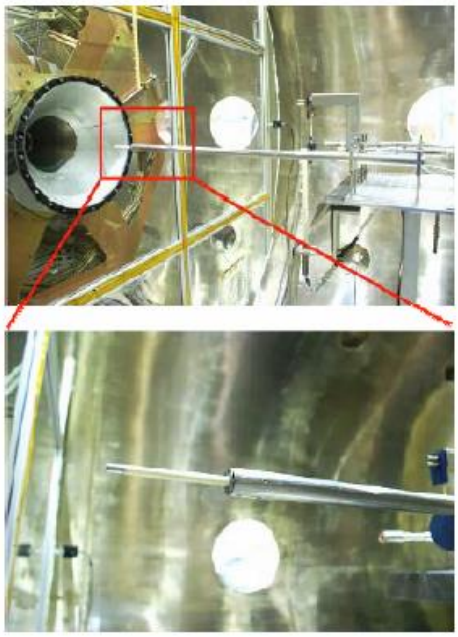

Figure 16. Photograph of a Langmuir probe with guard ring on a 70 cm extension shaft[6]**.**

The density profile was derived using the image read function in MATLAB® and an assumed average velocity of 25 km/s, which is shown to be accurate in Figure 21 (24.4 km/s). A plot of the density profile as a function of radial distance away from the plume centerline is shown in Figure 17 and is scaled to the maximum mass flow rate of argon used in VX-200 research. This density profile was then further processed in MATLAB®, using file "DensityProfile.m" in APPENDIX K, to create a narrow baseline density profile, where more particles are near the plume centerline, and a 20% wider density profile, where more particles initiate in the plume fringe (r > 0.3 m). The two density profiles are shown in Figure 18. The area under the curve is the same for both profiles.

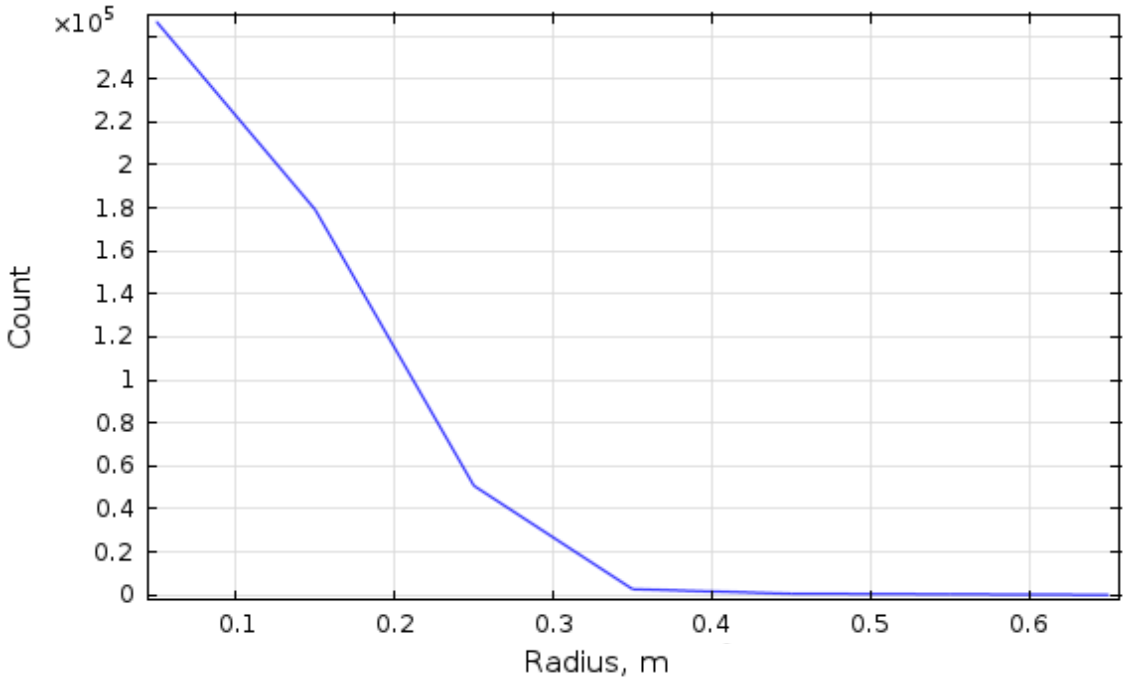

Figure 17. Ion density profile as a function of radial distance from the plume centerline at t = 0 s for Run 5.

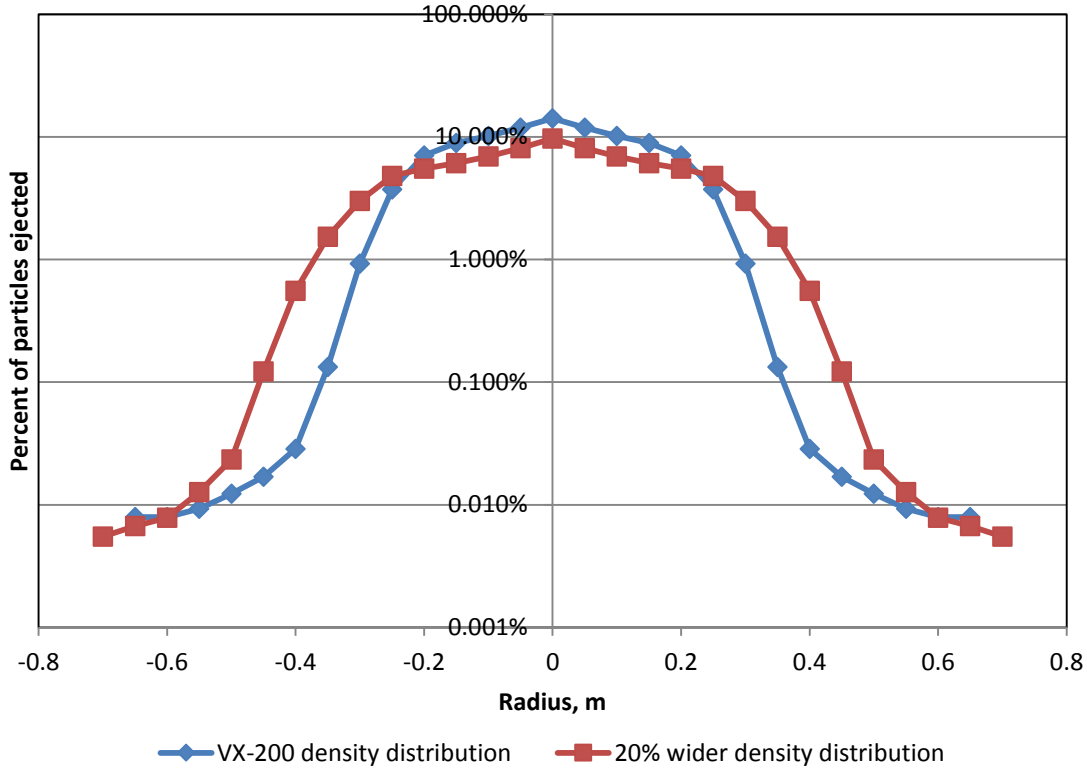

Figure 18. Log scale density distribution derived from the VX-200 plasma current density at ICH/RF≈3 and a 20% wider distribution.

4.3.2.1.4 Plume exit velocity distribution

The velocity distribution of particles was derived from the ion energy distribution graph (Figure 19) measured by Bering et al.[6]. The ion energy at the three RF power configurations were used when the ratio between power to the ion cyclotron resonance heating (ICH) radio frequency antenna and the helicon radio frequency antenna is equal to three and six (ICH/RF = 3 and 6). The velocity magnitude (along the plume's centerline) was calculated using the ion energy distribution on the assumption that the

retarding potential analyzer (RPA) was detecting the velocity magnitude because it was in a horizontal position downstream at z = 0.3 m.

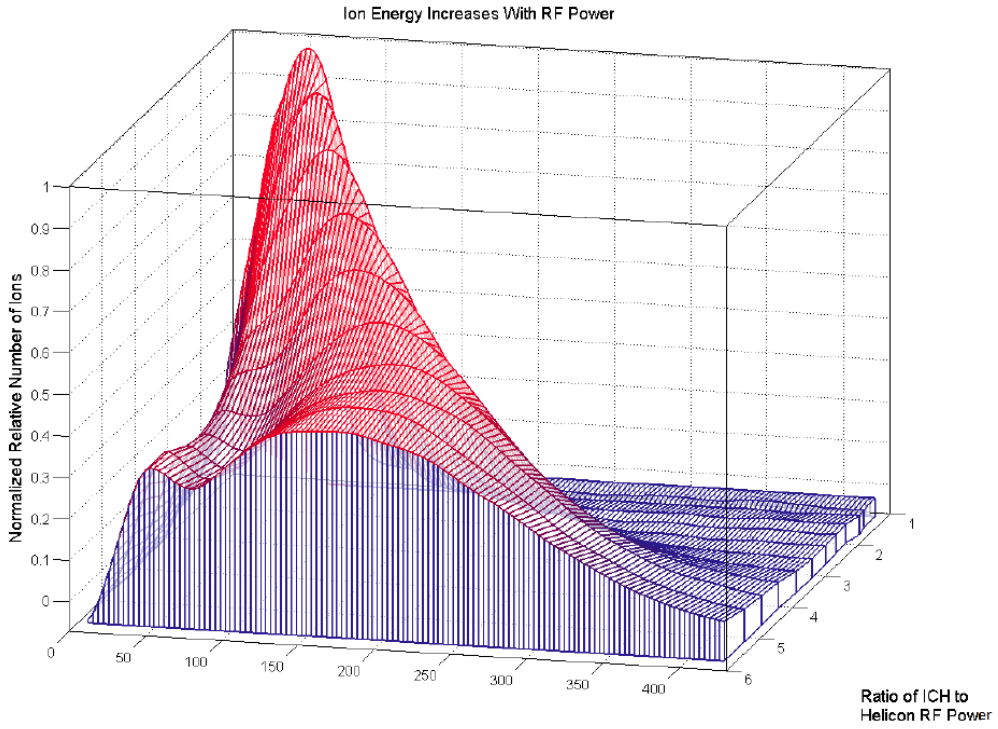

Figure 19. Experimental ion energy distribution function taken with RPA at z = 0.3 m from VX-200[6]**.**

The initial velocity distribution of the ejected ions when the ICH/RF ratio was 6 is displayed in Figure 20 and shows a “double hump”. The initial velocity distribution when the ICH/RF ratio was 3 is presented in Figure 21 and shows a single hump that is skewed slightly toward slower ion velocities.

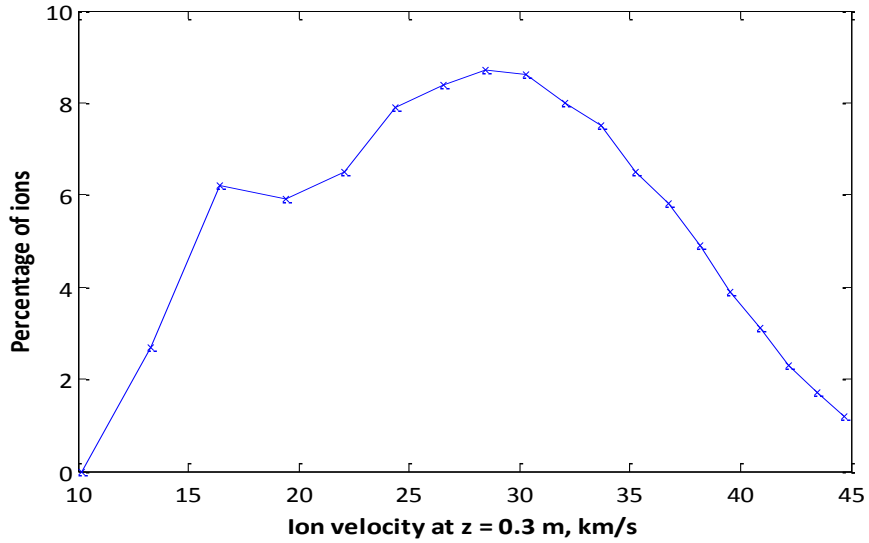

Figure 20. Velocity distribution ("double hump") derived from the VX-200 plasma ion energy at ICH/RF=6 (FWHM = 23, V_{avg} = 29.7 km/s) in Figure 19.

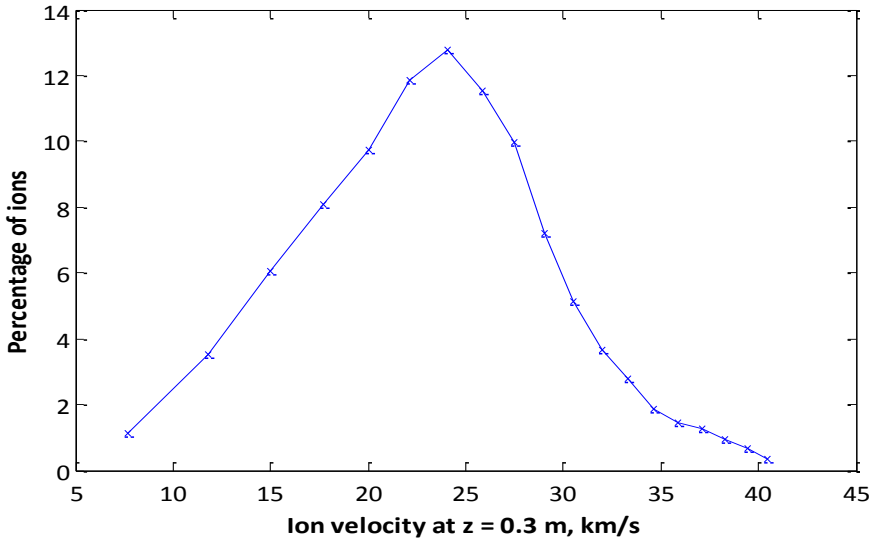

Figure 21. Velocity distribution derived from the VX-200 plasma ion energy at ICH/RF=3, FWHM = 10, V_{avg} = 24.4 km/s in Figure 19.

The velocity distribution used in the model was uniform for the entire inlet disc ($0 \text{ m} < r < 0.7 \text{ m}$) but was measured only at the centerline ($r = 0 \text{ m}$). This extrapolation was made because the radial dependence of the ion velocity distribution is unknown. It might be expected that the percentage of lower velocity ions is much greater in the plume fringe ($r > 0.3 \text{ m}$), and this would lead to more ions entering the backfield but at lower kinetic energies. As additional experimental data or improved assumptions on the radial variations of the ion velocity distribution function become available, this model can be improved.

4.3.2.2 Equations

4.3.2.2.1 Magnetic Field Equations

As was discussed in Section 4.3.2.1, two magnetic field strengths were used to determine the interaction that the magnetic field has with the plasma velocity profile and density distribution downstream of the engine. These two field values were achieved by modifying the electrical current in the magnetic coils ($I = 70 \text{ A}$ and $I = 140 \text{ A}$). Figure 22 shows the magnetic field streamlines emanating from the three coils within the engine. The streamlines are identical but of different strength values.

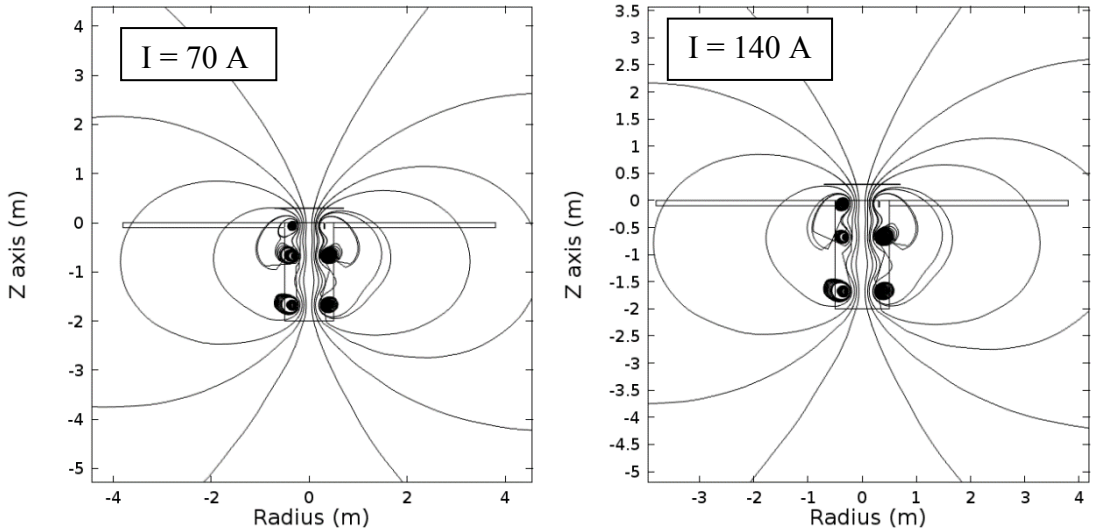

Figure 22. Magnetic field lines for I = 70 A (factor B-) and I = 140 A (factor B+). While the field strength changes, the field lines themselves are essentially the same.

Figure 23 illustrates the difference in field strength in Teslas, with the maximum B_{mag} of I = 70 A being essentially half of the maximum B_{mag} of I=140 A.

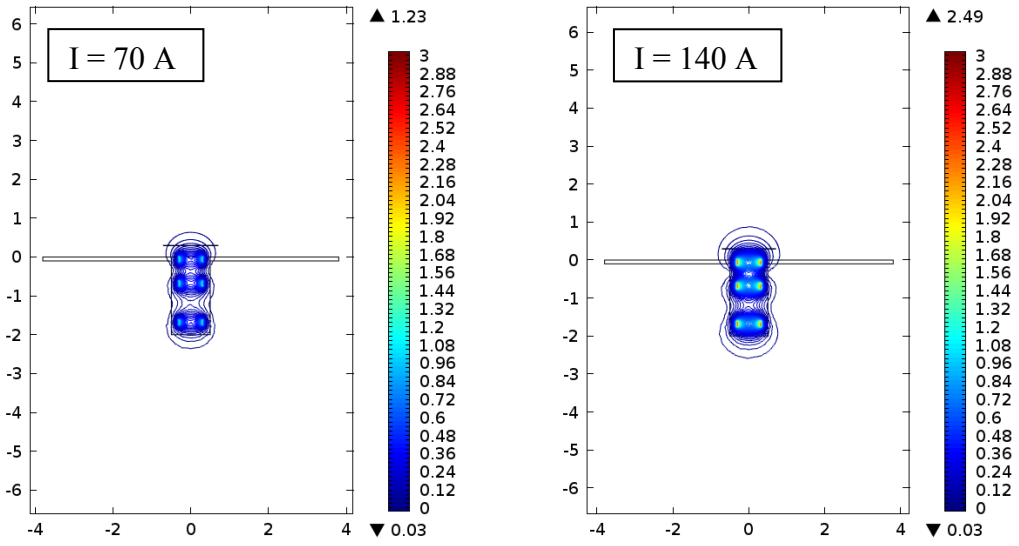

Figure 23. Magnetic field strength for I = 70 A (factor B-) and I = 140 A (factor B+). The field strength is strongest within the coils and is essentially double for the right plot compared to the left plot.

The magnetic field was calculated first in the numerical model using Ampere's Law for each of the three multi-turned coils:

$$B = \mu_0 \frac{N}{l} I \tag{4-1}$$

where B = magnetic field strength

μ_0= magnetic constant (1.25664 x 10^{-6} T m/A)

N = number of turns in the coil

l = length of the coil

I = electrical current through the coil

The model included magnetic insulation at the edges of the 30 m sphere so that the magnetic field lines could continue on into infinity and not be constrained by the 30 m limit.

4.3.2.2.2 Electric Field Equations

As determining the plume-generated electric field for every engine configuration was not practical, it was decided to use the Ad Astra measured electric potential (Figure 12 and Figure 13) and assume a point charge generated electric field such as

$$\boldsymbol{V}(r) = \frac{Q_r}{4\pi\varepsilon_0 r} \text{ and } \boldsymbol{V}(z) = \frac{Q_z}{4\pi\varepsilon_0 z} \tag{4-2}$$

However, there was a slight difference in the electric potential for the radial and axial directions so an average of the two was taken such that

$$\boldsymbol{V}(r,z) = \frac{1}{2}\left[\frac{Q_r}{4\pi\varepsilon_0 r} + \frac{Q_z}{4\pi\varepsilon_0 z}\right] \tag{4-3}$$

which then had x and y substituted for r and was mathematically reduced to

$$\boldsymbol{V}(x,y,z) = \frac{2.092}{\sqrt{x^2+y^2+z^2}} \tag{4-4}$$

Equation 4-4 was utilized by the numerical model to generate an electric field around the generic plasma spacecraft engine.

4.3.2.2.3 Plume Density Profile (or Plume Width)

The plume density profile is how the ions are distributed across the engine's exit (and the computer model's inlet) in the radial direction at z = 0.3 m. As discussed in the previous section, the plume density profile used as the baseline in this research was derived from Figure 15[31] to create an interpolated curve. This curve is called "int34" in the numerical model and shown in Figure 24 below. Therefore, whenever the numerical model released a group of ions (discussed in the next subsection), the program multiplied the number of ions by the following equation to determine the radial distribution:

$$\rho = int34(\sqrt{x^2 + y^2}) \tag{4-5}$$

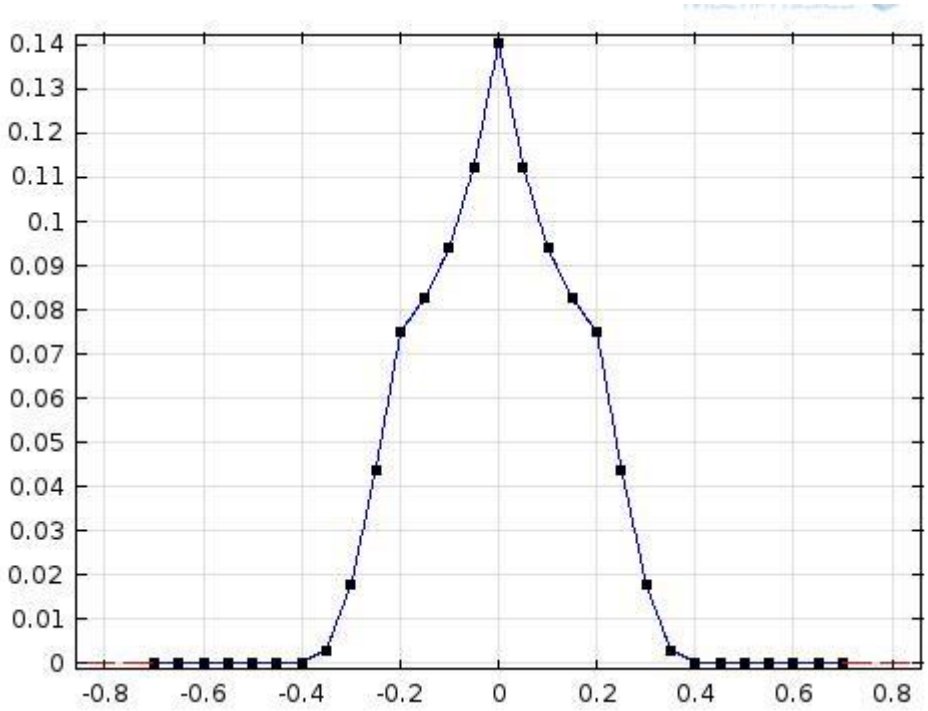

Figure 24. Interpolated ion density for the baseline narrow plume over -0.7 m < r < 0.7 m of the plume radius (int34). This interpolation is used as factor A+ as discussed in section 4.3.1.1.

The curve in Figure 24 was then increased by 20% Full Width Half Maximum (FWHM) which stretches the density distribution towards the plume fringe. This curve became "int35" and was called by the numerical model during the initial ion placement.

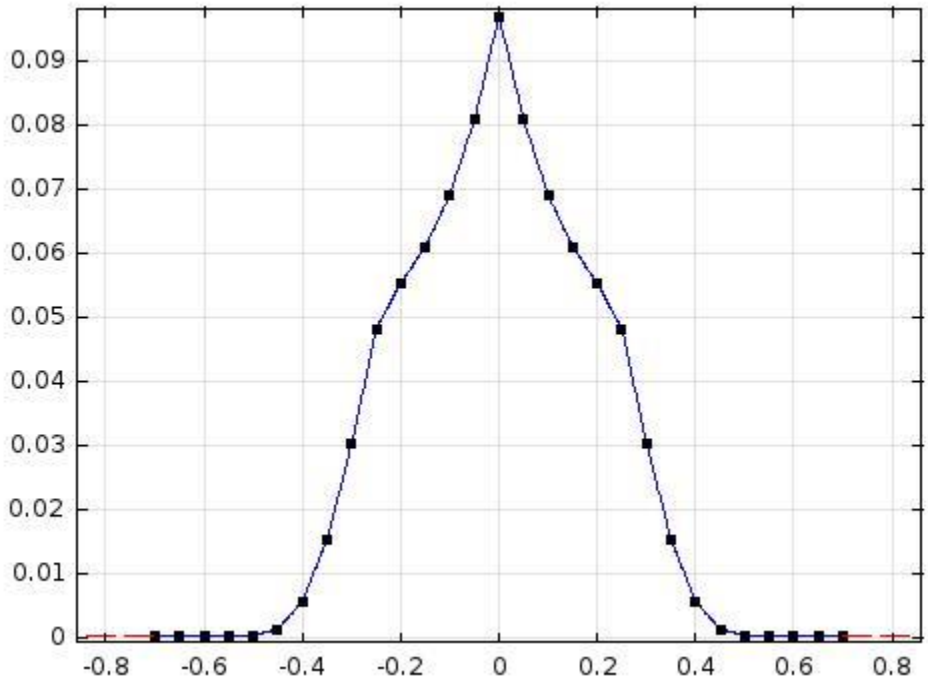

Figure 25. Interpolated ion density for the 20% wider plume over -0.7 m < r < 0.7 m of the plume radius (int35). This interpolation is used as factor A- as discussed in section 4.3.1.1.

4.3.2.2.4 Plume Exit Velocity Distribution

The initial velocity of each particle was originally such that the particles only moved in the z direction, but this led to an excessive loss of kinetic energy for each ion as it immediately moved to reconnect to the nearest magnetic field line. Therefore, it was decided to assume that ions would be following the magnetic field lines at the start of the simulation and their initial velocity was governed by these equations:

$$V_X = V_{mag}\left(\frac{x}{|x|}\right)\left(\frac{B_x}{B_{mag}}\right) \tag{4-6}$$

$$V_Y = V_{mag}\left(\frac{y}{|y|}\right)\left(\frac{B_y}{B_{mag}}\right) \tag{4-7}$$

$$V_Z = V_{mag}\left(\frac{z}{|z|}\right)\left(\frac{B_z}{B_{mag}}\right) \quad (4\text{-}8)$$

where V_{mag} = the magnitude of the velocity for the ion derived from Figure 19 (m/s)

B_{mag} = the magnitude of magnetic field strength at the ion's initial position (T)

x = initial location of the ion at t = 0 s in the x-direction (m)

y = initial location of the ion at t = 0 s in the y-direction (m)

z = initial location of the ion at t = 0 s in the z-direction (m)

B_x = magnetic field strength in the x-direction at the ion's initial position (T)

B_y = magnetic field strength in the y-direction at the ion's initial position (T)

B_z = magnetic field strength in the z-direction at the ion's initial position (T)

The velocity distribution was broken up into 19 groups with varying velocity ranges. There is one set of 19 groups of ions for the faster average exit velocity condition (Factor A+) and one set for the slower average exit velocity condition (Factor A-) which was discussed in Section 4.3.1. These two sets are displayed in Table 2.

Table 2. Ion quantity, kinetic energy, and velocity magnitude for each of 19 groups for Factor A+ and A-.

	Factor A+			Factor A-		
Group	Ion Quantity	Ion Energy (eV)	V Mag (m/s)	Ion Quantity	Ion Energy (eV)	V Mag (m/s)
1	202	21	10178	11396	12	7660.6
2	27270	37	13309.5	35423	29	11789.6
3	62037	56	16455	60457	47	15013
4	58748	78	19444.3	80837	65	17689.5
5	65301	101	22089.3	97196	83	20043
6	79305	123	24388.5	118663	101	22140.1
7	84471	146	26520.6	127914	120	24054.2
8	86550	168	28476.6	115400	138	25825.1
9	85696	190	30302.8	99696	156	27470.9
10	80095	212	32033.6	72186	175	29036.3
11	75497	235	33666.6	51361	193	30516.9
12	65355	257	35231.2	36579	211	31958.2
13	57769	279	36727.5	27708	230	33308.7
14	48816	302	38178.4	18677	248	34627.2
15	39180	324	39562.7	14705	267	35907.5
16	31171	346	40897.4	12436	285	37120.2
17	23022	369	42192.6	9532	303	38289
18	17340	391	43454.3	6547	322	39415.3
19	12174	413	44668.9	3286	339	40488.3
Total	**999999**		**Total**	**999999**		

4.3.2.3 Computational Domain

Figure 26 and Figure 27 illustrate the model generated in COMSOL Multiphysics®. The model consists of:

A. (1) large sphere

B. (1) small cylinder downstream of the magnetoplasma engine

C. (1) engine housing

D. (4) radiator panels

E. (3) identical concentric rings

The large sphere has a 30 m radius (Figure 26) and represents the ideal outer space environment (zero pressure, zero particle density) and is the domain for which the magnetic field and particle trajectories are modeled. The sphere has an outer layer that is 0.5 m thick so that the numerical model will treat the magnetic field lines as extending into infinity instead of ending at the sphere boundary. Particles that reach and intersect the sphere boundary (wall) are frozen in place. A 45 m sphere and 60 m sphere was also used to see what effect the domain size had on the results. It was found that increasing the domain size only resulted in an average of 0.22% more particles entering the backfield but exponentially increased the computation time required to run the model. Therefore, it was determined that the 30 m radius sphere domain was adequate to obtain a worst case estimate of erosion rates and electrical charging due to recirculating particles. Future work may include larger spheres for less uncertainty. The 30 m limit is valid for this research because the magnetic field strength is essentially zero at 30 m from the engine and the particles are expected to be detached through a loss of adiabaticity as discussed in Section 2.7 Particle Detachment from Magnetic Fields. In Figure 27, the large circles are the sphere from two different directions. The magnetoplasma engine model is visible at the center of the domain.

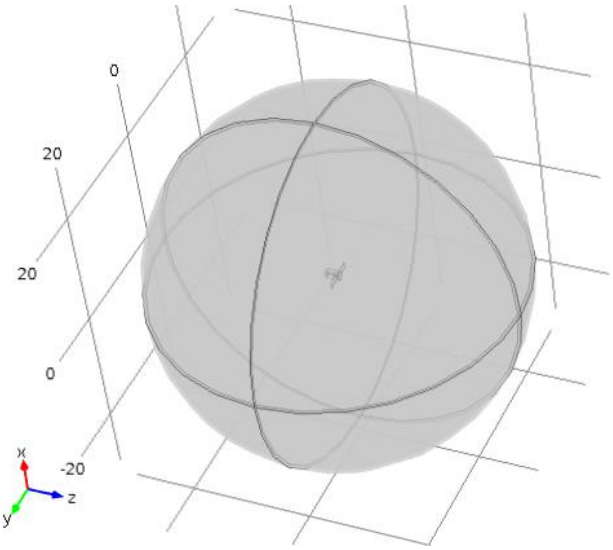

Figure 26. Schematic showing the 30 m radius sphere in the numerical model. The magnetoplasma engine is at the center of the sphere.

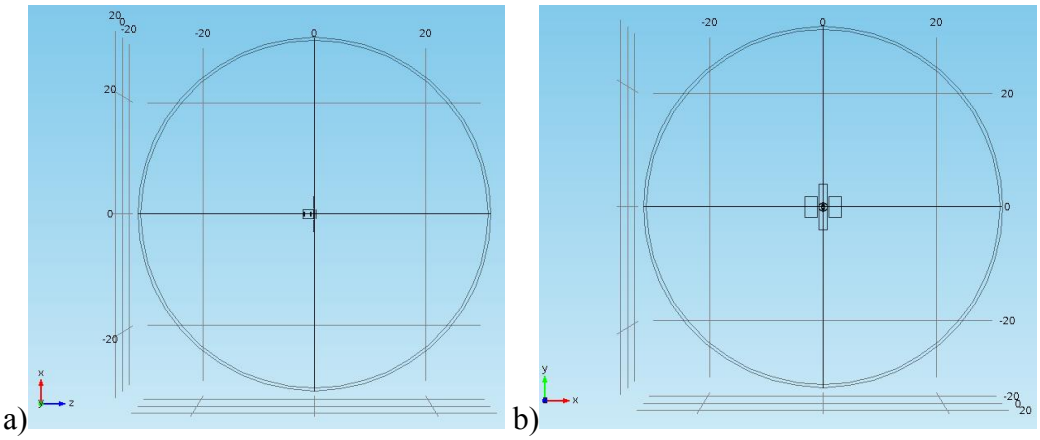

Figure 27. Schematics showing a magnetoplasma engine within the numerical model from a.) the x – z plane and b.) the y – x plane. The engine is surrounded by a 30 m radius sphere representing the ideal outer space environment.

The small cylinder located 0.3 m downstream of the engine is a 0.7 m radius x 0.01 m thick inlet disc (Figure 28) from which all particles originate in the model and are ejected in the positive z direction. This was done because a.) the conditions at the engine

throat are not known, and b.) the experimental data used as boundary conditions (section 4.3.2.1) were taken at z = 0.3 m downstream of the engine exit. The inlet disc has a 0.7 m radius because the density distribution (section 4.3.2.2) from experiment ranges from r = 0 m to r = 0.7 m.

The magnetoplasma engine housing is represented in the model by a 1 m wide x 1 m high x 2 m thick box. The engine throat is located at z = 0 m and the plume centerline is at x = y = r = 0 m. The selection of a box is arbitrary and meant as a representation of the actual engine housing to encase a magnetoplasma engine (Figure 28).

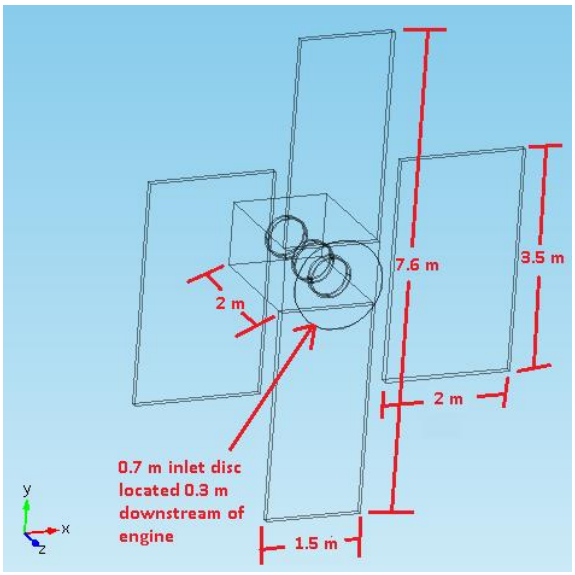

Figure 28. Schematic showing a magnetoplasma engine within the numerical model. The values chosen were arbitrary and can be modified for a specific engine. Larger panels may result in more ion impacts.

Four radiator panels were added to the model because radiator panels are likely to be used in order to radiate waste heat from the magnetoplasma engine. As for the

engine housing, the radiator panels in this model are meant to be representations. The models' radiator panels are 3.3 m x 1.5 m x 0.1 m and 3.5 m x 2 m x 0.1 m in size and assumed to be made of aluminum.

Three identical concentric rings are located at z = -1.62 m, z = -0.62 m, and z = 0 m to represent the multi-turn niobium-tin (Nb_3Sn) magnetic coils that generate the magnetic field. Niobium-tin is a Type II superconductor with a critical temperature of roughly 18 K and a critical magnetic field of 24.5 Tesla[32]. The coils currently being used for the VX-200 are made of Nb_3Sn and are kept at liquid nitrogen temperature. Great effort was expended in the positioning of these coils within the model to obtain a magnetic field strength and field line geometry that is very close to the actual experimental data.

In order to simulate the plasma environment, the model requires the following inputs to simulate particle impacts:

1. Information on the superconducting electromagnets such the number of coils, the material properties, coil location(s), and electrical current to model the magnetic field.
2. Information on the propellant gas entering the magnetoplasma engine such as the gas properties, mass flow rate, and density.
3. Electric potential of the spacecraft surfaces.
4. Spacecraft dimensions and geometry.

5. The plume velocity profile that can be split into 19 groups, which consist of the number of particles to be released and equations governing the initial particle velocity vector.
6. The plume density profile which tells the model how the number of particles being released are to be dispersed across the plume radius.
7. Model-specific values such as time step size and time duration.

4.3.2.3.1 Magnetic Field Calculation

The AC/DC module in COMSOL was used to simulate the magnetic and specify the electrical fields to impart forces on the argon ions. The magnetic field for the magnetoplasma engine was assumed to be static over time and is defined by Gauss's law of magnetism as:

$$\boldsymbol{B} = \nabla \times \boldsymbol{A}_m \tag{4-9}$$

where **B** is the magnetic field and $\mathbf{A_m}$ is the magnetic vector potential. The magnetic current density created by the magnetic field is given as:

$$\nabla \times \boldsymbol{B} = \boldsymbol{J}_e \tag{4-10}$$

where **H** is magnetic field strength (A/m) and in a vacuum is equal to B, and $\mathbf{J}_e$ is the electrical current density (A/m^2). For a multiple turn coil of wire with an electrical current running through it, a very powerful magnetic field can be generated. Current densities on the order of 1×10^9 A/m^2 are achieved through the use of superconducting Nb_3Sn in the VX-200 and are governed by

$$\boldsymbol{J}_e = \frac{NI_{coil}}{A}\boldsymbol{e}_{coil} \tag{4-11}$$

where N is the number of turns of the coil, I_{coil} is the electrical current (A) running through the coil, A is the cross-sectional area of the coil between outer radius and inner radius (m^2), and $\mathbf{e}_{coil}$ is the electrical vector of the coil. The current, number of turns, size, location, and coil materials were specified in the numerical model so that the magnetic field calculated closely matched both the radial and axial magnetic field of the VX-200 experimental data and is illustrated in Figure 29.

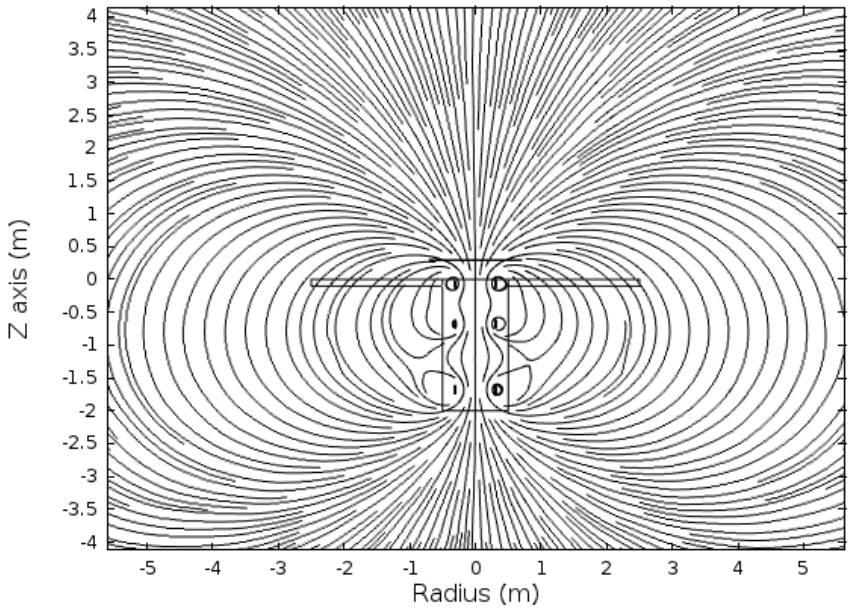

Figure 29. Schematic showing magnetic field lines in the COMSOL model. The magnetoplasma engine and radiator panels are in the center of the figure. The engine plume's center line is at Radius = 0 m and 0 < Z < 4 m.

4.3.2.3.2 Charged Particle Trajectories (CPT)

The trajectory of each ionized particle was simulated to determine which particles entered the magnetoplasma engine's backfield, which particles impacted the engine housing or radiator panels, and the particles average kinetic energy. The force acting on each particle affects the trajectory over time and is governed by Newton's second law:

$$\frac{d\left(m_p \mathbf{v}\right)}{dt} = F_t \tag{4-12}$$

where m_p is the ion mass (kg), **v** is the ion velocity vector, and F_t is the force as a function of time. The force due to the magnetic field is

$$F = Ze\left(\mathbf{v} \times real\left(\mathbf{B}e^{j\omega t}\right)\right) \tag{4-13}$$

where Z is the charge number, e is the electric charge (1.602 x 10^{-19} C), **v** is the velocity vector (m/s), **B** is the magnetic field (T), and ω is the angular frequency. The force due to the electrical field on each ion is

$$F = eZ\mathbf{E} \tag{4-14}$$

where E is the electric field (A/m), Z is the charge number, and e is the electric charge.

c. Time Steps

The numerical model used sequential time steps with the Charged Particle Tracing solver to calculate the position of each particle across 0.003 seconds which is the amount of time the slowest particles could reach the 30 m model limit, even on an arced trajectory. It was found that all particles impacted well before the model solver reached the end of the time span. The method used by the solver was generalized alpha

and the solver was allowed to freely change the value of each time step to aid in solving calculations. The individual time steps are listed in a table in Appendix L. The time steps range from 1.88 x 10^{-7} seconds to 1.92 x 10^{-4} seconds. The amplification factor was 0.75 and the predictor method for where each particle would move to was linear.

4.3.3 Electrical Charging Model

4.3.3.1 Boundary & Initial Conditions

The following conditions were used in the electrical charging model:

1. The VX-200 measured electric field was utilized in the numerical model so that the ions would see some charge separation forces, as was mentioned in Section 4.3.2.1.b.
2. The initial conditions are the output of the trajectory model, specifically the number of ions impacting structure and their kinetic energy for each run.

4.3.3.2 Equations

In order to determine the electrical charging on a spacecraft from a magnetoplasma engine, the current balance between ions and electrons must be found for the sheath surrounding the spacecraft[33]. This is because a spacecraft is said to be charged when its potential is non-zero relative to the surrounding plasma[34]. As each individual ion that impacts structure has a charge, a velocity, and kinetic energy, these can be used to determine the potential, Φ, or charge on the spacecraft due to the impacting particles. The kinetic energy of the electrons is assumed to be equal to the ion

kinetic energy as both particles gained their energy from the same RF source and energy is assumed to be conserved. If $KE_{electron} = KE_{ion}$, then the electron velocity is

$$V_E = \sqrt{\frac{2*KE_{ion}}{m_E}} \tag{4-15}$$

where V_E = electron velocity (m/s)

KE_{ion} = ion kinetic energy at impact (J)

m_E = electron mass (kg)

Similarly, the ion velocity can be calculated:

$$V_I = \sqrt{\frac{2*KE_{ion}}{m_I}} \tag{4-16}$$

where V_I = ion velocity (m/s)

KE_{ion} = ion kinetic energy at impact (J)

m_I = ion mass (kg)

The electron velocity can then be used to calculate the electron temperature of the plasma as

$$\frac{3}{2}k_B T_E = \frac{1}{2}m_E V_E^2 \tag{4-17}$$

The electron temperature allows the Bohm velocity, the velocity in the plasma sheath in contact with the engine surface, to be calculated as

$$V_{Bohm} \geq \sqrt{\frac{k_B T_E}{m_I}} \tag{4-18}$$

where V_{Bohm} = Bohm velocity (m/s)

k_B = Boltzmann constant (1.38×10^{-23} J/k)

T_E = electron temperature (K)

m_I = ion mass (for Argon, 6.63 x 10^{-26} kg)

The Bohm velocity can be utilized to determine the ion current density and electric Potential on the spacecraft surface using

$$J_I = qN_I V_{Bohm} \tag{4-19}$$

$$\Phi = -\frac{1}{2}\frac{m_I}{q}(V_I^2 - V_{Bohm}^2) \tag{4-20}$$

where J_I = current density (A/m^2)

q = elementary charge (-1.602 x 10^{-19} C)

N_I = ion density (m^{-3})

Φ = electric potential on the spacecraft surface (Volts)

These equations were used to calculate the values in Table 3. The density of impacting ions in the plasma sheath was determined by use of a binning program in MATLAB® with individual ion locations and a scaling factor to match the mass flow rate of argon used experimentally. This program provided both an average density and a maximum density. The maximum density was used for the sheath potential calculation to determine the maximum potential. The charging is a surface charge and not an internal charge because a.) the highest average ion kinetic energy (and thus ion temperature) out of all 8 runs was 41.78 eV, and b.) temperature ranges of 0 to 50 keV usually correlate to surface charging[35]. It is important to note that with the assumption that the ion and electron kinetic energies are equal, the Potential is now only a function of the impacting ions average kinetic energy and the masses of the argon ions and electrons.

4.3.4 Erosion Model

4.3.4.1 Boundary & Initial Conditions

The initial conditions for the erosion model are the number of ions impacting structure and their kinetic energy at impact for each run. This data is output by the trajectory model.

4.3.4.2 Equations

Equation 2-1 was used by W. Eckstein to derive the curve shown in Figure 6 and Figure 7[30]. This curve was interpolated and used by the numerical model discussed in the next section. As mentioned in Section 4.2, the angle of impact was found to have a negligible effect on the erosion rate and is discussed in Appendix I.

4.3.4.3 Computational Domain

Using Figure 6 and Figure 7[30] with the kinetic energy calculated for each impacting argon ion on aluminum and silicon, the estimated sputtering yield or particles eroded can be determined for each material. The estimates came from the curves in Figure 6 and Figure 7 by extrapolating between points on the graphs using MATLAB® code (see Postprocessing.m in APPENDIX K) to generate an erosion rate when supplied the average kinetic energy of all impacting ions in the model run and then multiplied by the total number of impacting ions. The use of extrapolation for the graphs is a source of error in the estimated erosion rate.

4.3.5 Application of the Numerical Model

The procedure for how the trajectory, electrical charging, and erosion results were determined is listed in this section. First, the trajectory model was used to quantify how many ions would enter the backfield and how many of those would impact the engine and radiator panels. Second, the data from the numerical model was exported as MS Excel spreadsheets to be input for the MATLAB post-processing programs that are presented in APPENDIX K. Next, these programs created the plots showing where individual ions impacted on the spacecraft, the electrical charging and erosion that were a result of these impacts, and the many graphs used throughout this document. Finally, MS Excel was again used to create the presented tables and calculate the amount of interaction and correlation between the Full Factorial factors.

The specific procedure for determining the erosion and electrical charging is listed below:

1. Verify that a COMSOL Multiphysics® AC/DC and Particle Tracing module license is available to the computer and then open the included "Run 5.mph" file in COMSOL Multiphysics®.
2. Open the included "DensityProfiles.m" file in MATLAB® and modify with the density profiles desired. Use the data generated here to input the density profile equations for the next step.
3. Modify the parameters within "Run 5.mph" to represent a specific magnetoplasma engine, especially the magnetic field geometry and velocity

profile of ejected particles. Specify the number of particles, the density profile, and the direction for each set of particle releases. Specify the time step.

4. Activate the solver for "Run 5.mph". This may take many hours or days. Modify the file and rerun the solver for each engine configuration run of interest.
5. Output the kinetic energy, velocity, and the radial and axial position for each particle at the first and last time step as a MS Excel® csv spreadsheet. The last time step should be after all particles have impacted or reached the boundary wall. The output needs to be in the order of cpt.Ep (J), cpt.vx (m/s), cpt.vy (m/s), x (m), y (m), and z (m) for the next steps to work properly.
6. [Optional] Open the csv spreadsheets in MS Excel®. Sort the spreadsheets so that only particles that exist within $-0.1\ \text{m} < z < 0.1\ \text{m}$ and $-4\ \text{m} < r < 4\ \text{m}$, depending on the magnetoplasma engine's size. These are the particles that have impacted the radiator panels or engine housing.
7. Open the included "Postprocessing.m" file in MATLAB® and modify the file to call the csv spreadsheets from step 5. Run the file to determine the average kinetic energy, total erosion on AL and SI surfaces, and electrical potential. If the csv files were not created with the order described in step 5, then the MATLAB® program will not run correctly.
8. Open the included "Multiple_Bursts_Beta.m" file in MATLAB® and modify the file to call the csv spreadsheets from step 5. Run this file to determine the Alfvénic velocity and Beta for the plasma plume over 1 second.

9. Open the included “Contour_plot.m” file in MATLAB® and modify the file to call the csv spreadsheets from step 5. Run this file to generate plots that show the initial velocity and initial radial position in the plume for impacting ions.

This section presented the computer simulation model used to determine the plasma environment around a spacecraft using a magnetoplasma engine. In the next section, the results derived from the simulation model will be presented and discussed.

5. RESULTS

5.1 Introduction

In the previous sections, an understanding of magnetic nozzles, the VASIMR® engine, the detachment mechanisms, and the plasma environment was given. The steps necessary to obtain the relevant data were also listed. The computer model used to simulate the plasma environment was described in detail. In this section, the results derived from this computer model are presented and discussed. The second, or next, section will go into what limitations are present with this research to qualify the results. The third section will explain the ion trajectories that were simulated. The fourth section will discuss the electrical charging found in each run. The fifth and final section will specify the erosion determined on both aluminum and silicon surfaces. This section will also explain the relationships and interactions between the three factors that were varied during this research.

A quick synopsis of the computer simulation is in order to better understand the results. The numerical model utilized to generate these results tracked the trajectories of one million ions to determine what percentage entered the backfield and what subset of those impacted the engine housing and radiator panels. The density distribution was taken from experimental data and is believed to be sufficiently accurate. The magnetic field also comes from experimental data and is as accurate as possible at this time. The electric field was found to have a minor effect on the trajectories and came from the electric field measured by Ad Astra, instead of being directly determined in the software model because this was not practical. The temperature in the parallel and perpendicular

directions were assumed to be the ion kinetic energy but could be derived from experimental results once available. The radial location at z = 0.3 m downstream from the engine throat, which was chosen as the inlet condition, also affects whether the ions will enter the backfield or not. This inlet position was chosen due to the availability of experimental data and because the plasma plume is sufficiently rarefied at this location.

5.2 Limitations

1. The lack of a self-consistent electric field from the modelled engine plume in each run below introduces an estimated 7% uncertainty in the determined erosion rates. However, the electric potential from Ad Astra published data for the VX-200 was used to generate an electric field for this model.
2. The only detachment methods utilized in this research were Kinetic and Loss of Adiabaticity detachment because the other methods relied on fluid properties. This numerical model was based on particle kinetic theory due to the plume being rarified and not a continuum. Therefore, this research does not incorporate all of the possible ways in which ejected plasma particles might escape the engine's magnetic field and reduce the amount of erosion on nearby spacecraft surfaces. This is a worst case scenario to find the maximum amount of erosion for different engine conditions.
3. One form of detachment, magnetic reconnection, where the ejected plasma deforms the magnetic field lines into detached islands, was not simulated in this research. The magnetic field was assumed to be static. Therefore, more ions may

escape in the actual plume than in this model with a resultant lower erosion rate. As mentioned earlier, this is a worst case scenario. However, Olsen[36] found that the magnetic field lines were not being distorted by the ejected plasma.

4. The velocity distribution variation was taken from RPA data at r = 0 m and extrapolated over the entire 0.7 m inlet disc and would be more accurate if velocity data in the radial direction at z = 0.3 m was incorporated into the model. This is the greatest source of uncertainty in the model because actual test data across the entire inlet would be better than the interpolated data from just the centerline. This research assumes that the velocity profile throughout the inlet is the same as the velocity profile measured at the inlet centerline.
5. If the Langmuir probe which provide the data used in the plume exit velocity profile was actually located at z = 0.2 m instead of at 0.3 m as stated in Bering et al[6], then there is an additional 5.52% error to these results.
6. The mesh could be made to be finer to capture individual ion movements more accurately.
7. Smaller time steps could be used to capture individual ion movements more accurately.
8. As mentioned in Section 4.3 Solution Approach, using the average kinetic energy of all impacting ions to determine the erosion rate leads to a slightly higher value for averages greater than the material threshold energy and a slightly lower value for averages less than the material threshold energy. These errors could be

eliminated by calculating the erosion caused by each individual impacting ion and then summing up the total erosion.

9. Lastly, the number of particles can be increased for better statistical accuracy. There was a negligible difference between an earlier 500,000 particle model and the 1,000,000 particle model used here, as explained in Appendix G.

5.3 Trajectory Results

The trajectory of 1 million ions was simulated for each of the 8 runs to determine how many ions would be expected to enter the backfield (i.e. the area outside the engine that is upstream of the nozzle) and which of those ions would impact the engine housing and radiator panels. It was assumed that any ions that reach the 30 m limit of the computer model have escaped the engine's magnetic field and will not return because the magnetic field strength at 30 m is negligible. Figure 30 shows the individual ions (with color indicating particle velocity) in the numerical model at t = 0.0003 seconds after ejection in Run 5. Ions are traveling from left to right in Figure 29.

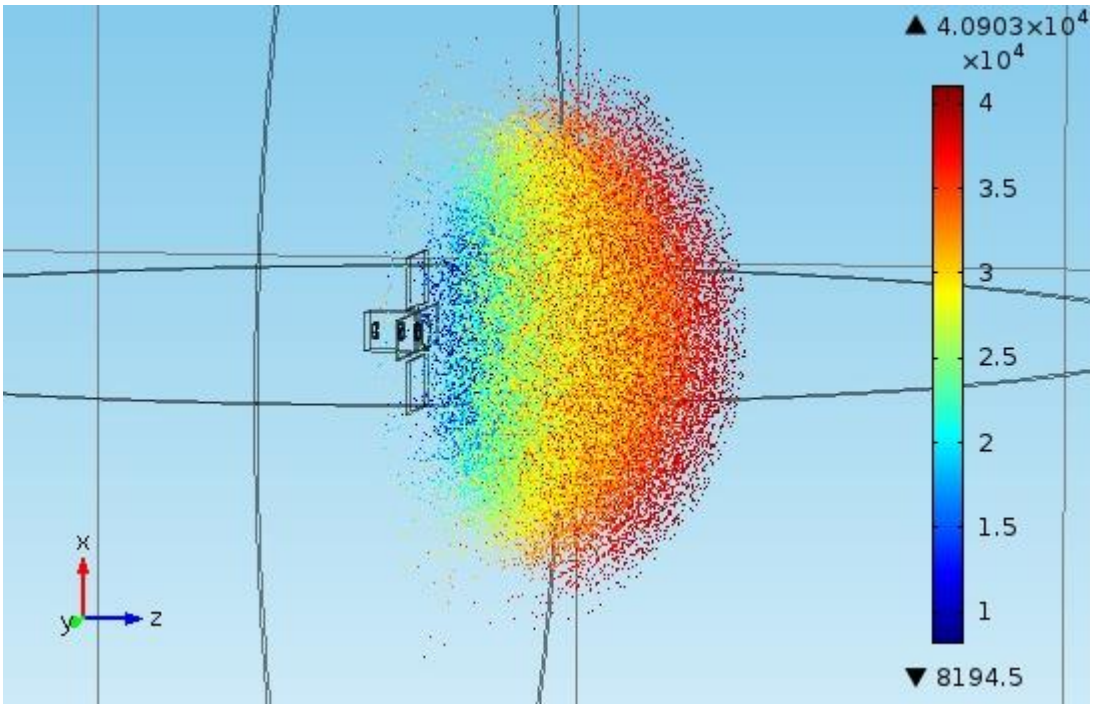

Figure 30. Individual ions from COMSOL Multiphysics® software simulation (Run 5). Red ions are travelling around 40 km/s while blue ions are traveling around 10 km/s. The colorbar represents velocity in 10^1 km/s.

Similarly, the individual ions can be represented on a Poincaré map such as in Figure 31 below. Ions are traveling from bottom to top in Figure 31. The majority of the ions in the model are diverging from the centerline due to their following the curvature of magnetic field lines emanating from the magnetoplasma engine. The curvature is greater the farther away the ions are from the engine centerline (purple arrow) so that the ions at the centerline are practically going in a straight line away from the engine and ions near the edges are following a curved path. As this computer model only considers plasma detachment from magnetic field lines through Kinetic and Loss of Adiabaticity detachment, Figure 31 is logical. As mentioned in Section 2.7 Particle Detachment from Magnetic Fields, by considering only kinetic and loss of adiabaticity detachment, the

impact and erosion rates determined by this research can be considered the upper limit. Other forms of detachment, if present, will likely reduce the number of ions returning to the spacecraft to cause less erosion overall.

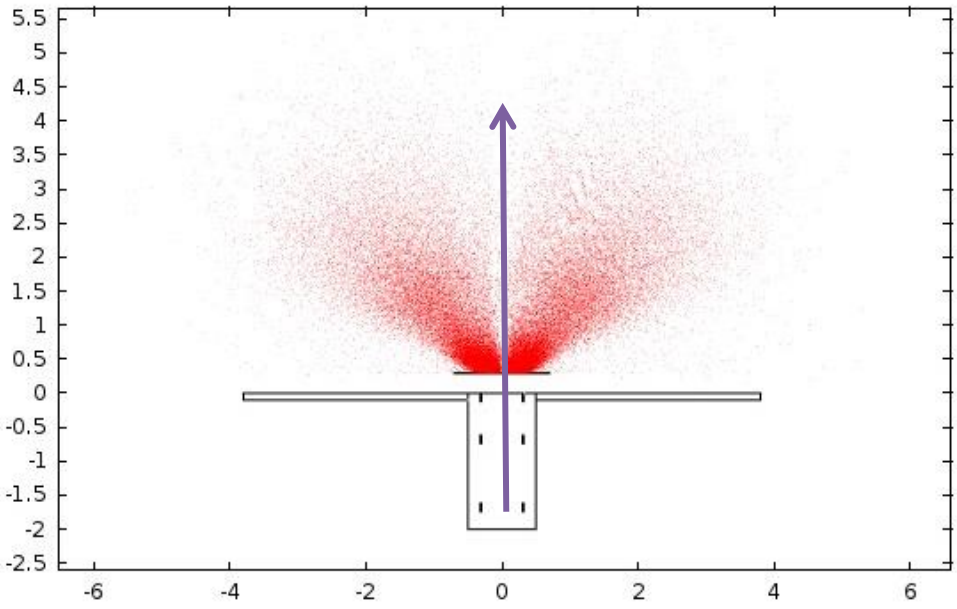

Figure 31. Poincaré map of individual ions at 0.00015 s at x = 0 m (Run 5).

The ion trajectories are shown over a time period from 0 s to 0.0002 s in Figure 32, with ions travelling from bottom to top. The plume does not look like a standard rocket plume because the ions within are mostly following the magnetic field lines which diverge from the centerline. There is also no atmosphere to focus and constrict the plume, which expands greatly in all directions here.

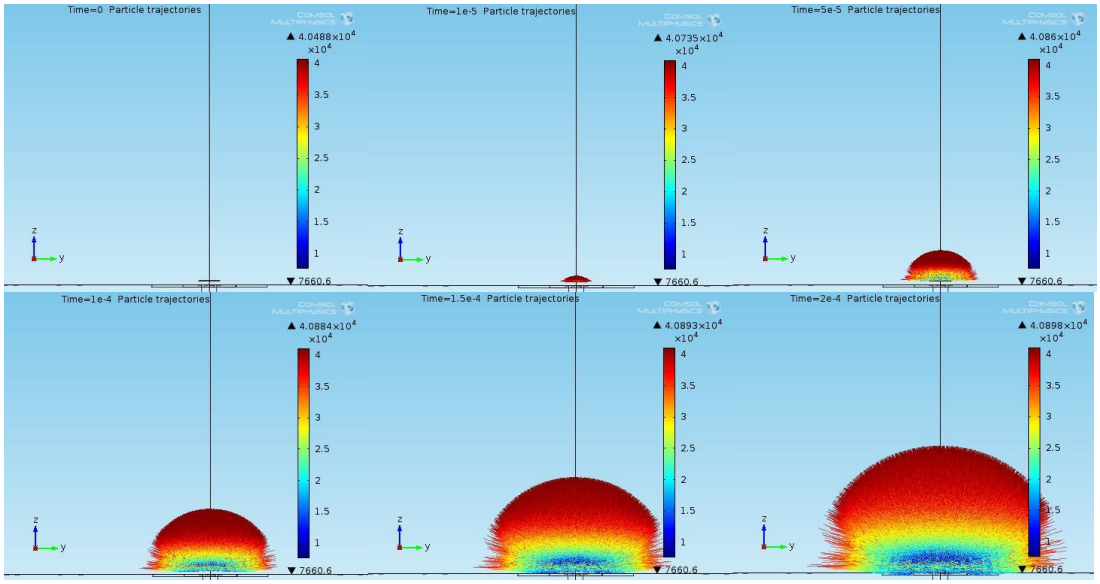

Figure 32. Ion trajectories from 0 s to 0.0002 s (Run 5). Red ions are traveling faster than yellow or blue ions. The black line is the engine centerline. The plume is ejected upwards in these plots.

Figure 33 is a 2x magnification of the ion trajectories shown in Figure 32. It is important to note that the returning ions are not coming from afar and a long time after being ejected. The ions that impact structure hit almost immediately after being ejected and follow the magnetic field lines which have the greatest curvature (e.g. on the edges of the plume).

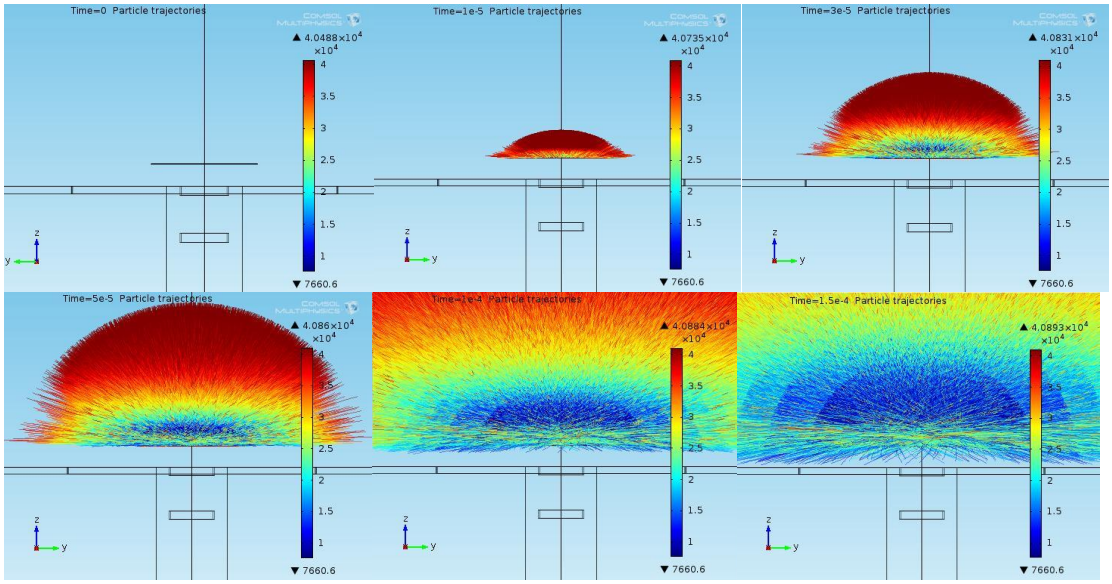

Figure 33. Ion trajectories from 0 s to 0.0002 s, 2x magnification (Run 5). Some ions can be seen moving towards the spacecraft instead of away.

Similarly, Figure 34 is a 4x magnification of the ion trajectories from 0.00005 s to 0.00015 s so that individual ions can be seen approaching the spacecraft surfaces just before impact.

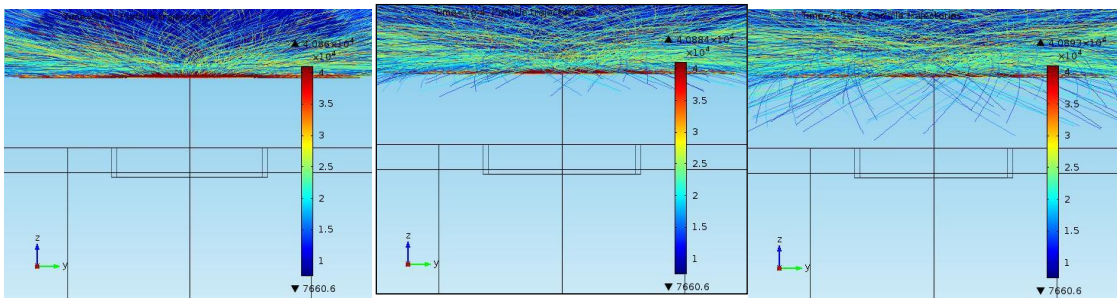

Figure 34. Ion trajectories from 0.00005 s to 0.00015 s, 4x magnification (Run 5). Ions that are trapped by the magnetic field can be seen moving towards spacecraft surfaces.

The effect of using a magnetic nozzle is apparent in Figure 35, where ions experience acceleration near the engine, but then as the magnetic force acting on each ion diminishes with increasing distance from the engine, the ions' average velocity plateaus. The left graph shows the average velocity of all ions over the first 0.7 ms of model elapsed time. The right graph shows the average velocity of all ions over 12 m downstream of the engine. The curve shows a classic effect of rocket nozzles.

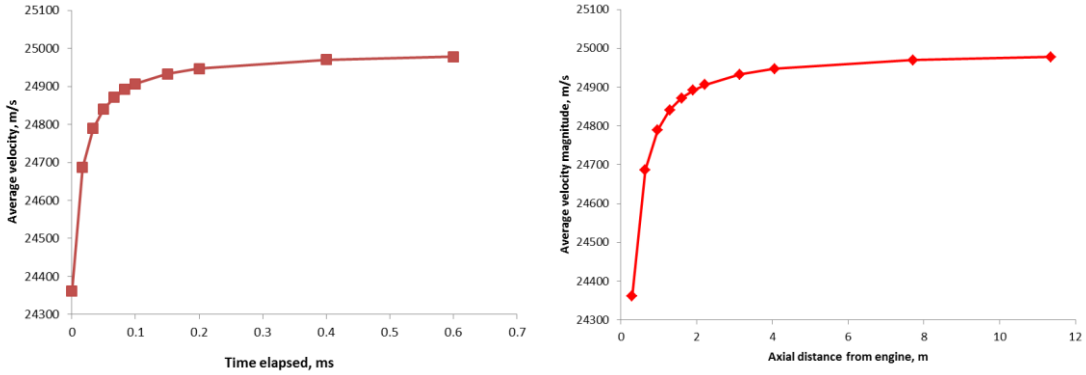

Figure 35. The average velocity magnitude of ejected ions as a function of elapsed time (left) and axial distance (right) of Run 5. The magnetic nozzle is accelerating the ejected ions.

5.3.1 Impacts

The Poincaré maps for each run showing impacts on the engine housing or radiator panels are presented below (Figure 36 through Figure 43). Of all 8 runs, Run 5 (Figure 40) and Run 7 (Figure 42) show the greatest number of impacts. It is important to note that all impacts occurred on the radiator panels and not the backward-facing part of the engine, no matter which run. However, if the radiator panels were not present, then these ions would most likely have impacted the exterior engine housing along the

sides of the engine. As such, the radiator panels acts as shields for the engine housing.

Figure 37 and Figure 43 come from Runs 2 and 8 and have the least amount of impacts.

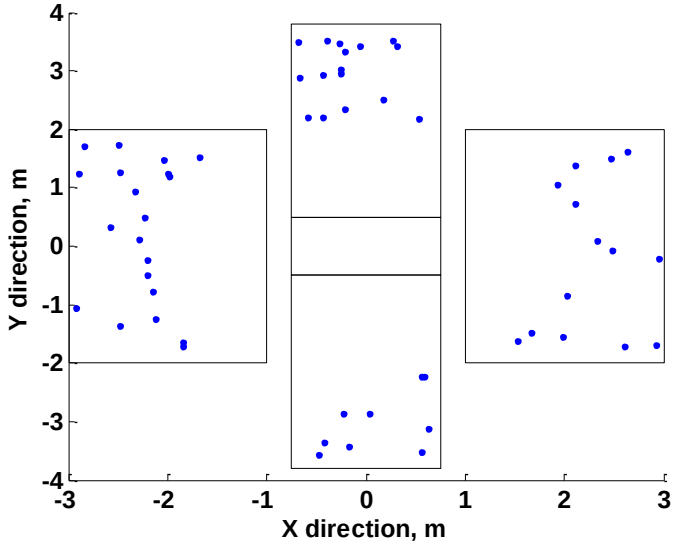

Figure 36. Ion impacts from Run 1 (with slower ions, weaker magnetic field, and wider plume).

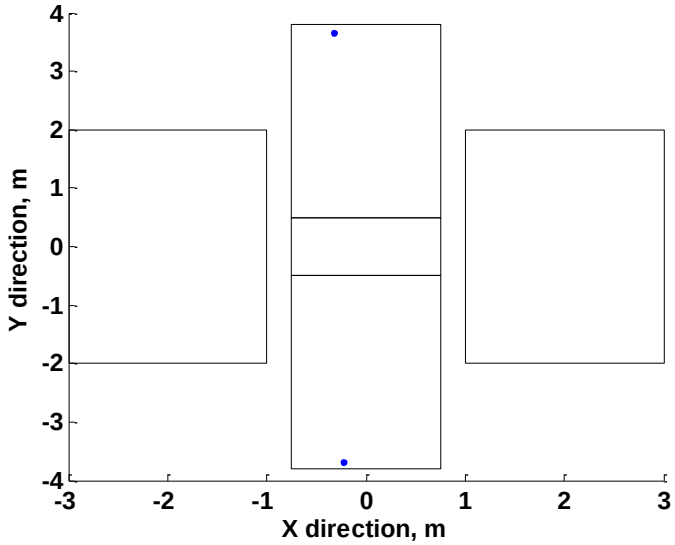

Figure 37. Ion impacts from Run 2 (with faster ions, weaker magnetic field, and wider plume).

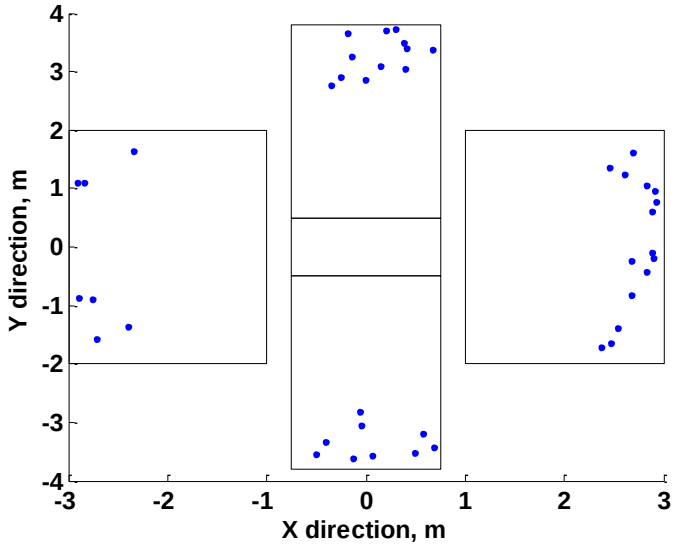

Figure 38. Ion impacts from Run 3 (with faster ions, stronger magnetic field, and wider plume).

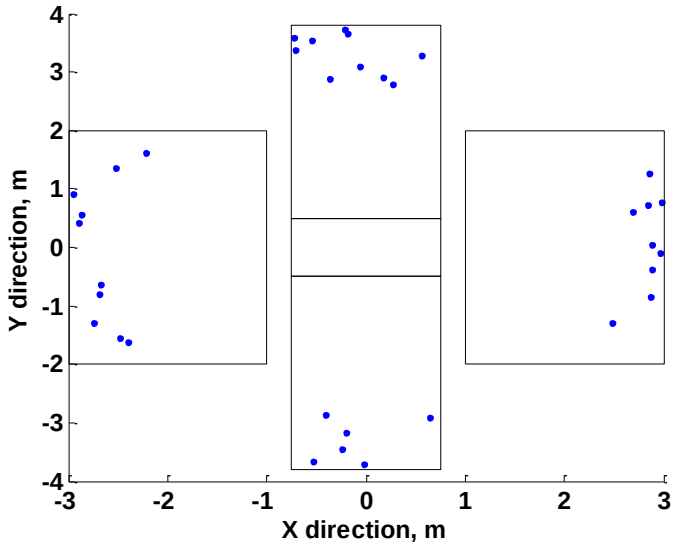

Figure 39. Ion impacts from Run 4 (with faster ions, stronger magnetic field, and narrower plume).

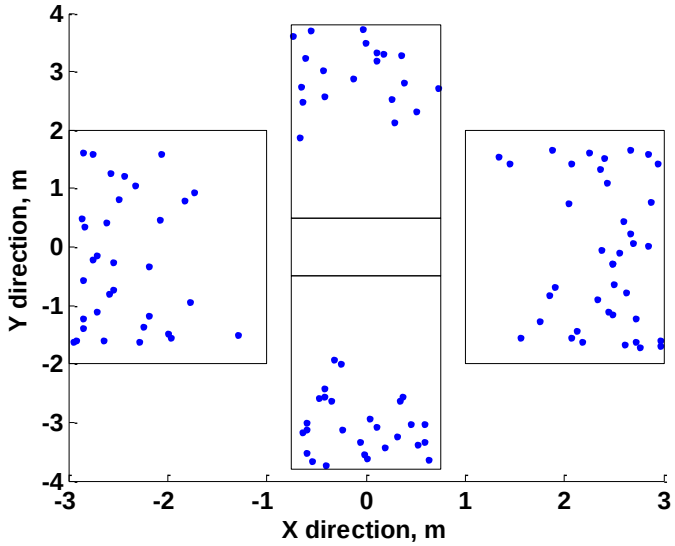

Figure 40. Ion impacts from Run 5 (with slower ions, stronger magnetic field, and narrower plume).

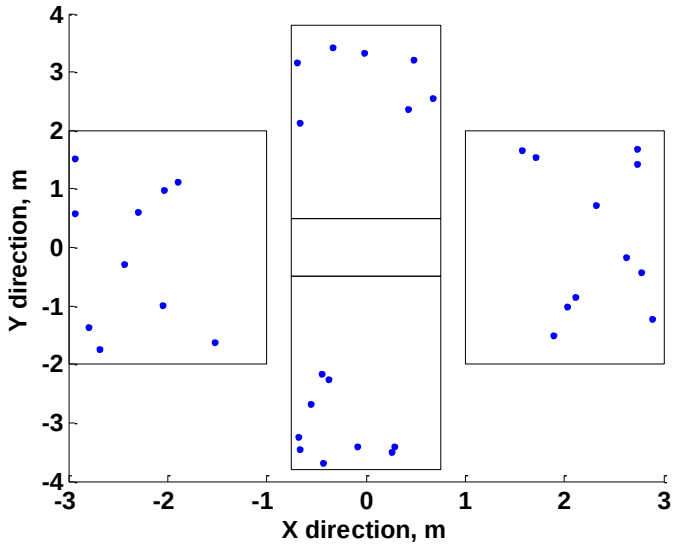

Figure 41. Ion impacts from Run 6 (with slower ions, weaker magnetic field, and narrower plume).

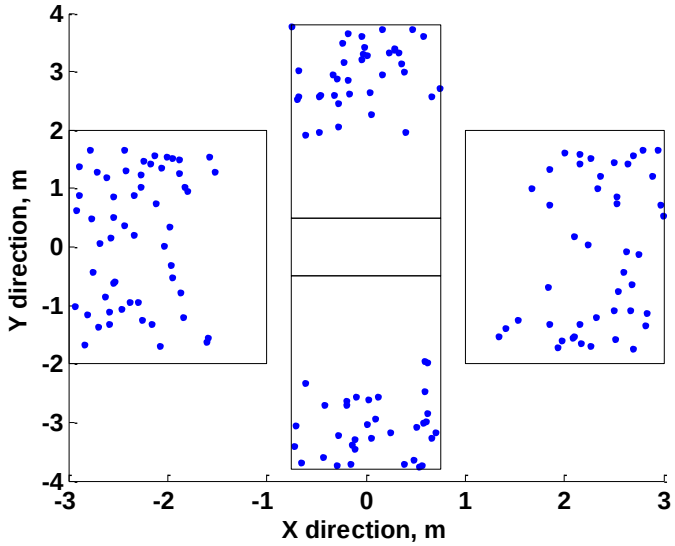

Figure 42. Ion impacts from Run 7 (with slower ions, stronger magnetic field, and wider plume).

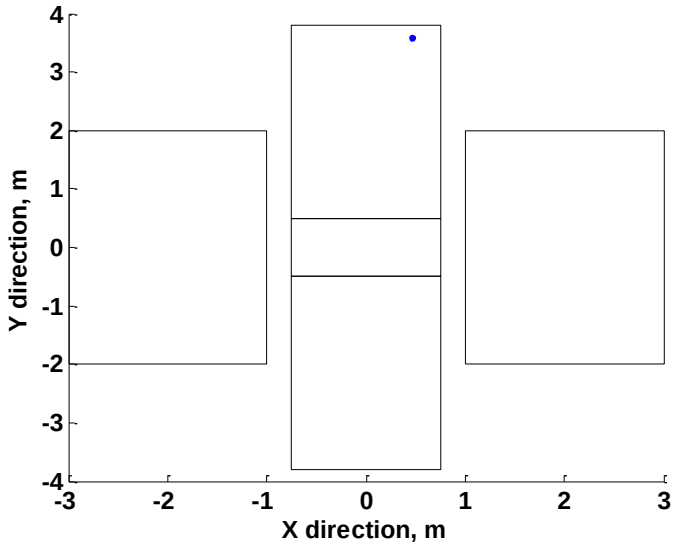

Figure 43. Ion impacts from Run 8 (with faster ions, weaker magnetic field, and narrower plume).

5.4 Electrical Charging Results

The sheath potential, ϕ, was calculated using a MS Excel® spreadsheet. The equations listed in Section 4.3.3 were used along with the average impacting ion kinetic energy for each run. Temperature is essentially the average kinetic energy of all particles within a plasma if the distribution is Maxwellian (i.e. the plasma is in quasi-equilibrium)[37]. The temperature is also needed to calculate the Bohm velocity and electric potential. Therefore, the average kinetic energy of all ions in a run was used to calculate one potential for that run instead of calculating potential from each impact and summing them together which would have resulted in adding potentials from many different plasma sheaths. The results are shown below:

Table 3. Spacecraft potential when the plasma is assumed to be in quasi-equilibrium*

Run #	$\langle KE \rangle_i$ (eV)	$\langle KE \rangle_i$ (J)	Ni max (#/m^3)	Electron Velocity (m/s)	Electron Temperature (K)	V_{Bohm} (m/s)	J_I (A/m^2)	Potential, ϕ (V)
1	18.78	3.01E-18	5.25E+15	2.57E+06	1.45E+05	5499.235	4.63	-12.52
2	38.96	6.24E-18	1.78E+14	3.70E+06	3.02E+05	7920.707	0.23	-25.97
3	41.76	6.69E-18	3.83E+15	3.83E+06	3.23E+05	8200.394	5.03	-27.84
4	41.78	6.69E-18	3.12E+15	3.83E+06	3.23E+05	8202.358	4.09	-27.85
5	31.22	5E-18	1.06E+16	3.31E+06	2.42E+05	7090.403	12.03	-20.81
6	19.49	3.12E-18	3.29E+15	2.62E+06	1.51E+05	5602.223	2.96	-12.99
7	26.99	4.32E-18	1.53E+16	3.08E+06	2.09E+05	6592.588	16.17	-17.99
8	38.89	6.23E-18	8.90E+13	3.70E+06	3.01E+05	7913.588	0.11	-25.93

From Table 3, it can be seen that Runs 3 and 4 have the highest charging (i.e. potential, ϕ) as a result of ion impacts. This result is logical as potential here is only a function of average impacting kinetic energy and these runs have the highest kinetic

energy (the reason for the *). Assuming that the plasma is in quasi-equilibrium, the electron kinetic energy is equal to the ion kinetic energy as both ions and electrons were exposed to the same RF power source. Similarly, Runs 2 and 8 have almost the same potential due to their high average kinetic energies even though their ion densities were much lower, which indicates a weakness in using the kinetic energies are equivalent assumption. The kinetic energies were assumed to be equal because the electrons and ions received their energy from the same RF power source and no experimental data on electron vs. ion velocities at the surface was available. The plasma fluence, or flux per time increment, is the flux (column J_I) divided by 1 second because the impacting ions were calculated using a mass flow rate over 1 second for a total of 2.26×10^{21} ions. As the plasma was also assumed to be quasi-neutral, the electron current density is equal to the ion current density (column J_I). There is, however, an alternative method to determining the electric potential on the spacecraft surface which is explored in Appendix M. This alternative method was not used here because it assumed that the electron and ion temperatures, the number of ions and electrons, and also the electron and ion kinetic energies are equivalent while the method used in this section only assumes that the electron and ion kinetic energies are the same.

If the velocity of impacting ions is taken as the Bohm velocity, then the maximum current density in A/m^2 is 8.01 (Run 1), 0.39 (Run 2), 8.71 (Run 3), 7.10 (Run 4), 20.85 (Run 5), 5.11 (Run 6), 27.97 (Run 7), and 0.20 (Run 8) for an increase from Table 3 of roughly 73%.

It is important to note that the plasma contactors currently installed on the ISS routinely handle floating potentials of -160 V DC and may be able to handle charging due to the firing of a magnetoplasma engine. However, longer engine run times will either require more frequent activation of the plasma contactors or the need for a dedicated plasma contactor for magnetoplasma engine testing. Whether the PCUs can handle the load has not be determined.

How charging relates to ion exit velocity, magnetic field strength, and ejected ion density profiles was determined using Design of Experiment (DOE) criteria with a Full Factorial experiment and is presented below in a Pareto plot, Figure 44. The effect of A, B, C is shown as it relates to Potential (Volts).

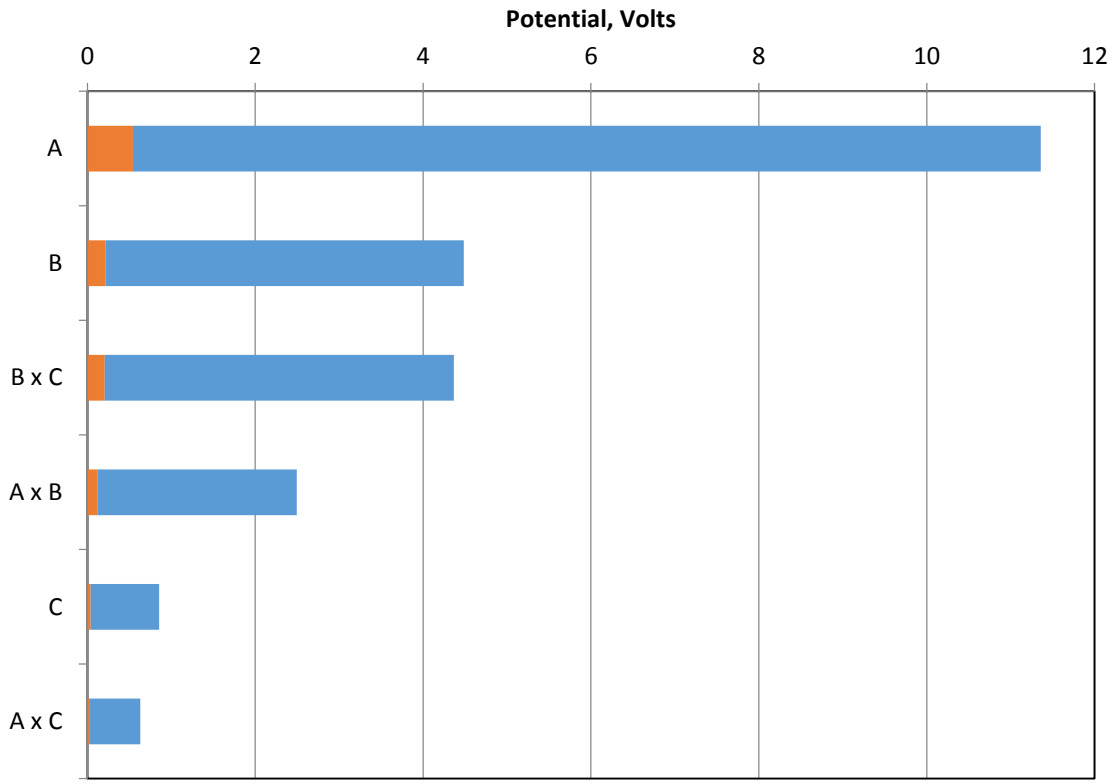

Figure 44. Pareto plot of the effect A, B, and C factors have on the spacecraft potential, V, resulting from ion impacts for a quasi-neutral isothermal plasma. The red bar represents the possible error.

Factor A, the exit velocity of ejected ions, had the greatest effect. The faster the ions exited the engine, the higher the returning ions' average kinetic energy (and thus plasma temperature) was and greater the surface potential became. This is somewhat surprising as the faster the ion exit velocity is, the fewer ions return and impact, but potential here is a factor of the average impacting ion kinetic energy and particle mass only in Figure 44. Factor B, the magnetic field strength, had the second greatest effect. A stronger magnetic field causes more ions with higher kinetic energies to return and impact the spacecraft surface thus causing greater surface potential. Factor C, the density

distribution of the exiting ion velocities in the plume, had only a marginal effect on spacecraft potential. However, it is interesting to note that the interaction of magnetic field strength and density distribution does have a significant effect on spacecraft potential with a strong magnetic field trapping more ions when the plume is wider than when the plume is very narrow. The interaction of ion exit velocity and magnetic field is also significant with a strong magnetic field and faster ion exit velocity causing a decrease in spacecraft potential. This is surprising as it means that faster ions at a lower magnetic field strength cause the spacecraft potential to increase more than faster ions at a stronger magnetic field strength. The next section will explain the erosion rate found in each of the 8 runs.

5.5 Erosion Results

This section explains the erosion rates found using 8 versions of the numerical model to simulate different configurations of a magnetoplasma spacecraft engine. Table 4 lists the percentage of ions entering the backfield ("Enter backfield"), the percentage of ions that impact the engine and radiator panels ("Impact"), the average kinetic energy of impacting ions in eV ("Impact <KE>"), and the erosion rate from argon ions transferring the average kinetic energy onto an aluminum surface in nm/month ("Erosion AL") and onto a silicon surface ("Erosion Silicon"). The situations where the most ions recirculate and enter the backfield are Runs 7 and 3 when the magnetic field is at its greatest strength and the plume is widest. This result is logical in regards to density distribution because ions that begin in the plume fringe ($r > 0.3$ m) are exposed to a

greater B_r than those in the centerline and thus are more likely to follow the curved field lines into the backfield.

Table 4. Results of Full Factorial Experiment.

Run	A	B	C	Enter backfield	Impact	Impact <KE> eV	Erosion nm/month AL	Erosion nm/month Silicon	AxB	BxC	AxC
1	-1	-1	-1	0.22%	0.0059%	18.78	0.050	0.000	1	1	1
2	1	-1	-1	0.07%	0.0002%	38.96	0.023	0.006	-1	1	-1
3	1	1	-1	0.24%	0.0043%	41.76	0.853	0.357	1	-1	-1
4	1	1	1	0.10%	0.0035%	41.78	0.700	0.294	1	1	1
5	-1	1	1	0.21%	0.0119%	31.22	1.386	0.611	-1	1	-1
6	-1	-1	1	0.09%	0.0037%	19.49	0.037	0.000	1	-1	-1
7	-1	1	-1	0.58%	0.0172%	26.99	1.129	0.471	-1	-1	1
8	1	-1	1	0.04%	0.0001%	38.89	0.011	0.003	-1	-1	1

where A = ejected particle velocity, B = magnetic field strength, and C = plume width

Five trends are immediately apparent from Table 4. These trends are:

1. The conditions in Run 1 (slower velocity, weaker magnetic field, and wider plume) and Run 6 (slower velocity, weaker magnetic field, and narrow plume) are the best if the goal is to have the least amount of erosion on the engine housing and radiator panels. This is because even though more ions impact than the average of all 8 runs (0.00585%), the impacting ions have a kinetic energy that is generally lower than the minimum breakaway energy for both aluminum and silicon. Therefore, negligible aluminum or silicon atoms are eroded from the spacecraft surfaces. However, if the goal is to have the least number of ions enter the backfield, then the engine configurations in Runs 8 and 2 are best. These two configurations have the faster average

initial ion velocity and weaker magnetic field strength in common, which indicates that by either increasing ion exit velocity or by decreasing the engine's magnetic field strength, you can significantly reduce the number of trapped ions. Run 2 (faster velocity, weaker magnetic field, and wider plume) and Run 8 (faster velocity, weaker magnetic field, and narrow plume) only differ in plume width and also cause very little erosion, but for the opposite reason as in Runs 1 and 6: the weaker magnetic field fails to trap many ions but those that do impact have a higher kinetic energy to cause slightly more erosion. Conversely, if you wish to trap more ions, such as to generate a plasma sail (i.e. the mini-magnetospheric plasma propulsion (M2P2) engine [38, 39]), then decreasing the ion exit velocity or increasing the magnetic field strength will help trap the plasma needed.

2. The engine configurations in Run 5 (slower velocity, stronger magnetic field, and narrow plume) and Run 7 (slower velocity, stronger magnetic field, and wider plume), the stronger magnetic field versions of Runs 1 and 6, are the worst in terms of having the highest erosion of both aluminum and silicon. These relationships are better shown with the sorted tables in Appendix J.
3. The velocity profile had a major impact on the percentage of ions impacting, with more ions returning on average when the velocity of exiting ions was lowest (0.275% for slower exiting ions condition vs. 0.112% for fast exiting ion condition on average). The lower initial velocity ions returned almost 2.5 times more often than higher initial velocity ions did. This indicates that the

lower the initial velocity is for the ejected plasma, the more particles will be trapped in the magnetic field, recirculate, and impact the engine housing and radiator panels.

4. Understandably, the erosion rate was highest on runs with the most impacting ions (i.e. Run 7 and 5), where the slower ions were ejected and trapped by a stronger magnetic field. This indicates that although the impacting ions have less kinetic energy than in Runs 3 and 4 (the next highest erosion rates), there are so many ions impacting with kinetic energy above the sputter energy threshold for aluminum or silicon that greater overall erosion results. The result that with a stronger magnetic field, significant erosion is caused in either a case of slower ejected particles or faster ejected particles indicates that there is a zone where erosion occurs. This zone would begin with increasing initial average ion velocity (greater than the sputter energy threshold) and then end as the number of impacting ions approaches zero. The "erosion zone" is discussed in section 5.5.1.
5. Lastly, the narrowness of the plume has a significant effect on whether an ion will return or not. A narrower plume decreases the amount of recirculating ions by between 175% and 276%.

The erosion rates in Table 4 can be put into context by comparing them to those measured from samples placed onboard a satellite in low earth orbit for 3.95 years during the NASA MISSE 2 experiment[40], as discussed in section 2.8 Plasma Plume – Spacecraft Interaction. Numerous polymer samples were exposed to an atomic oxygen

flux of 8.43 x 10^{21} atoms/cm^3 from the Earth's atmosphere. The average erosion rate of Kapton H was measured to be 5263 nm/month. Kapton H has about half the density of AL (1.42 g/cm^3 and 2.7 g/cm^3, respectively). Using Polytetrafluoroethylene (PTFE Teflon), a material with a density closer to AL (ρ = 2.2 g/cm3), the measured erosion rate was 245 nm/month. Therefore, erosion due to a magnetoplasma spacecraft engine firing is considerably less than erosion caused by atomic oxygen in low earth orbit.

5.5.1 Sensitivity of Erosion Rates to Changes in Factors A, B, and C

To better understand which factor is driving erosion, the effect of changes in each factor (ejected particle velocity [or A], magnetic field strength [or B], or plume width [or C]) on the erosion rate was determined. The average erosion rate for all factor N+, where N = A, B, or C, was subtracted from the average erosion rate for all factor N-, and this value was divided by the percentage difference between N+ and N- (e.g. difference between the A+ and A- average velocities and divided by the A+ average velocity) using the following equation:

$$Effect = \frac{A^{+} - A^{-}}{\Delta A} \qquad (5\text{-}1)$$

The results were:

A = -0.0142 nm/month per % change

B = 0.01974 nm/month per % change

C = 0.00099 nm/month per % change

Thus, the velocity profile (A) has almost the same effect that the magnetic field strength (B) has on aluminum erosion for each percent change (but in the opposite direction). The magnetic field (B) has about 20 times the effect that the density distribution (C) has on aluminum erosion. Therefore, changes in the magnetic field strength will result in the greatest change in the erosion rate of an aluminum plate. However, the erosion rate does not continue with increasing average ion kinetic energy unabated. Instead an "erosion zone" exists which begins when impacting ions have greater kinetic energy than the minimum aluminum sputter yield threshold (as discussed in section 2.8.2) and ends when the number of impacting ions drops to so few that erosion is negligible as shown in Figure 45. The effect Factor A has on the percentage of ions impacting was determined in the same method for erosion (eq. 5-1) and found to be -0.0004286% of ions impacting for each percentage change in Factor A. The green box in Figure 45 represents the "erosion zone" and where the amount of erosion caused due to increased kinetic energy crosses the decreasing amount of ions that actually impact due to increased kinetic energy is where the maximum erosion condition is likely to occur. It is important to note that Figure 45 was created on the assumption that the erosion sensitivity was linear and was derived using only two points (i.e. Factor A+ and A-). More computational runs with a variety of Factor A are needed to determine if the relationship between erosion caused and percent of ions that impact due to increasing average ion velocity is indeed linear. However, even if not a linear relationship, an "erosion zone" will exist between ions being too slow to cause erosion (left side of

Figure 45) and too few ions impacting to cause discernable erosion (right side of Figure 45).

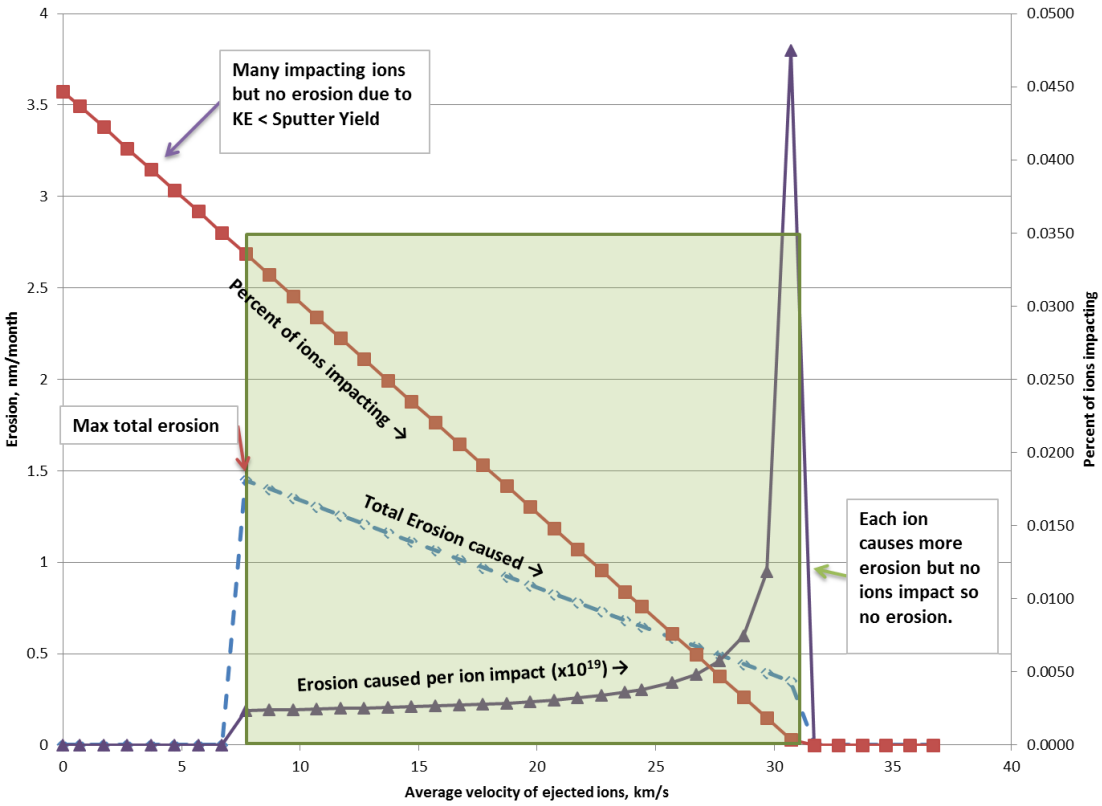

Figure 45. The total amount of erosion (blue dotted line) of an aluminum plate (Run 5) caused by impacting ions and the percentage of impacting ions (red line) are plotted in relation to the average initial velocity, or ejected ion velocity, of ions within the plume. The purple line is the erosion caused per individual impacting ion. The green box is the "erosion zone" where erosion begins once the kinetic energy of impacting ions is greater than the minimum aluminum sputter yield threshold and ends when the percentage of impacting ions reaches a value of essentially zero.

Figure 46 illustrates the effect the magnetic field strength has on the erosion rate with a stronger magnetic field increasing the erosion rate until all ejected ions are

trapped, impact, and cause erosion. The erosion zone here does not start until the magnetic field strength is strong enough to trap a significant amount of ions.

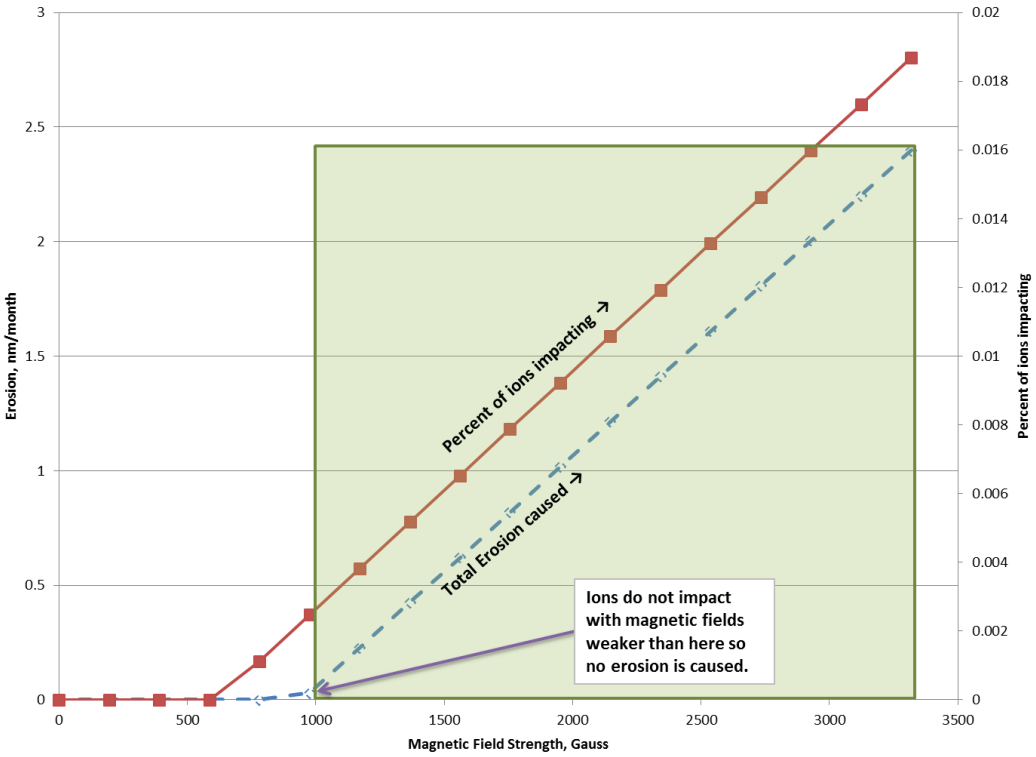

Figure 46. The amount of erosion of an aluminum plate (Run 5) caused by impacting ions and the percentage of impacting ions are plotted in relation to the magnetic field strength within the plume. The green box is the "erosion zone" where erosion begins once the number of particles trapped is not negligible.

To better explain the relationship factors A, B, and C have, the baseline condition, which is Run 5, will be discussed in the next section. After showing the baseline, how each run compares to Run 5 will then be presented.

5.5.2 Baseline - Run 5: A-, B+, C+

This model run utilized the slower velocity profile ($\bar{V}_{mag}$ = 24.4 km/s, FWHM = 10 km/s), the nominal magnetic field (I = 140 A), and the nominal density distribution ($\bar{r}$ = ±0.205 m). This run represents the nominal engine configuration used to validate the computer model because both the velocity profile and the density profile use the same ICH/RF ratio of 3.

The distribution of ions entering the backfield in Figure 47 is between 7.66 km/s and 33.31 km/s, with the average initial velocity being 17.93 km/s. The trend for returning ions to have a slower average initial velocity (i.e. for these plots to skew left) is common to all 8 runs and indicates that ions with higher initial velocities are more likely to escape the magnetic field to provide thrust. The saw-tooth peaks present in Figure 47 are due to the ion distribution being 19 groups of ions with differing initial velocities and quantities as mentioned in section 4.3 Solution Approach. If the number of levels was increased from 19 to a much higher number, the graph would be a smooth curve, but this would incur a large CPU time penalty. These saw-tooth peaks are present in all 8 runs' figures showing initial velocity and radial position.

The distribution of ions impacting structure in Figure 47 is between 7.66 km/s and 17.69 km/s, with the average initial velocity being 11.48 km/s. This average is close to the average of all runs (11.7 km/s) and makes Run 5 a good baseline because it serves as the median of all 8 runs.

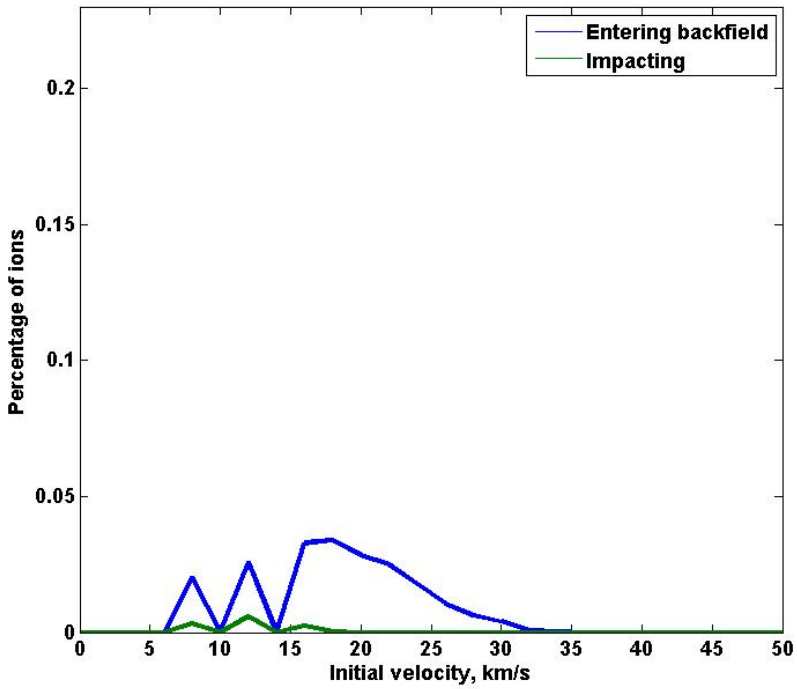

Figure 47. Percentage of ions entering the backfield (blue) and impacting engine/radiators (green) as a function of initial velocity in the z direction for Run 5. The jagged peaks are a result of the 19 velocity groups and would likely be a continuous curve if more velocity groups than 19 were used.

The distribution of initial radial positions of all ions entering the backfield is from 0.344 m to 0.698 m, with the average being 0.563 m. This average is close to the average of all 8 runs (0.549 m). The distribution of initial radial positions of impacting ions only is from 0.44 m to 0.697 m, with the average being 0.595 m. This average is close to the average of all 8 runs (0.62 m) which supports the assertion that Run 5 is a good baseline.

The majority of returning ions originate the farthest in the plume fringe (i.e. the graph skews right) in Figure 48, indicating that the far fringe is particularly vulnerable to

trapping ejected ions. The factors that are responsible for this trapping will be discussed in the next section.

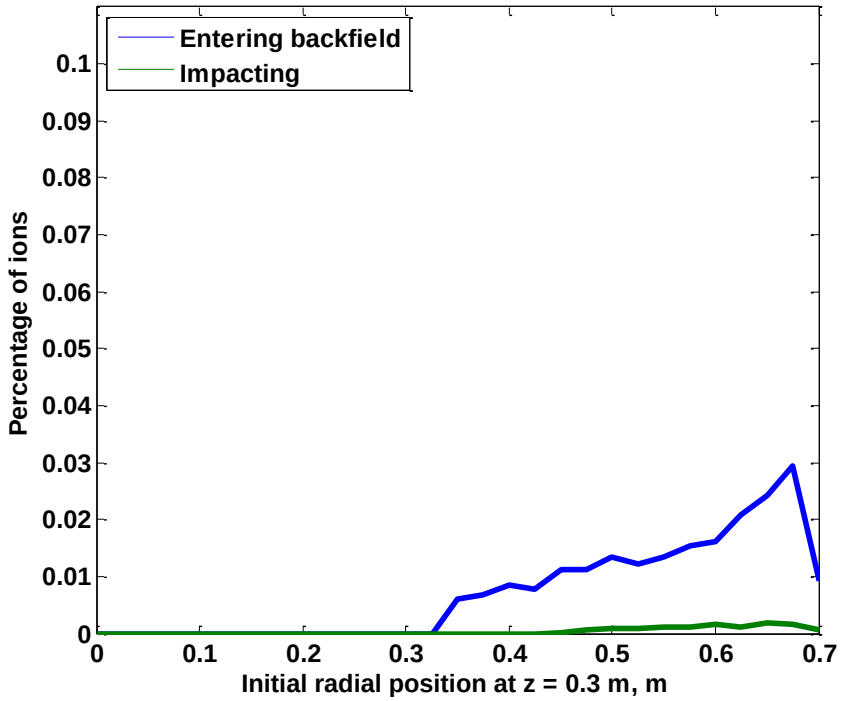

Figure 48. Percentage of ions entering the backfield (blue) and impacting engine/radiators (green) as a function of initial radial position for Run 5. The blue average is 0.563 m and the green average is 0.595 m.

The "islands" or concentrations of all returning ions (Figure 49) and impacting ions (Figure 50) are mostly concentrated at lower initial velocities and at initial radial positions that are farther in the plume fringe, indicating that almost all of the ions are escaping as thrust and that no ions near the plume centerline are recirculating and impacting.

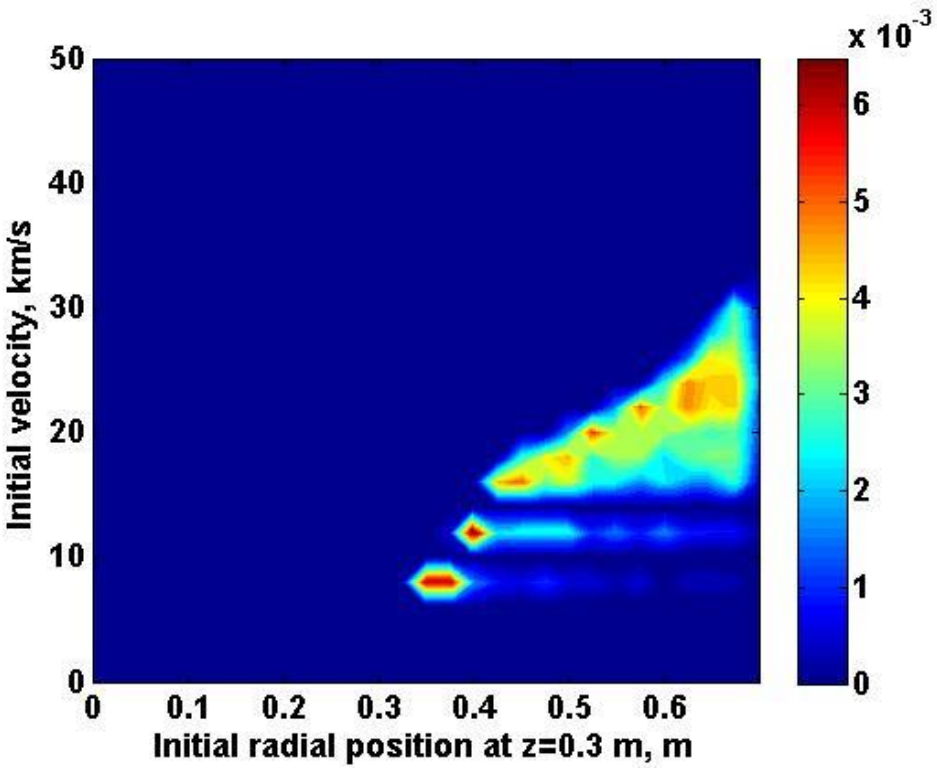

Figure 49. Contour plot of percentage of ions entering the backfield as a function of initial velocity in the z direction and radial position for Run 5.

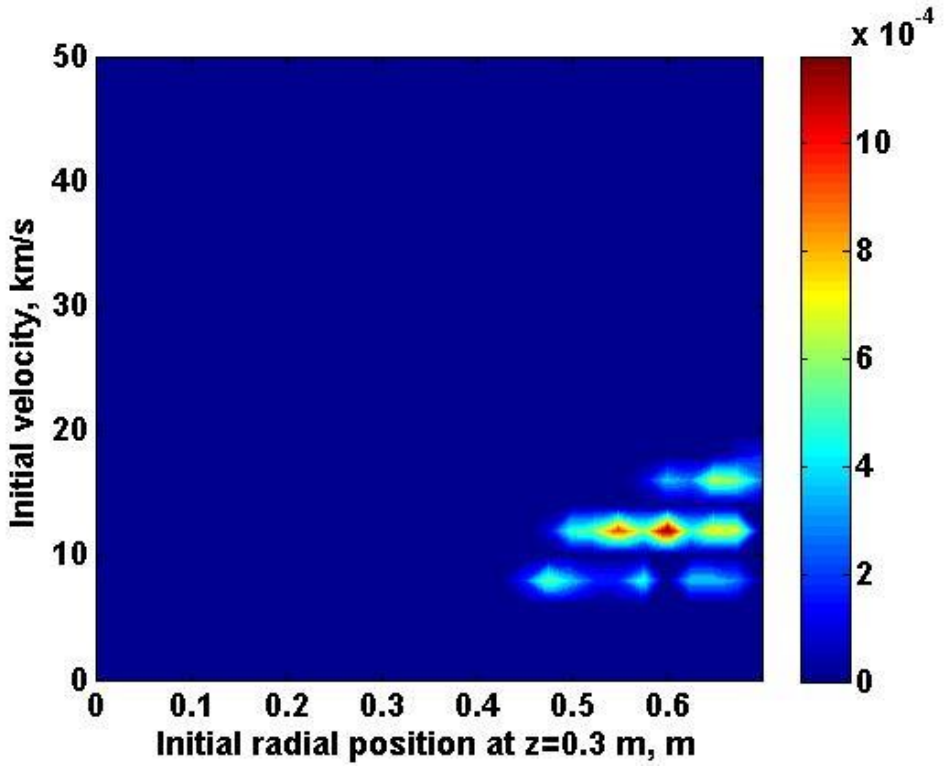

Figure 50. Contour plot of percentage of ions impacting structure as a function of initial velocity in the z direction and radial position for Run 5.

To verify that these results correlate with the Kinetic detachment described in section 2.7 Particle Detachment from Magnetic Fields, the results needed to go from one burst of all the argon ions in one second (i.e. 2.26 x 10^{21}) to a continuous flow, which is how magnetoplasma engines will operate. However, simulating continuous flow was found to be too CPU time-intensive so, in lieu of continuous flow, many bursts of fewer particles over one second were used. A MATLAB® program was written that took the results of 10 time steps from time = 0 s to time = 0.0009 s (the range in which most of the ions were still within the 30 m model sphere) and then added the particles in these time steps such that instead of one burst at time= 0 s, there were 10 bursts over 1 second

as represented in Table 5. This program converted the flow from a Euler space to a Lagrangian space. The number of particles for each burst was scaled so that the mass flow rate of 2.26 x 10^{21} kg/s was conserved.

Table 5. Time steps used to create multiple bursts to simulate continuous flow.

	Timesteps										
	1	**2**	**3**	**4**	**5**	**6**	**7**	**8**	**9**	**10**	**11**
	0	0.0001	0.0002	0.0003	0.0004	0.0005	0.0006	0.0007	0.0008	0.0009	0.001
Burst 1	1	2	3	4	5	6	7	8	9	10	11
Burst 2		1	2	3	4	5	6	7	8	9	10
Burst 3			1	2	3	4	5	6	7	8	9
Burst 4				1	2	3	4	5	6	7	8
Burst 5					1	2	3	4	5	6	7
Burst 6						1	2	3	4	5	6
Burst 7							1	2	3	4	5
Burst 8								1	2	3	4
Burst 9									1	2	3
Burst 10										1	2
Burst 11											1

The individual ions from each burst were placed in one vector which was then sorted so that only ions within -0.05 m < x < 0.05 m were used. A slice of the plume is acceptable as the plume is axisymmetric. This slice was then binned to determine the ion density, the average velocity in the volume, and the average magnetic field strength in the volume. These values were calculated for a 122 x 122 matrix representing a circle 60 m in diameter. From ion density and average magnetic field strength, the Alfven velocity was found using Eq. 2-2 for each cell of the matrix. Using the average velocity and Alfven velocity of each cell, the Beta (eq. 2-1) was determined for each cell. K. Sankaran asserted that once particles achieve a Beta of one or greater, the particles

detach from the magnetic field lines and escape as thrust [4]. This assertion is confirmed in Figure 51 because almost all of the ions have achieved a Beta greater than unity (red to maroon) and are no longer attached to the magnetic field lines. However, a relatively small amount of particles are sub-Alfvénic (green to orange), remain connected to the magnetic field lines, and do impact the engine housing or radiator panels.

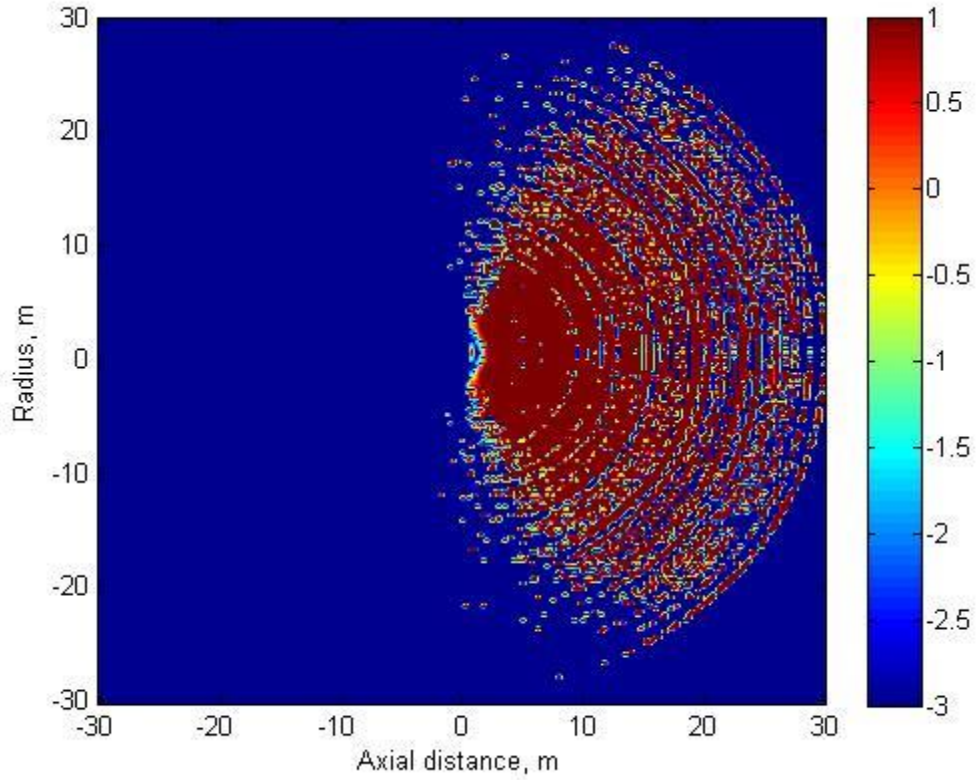

Figure 51. Log10 plot of Beta for Run 5 found for each cell where an interpolation function was used to smooth the color edges. The radius axis is the vertical direction, and the axial distance is the horizontal direction with the engine exit sitting at [0,0] and the plume exiting towards the right. The super-Alfvénic particles (red to maroon) are detaching from the magnetic field lines to provide thrust. The sub-Alfvénic particles (green to orange) remain trapped.

Run 5 confirms that Kinetic detachment is occurring when the ejected ions reach the Alfvén velocity. Olsen[41] used experimental data to determine where the transition

existed between the plume particles being sub-Alfvénic and super-Alfvénic, which was found to be around 1.4 m from the engine exit. The red line in Figure 52 (a) indicates the transition point in the plasma. The dark red illustrates the plasma that is expected to be detached per Sankaran[4]. The axial distance range in (a) corresponds to 0.2 m to 2.4 m from the engine exit. The red line in Figure 52 (b) indicates the same transition point in the numerical model, which is identical to the 1.4 m point determined experimentally. The angle of the line is different between (a) and (b), however, and is likely due to the difference in vacuum pressure between the experiment (1×10^{-8} to 2×10^{-4} torr) and the numerical model (0 torr). The lower pressure of the numerical model is expected to cause the plume to fan out at a greater angle.

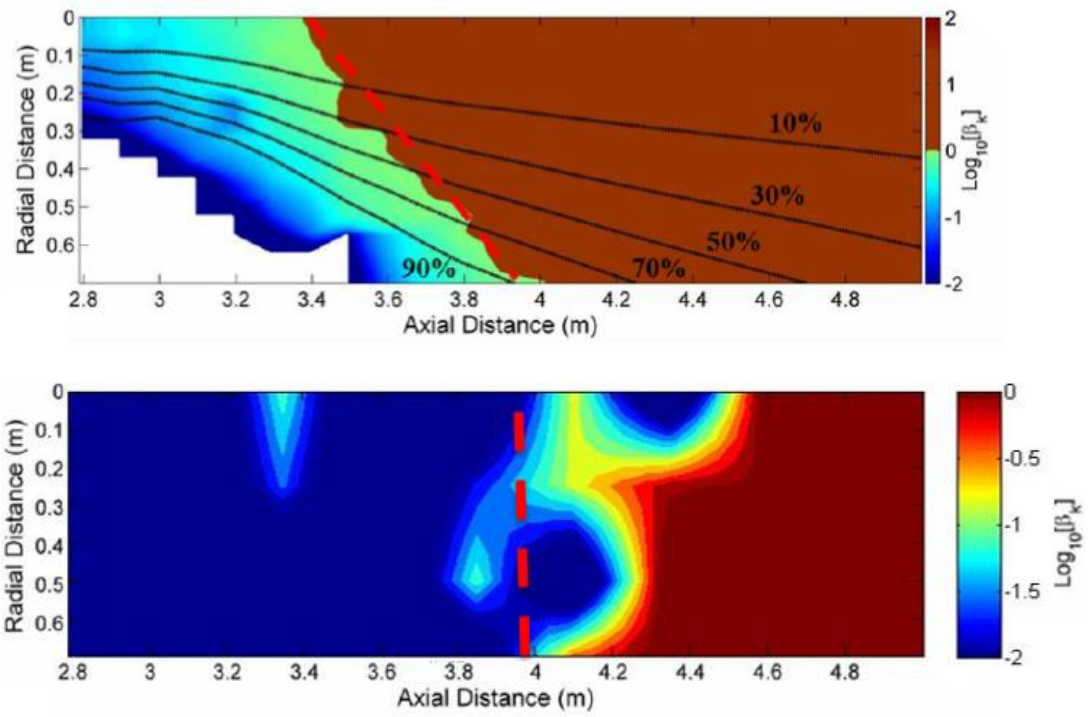

Figure 52. Contour maps of plasma kinetic Beta during ICH use derived from (a) VX-200 experimental data[36] **and (b) the numerical model. The red lines indicate the transition point between the plume particles being sub-Alfvénic and super-Alfvénic, which was found to be around 1.4 m from the engine exit.**

Figure 52 validates the numerical model as (a) was not available at the time of model creation and the predicted result in (b) closely matches the experimental values. The differences between the two plots most likely arise from differences in the background vacuum pressure, mesh size of the numerical model, and slightly different initial conditions.

This section served to explain the results from Run 5 and to validate the results using experimental data from Literature. In the next section, the remaining 7 runs are compared to Run 5 to expand on the trends discussed earlier.

5.5.3 Individual Run Results

This section presents the results for each of the 7 remaining runs and compares the results to those from Run 5. At the end of the section, a comparison of all run results is presented with a discussion on similarities between runs.

5.5.3.1 Run 1: A-, B-, C-

This model run utilized the slower velocity profile ($\bar{V}_{mag}$ = 24.4 km/s, FWHM = 10 km/s), the weaker magnetic field (I = 70 A), and the wider density distribution ($\bar{r}$ = ±0.25 m). The range of initial velocities for all ejected ions in this run is from 7.66 km/s to 40.48 km/s. The percentage of ions following the magnetic field lines and entering the backfield is 0.22%, which is very close to the average for all runs (0.194%). The percentage of ions actually impacting is 0.0059%, which is identical to the average of all runs (0.0059%). Figure 53 is similar to the initial velocity profiles from all 8 runs, with only the slowest ions being trapped by the magnetic field and recirculating. The distribution of all ions entering the backfield is from 7.66 km/s to 25.8 km/s with the average being 12.56 km/s. The average is significantly less than the average in Run 5 (17.93 km/s) or for all runs (16.2 km/s) indicating that a weaker magnetic field and wider plume results in only the slower ions becoming trapped. It's important to note that the initial velocity is the lowest that the model ejected (7.66 km/s), so if the plume contained ions traveling slower than 7.66 km/s, they would likely be trapped as well. The faster ions simply escape as thrust. However, the percentage of ions entering the backfield and the percentage of impacting ions is third highest in Table 4 indicating that

more ions are trapped in this configuration than most others. Conversely, the kinetic energy of the impacting ions is so low that it falls below the sputter yield threshold for either AL or SI resulting in negligible erosion damage. As erosion is detrimental to spacecraft performance, this run and Run 6 represent the best configurations for operating a magnetoplasma spacecraft engine to minimize physical damage.

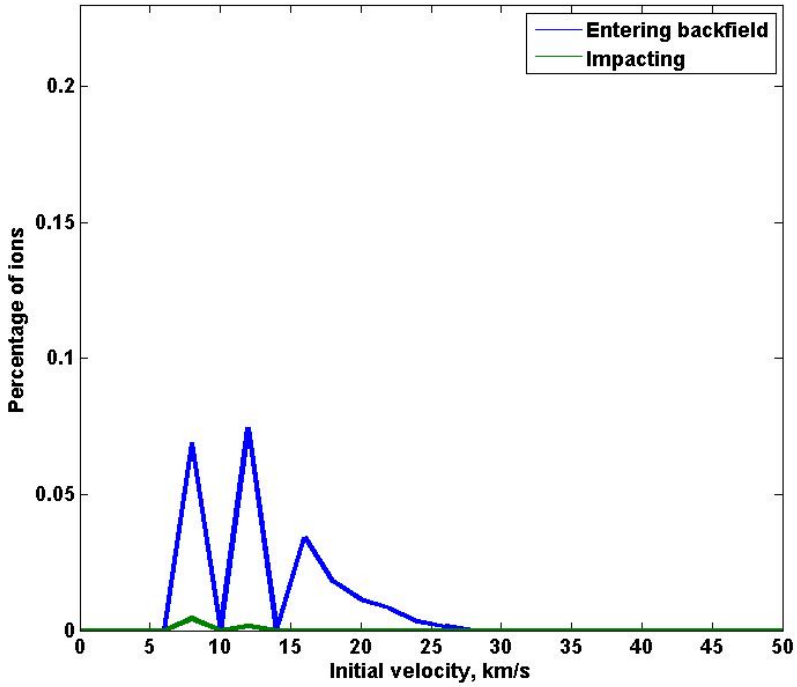

Figure 53. Percentage of ions entering the backfield (blue) and impacting engine/radiators (green) as a function of initial velocity in the z direction for Run 1. The jagged peaks are a result of the 19 velocity groups and would likely be a continuous curve if more velocity groups than 19 were used.

The initial radial position of returning ions is spread out (Figure 54) between 0.3 m and 0.7 m. The average initial radial position of ions entering the backfield is 0.502 m. However, the ions that actually impact the engine housing or radiator panels are

concentrated farther in the plume fringe (0.47 m < r < 0.7 m) with the average being 0.592 m. This indicates that only very slow ions at the edge of the plume fringe impact structure. It is important to note that the "peak – valley – peak" characteristic of Figure 54 is only replicated in runs that have the wider plume (Factor C-) in common, indicating that a wider plume results in more ions that originate closer to the centerline being pulled into the backfield.

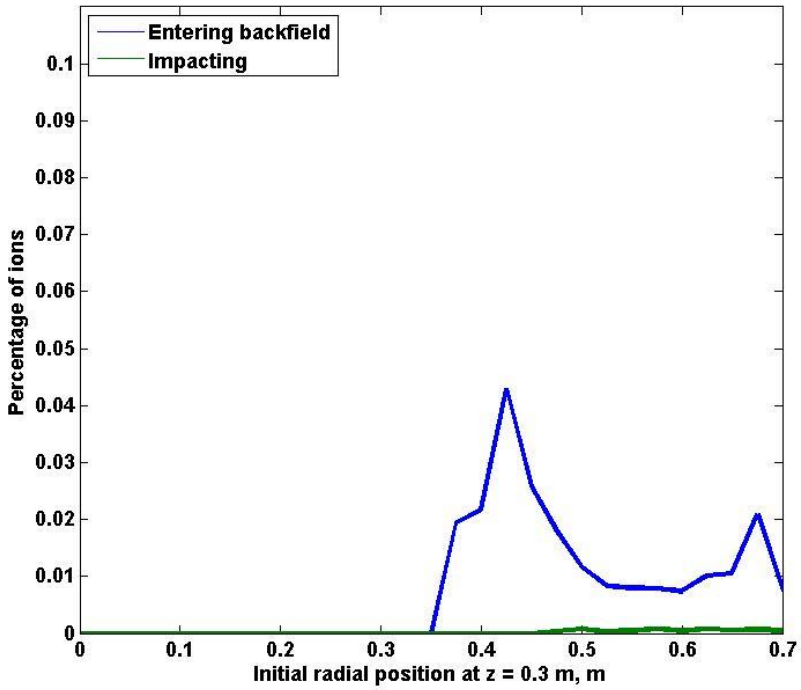

Figure 54. Percentage of ions entering the backfield (blue) and impacting engine/radiators (green) as a function of initial radial position for Run 1. All runs that have the double peak above have the wider plume in common.

The observation that only the slowest ions farthest from the plume centerline are entering the backfield can be clearly seen in Figure 55 where "islands" of returning ions originate between initial radial positions of 0.37 m and 0.698 m and initial velocities of

7.66 km/s and 25.8 km/s. The largest concentration is at V_{avg} = 12.6 km/s, which is the average initial velocity for backfield ions in this run. If an ion is located at another radial position or another velocity outside of these "islands", it will escape to provide thrust. No ions within the plume (r < 0.3 m) enter the backfield or impact structure for this or any of the 8 runs. Only ions that originate in the plume fringe enter the backfield and impact. It is important to note that although the area between 0.5 m and 0.7 m below 10 km/s looks empty in Figure 55, it is only due to the much higher concentration elsewhere in the graph that washes these slower ions out. There are many ions with a velocity less than 10 km/s and starting between 0.5 m and 0.7 m that enter the backfield and are visible in Figure 56. The "islands" in Figure 56 are concentrated between 0.46 m and 0.7 m of the plume, verifying that only the slowest ions at the far fringe of the plume actually impact structure.

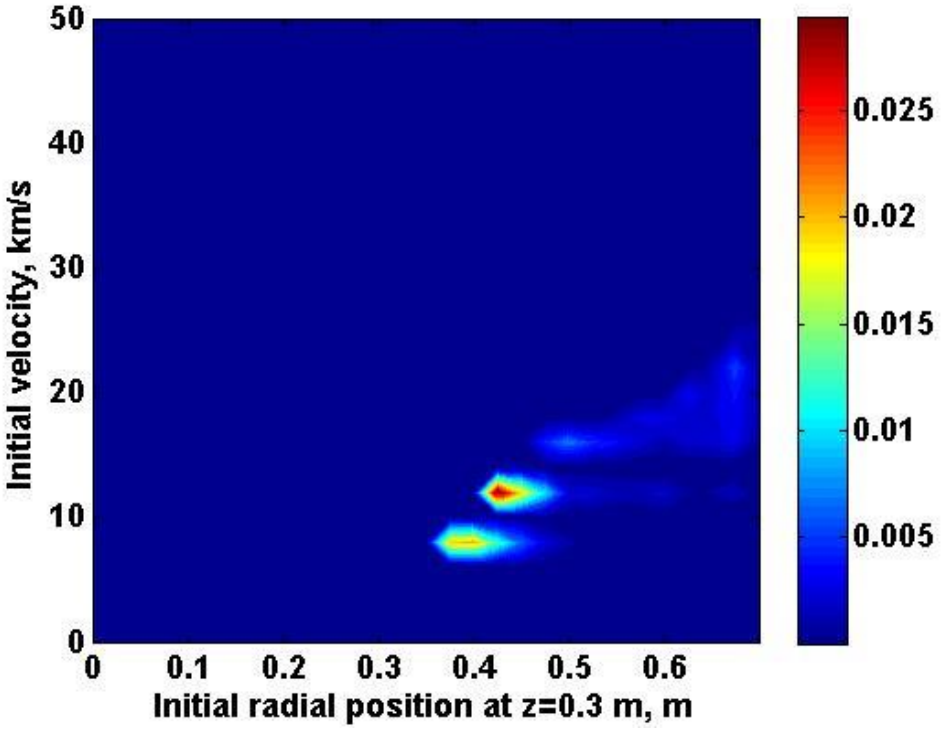

Figure 55. Contour plot of percentage of ions entering the backfield as a function of initial velocity in the z direction and radial position for Run 1.

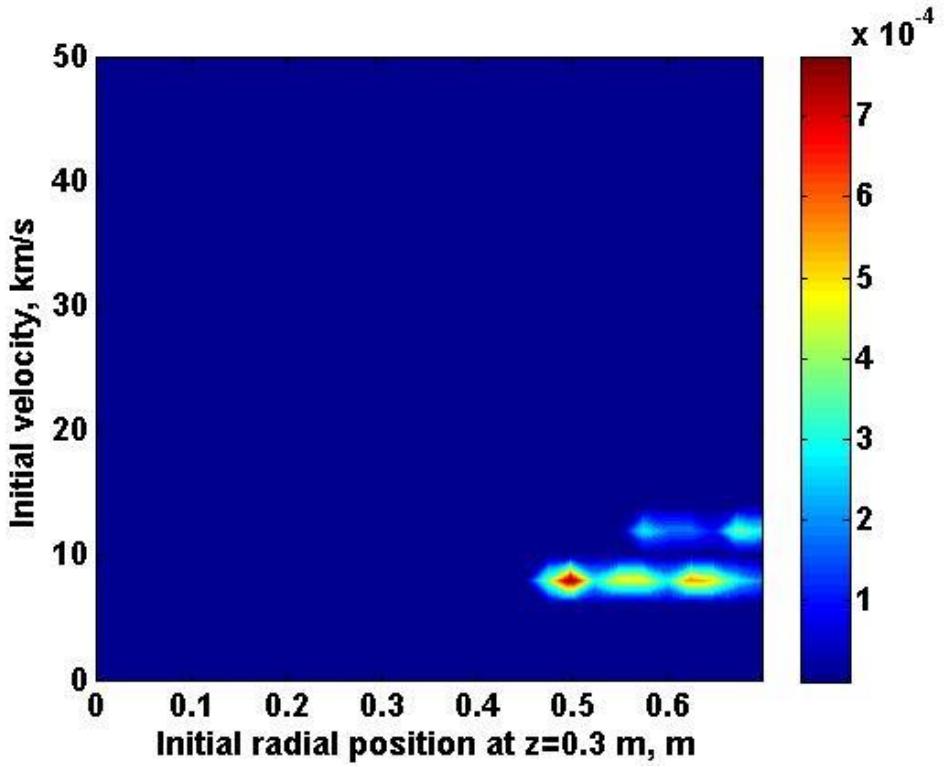

Figure 56. Contour plot of percentage of ions impacting structure as a function of initial velocity in the z direction and radial position for Run 1.

5.5.3.2 Run 2: A+, B-, C-

This model run utilized the faster velocity profile ($\bar{V}_{mag}$ = 29.7 km/s, FWHM = 23 km/s), the weaker magnetic field (I = 70 A), and the wider density distribution ($\bar{r}$ = ±0.25 m). The range of initial velocities for all ejected ions in this run is from 10.2 km/s to 44.67 km/s. The percentage of ions following the magnetic field lines and entering the backfield is 0.07%, which is much less than the average of 0.194% for all runs. The fewest ions enter the backfield in this run (0.07%) than in any other run, except for Run 8 (0.04%).The percentage of ions actually impacting is only 0.0002%, which is also much less than the average of all runs (0.0059%), indicating that very few ions impact

the engine housing or radiator panels. Along with Run 8, these conditions (A+, B-, C-) result in very low impact rates and very low erosion. Except for Runs 1 and 6 which have ions with so little kinetic energy that they do not cause erosion, Runs 2, 7, and 8 are the best configurations to use for the least amount of erosion.

The distribution of Figure 57 for ions entering the backfield with an initial velocity is between 10.18 km/s and 28.5 km/s with the average being 15.7 km/s. The distribution of ions actually impacting is between 13.309 km/s and 13.31 km/s, with the average initial velocity being 13.31 km/s. As only 2 ions returned out of the 1 million simulated, it is questionable that such a small amount can be scaled up accurately.

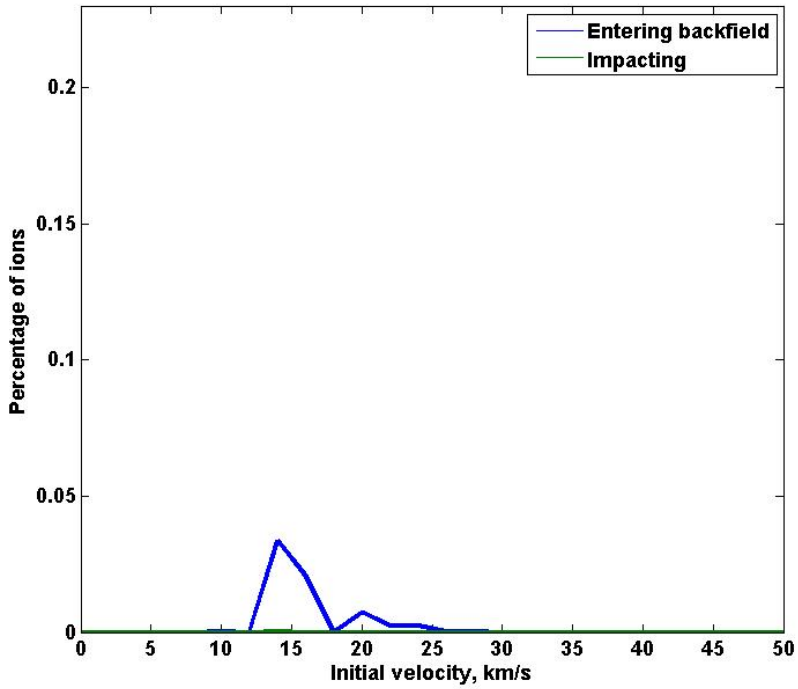

Figure 57. Percentage of ions entering the backfield (blue) and impacting engine/radiators (green) as a function of initial velocity in the z direction for Run 2.

The distribution in Figure 58 of the initial radial position of ions entering the backfield is between 0.41 m and 0.697 m, with the average being 0.56 m, which is close to the average of all runs (0.55 m). The distribution of the initial radial position of impacting ions is between 0.661 m and 0.677 m, with the average being 0.669 m, which is farther into the plume fringe than any other run, except for Run 8, indicating that only ions farthest away from the plume centerline are being trapped. As discussed in Run 1, the "peak – valley – peak" characteristic is observed in Figure 58 because Run 2 shares the wider plume with Run 1.

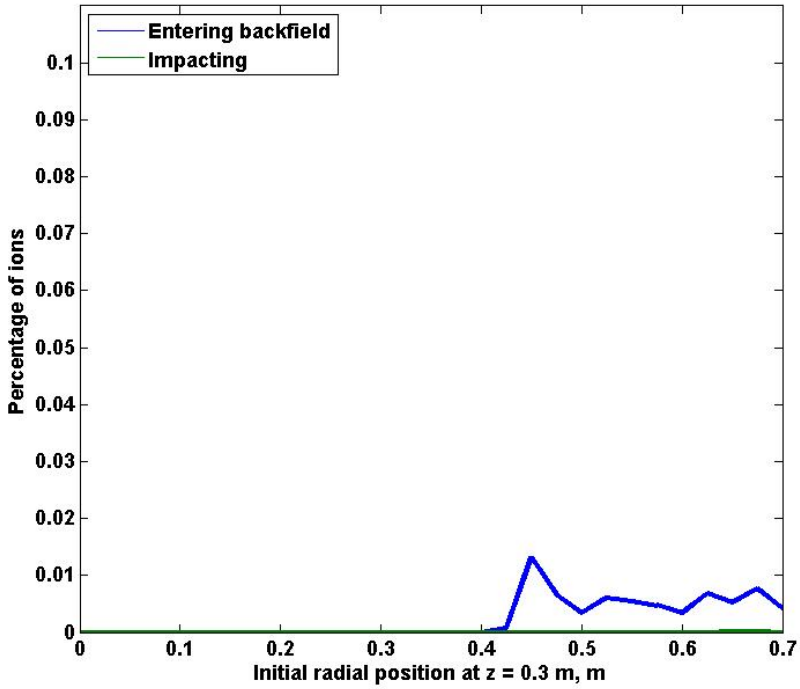

Figure 58. Percentage of ions entering the backfield (blue) and impacting engine/radiators (green) as a function of initial radial position for Run 2.

Figure 59 has one "island" and is much more concentrated than in Run 5. As Run 2 is the inverse to Run 5, it is logical that 3 times fewer ions return in Run 2 because there are fewer slow ions to become trapped and the magnetic field is weaker. Having a faster velocity profile leads to all returning ions coming only from the plume fringe (0.4 m < r < 0.7 m). For this run, no ions that originated between r = 0 m and r = 0.4 m return. As mentioned previously, the initial velocity of a trapped ion is proportional to its initial radial position, with faster returning ions originating far from the plume centerline and slower returning ions originating mostly closer to the plume centerline. Faster ions near to the centerline escape as thrust. All ions originating at less than 0.3 m radially escape.

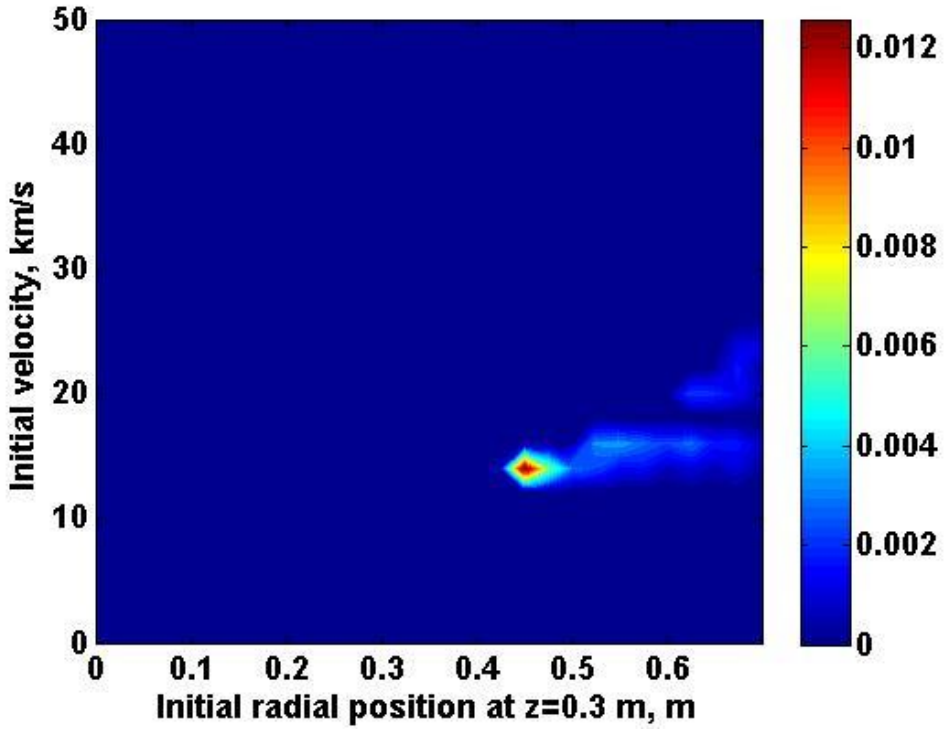

Figure 59. Contour plot of percentage of ions entering the backfield as a function of initial velocity in the z direction and radial position for Run 2.

The concentration of impacting ions is very distinct in Figure 60 indicating that only ions in the extreme plume fringe (0.6 m < r < 0.7 m) will return and impact structure.

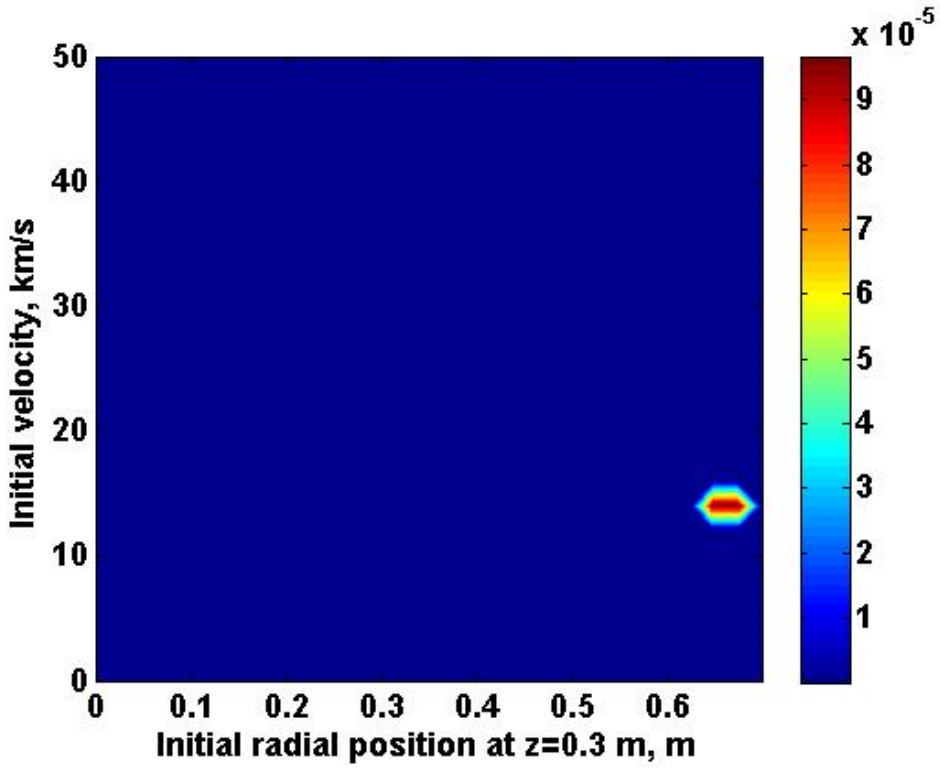

Figure 60. Contour plot of percentage of ions impacting structure as a function of initial velocity in the z direction and radial position for Run 2.

5.5.3.3 Run 3: A+, B+, C-

This model run utilized the faster velocity profile ($\bar{V}_{mag}$ = 29.7 km/s, FWHM = 23 km/s), the nominal magnetic field (I = 140 A), and the wider density distribution ($\bar{r}$ = ±0.25 m). The range of initial velocities for all ejected ions in this run is from 10.2 km/s to 44.67 km/s. The percentage of ions following the magnetic field lines and entering the

backfield is 0.24%, which is greater than the average of 0.194% for all runs. The percentage of ions actually impacting is 0.0043%, which is less than the average of all runs (0.0059%).

The erosion rate caused by Run 3 and Run 4 is the greatest of all runs, possibly due to the combination of a faster velocity profile, stronger magnetic field, and a wider plume. More ions enter the backfield on average and with higher kinetic energies than average (32.23 eV) with this run, resulting in greater erosion. The distribution of initial velocities in the z direction is broader than in the previous runs (Figure 61) and there is a distinct concentration around 15 km/s. The distribution of initial velocities for all returning ions is between 10.18 km/s and 35.23 km/s, with the average being 17 km/s which is slightly higher than the average for all runs (16.2 km/s). It is interesting to note that the upper limit of 35.23 km/s is the highest of all runs, indicating that Run 3 traps the fastest ions possibly due to the stronger magnetic field and wider plume.

The distribution of initial velocities for ions impacting structure is between 13.3 and 16.45 km/s, with the average being 13.75 km/s, which is the second fastest for returning ions of all 8 runs, behind Run 4. The high velocity of returning ions and the fact that Run 3 has the second greatest percentage of returning ions of the 8 runs indicates that a stronger magnetic field will trap more of the faster ions.

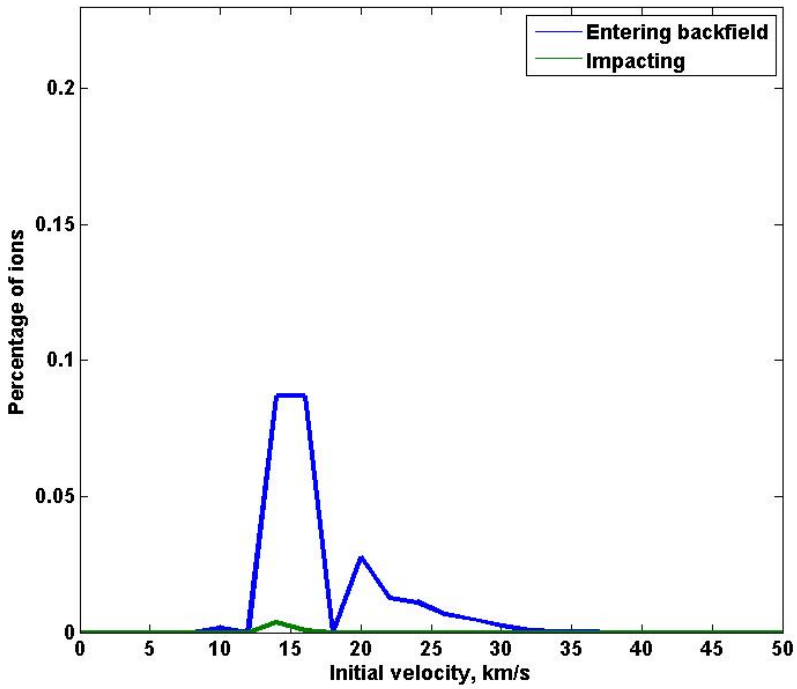

Figure 61. Percentage of ions entering the backfield (blue) and impacting engine/radiators (green) as a function of initial velocity in the z direction for Run 3.

The distribution of initial radial position of ions entering the backfield in Figure 62 (blue line) is very similar in structure to Runs 1, 2, and 7, which have the wider plume in common. The "peak – valley – peak" is distinct to every run using the wider plume, whereas the narrow plume produces a single peak near r = 0.7 m. The distribution of initial radial position of impacting ions is between 0.51 m and 0.697 m, with the average being 0.62 m, which is exactly the average for all 8 runs. The initial radial position of ions that impact the engine housing and radiators is skewed towards the plume fringe.

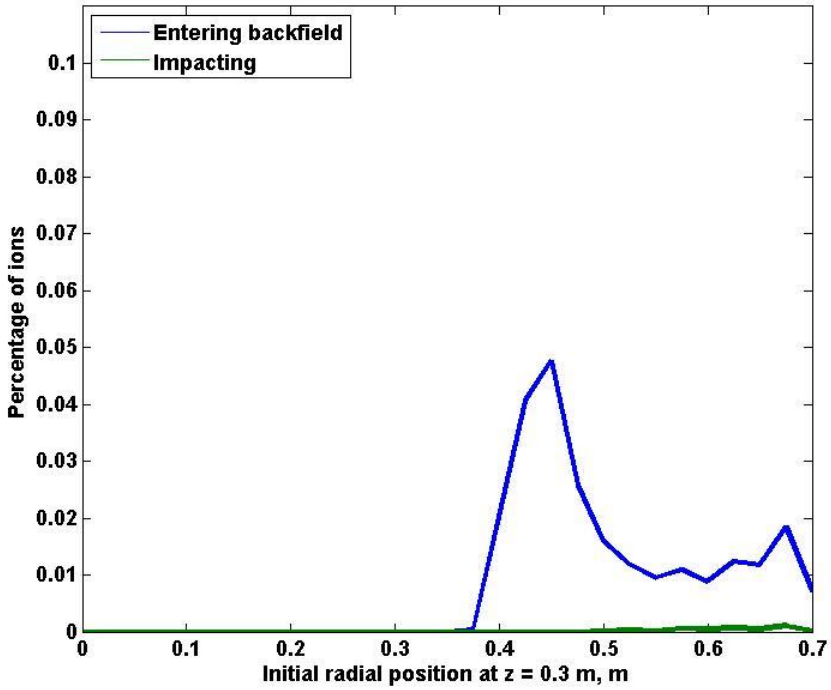

Figure 62. Percentage of ions entering the backfield (blue) and impacting engine/radiators (green) as a function of initial radial position for Run 3. The "peak – valley – peak" of the blue line is shared with Runs 1, 2, and 7, which have the wider plume in common.

The "island" that appears in Figure 63 is concentrated around r = 0.45 m and 15 km/s. The average is 0.51 m and 17 km/s. Run 3's Figure 63is different to Run 5's Figure 49 in that the magnitude of Run 3's concentration is 5 times greater than Run 5's. The difference between Run 3 and 5 is that Run 3 uses the faster velocity profile and wider plume, indicating that the wider plume causes more of the faster ions closer to the plume centerline to enter the backfield. The plume centerline has a much greater density of high velocity ions than the plume fringe and it is these ions that cause Run 3 to have the highest erosion rate of all 8 runs. Run 3 represents the worst configuration to operate

the VF-200 in, if the desire is to limit erosion damage. Although Run 5 has almost 3 times as many ions impacting as Run 3 (and Run 4), the erosion rate is much greater in Run 3 (and Run 4) because the ions have 10 eV more kinetic energy on average than ions in Run 5.

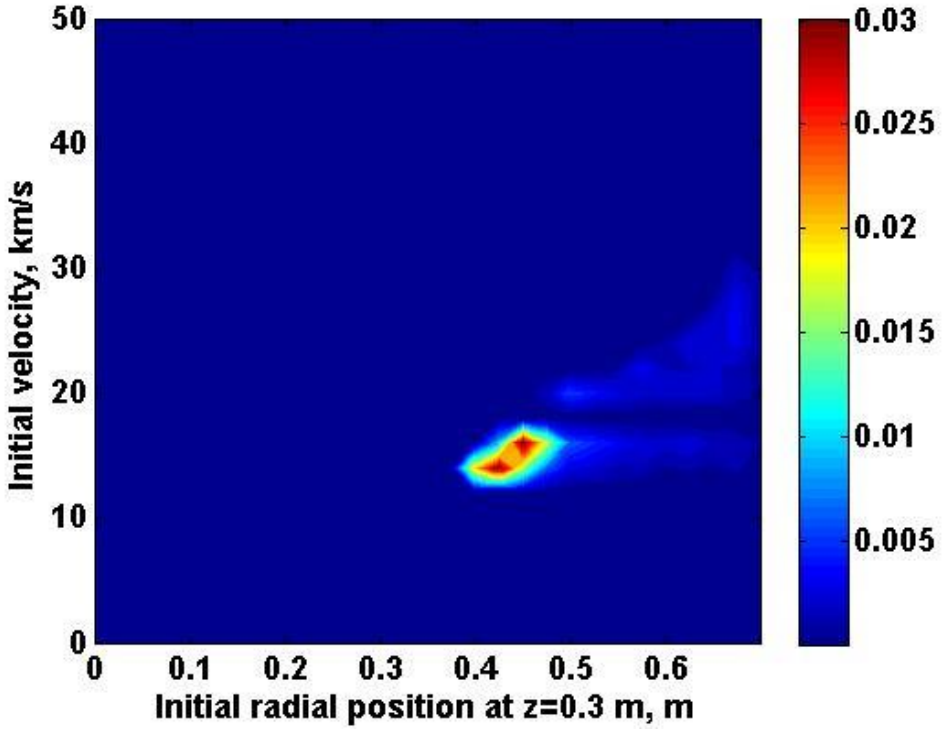

Figure 63. Contour plot of percentage of ions entering the backfield as a function of initial velocity in the z direction and radial position for Run 3.

The distribution of impacting ions in Figure 64 illustrates that while most of the returning ions are from closer to the plume centerline, the ions that actually impact are from the plume fringe (0.5 m < r < 0.7 m) with most from the extreme fringe (≈ 0.7 m). As mentioned previously, the initial velocity of a trapped ion is proportional to its initial radial position, with faster returning ions originating far from the plume centerline and

slower returning ions originating mostly closer to the plume centerline. Faster ions near to the centerline escape as thrust. All ions originating at less than 0.3 m radially escape.

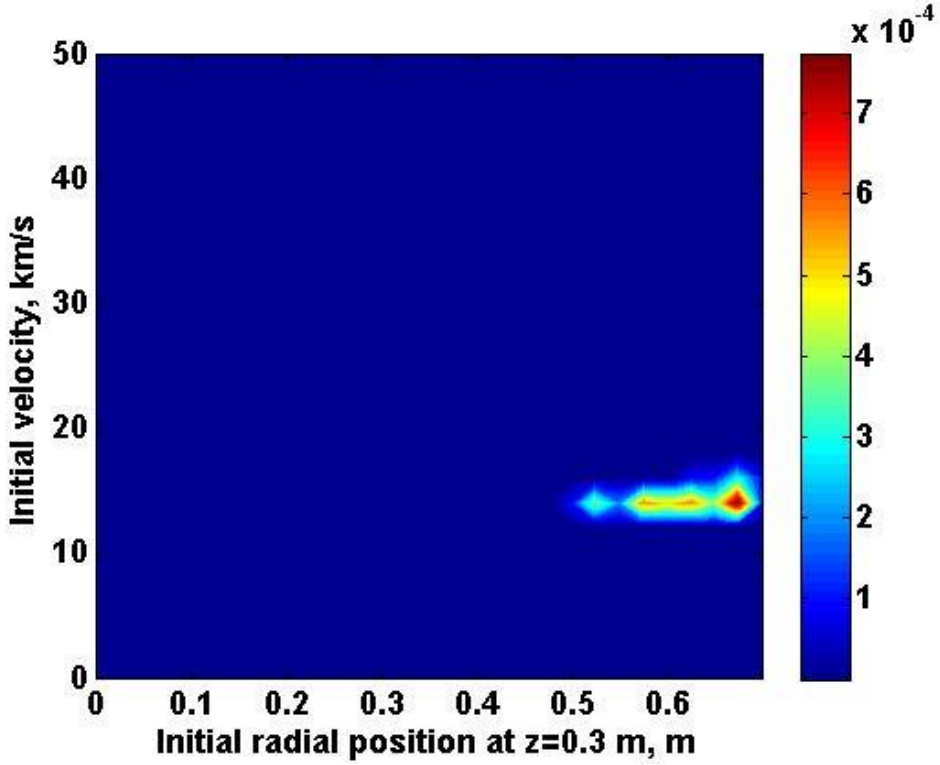

Figure 64. Contour plot of percentage of ions impacting structure as a function of initial velocity in the z direction and radial position for Run 3.

The next section will cover Run 4 and how it relates to Run 5, the baseline.

5.5.3.4 Run 4: A-, B+, C+

This model run utilized the faster velocity profile ($\bar{V}_{mag}$ = 29.7 km/s, FWHM = 23 km/s), the nominal magnetic field (I = 140 A), and the nominal density distribution ($\bar{r}$ = ±0.205 m). The range of initial velocities for all ejected ions in this run is from 10.2 km/s to 44.67 km/s. The percentage of ions following the magnetic field lines and

entering the backfield is 0.10%, which is less than the average of 0.194% for all runs. The percentage of ions actually impacting is 0.0035%, which is less than the average of all runs (0.0059%).

The engine configuration for Run 4 is very similar to Run 5 but uses the faster initial ion exit velocity. Run 4 is not the baseline because it uses the maximum operating conditions for the VF-200 engine as when this research began and is not representative of nominal operations. However, this run has the highest magnetic field strength, fastest velocity profile, and narrowest plume density distribution which results in the highest erosion rate of both AL and SI of all 8 runs. This run represents the second worst configuration to operate the VF-200 behind Run 3 if the object is to minimize erosion on the spacecraft.

Although Run 5 has almost 3 times as many ions impacting as Run 4 (and Run 3), the erosion rate is much greater in Run 4 (and Run 3) because the ions have 10 eV more kinetic energy on average than ions in Run 5.

The distribution of initial velocity for ions entering the backfield is from 10.2 km/s to 33.7 km/s, with the average being 19.5 km/s, which is the highest average of all 8 runs, indicating that more fast ions are being trapped with this configuration than any other. The distribution of initial ion velocity for impacting ions is from 13.31 km/s to 16.45 km/s (Figure 65). The average initial velocity of impacting ions is 13.75 km/s, which is much higher than the average for all 8 runs (11.72 km/s) and is the highest of all runs, indicating that stronger magnetic field is causing more of the faster ions to impact structure, resulting in the highest erosion rate of all runs.

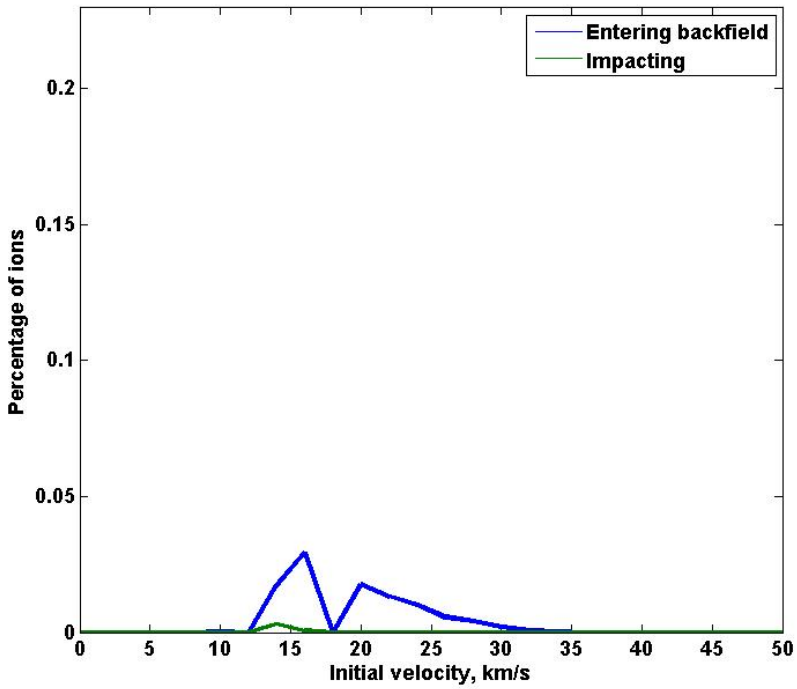

Figure 65. Percentage of ions entering the backfield and impacting engine/radiators as a function of initial velocity in the z direction for Run 4.

The distribution of initial radial position for ions entering the backfield ranges from 0.4 m and 0.7 m, with the average being 0.58 m, which is slightly higher than average for all 8 runs (0.549 m) and is tied with Run 6. Runs 4 and 6 have the narrower plume in common. Therefore, it appears that the narrower the plume is, the more likely returning ions will have originated in the far plume fringe (r = 0.7 m). As the only difference from Run 3 is that this run uses a narrower density distribution, it appears that density distribution has a minor effect on the percentage of ions impacting, with slightly fewer ions impacting with the narrower density distribution.

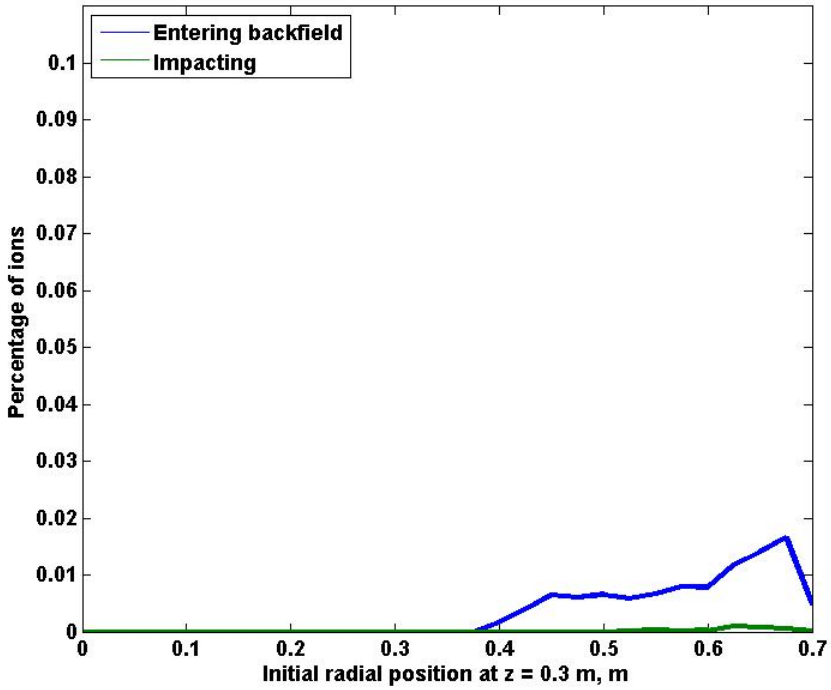

Figure 66. Percentage of ions entering the backfield and impacting engine/radiators as a function of initial radial position for Run 4.

The “islands” evident in Figure 67 and Figure 68 are of comparable concentrations to Run 5 with most of the impacting ions originating in the far plume fringe, which indicates that a faster initial ion velocity profile results slightly affects how far from the centerline ions will be trapped. The returning ions are concentrated with low initial velocities and initial radial positions far in the plume fringe.

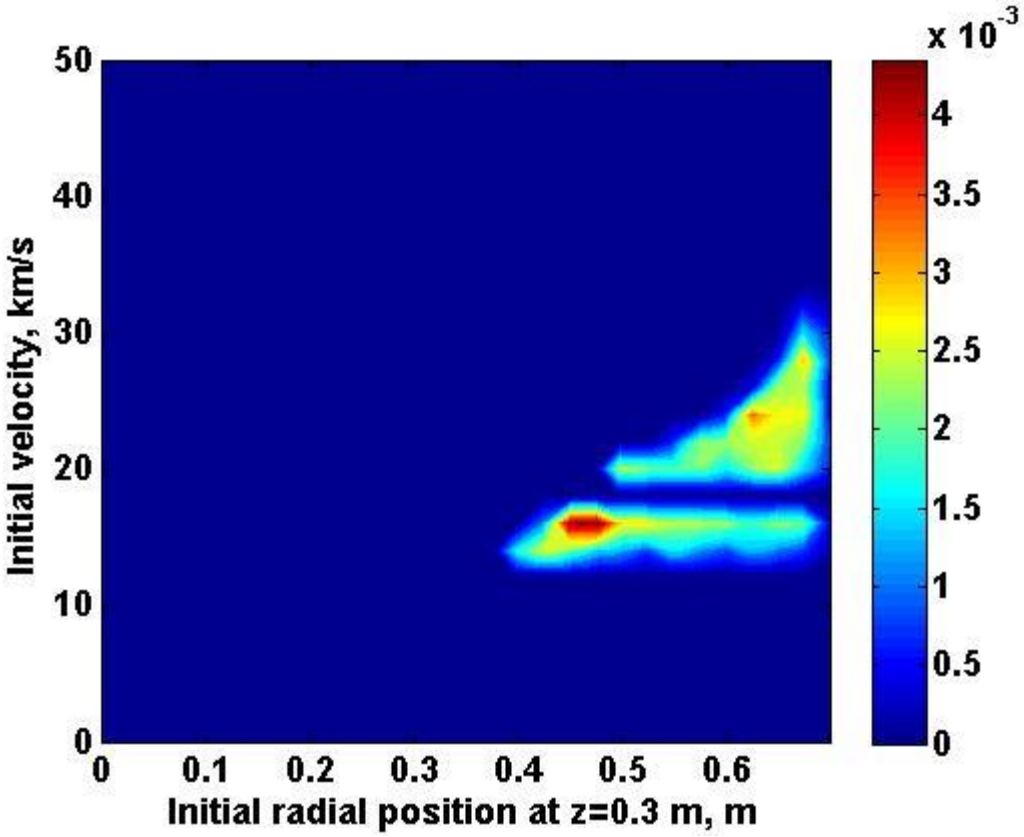

Figure 67. Contour plot of percentage of ions entering the backfield as a function of initial velocity in the z direction and radial position for Run 4.

As mentioned previously, the initial velocity of a trapped ion is proportional to its initial radial position, with faster returning ions originating far from the plume centerline and slower returning ions originating mostly closer to the plume centerline.

Faster ions near to the centerline escape as thrust. All ions originating at less than 0.3 m radially escape.

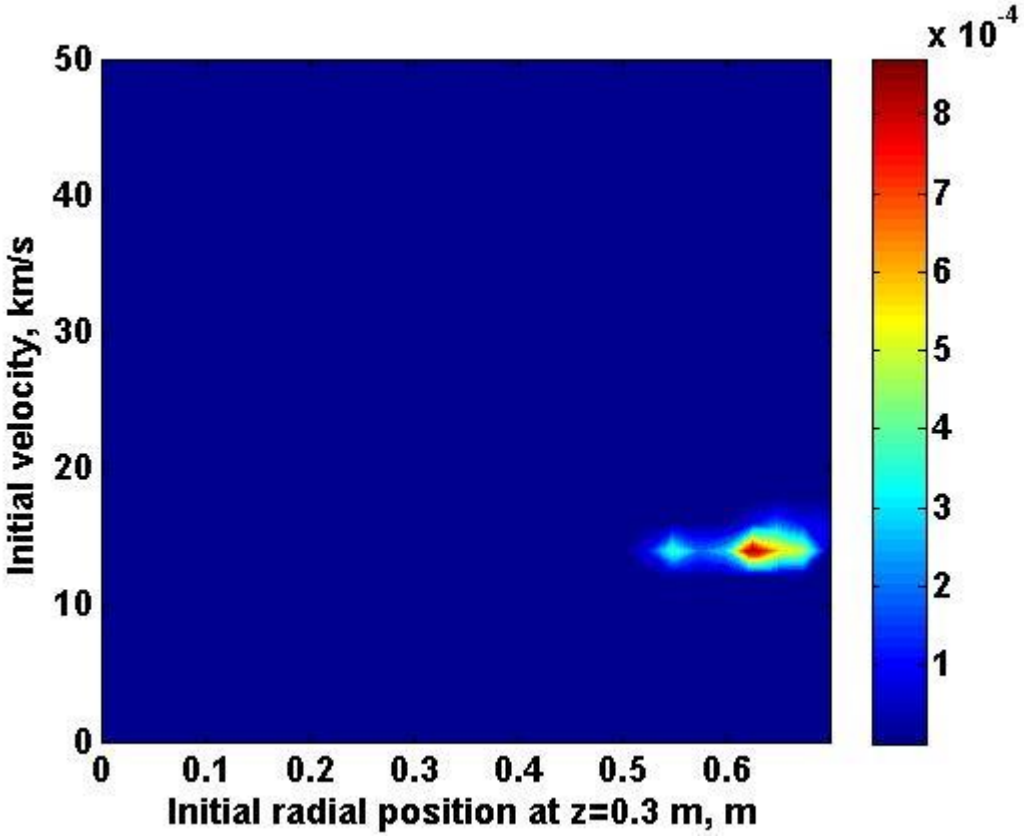

Figure 68. Contour plot of percentage of ions impacting structure as a function of initial velocity in the z direction and radial position for Run 4.

The next section will cover Run 6 and how it relates to Run 5, the baseline.

5.5.3.5 Run 6: A-, B-, C+

This model run utilized the slower velocity profile ($\bar{V}_{mag}$ = 24.4 km/s, FWHM = 10 km/s), the weaker magnetic field (I = 70 A), and the nominal density distribution ($\bar{r}$ = ±0.205 m). The range of initial velocities for all ejected ions in this run is from 7.66

km/s to 40.48 km/s. The percentage of ions following the magnetic field lines and entering the backfield is 0.09%, which is much less than the average for all runs (0.194%). The percentage of ions actually impacting is 0.0037%, which is less than the average of all runs (0.0059%). The distribution of initial velocity for ions entering the backfield is from 7.66 km/s to 25.8 km/s, with the average being 15.68 km/s, which is the slightly less than the average of all 8 runs (16.2 km/s). The distribution of initial velocity for impacting ions is from 7.66 km/s to 11.79 km/s (Figure 65), with the average being 8.88 km/s. The maximum initial velocity of impacting particles is tied with Run 1 with being the lowest, which indicates that only the slowest ions are impacting structure. Also like in Run 1, the kinetic energy of impacting ions is too low for erosion to occur so none of the structure surface is eroded for either aluminum or silicon. As these two runs share the slower initial velocity profile and weaker magnetic field in common, this indicates that only the slowest ions are being trapped.

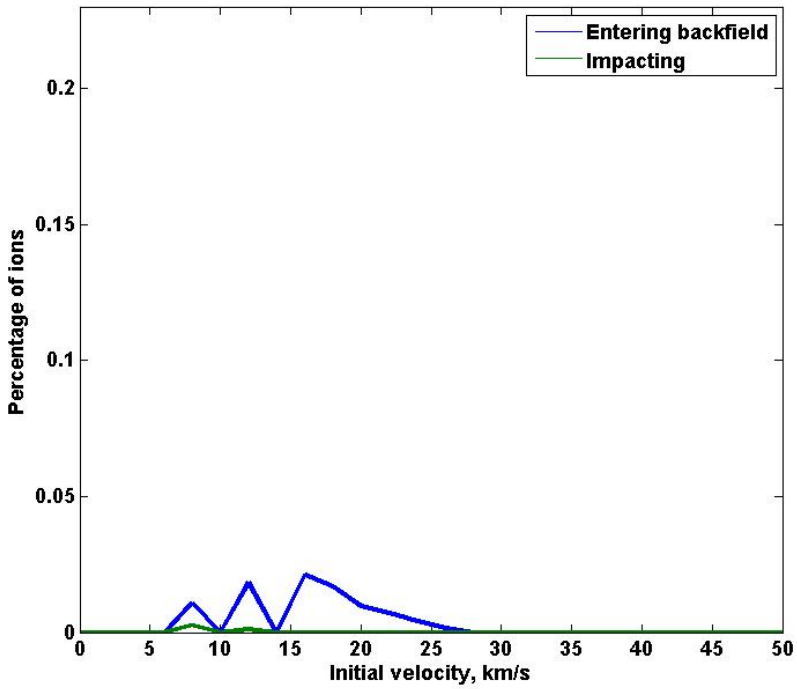

Figure 69. Percentage of ions entering the backfield (blue) and impacting engine/radiators (green) as a function of initial velocity in the z direction for Run 6. The jagged peaks are a result of the 19 velocity groups and would likely be a continuous curve if more velocity groups than 19 were used.

The distribution of initial radial position for ions entering the backfield (Figure 69) ranges from 0.37 m and 0.7 m, with the average being 0.58 m, which is slightly higher than average for all 8 runs (0.549 m) and is tied with Run 4. Runs 4 and 6 have the narrower plume in common. Therefore, it appears that the narrower the plume is, the more likely returning ions will have originated in the far plume fringe (r = 0.7 m). The distribution of initial radial position for impacting ions (Figure 70) is between 0.46 m and 0.68 m, with the average being 0.594 m, which is almost identical to Run 5's average. Because the only difference between Run 5 and 6 is the magnetic field strength,

the fact that the average radial position of both all ions entering the backfield and impacting are essentially identical indicates that magnetic field strength does not affect where the recirculating or impacting ions originate within the plume. The percentage of ions entering the backfield decreased by a factor of 2.3, and the percentage of ions impacting decreased by a factor of 3.2 with this run compared to Run 5 because Run 6 uses a weaker magnetic field. Therefore, a strong magnetic field increases the amount of recirculating ions significantly, and traps more of the high velocity ions along with the slower ones.

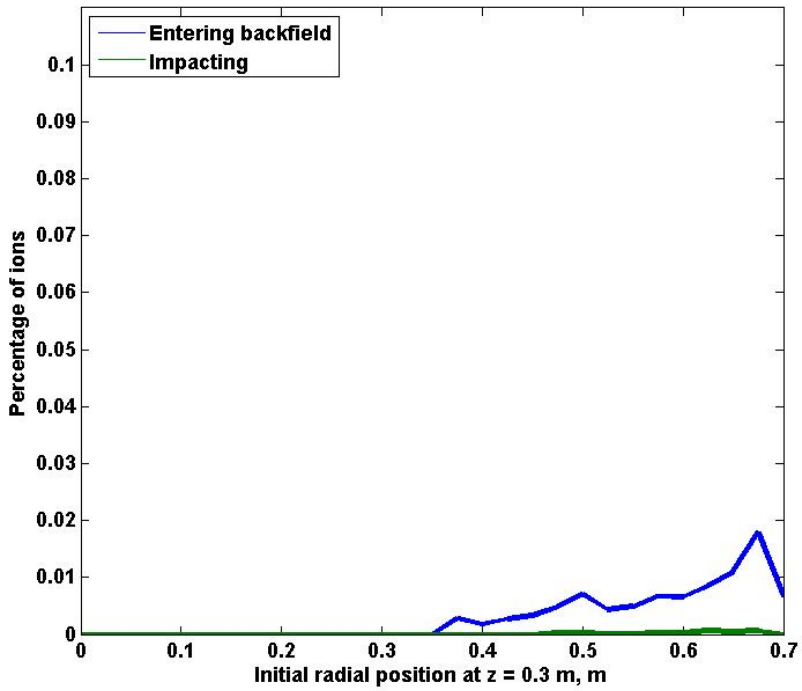

Figure 70. Percentage of ions entering the backfield (blue) and impacting engine/radiators (green) as a function of initial radial position for Run 6.

Figure 71 and Figure 72 illustrate that although the ions entering the backfield come from the across the plume (for radius greater than 0.3 m), the ions impacting is concentrated near the extreme far fringe, which is also seen in Runs 4, 5, and 8, which all the narrow plume in common.

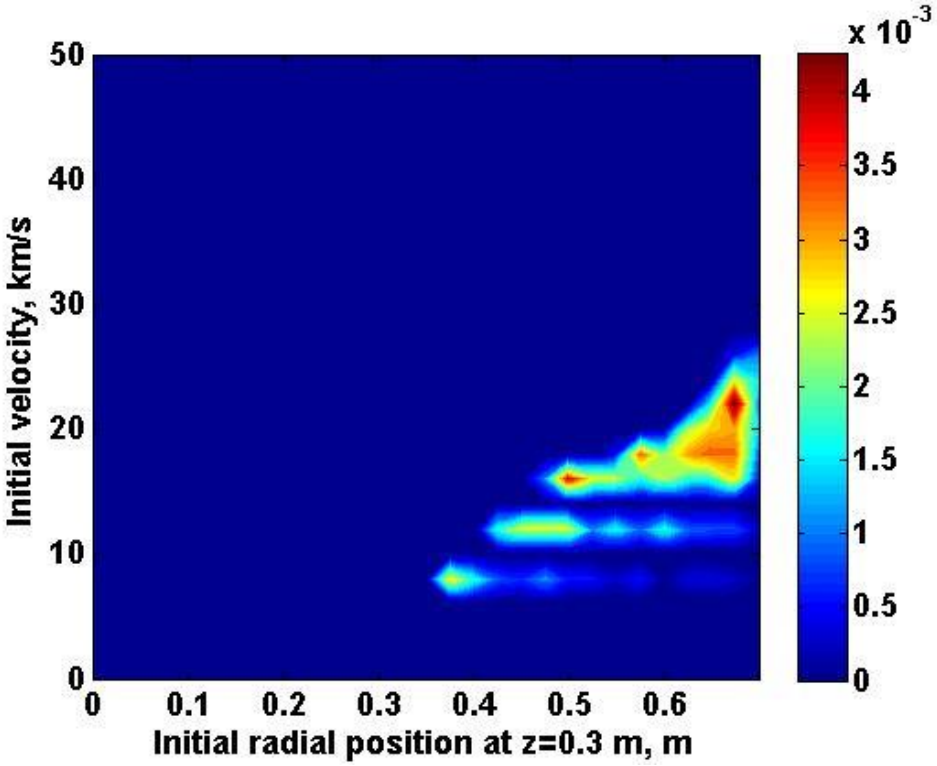

Figure 71. Contour plot of percentage of ions entering the backfield as a function of initial velocity in the z direction and radial position for Run 6.

As mentioned previously, the initial velocity of a trapped ion is proportional to its initial radial position, with faster returning ions originating far from the plume centerline and slower returning ions originating mostly closer to the plume centerline. Faster ions near to the centerline escape as thrust. All ions originating at less than 0.3 m radially escape.

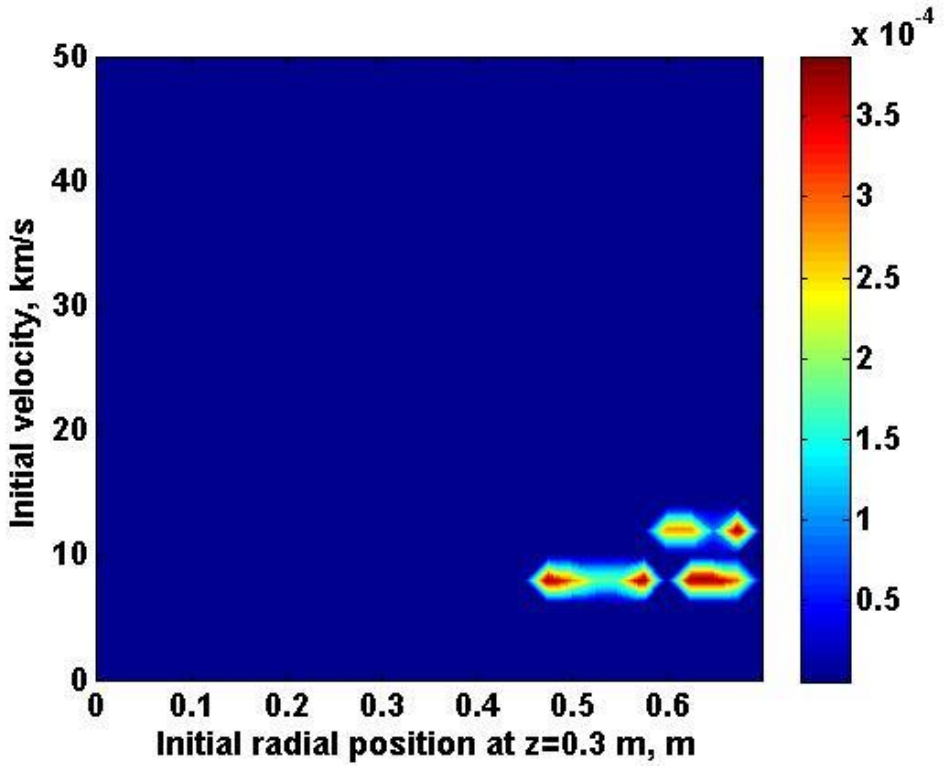

Figure 72. Contour plot of percentage of ions impacting structure as a function of initial velocity in the z direction and radial position for Run 6.

The next section will cover Run 7 and how it relates to Run 5, the baseline.

5.5.3.6 Run 7: A-, B+, C-

This model run utilized the slower velocity profile ($\bar{V}_{mag}$ = 24.4 km/s, FWHM = 10 km/s), the nominal magnetic field (I = 140 A), and the wider density distribution ($\bar{r}$ = ±0.25 m). The range of initial velocities for all ejected ions in this run is from 7.66 km/s to 40.48 km/s. The percentage of ions following the magnetic field lines and entering the backfield is 0.58%, which is much higher than the average for all runs (0.194%) and is by far the highest of all runs, which indicates that a strong magnetic field and a slower initial velocity profile results in the greatest number of returning ions. If the goal is to

reduce the amount of returning ions, then Run 7 is by easily the worst configuration to use with the VF-200. The percentage of ions actually impacting is 0.0172%, which is also much greater than the average of all runs (0.0059%). This run has the highest percentage of ions impacting than any other run by a large margin (45% greater than the second highest, Run 5).

The distribution of initial velocity for ions entering the backfield (Figure 73) is from 7.66 km/s to 33.3 km/s, with the average being 14.5 km/s, which is second lowest of all runs behind Run 1, indicating that a wider plume and slower initial velocity results in mostly slower ions being trapped. The distribution of initial velocity for impacting ions is from 7.66 km/s to 17.69 km/s, with the average being 10.5 km/s, which is less than the average of all 8 runs (16.2 km/s). However, the maximum initial velocity of impacting ions, 17.6 km/s, is tied with Run 5 as the highest, indicating that plume width (the only difference between the runs) does not affect how fast the ions are that become trapped but does result in more ions recirculating and impacting. Therefore, more ions are trapped with this engine configuration than any other because the magnetic field is strongest, the velocity profile is the slowest, and the plume density distribution the widest. However, the erosion in Run 5 is significantly greater than in Run 7 because the average kinetic energy of impacting ions is greater in Run 5. Therefore, although fewer ions return in Run 5, they cause more erosion than in Run 7 because the average kinetic energy is only 54% of the highest (Runs 3 and 4) due to use of the slower velocity profile.

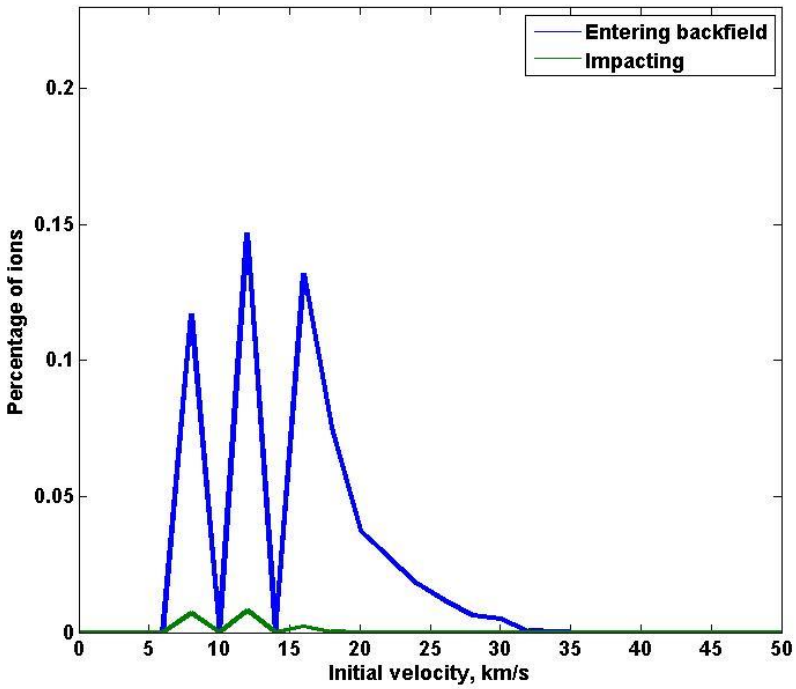

Figure 73. Percentage of ions entering the backfield (blue) and impacting engine/radiators (green) as a function of initial velocity in the z direction for Run 7. The jagged peaks are a result of the 19 velocity groups and would likely be a continuous curve if more velocity groups than 19 were used.

The distribution of initial radial position for ions entering the backfield is from 0.343 m to 0.698 m (Figure 74), with the average radial position is 0.481 m, which is the closest to the plume centerline of all 8 runs, indicating that a strong magnetic field and a wide plume causes ions closer to the plume to become trapped and recirculate into the engine backfield. The "peak – valley – peak" characteristic is most pronounced in Run 7, sharing this with Runs 1, 2, and 3, which have the wide plume in common.

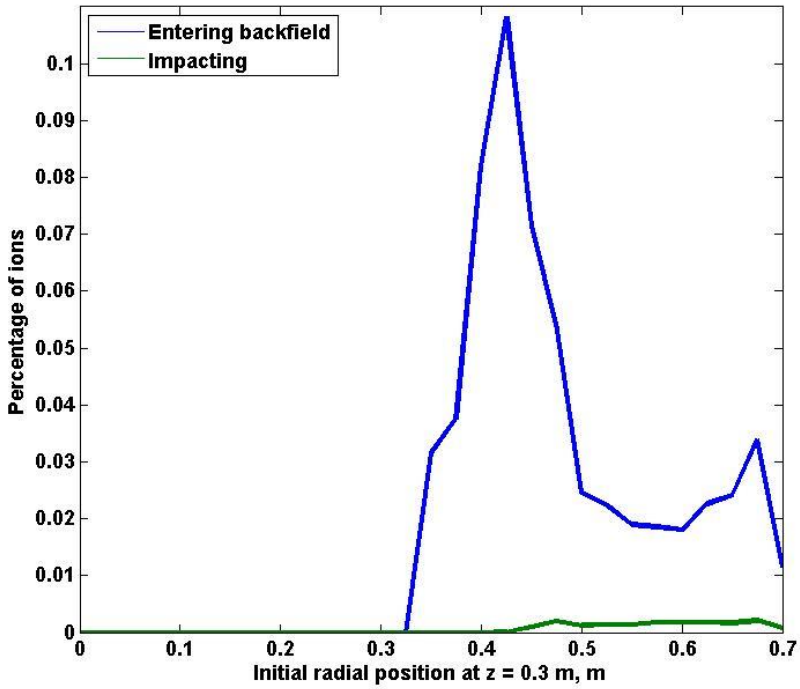

Figure 74. Percentage of ions entering the backfield (blue) and impacting engine/radiators (green) as a function of initial radial position for Run 7.

The "island" in Figure 75 is broad with a range from r = 0.3 m to r = 0.7 m, but with most returning ions (81%) originating between 0.3 m and 0.5 m , which is similar to Runs 1 and 3. The distribution of returning ions' initial radial position (Figure 76) is distributed almost equally between r = 0.4 m and r = 0.7 m. As mentioned previously, the initial velocity of a trapped ion is proportional to its initial radial position, with faster returning ions originating far from the plume centerline and slower returning ions originating mostly closer to the plume centerline. Faster ions near to the centerline escape as thrust. All ions originating at less than 0.3 m radially escape.

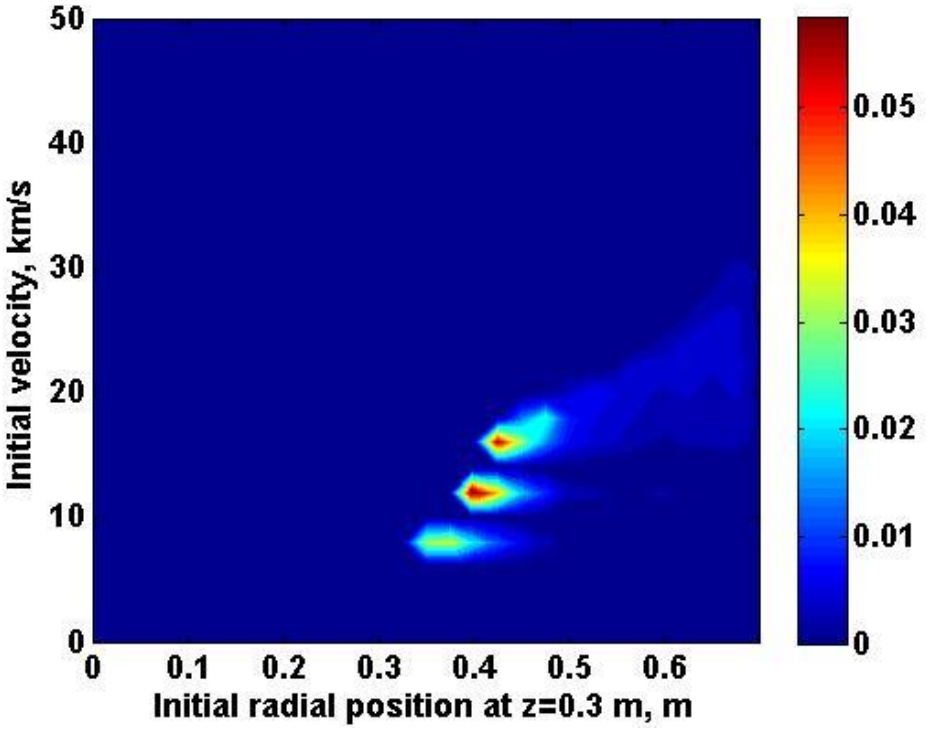

Figure 75. Contour plot of percentage of ions entering the backfield as a function of initial velocity in the z direction and radial position for Run 7.

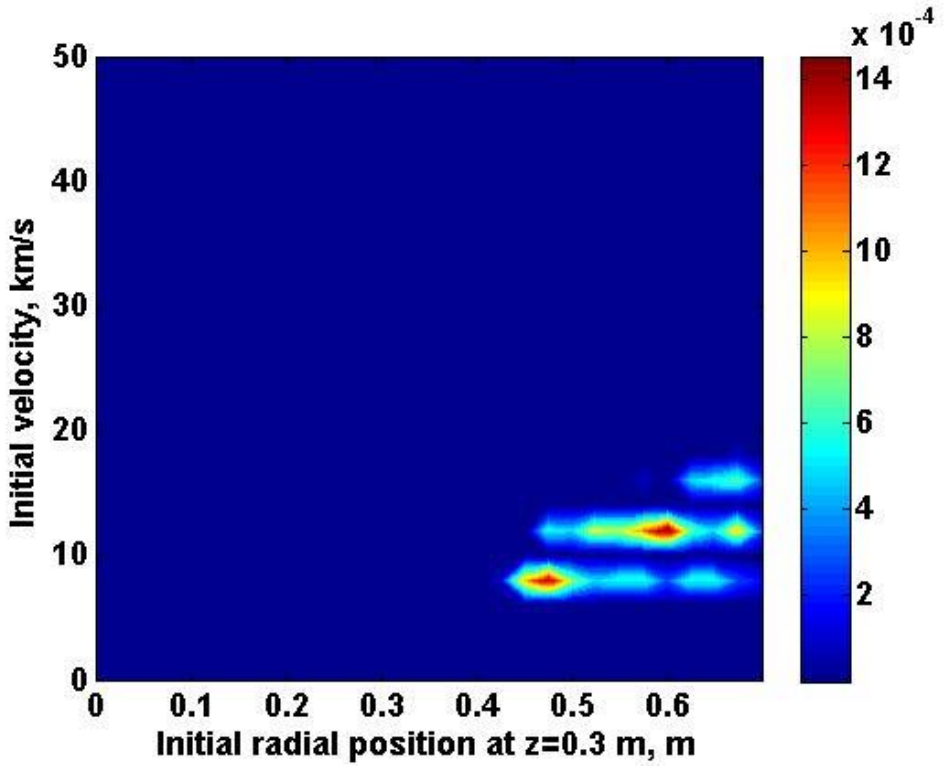

Figure 76. Contour plot of percentage of ions impacting structure as a function of initial velocity in the z direction and radial position for Run 7.

The next section will cover Run 8 and how it relates to Run 5, the baseline.

5.5.3.7 Run 8: A+, B-, C+

This model run utilized the faster velocity profile ($\bar{V}_{mag}$ = 29.7 km/s, FWHM = 23 km/s), the weaker magnetic field (I = 70 A), and the nominal density distribution ($\bar{r}$ = ±0.205 m). The range of initial velocities for all ejected ions in this run is from 10.2 km/s to 44.67 km/s. The percentage of ions following the magnetic field lines and entering the backfield is 0.04%, which is much less than the average of 0.194% for all runs, indicating that weaker magnetic field and wider plume captures relatively few ions.

The percentage of ions actually impacting is 0.0001%, which is also much less than the average of all runs (0.0059%). As with Run 2, this run has the lowest percentage of returning ions.

The distribution of initial velocity for ions entering the backfield (Figure 77) is from 10.18 km/s to 26.5 km/s, with the average being 16.8 km/s, which is less than the average of all runs (0.194%). Run 8 is extremely similar to Run 2 with 100% of returning ions having an initial velocity less than 27 km/s. This is most likely because the faster velocity profile was used but the magnetic field was weak so only slower ions become trapped. As more of the ions have faster velocities, they escape as thrust. If the goal is to reduce the number of returning and impacting ions, then this run represents the best configuration for operating a magnetoplasma engine.

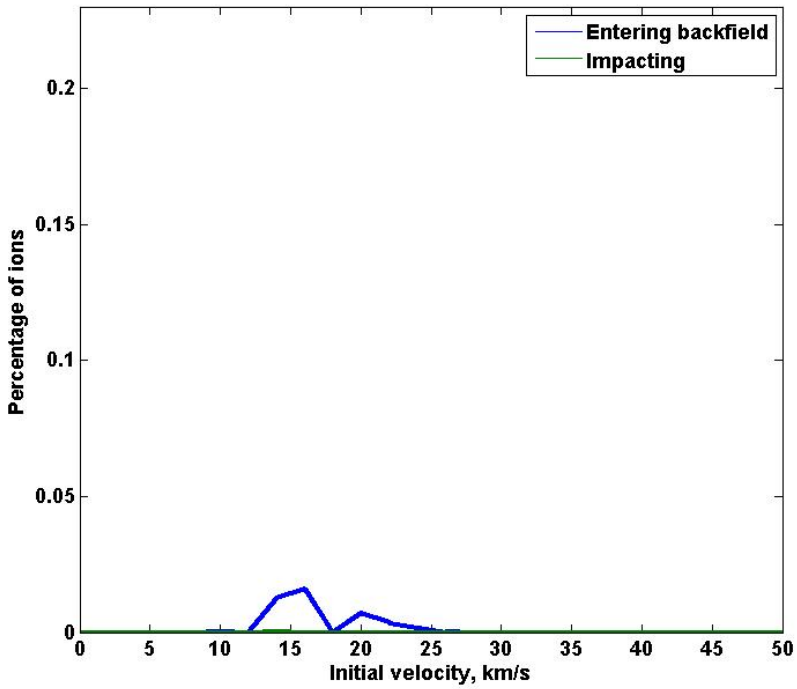

Figure 77. Percentage of ions entering the backfield and impacting engine/radiators as a function of initial velocity in the z direction for Run 8.

The distribution of initial velocity for impacting ions (Figure 77) is from 13.3 km/s to 13.3 km/s because only one ion was simulated impacting structure. As such, the validity of using only one impact and scaling it up to determine erosion is in question.

The distribution of initial radial position for ions entering the backfield is from 0.435 m to 0.698 m (Figure 78), with the average radial position is 0.606 m.

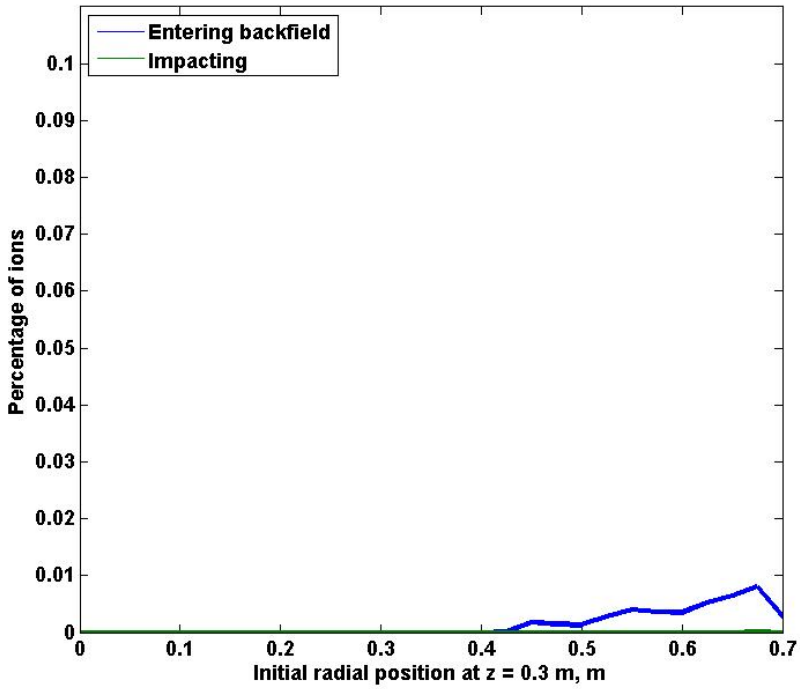

Figure 78. Percentage of ions entering the backfield and impacting engine/radiators as a function of initial radial position for Run 8.

Figure 79 and Figure 80 illustrate that the concentration of returning and impacting ions is towards the far plume fringe. As mentioned previously, the initial velocity of a trapped ion is proportional to its initial radial position, with faster returning ions originating far from the plume centerline and slower returning ions originating mostly closer to the plume centerline. Faster ions near to the centerline escape as thrust. All ions originating at less than 0.3 m radially escape.

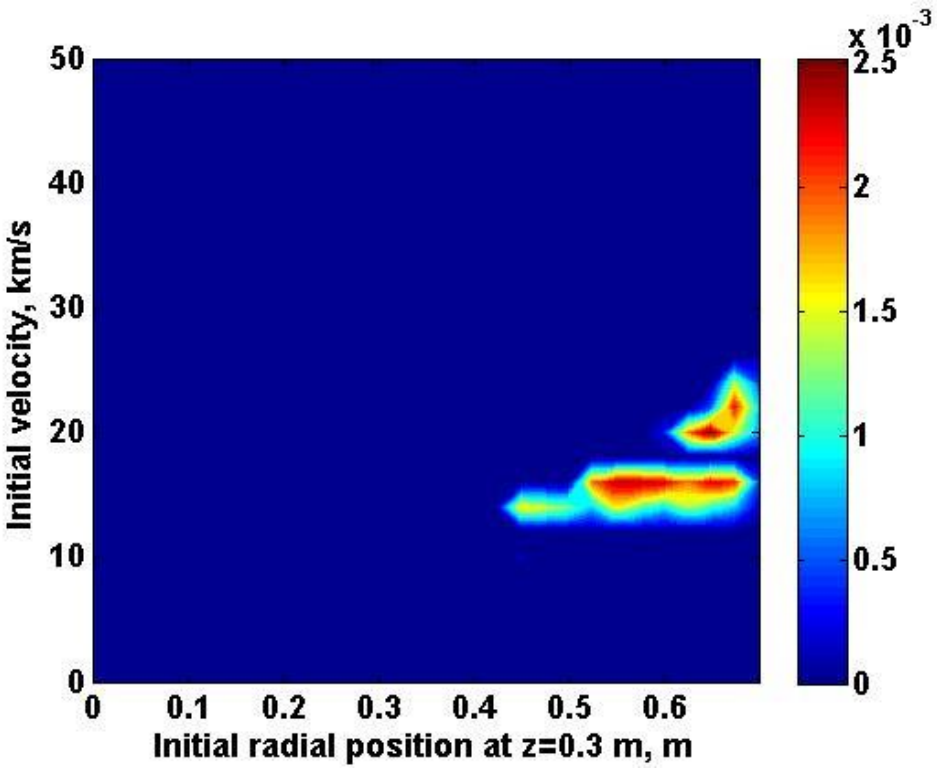

Figure 79. Contour plot of percentage of ions entering the backfield as a function of initial velocity in the z direction and radial position for Run 8.

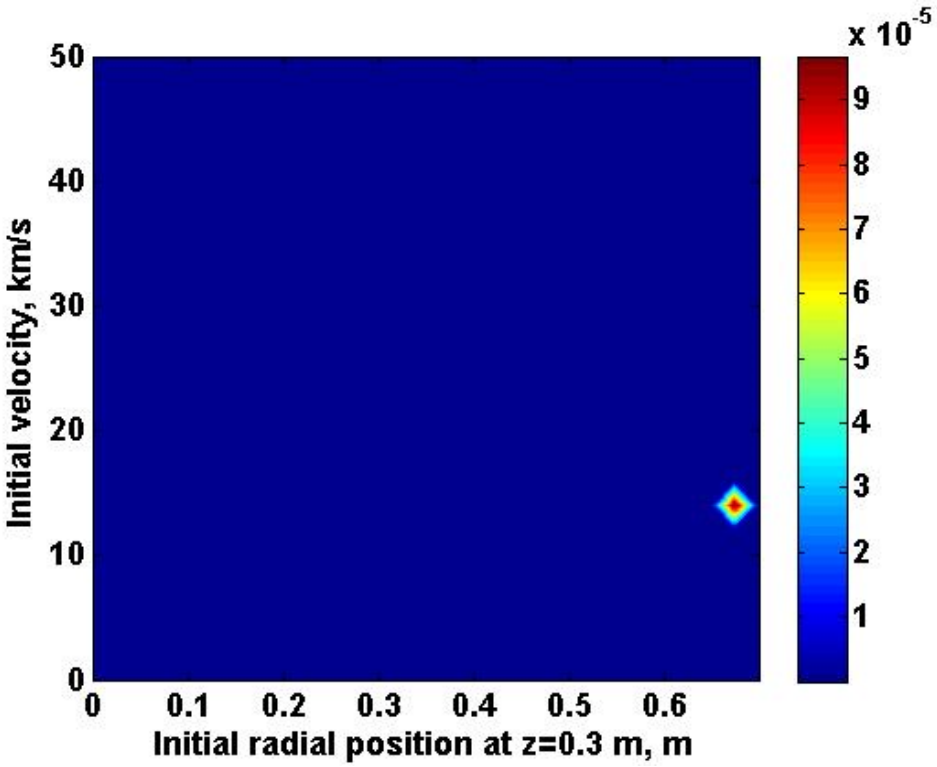

Figure 80. Contour plot of percentage of ions impacting structure as a function of initial velocity in the z direction and radial position for Run 8.

In the next section, all 8 runs are compared together to find trends.

5.5.3.8 Comparison of All Runs to Each Other

The following trends were discovered in the individual run results:

1. A weaker magnetic field and wider plume results in only the slower ions becoming trapped.
2. The wider the plume, the more impacting ions will come from the mid-range of the plume (next to the plume centerline) instead of the plume fringe.

3. A stronger magnetic field and wider plume results in more ions becoming trapped.
4. A stronger magnetic field traps more of the faster ions within a given plume.
5. Ejecting ions at a faster rate with a stronger magnetic field and a narrow plume traps more of the faster ions within a given plume than in any other configuration.
6. Conversely, ejecting ions at a slower rate with a weaker magnetic field results in only the slowest ions becoming trapped and impacting.
7. Ejecting slower ions with a stronger magnetic field and a wide plume results in the most ions becoming trapped, which might be useful if a solar sail like the one used by the M2P2[38, 39] spacecraft is desired.

These findings can be better explained by using the collective figures on the next few pages. The effect of initial ion velocity is clearly illustrated in Figure 81 with the percentage of returning ions significantly increased when ions have a slower initial velocity. The effect is greater with a stronger magnetic field and a wider plume.

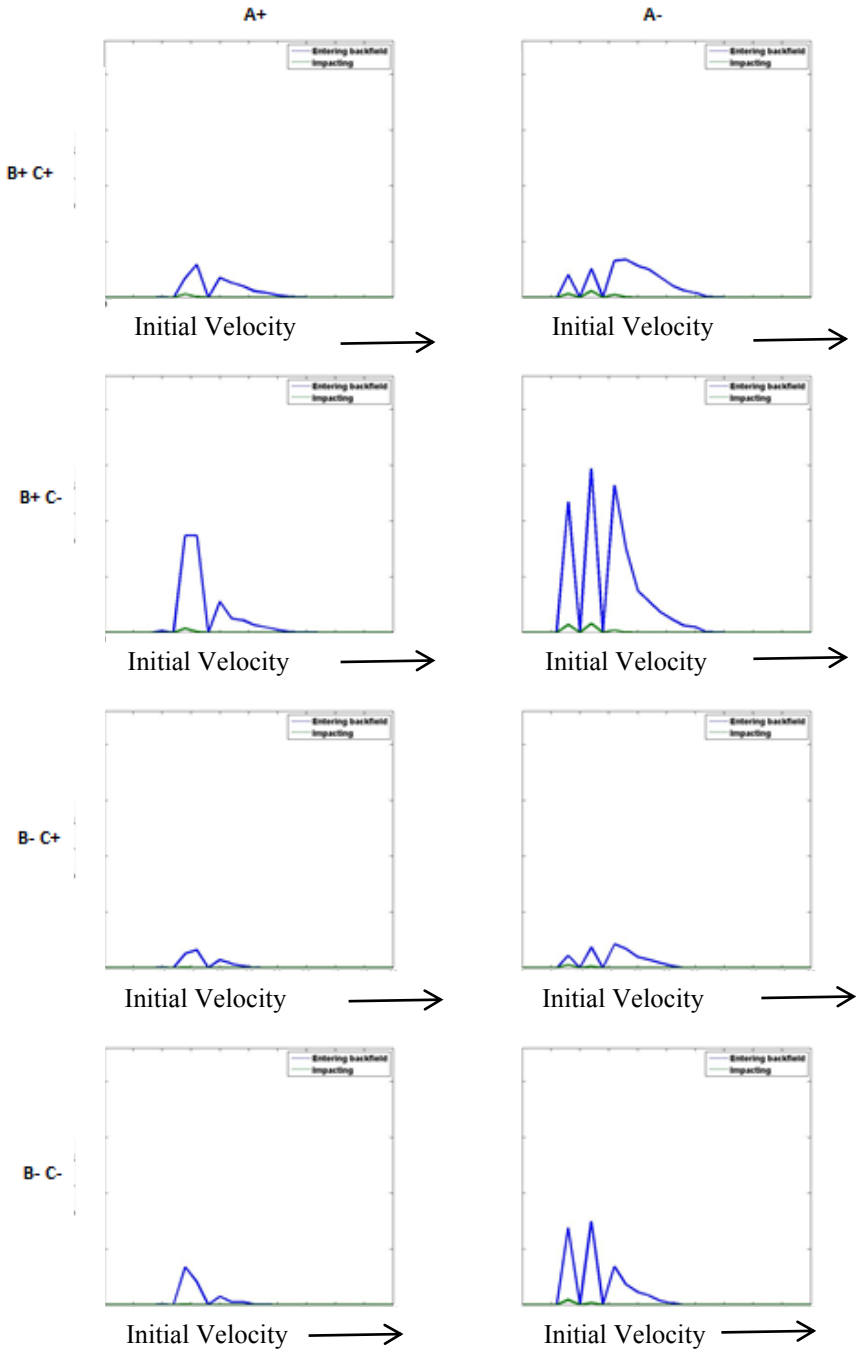

Figure 81. Collection of graphs showing the percentage of ions entering the backfield (blue) and impacting (green) as a function of initial exit velocity at z = 0.3 m for all 8 runs. The initial velocity ranges from 0 km/s (left) to 50 km/s (right). The percentage of returning ions ranges from 0% (bottom) to 0.2% (top) and increases with a slower ion initial velocity (A-), a stronger magnetic field (B+), or a wider plume (C-).

Using the collected figures from individual runs for percentage of ions versus initial radial position (Figure 82), the effect of plume width is very noticeable on where trapped ions originate along the plume radius. A wider plume results in more ions being retained from closer to the plume centerline than a narrower plume. The red circle and arrow point out that when all conditions are the same (i.e. initial velocity and magnetic field strength), two things occur: a.) there is a spike or second hump of returning ions near r = 0.4 m when the plume is wider, and b.) the percentage of returning ions originating in the plume fringe remains practically the same and is barely affected by changes in plume width as pointed out by purple arrows. Therefore, the width of the plume or the density distribution of the plume will cause a "double hump" to appear in a graph similar to Figure 82 when the plume is allowed to expand radially outward, possibly by reducing the magnetic field strength or changing the magnetic field line geometry.

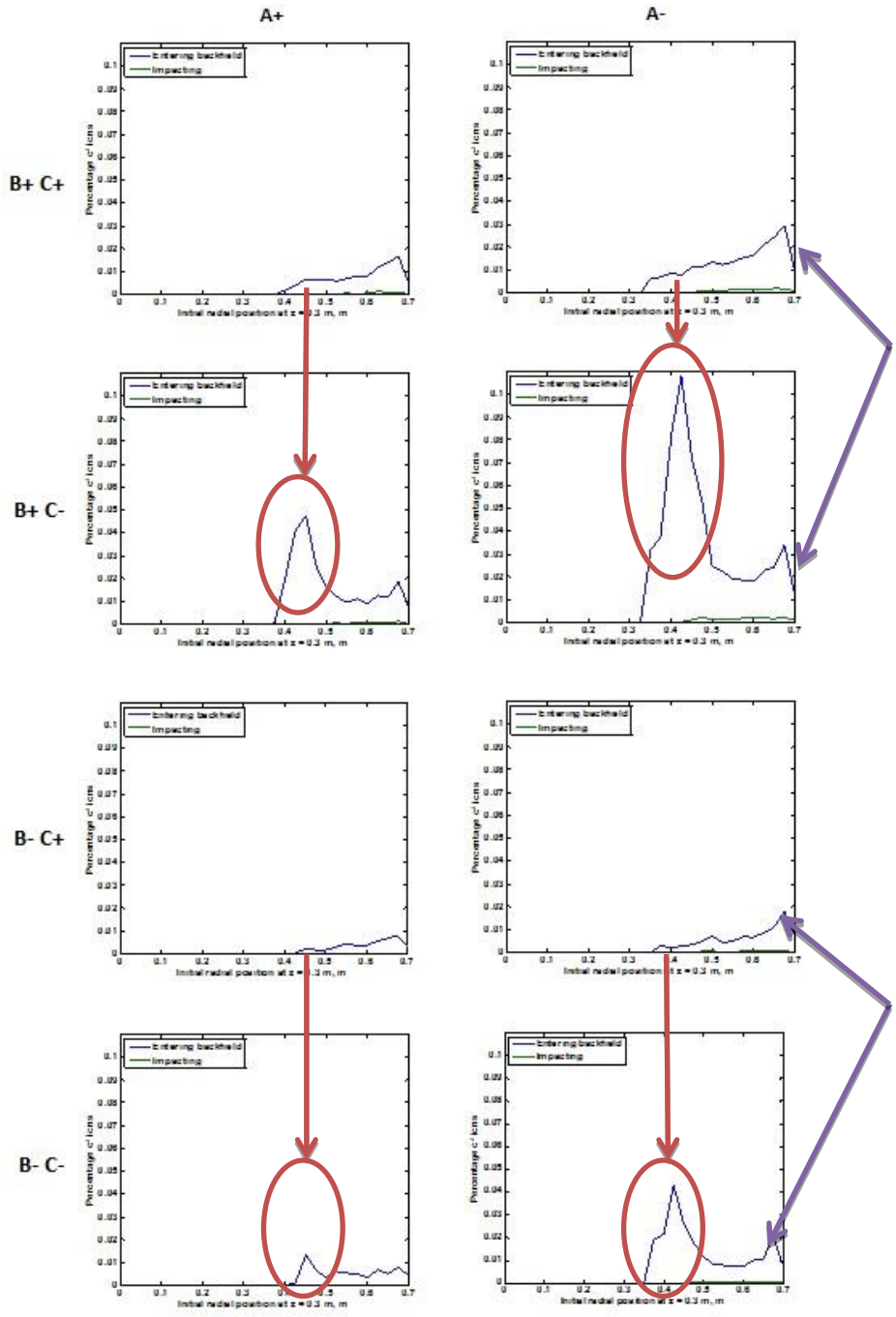

Figure 82. Percentage of ions entering the backfield (blue) and impacting (green) as a function of initial radial position at z = 0.3 m. The red arrows and circles indicate when all factors are the same but the plume is widened, a spike in the concentration of returning ions occurs in the mid-range radial position. Note that the amount of returning ions originating in the far fringe (right) barely changes when the plume is widened as pointed out by purple arrows.

The ion maximum and minimum initial velocity, for all ions entering the backfield and all ejected ions, and the maximum and minimum initial radial position for ions, for all ions entering the backfield and all ejected ions, is presented in Table 6. Run 5, the baseline, highlighted in yellow. Although Run 5 used the slower initial ion velocity profile and is expected to have a low average velocity like Runs 1, 6, and 7 which also share the same velocity profile, Run 5 actually has the second highest average.

Table 6. Initial Velocity and Radial Position for all Ions Entering the Backfield.

	Initial Velocity (m/s)			Initial Radius (m)			Initial Velocity Possible		Initial Radius Possible	
Run	Min	Max	Average	Min	Max	Average	Min	Max	Min	Max
1	7661	25825	12562	0.370	0.698	0.502	7660.6	40488.3	0.000	0.700
2	10178	28477	15771	0.413	0.697	0.560	10178.0	44668.9	0.000	0.700
3	10178	35231	17038	0.370	0.697	0.510	10178.0	44668.9	0.000	0.700
4	10178	33667	19452	0.399	0.698	0.584	10178.0	44668.9	0.000	0.700
5	7661	33309	17933	0.344	0.698	0.563	7660.6	40488.3	0.000	0.700
6	7661	25825	15680	0.371	0.698	0.586	7660.6	40488.3	0.000	0.700
7	7661	33309	14514	0.343	0.698	0.481	7660.6	40488.3	0.000	0.700
8	10178	26521	16857	0.436	0.698	0.606	10178.0	44668.9	0.000	0.700

The data in Table 6 is plotted in Figure 83 to illustrate that using a stronger magnetic field results in more of the faster ions being trapped and entering the backfield. Similarly, using a weaker magnetic field with a slower initial velocity for ejected ions results in only the slowest ions being trapped.

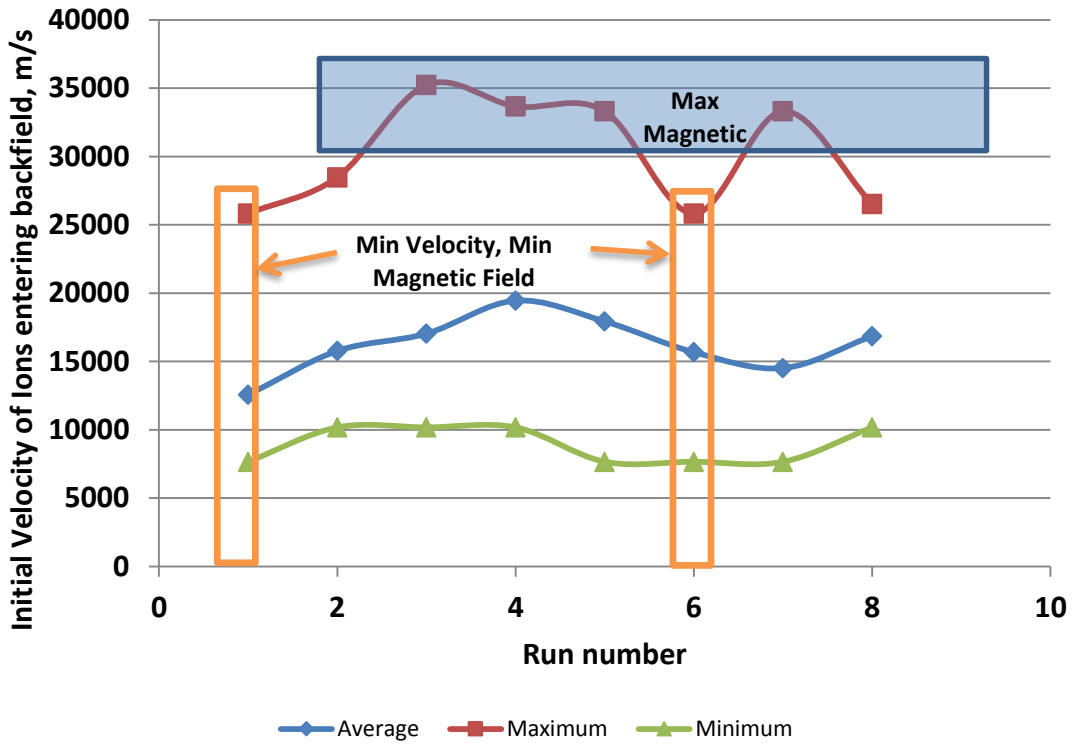

Figure 83. The average, maximum, and minimum initial velocity of ions entering backfield for each run.

Similar to Table 6, the maximum and minimum initial ion velocity, both for impacting and all ejected ions, and maximum and minimum initial radial position, both for impacting and all ejected ions, is presented in Table 7.

Table 7. Initial Velocity and Radial Position for Impacting Ions.

	Initial Velocity (m/s)			Initial Radius (m)			Initial Velocity Possible		Initial Radius Possible	
Run	Min	Max	Average	Min	Max	Average	Min	Max	Min	Max
1	7661	11790	8710	0.465	0.697	0.592	7660.6	40488.3	0.000	0.700
2	13309	13310	13310	0.661	0.677	0.669	10178.0	44668.9	0.000	0.700
3	13309	16455	13748	0.512	0.697	0.620	10178.0	44668.9	0.000	0.700
4	13309	16455	13759	0.524	0.695	0.626	10178.0	44668.9	0.000	0.700
5	7661	17690	11478	0.442	0.697	0.595	7660.6	40488.3	0.000	0.700
6	7661	11790	8888	0.464	0.682	0.594	7660.6	40488.3	0.000	0.700
7	7661	17690	10556	0.435	0.697	0.577	7660.6	40488.3	0.000	0.700
8	13309	13309	13309	0.687	0.687	0.687	10178.0	44668.9	0.000	0.700

The data in Table 7 is plotted in Figure 84 to reconfirm that a stronger magnetic field captures faster ions. The minimum number of impacts are pointed out with blue circles and correspond to runs that used the fastest initial ion velocity profile and weakest magnetic field strength.

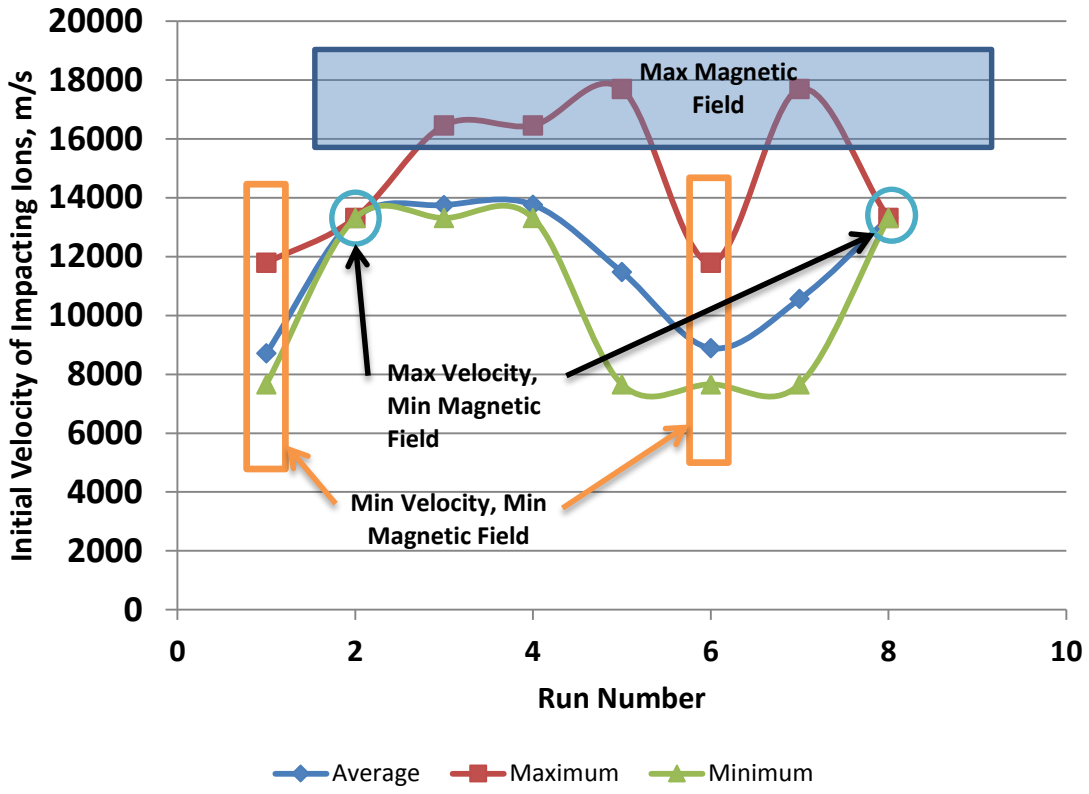

Figure 84. The average, maximum, and minimum initial velocity of impacting ions for each run.

The next section will discuss the interactions between the three factors that were varied.

5.5.4 Interactions between A, B, and C

This subsection delves into the interactions between the 3 factors A, B, and C (i.e. velocity profile, magnetic field strength, and plume width). An interaction is one where the results from a component single-factor experiment are compared with other single-factor experiments to determine if the results are different. If the results are the same, then no interaction is found. The interactions between the velocity profile, magnetic field strength, and plume width will now be discussed.

As shown in Table 8, the effect on the percentage of impacting ions and the erosion rate is greatest when the magnetic field is strongest. The average kinetic energy of impacting ions is highest when the velocity profile of exiting ions is the fastest. Obviously, when the ions have a higher exit velocity, their average kinetic energy is greater. However, the faster the exit velocity, the fewer number of the ions will recirculate.

Table 8. Interaction of A x B: velocity profile and magnetic field strength.

A	B	<Impact>	<KE>	Erosion	AxB
-1	-1	0.005%	19.135	0.044	1
-1	1	0.015%	29.105	1.257	-1
1	-1	0.000%	38.926	0.017	-1
1	1	0.004%	41.770	0.776	1

Table 8 was used to generate Figure 85 and Figure 86 to illustrate that as these two lines appear to cross at a point with a weaker magnetic field, the velocity profile strongly interacts with the magnetic field strength in relation to the number of ions that impact structure. Very few ions were trapped by the weaker magnetic field. It's

important to note here that the stronger magnetic field results in more ions being trapped, and the lower velocity profile results in more ions being trapped.

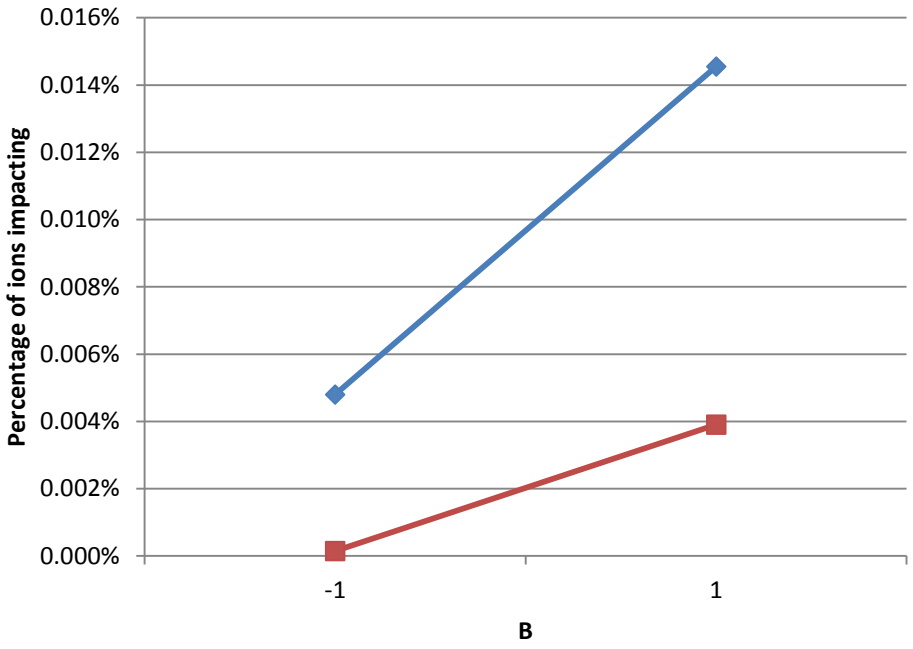

Figure 85. Percentage of ions impacting as a function of A x B: velocity profile and magnetic field strength. The A_{high} (red line) and A_{low} (blue line) show a limited interaction. The two lines appear to cross at a weaker magnetic field than was used here.

The effect of initial ion velocity and magnetic field strength on aluminum surface erosion is even more pronounced in Figure 86 than in the previous figure, as the lines cross at the weaker magnetic field condition. This crossing indicates a very strong correlation with the initial velocity of ejected ions contributing greatly to the total erosion, which is logical as kinetic energy of each ion is both dependent on the ion velocity and is a factor in particle erosion.

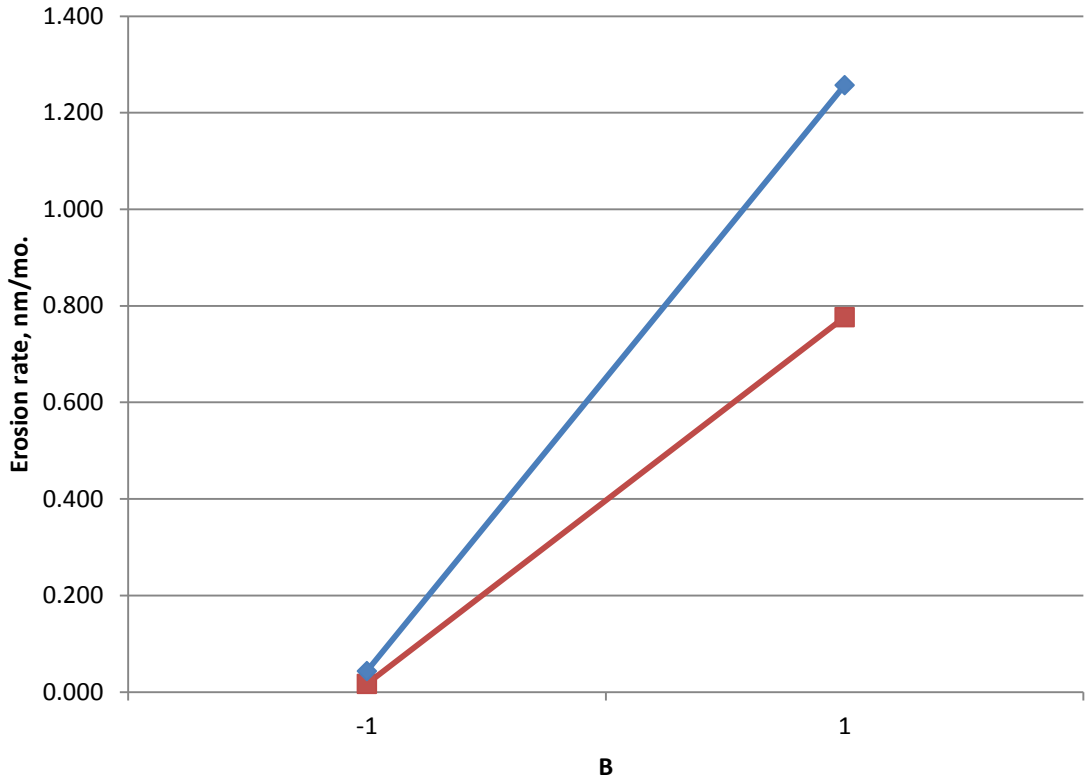

Figure 86. Erosion rate as a function of A x B: velocity profile and magnetic field strength. The A_{high} (red line) and A_{low} (blue line) show a strong interaction. Increasing the average initial velocity of ejected ions increases the erosion rate by over a factor of 4 at the higher magnetic field strength.

The interaction between B and C or the magnetic field strength and density distribution (or plume width) is presented in Table 9. The percentage of impacting ions, their kinetic energy at impact, and the erosion caused are all greatest when the magnetic field strength is strongest.

Table 9. Interaction of B x C: magnetic field strength and density distribution.

B	C	<Impact>	<KE>	Erosion	BxC
-1	-1	0.003%	28.870	0.036	1
-1	1	0.002%	29.190	0.024	-1
1	-1	0.011%	34.375	0.991	-1
1	1	0.008%	36.500	1.043	1

Table 9 was used to generate Figure 87 and Figure 88 and further illustrates that the percentage of ions impacting decreases with a narrowing density distribution. The interaction between magnetic field strength and the plume's density distribution correlates weakly as both lines are essentially parallel. The percentage of ions impacting is highest when the magnetic field is strongest and the plume's density distribution is widest. The average kinetic energy is higher with the stronger magnetic field as more of the faster ions are being trapped.

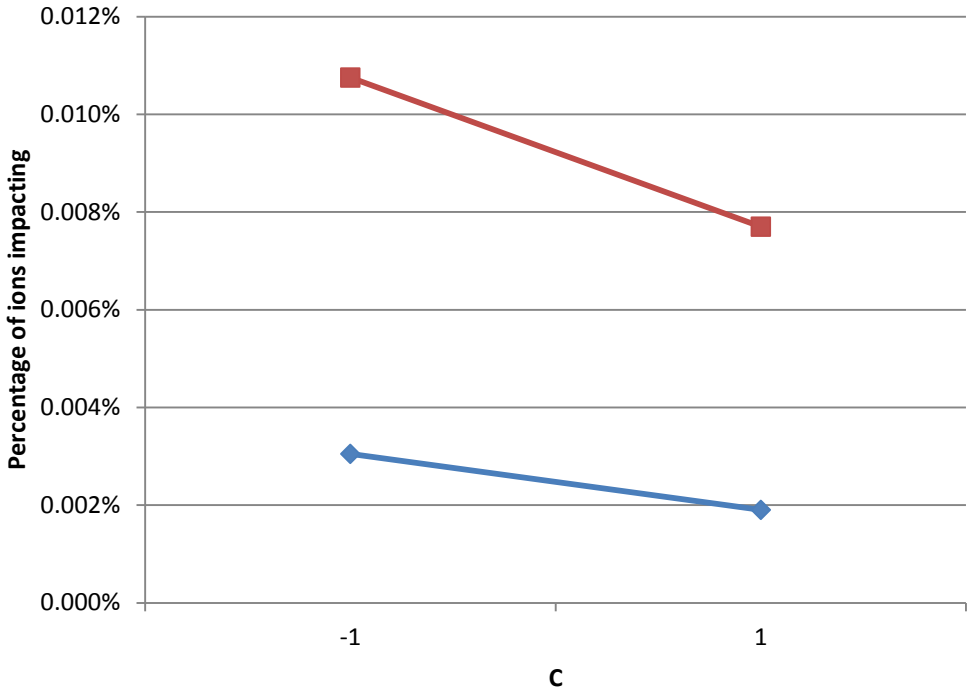

Figure 87. Percentage of ions impacting as a function of B x C: magnetic field strength and density distribution. The B_{high} (red line) and B_{low} (blue line) show no interaction as the lines are essentially parallel.

Similar to Figure 87, the lines in Figure 88 show only a weak interaction and are almost parallel. Therefore, the magnetic field strength and plume width or plume width have very little interaction with each other. However, in a physical sense, the strength of the magnetic field does affect how wide the plume is allowed to expand radially.

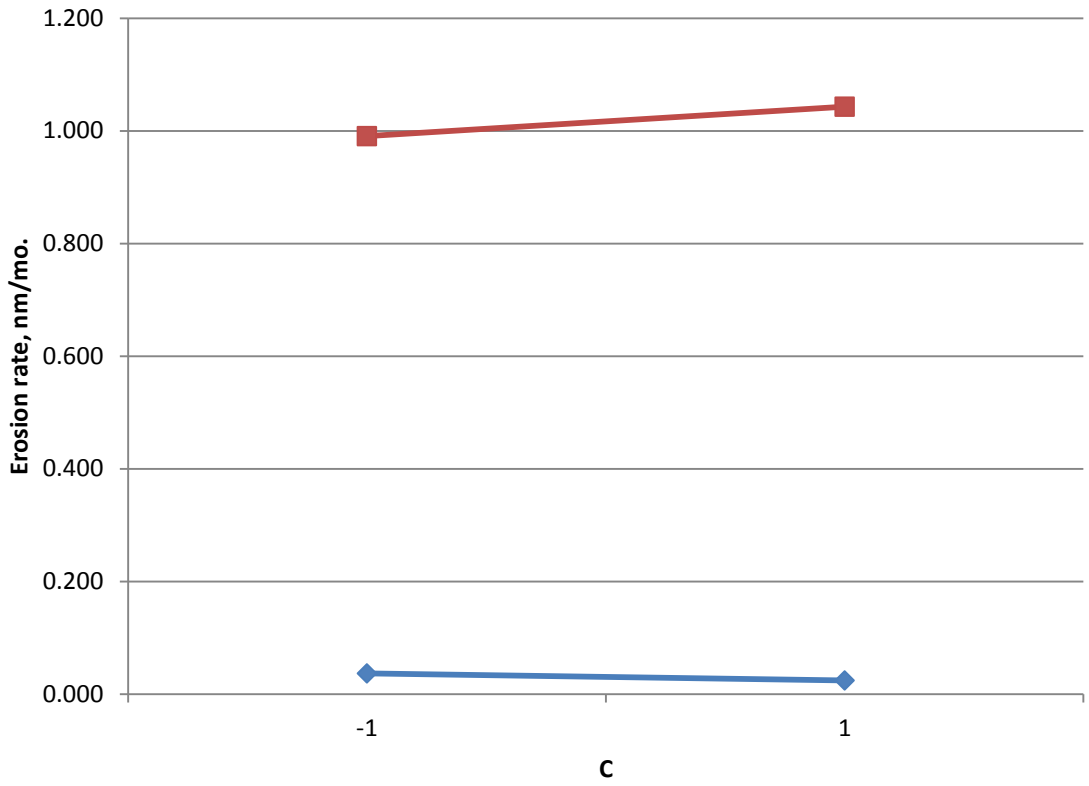

Figure 88. Erosion rate as a function of B x C: magnetic field strength and density distribution. The B_{high} (red line) and B_{low} (blue line) show a limited interaction. The lines are almost parallel indicating that plume density distribution only slightly increases the erosion rate at higher magnetic field strength.

As shown in Table 10, the effect of a lower velocity profile is that more ions return, but correspondingly do less erosion due to the lower average kinetic energy. The faster the velocity profile is, the more erosion results, but the significantly fewer ions are trapped.

Table 10. Interaction of A x C: velocity profile and density distribution.

A	C	<Impact>	<KE>	Erosion	AxC
-1	-1	0.012%	22.885	0.590	1
-1	1	0.008%	25.355	0.711	-1
1	-1	0.002%	40.361	0.438	-1
1	1	0.002%	40.335	0.356	1

Table 10 was used to generate Figure 89 and Figure 90 to show that there is a correlation between the velocity profile of ejected ions and the plume's density distribution, as these two lines can eventually intersect. As mentioned above, the lower the velocity profile is, the more ions are trapped by the magnetic field. In addition, the wider the plume density distribution, the more ions are trapped.

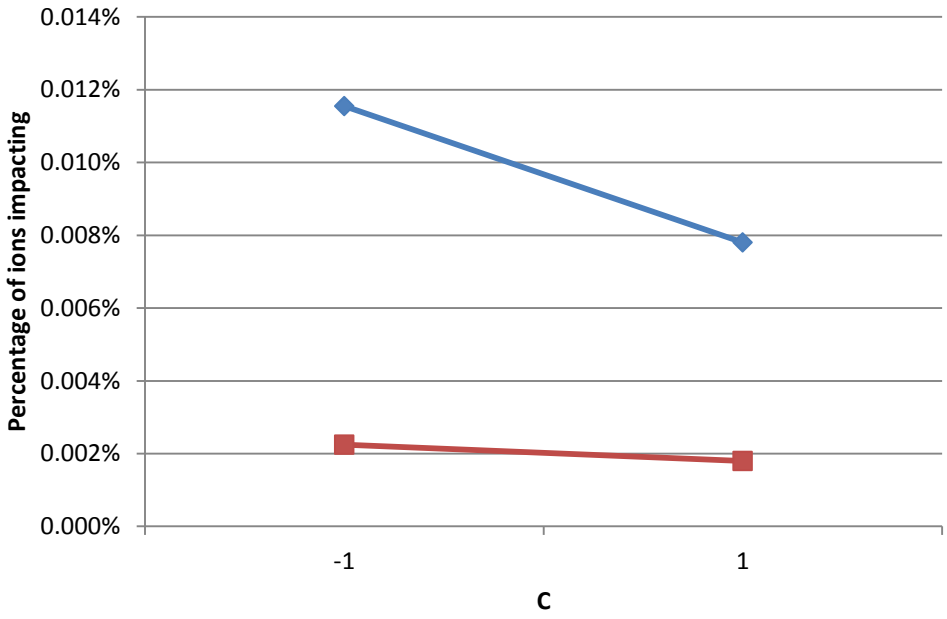

Figure 89. Percentage of ions impacting as a function of A x C: velocity profile and density distribution. The A_{high} (red line) and A_{low} (blue line) show limited interaction.

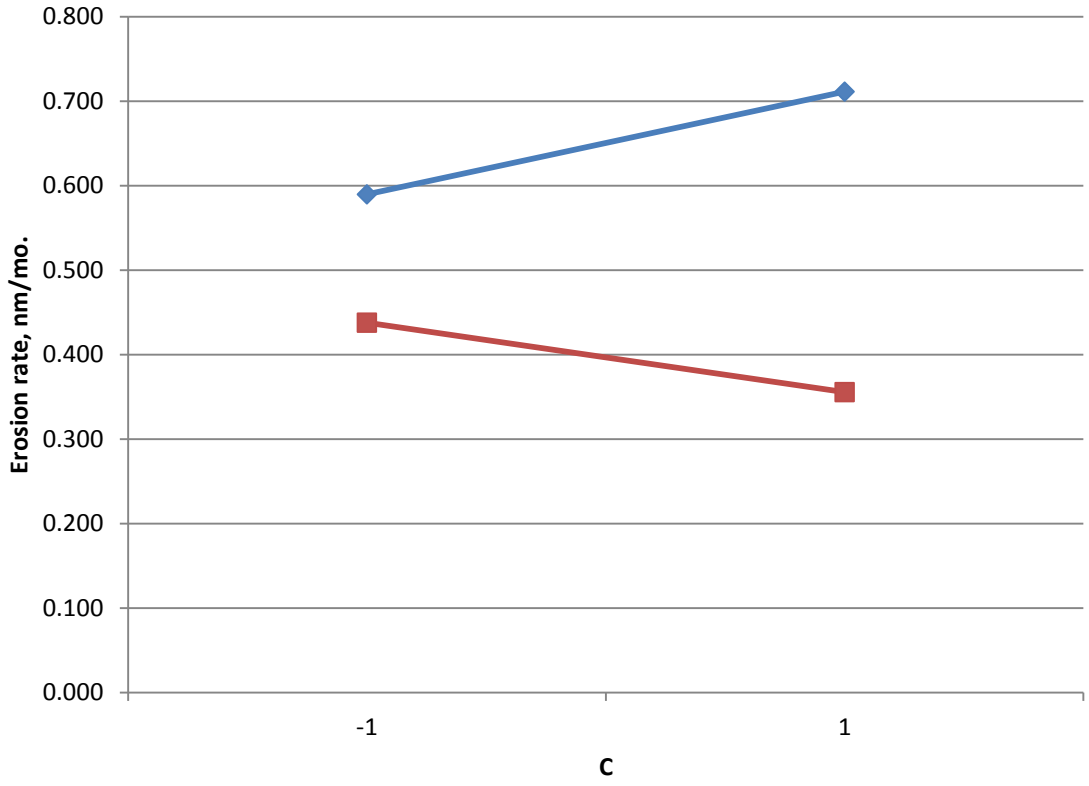

Figure 90. Erosion rate as a function of A x C: velocity profile and density distribution. The A_{high} (red line) and A_{low} (blue line) show significant interaction.

5.5.5 Most Important Interactions

To better understand what effect the 3 factors and their interactions have on the percentage of ions impacting, the average kinetic energy of impacting ions, and the erosion rate, the factors and their interactions were plotted in Figure 91, Figure 92, and Figure 93.

5.5.5.1 The Percentage of Impacting Ions

The factor that has the strongest influence on the percentage of ions impacting (Figure 91) is clearly A, the initial ion velocity in the plume or the exit velocity from the engine throat. The slower the ions are, the more ions become trapped and impact the engine and radiator panels. The faster the ions are, the more escape the magnetic field.

The strongest interaction is B x C, which is the interaction of the magnetic field strength with the plume density distribution or plume width. Specifically, a strong magnetic field and narrow plume result in a subtraction of 0.005% on the total percentage of impacting ions. The relationship is complex as a stronger magnetic field will trap more ions but a narrower plume will allow more ions to escape. The second strongest interaction is A x B, which is the interaction of ion initial velocity and magnetic field strength, with faster ions and a stronger magnetic field resulting in a subtraction of 0.003% on the total percentage of impacting ions. This interaction effect is likely because the effect of A, initial ion velocity, is stronger than B, the magnetic field strength, such that faster ions reduce the number of impacting ions but a stronger magnetic field increases it. However, the difference in how A and B affect the percentage of impacting ions are very close and much greater than C, the plume width. Understandably, the interaction between initial ion velocity and plume density distribution (A x C) has the least effect.

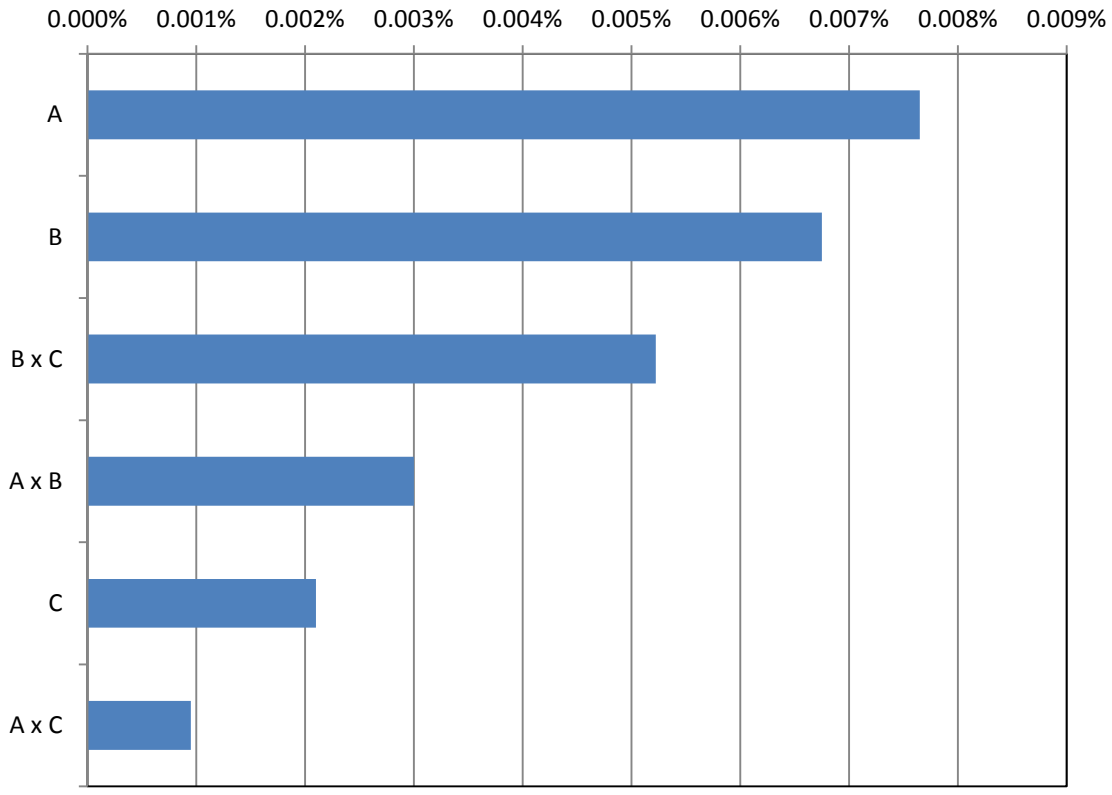

Figure 91. The effect A, B, and C factors have on the percentage of ions impacting the engine/radiators.

5.5.5.2 Average Kinetic Energy of Impacting Ions

The factor that has the strongest effect on the average kinetic energy of impacting ions is overwhelmingly the initial ion velocity, or Factor A (Figure 92). This is logical because as the velocity of ejected ions increases, the fewer ions are trapped but those ions that are trapped have a higher kinetic energy. The interaction that has the most effect is B x C, the magnetic field strength and the plume density distribution and is only slightly less than the effect of B itself. The amount this interaction affects the average

kinetic energy of impacting ions is interestingly different from the interaction discussed in section 5.5.3 for B x C where the correlation is very weak.

The plume width (Factor C) was found to be the least important factor in the average kinetic energy of impacting ions. This is most likely because the difference in C+ and C- was only 20%. A larger difference may increase this factor's importance.

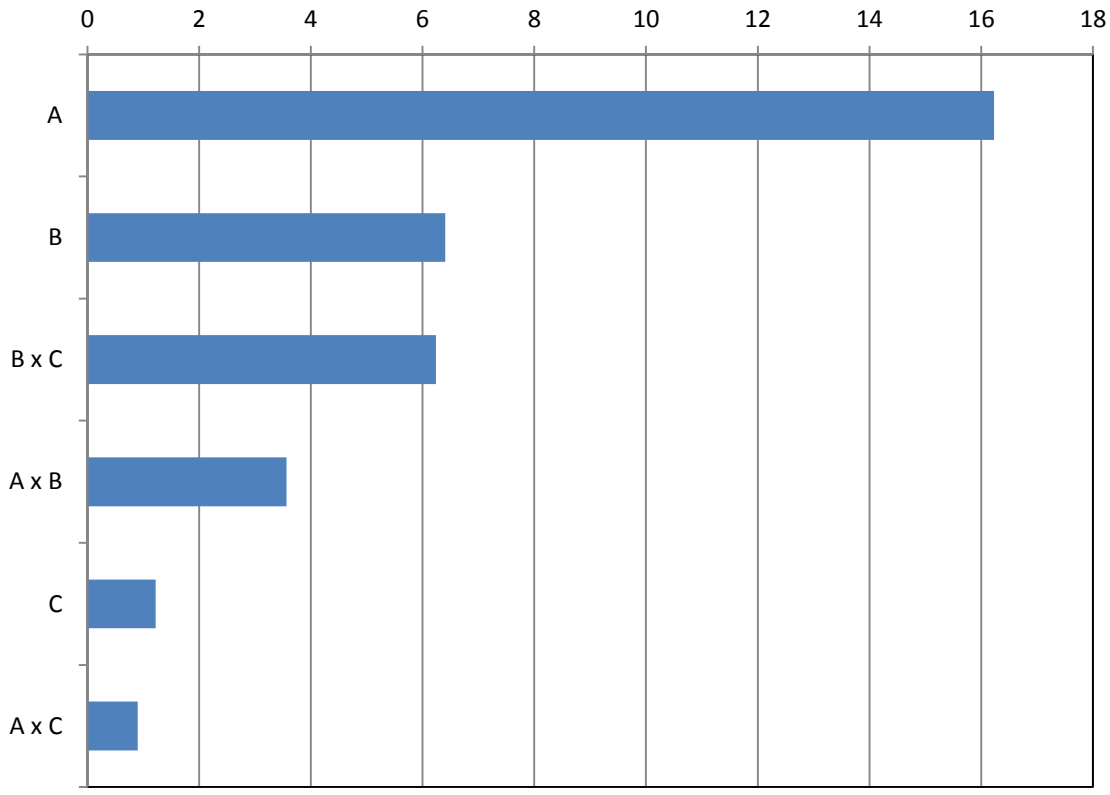

Figure 92. The effect A, B, and C factors have on the average kinetic energy, eV, of ions impacting the engine/radiators.

5.5.5.3 The Erosion Rate

The factor that has the greatest effect on erosion rate is the magnetic field strength, or Factor B (Figure 93). The factor with the second greatest effect on erosion rate is the initial ion velocity of ejected ions, or Factor A, which is logical as the erosion rate is dependent on the impacting ion's kinetic energy which is dependent on the ion's velocity.

The interaction that has the greatest effect on erosion rate of an AL plate is B x C, or magnetic field strength and plume width. This is also logical as more ions are trapped by a stronger magnetic field and by a wider plume width, which increases the total erosion. As in the other interaction plots, A x C has very little effect here possibly because Factor C was varied to a lesser degree than the magnetic field strength was.

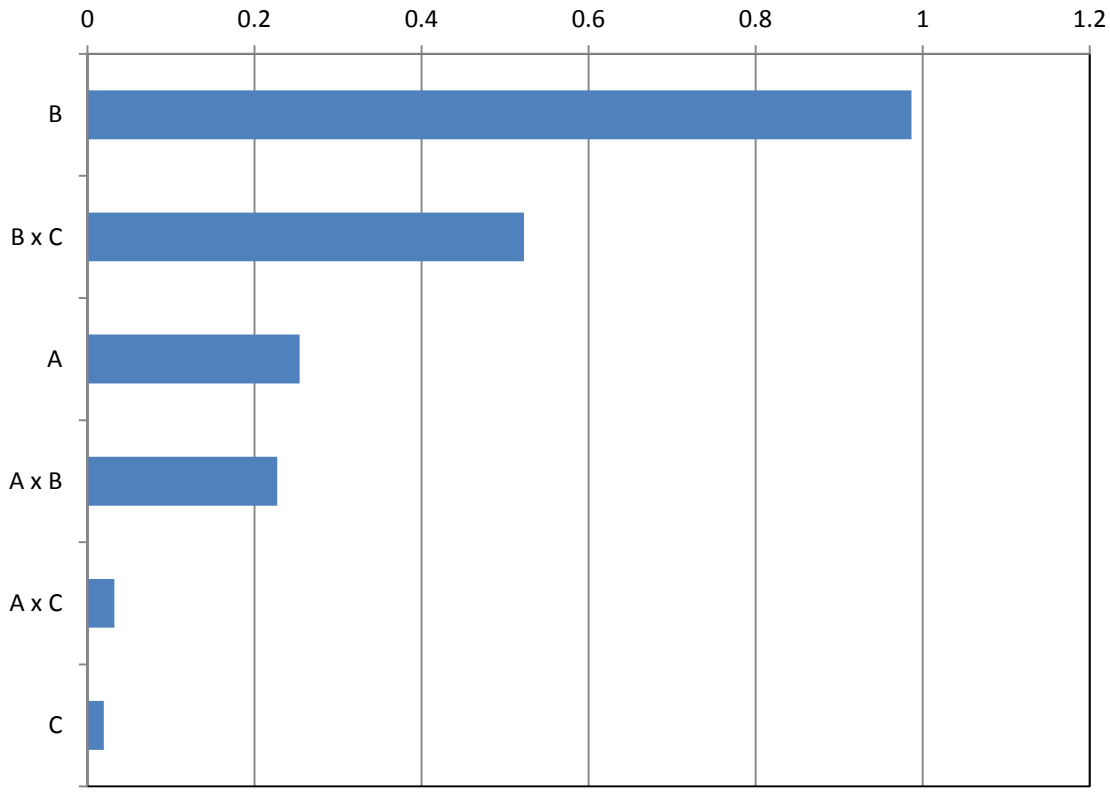

Figure 93. The effect A, B, and C factors have on the erosion rate, nm/month, caused by ions impacting the engine/radiators.

The results displayed in Table 4 were sorted by highest percentage of impacting ions and then by the highest erosion rate and average kinetic energy to better show the effect each of the 3 factors have on these important quantities and can be found in Appendix J.

In this section, the results derived from the numerical model were presented and discussed. In the next section, findings and conclusion from this research are presented and future studies are recommended.

6. CONCLUSIONS

6.1 Introduction

This section will summarize the many findings that came from the previous section and will tie together the results from electrical charging and surface erosion. The next section is the summary of all previous sections. The third section is a list of the general findings meant to assist in the design and testing of any future magnetoplasma spacecraft engines, including the important relationships between plume exit velocity, magnetic field strength, and plume width. The fourth section is a list of findings that are specific to the VX-200 engine from which experimental data was used to develop the numerical model. The fifth section is an explanation of the main conclusions from this research. The sixth section is a list of recommendations for future magnetoplasma engine designers to follow based on this research. The seventh and last section is a collection of recommendations for future studies and where new technologies or resources could be used to refine the results presented here.

6.2 Summary

Section 1 introduced the fundamental problem with magnetoplasma engines which is that plasma detachment has not been fully explained and proven to exist. If the ejected plasma does not detach from the engine's magnetic field then no thrust is generated and the spacecraft does not move. This section listed the relevance and objective of this research, with the objective being to predict the structural damage due to the erosion and electrical charging on the surface of a spacecraft operating a

magnetoplasma engine caused by recirculating particles and how engine operational parameters affect the amount of damage.

In Section 2, there are several mechanisms presented which could lead to plasma detachment, with Kinetic detachment and Loss of Adiabaticity detachment being used in this research. Kinetic detachment supposes that when the local plasma velocity is greater than the local Alfvénic velocity of the plasma, then the plasma particles are at a location where the magnetic field strength is not sufficient to overcome the particles' forward velocity. The particles are said to detach from the magnetic field lines at this point. Loss of Adiabaticity detachment occurred when the magnetic field changed at a greater rate (i.e. decreased) such that a particle could not react fast enough and detached from the magnetic field line. A thorough explanation of magnetic nozzles was given as well as a list of engines that have or will use magnetic nozzles to provide thrust. Lastly, the plasma engine plume and its interaction with spacecraft were discussed.

Section 3 is a comprehensive breakdown of what is needed to accomplish the research objective and the properties that need to be determined for an accurate result. The needs were broken down into determining the plume particle trajectories from around the plume and determining the plume particle trajectories for the subset of particles that reach the engine backfield.

The rationale for utilizing a numerical model to determine particle trajectories is presented in Section 4 along with how the model was created. As testing an actual magnetoplasma engine in space is not feasible for the near future and current vacuum chambers cannot generate the vacuum present in high Earth orbit, a numerical model

was selected. The initial and boundary conditions for the model were also listed with the assumptions used.

In Section 5, the results from the numerical model were explained, and how the results compared to experimental data to validate the model was explored.

6.3 General Findings

There are many general findings that come from the numerical model runs. These findings should apply to any magnetoplasma engine that exists or in the future.

1. The stronger the magnetic field is, the more ions will recirculate and impact structure, and the higher the erosion rate will be. The magnetic field strength is the most important contributor to erosion of aluminum and silicon spacecraft surfaces. However, this doesn't mean that a strong magnetic field should be avoided as it is necessary to keep plasma away from internal engine surfaces and to form the magnetic nozzle.
2. The more tightly confined the plume is around the centerline (narrow density distribution), the fewer ions will recirculate and impact structure.
3. The more tightly confined the plume is, the more likely it is that the returning ions will originate in the plume fringe. The wider the plume density distribution is, the more returning ions will be pulled from closer to the plume centerline. By changing the magnetic field geometry to decrease the plume width, one can reduce the number of trapped particles.
4. There exists an "Erosion Zone" where the trapped particles exist with sufficient kinetic energy to erode aluminum or silicon surfaces as shown in Figure 45. The

zone's size is dependent on the average exit velocity of ejected particles and magnetic field strength. At slower exit velocities, more particles are trapped and impact, but the kinetic energy of individual particles may be below the surface material's sputter yield. At very fast exit velocities, the erosion per impacting particle is much higher, but there are much fewer trapped and impacting particles because most particles are escaping the magnetic field. At weak magnetic field strength, fewer particles are trapped and impact to cause erosion, while at ever stronger magnetic field strength, more particles impact to cause significant erosion.

5. The higher the average ion velocity is in the plume, the fewer ions recirculate and impact structure, but the higher the erosion rate per impact (up to the point when the number of impacting ions drops to zero).
6. The greatest number of recirculating ions and impacting ions occurred on runs where the velocity of exiting ions was slowest and the magnetic field was strongest. However, this did not result in the greatest erosion because the slower ions had less kinetic energy to impact with.
7. The faster the exit velocity of ejected ions is, the fewer ions are trapped but the more erosion and electrical charging occur (up to a threshold when the percentage of returning ions reaches zero). The ion exit velocity is the most important contributor to the amount of ions that impact, their kinetic energy, and the amount of electrical charging on spacecraft surfaces.

8. The wider the plume is, the more ions are trapped. This can be used to capture and recirculate ions around a spacecraft such as needed for the M2P2[38, 39] spacecraft.
9. A wider plume results in more ions being retained from closer to the plume centerline than a narrower plume.
10. The plume exit velocity has the greatest effect on the number of returning ions and the kinetic energy at time of impact.
11. However, magnetic field strength had the greatest effect on the actual erosion rate.
12. Ejecting slower ions with a stronger magnetic field and a wide plume results in the most ions becoming trapped, which might be useful if a solar sail like the one used by the M2P2[38, 39] spacecraft is desired.

6.4 Specific Findings

The following findings are specific to the magnetic field geometry, argon gas properties, and electric field strength from the experimental data used in this research:

1. Under nominal conditions (Run 5), roughly 0.012% of ejected ions should recirculate and impact resulting in an erosion rate of 1.386 nm per month on aluminum surfaces and 0.611 nm per month on the silicon surfaces such as solar power panels.
2. The erosion rate is 0.700 nm/month of an AL surface using argon in the maximum condition with the stronger magnetic field, narrow plume, and a velocity profile created when power to the ICH antenna was at a maximum

(ICH/RF = 6). The worst erosion rate is 1.386 nm/month using a magnetoplasma spacecraft engine firing in the baseline configuration with antenna power and magnetic field ratio at ICH/RF ≈ 3.

3. The maximum electrical charge was found in the baseline configuration and was -27.85 V. However, an alternative method to calculating the surface potential found that the potential maximum was -166.72 V.
4. The worst engine configuration (i.e. slower ejected particles, stronger magnetic field, and narrow plume) happens to be the baseline, which indicates that to reduce erosion and electrical charging, a change in one or all of these conditions is warranted. For instance, using faster ejected particles results in almost half the erosion rate of aluminum or silicon surfaces. Using the weaker magnetic field leads to an erosion rate that is 37 times less for aluminum surfaces.
5. However, the erosion rate on aluminum surfaces is extremely low for all 8 different engine configurations.
6. The erosion rate on silicon surfaces is also extremely low and peaked when the engine configuration using a stronger magnetic field and slower ejection of ions was chosen.
7. The four highest erosion rates come from engine configurations with the stronger magnetic field and the full factorial experiment used in this research determined that magnetic field strength was the factor that had the greatest effect on erosion rate. Therefore, it was shown in Figure 46 that as a magnetoplasma engine uses a

stronger and stronger magnetic field, the erosion rate on an aluminum surface will increase as well.

8. The spacecraft received the greatest amount of electrical charging when the exiting ions were the fastest and the magnetic field the strongest, as more ions with high kinetic energy were trapped and impacted the spacecraft surface.
9. The ejected particles were accelerated slightly by the magnetic nozzle depending on the initial velocity. For factor A+, where the average initial velocity was 29.7 km/s, the ions' final velocity increased an average of 2.88%. However, for factor A-, where the average initial velocity was only 24.4 km/s, the ions' final velocity increased an average of 4.29%, which indicates that plumes made up of slower ions benefit more from a magnetic nozzle than plumes made up of faster ions. Therefore, the faster the plume ions are, the less effect a magnetic nozzle has on the ions. If the relationship between acceleration and initial ion velocity is linear or even exponential, then above 50 km/s, the ions would not be accelerated at all. This may be because the longer the ions are near and affected by the magnetic nozzle, the more acceleration is imparted on the ions. Ergo, a shorter residency time for the plume ions means the magnetic nozzle will be less effective (e.g. if the particles exited at the speed of light, the residency time would essentially be zero, and there would be no effect from the magnetic nozzle on particle acceleration).

The results represent a worst case scenario for erosion as only Kinetic and Loss of Adiabaticity detachment were used in this research because the other detachment processes relate to fluids and not to the particle kinetic theory utilized here. As these detachment processes occur to some degree, the actual erosion rates will likely be less.

The plume velocity profiles utilized for this research come from experimental data using power ratios of ICH/RF ≈ 3 and 6. The velocity profile was taken at the plume centerline but was used for the entire inlet disc (0 m < r < 0.7 m). As such, the percentage of slower velocity ions is likely much greater in the fringe (r > 0.3 m) and, thus, more ions will enter the backfield and impact the engine housing and radiator panels. Erosion rates due to electrons were not included as their kinetic energies are negligible and often below the sputter yield threshold for AL or SI atoms.

6.5 Conclusions

In conclusion, the structural damage due to the erosion and electrical charging on the surface of a spacecraft operating a magnetoplasma engine caused by recirculating particles was predicted. The effect of engine operational parameters on the amount of damage was also determined. The main conclusions are:

1. A particle kinetic simulation provides a reasonable upper-bound approximation of the number of particles recirculating, impacting, causing erosion, and charging of the spacecraft.
2. The erosion rate of an aluminum or silicon plate impacted by recirculating particles from a magnetoplasma engine is very low. In

comparison, the International Space Station experiences roughly 175 times more erosion from atomic oxygen in Low Earth Orbit (LEO). However, for optical equipment, such as star trackers or telescopes, this erosion could be a concern.

3. The electrical charging on a spacecraft due to impacts by recirculating particles from a magnetoplasma engine could lead to destructive arcing but could be neutralized with technologies similar to Plasma Contactor Units on a larger scale.
4. The exit velocity of ejected particles from a magnetoplasma engine has a strong effect on the amount of particles that impact with faster particle ejections leading to fewer particles recirculating, impacting, causing erosion, or charging the spacecraft.
5. The magnetic field strength also has a strong effect on the amount of particles recirculating, impacting, causing erosion, and charging the spacecraft with a stronger magnetic field leading to more impacts and damage.
6. The plume density distribution or width had a relatively small effect on the amount of particle recirculation, impact, erosion rate, or electrical charging but did effect where in the plume the impacting particles originated from. Wider plumes had more particles impact.

These conclusions come from the results based on an analysis of the plasma plume parameters and development of a numerical model using electrical, magnetic, and

particle motion equations. The numerical model simulated the movement of 1 million ions after being ejected from a magnetoplasma engine with initial and boundary conditions that come from experimental data. A full factorial experiment was done with the numerical model to determine the effect that particle exit velocity, magnetic field strength, and plume width (i.e. density distribution) had on the percentage of particles returning to the spacecraft and impacting structure, the erosion rate caused by these impacts on aluminum and silicon surfaces, and the electrical charging that resulted. The erosion rates and electrical charging values determined by this research represent a justifible upper limit for an operating magnetoplasma engine.

6.6 Recommendations

As the erosion rates are extremely low, it is recommended that a.) adding an extra layer of paint or sacrificial layers to plume-facing spacecraft components near the engine, b.) adding a thin shield near the radiator panels, or c.) slightly thickening the engine housing and radiator panels in order to handle the erosion. However, for delicate optical equipment such as telescopes near the rear of the vehicle, this erosion rate may be problematic.

The amount of electrical charging due to plasma particles impacting the engine housing and radiator panels was found to be manageable for current plasma contactors on the International Space Station but for an unknown amount of time. Although the potentials calculated by the two methods presented in this research vary significantly, both values could possibly be reduced or eliminated using current plasma contactor technology. It is recommended that any future spacecraft using a magnetoplasma rocket

engine be equipped with enough plasma contactors to handle this charging over time. If a way to recover and use this electrical charging productively was developed, then the spacecraft engine could be partially powered by its own recirculating particles.

6.7 Recommendations for Future Work

The effect of magnetic coil spacing on the percentage of ions impacting and the resultant erosion rate can be easily determined with this numerical model and is planned to be explored in the future. All of the data in this dissertation was calculated using argon as the propellant, but krypton or xenon could be easily substituted to determine if these gases would increase or decrease the erosion rate for the same conditions.

The electric field could be made more consistent and accurate by running the model with ions and electrons separately, finding the resulting electric field, entering that electric field into the model, and rerun until the resulting electric field converges on a single value.

As soon as the relationship between the propellant mass flow rate and the plume velocity profile is determined for different RF antenna power levels by the Ad Astra Rocket Company and published, the effect of mass flow rate on erosion can be established using this numerical model. Unfortunately, this cannot be done at this time as experiments with the VX-200 have shown that there are significant losses that vary by power level so that some of the energy is not absorbed by the plasma and converted into velocity.

The “erosion zone” needs to be further developed by running this model for different plume velocity profiles so that future engine designs can reduce or eliminate

the zone completely. Additionally, this zone could help future astronauts to know what the perfect setting for RF power, magnetic field strength, and flow rate would be for optimal performance.

It is also important to mention that although less than 1% of ejected ions entered the backfield, only a small fraction of these ions impacted the radiator panels and the engine housing meaning that most of these ions are free to impact other parts of the spacecraft, or in the case of the ISS, the solar arrays, external equipment, and visiting vehicles. A full model of the ISS is recommended to be employed in the numerical model to determine where the non-impacted but trapped particles travel to. Although the erosion rate and electrical charging are now known, there are other aspects of magnetoplasma engines that need to be characterized before magnetoplasma engines are ready to be used by spacecraft. The COMSOL Multiphysics® model and MATLAB® codes developed for this research are available to any magnetoplasma engine designer so that variables such as magnetic coil location, magnetic and electric field strength, and plasma gas properties can be modified and the effects quantified.

Lastly, the discovery that the width of the plume can be modified to reduce the number of escaping particles (which provide the engine with thrust) and increase the number of trapped particles could be used to create an orbiting shell around the spacecraft and should be explored for spacecraft such as M2P2[38, 39] that use a plasma shell as a solar sail for propulsion. A future astronaut could use this technique to switch a spacecraft's propulsion method from magnetoplasma rocket to a solar sail, resulting in significant propellant savings!

REFERENCES

[1] Jahn, R.G., "Physics of Electric Propulsion," *Physics of Electric Propulsion,* Dover Publications, Inc., Mineola, New York, 1996, pp. 29 - 32.

[2] Sutton, G.P., and Biblarz, O., "Rocket Propulsion Elements," 2010, John Wiley & Sons, New York.

[3] Hooper, E.B., "Plasma Detachment from a Magnetic Nozzle," *AIAA Journal of Propulsion and Power,* Vol. 9, No. 5, 1993.

[4] Sankaran, K., and Polzin, K., "Development of Numerical Tools for the Investigation of Plasma Detachment from Magnetic Nozzles," *AIAA-2007-4386,* 2007.

[5] Aray, D., Girimaji, S., Carter, M.D., "Parameterization of Magnetic Nozzle Flow Physics for an In-Space Propulsion Application," *AIAA-2011-4010,* 2011.

[6] Bering, E.A., Longmier, B., Olsen, C., "VASIMR®: Deep Space Transportation for the 21st Century," *AIAA-2011-7247,* 2011.

[7] Ahedo, E., and Merino, M., "Two-Dimensional Plasma Acceleration in a Divergent Magnetic Nozzle," *AIAA-2009-5361,* 2009.

[8] Winglee, R., Ziemba, T., Giersch, L., "Simulation and laboratory validation of magnetic nozzle effects for the high power helicon thruster," *Physics of Plasmas,* Vol. 14, 2007.

[9] Arefiev, A., and Breizman, B.N., "Magnetohydrodynamic Scenario of Plasma Detachment in a Magnetic Nozzle," *Physics of Plasmas,* Vol. 12, 2005.

[10] Kaufman, D.A., Goodwin, D.G., and Sercel, J.C., "Plasma separation from magnetic field lines in a magnetic nozzle," *AIAA-1993-817,* 1993.

[11] Charles, C., Boswell, R.W., Cox, W., "Magnetic steering of a helicon double layer thruster," *Applied Physics Letters,* Vol. 93, No. 201501, 2008.

[12] Li, M., Tang, H., Ren, J., "Modeling of plasma processes in the slowly diverging magnetic fields at the exit of an applied-field magnetoplasmadynamic thruster," *Physics of Plasmas,* Vol. 20, No. 103502, 2013.

[13] Ilin, A.V., Chang-Diaz, F.R., Squire, J.P., "Simulations of Plasma Detachment in VASIMR®," *AIAA-2002-346,* 2002.

[14] Squire, J.P., Chang-Diaz, F.R., Carter, M.D., "High Power VASIMR Experiments using Deuterium, Neon and Argon," *IEPC-2007-181,* 2007.

[15] Bering, E.A., Chang-Diaz, F.R., Squire, J.P., "High Power Ion Cyclotron Heating in the VASIMR® Engine," *AIAA-2007-586,* 2007.

[16] Bering, E.A., Longmier, B., Chancery, W.J., "Exhaust Plume Spatial Structure of the VASIMR VX-200," *AIAA-2010-622,* 2010.

[17] Ad Astra Rocket Company, "Press Release 080311, Ad Astra and NASA Sign Support Agreement on VASIMR® Technology," Ad Astra Rocket Company public release, March 2011.

[18] Cassady, L.D., Longmier, B., Olsen, C., "VASIMR® Performance Results," *AIAA-2010-6772,* 2010.

[19] Bering, E.A., Longmier, B., Glover, T., "High Power Electric Propulsion Using VASIMR: Results From Flight Prototypes," *AIAA-2009-245,* 2009.

[20] Deline, C., Gilchrist, B., Bengtson, R., "Simulation and Measurement of High-Beta Plasma in a Magnetic Nozzle," *AIAA-2007-5259,* 2007.

[21] Chang-Diaz, F.R., Squire, G., T., Petro, A.J., "The VASIMR Engine: Project Status and Recent Accomplishments," *AIAA-2004-0149,* 2004.

[22] Bering, E.A., Brukardt, M., Squire, J.P., "Recent Improvements In Ionization Costs And Ion Cyclotron Heating Efficiency In The VASIMR Engine," *AIAA-2006-766,* 2006.

[23] Bering, E.A., Squire, J.P., McCaskill, G., "Progress Toward the Development of a 50 kW VASIMR Engine," *AIAA-2005-369,* 2005.

[24] Longmier, B., Squire, J.P., Olsen, C., "VASIMR VX-200 Improved Throttling Range," *48th AIAA/ASME/SAE/ASEE Joint Propulsion Conference & Exhibit,* AIAA, Atlanta, GA, AIAA-2012-3930, 2012.

[25] Bering, E.A., Longmier, B., Squire, J.P., "Performance Measurements and Technology Demonstration of the VASIMR® VX-200," *AIAA-2010-8669,* 2010.

[26] Olsen, C., Ballenger, M., Carter, M.D., "An Experimental Study of Plasma Detachment from a Magnetic Nozzle in the Plume of the VASIMR® Engine," *33rd International Electric Propulsion Conference,* Vol. IEPC-2013-123, Washington, DC, 2013.

[27] Ebersohn, F.H., Girimaji, S., Staack, D., "Towards Computation of Resistive Magnetohydrodynamic Magnetic Nozzle Plasma Flow," AIAA-2012-3841, 2012.

[28] Olsen, C., "Experimental Characterization of Plasma Detachment from Magnetic Nozzles," 2013, pp. 261.

[29] Gabdullin, F.F., Korsun, A.G., and Tverdokhlebova, E.M., "The Plasma Plume Emitted Onboard the International Space Station Under the Effect of the Geomagnetic Field," *IEEE Transactions on Plasma Science,* Vol. 36, No. 5, 2008, pp. 2207.

[30] Behrisch, R., and Eckstein, W. eds., "Sputtering by Particle Bombardment: Experiments and Computer Calculations from Threshold to MeV Energies," Springer-Verlag, Berlin Heidelberg, 2007, pp. 33 - 133.

[31] Bering, E.A., Longmier, B., Ballenger, M., "Performance Studies of the VASIMR® VX-200," *AIAA-2011-1071,* 2011.

[32] Godeke, A., "A Review of the Properties of Nb3Sn and their Variation with A15 Composition, Morphology and Strain State," *Superconductor Science and Technology,* Vol. 19, 2006, pp. R68.

[33] Garrett, H., and Whittlesey, A. eds., "Guide to Mitigating Spacecraft Charging Effects," Chapter 2.3.1, John Wiley & Sons, 2012, pp. 17.

[34] Lai, S., "Fundamentals of Spacecraft Charging," Princeton University Press, Princeton, NJ, 2012, pp. Chapter 1, pg. 1.

[35] Garrett, H., and Whittlesey, A. eds., "Guide to Mitigating Spacecraft Charging Effects," Chapter 2.1.1, 2012, pp. 7.

[36] Olsen, C., "Experimental Characterization of Plasma Detachment from Magnetic Nozzles," 2013, pp. 211.

[37] Swanson, D.G., "Plasma Kinetic Theory," Chapman & Hall/CRC, Boca Raton, 2008, pp. 6.

[38] Winglee, R., Ziemba, T., Slough, J., "Laboratory testing of the Mini-Magnetospheric Plasma Propulsion (M2P2) prototype," *Space Technology and Applications International Forum,* Vol. 552, American Institute of Physics, 2001.

[39] Funaki, I., Kojima, H., Yamakawa, H., "Laboratory Experiment of Plasma Flow Around Magnetic Sail," *Astrophysics and Space Science,* Vol. Vol.307(1), 2007, pp. pp.63-68.

[40] Banks, B.A., Backus, J.A., Manno, M.V., "Prediction of Atomic Oxygen Erosion Yield for Spacecraft Polymers," *Journal of Spacecraft and Rockets,* Vol. 48, No. 1, 2011, pp. 14.

[41] Olsen, C., "Experimental Characterization of Plasma Detachment from Magnetic Nozzles," 2013, pp. 258-259.

[42] Ferraro, V.C.A., and Plumpton, C., "An Introduction to Magneto-Fluid Mechanics," Vol. 2nd edition, 1966, pp. 58.

[43] Todd, L., "Hartmann Flow between Parallel Planes," *Physics of Fluids,* Vol. 9, 1966, pp. 1602.

[44] Garrett, H., and Whittlesey, A. eds., "Guide to Mitigating Spacecraft Charging Effects," Appendix G, John Wiley & Sons, 2012, pp. pg. 153.

APPENDIX A

HAGEN-POISEUILLE FLOW

A laminar viscous flow of an incompressible fluid through a cylindrical pipe is governed by the Hagen-Poiseuille equation which can determine the pressure drop or velocity profile.

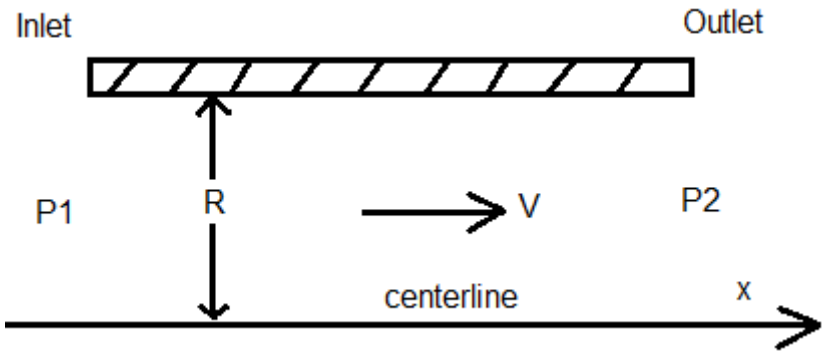

Figure A-1: Diagram of 2 meter long pipe (top half) for Hagen-Poiseuille flow

The Hagen-Poiseuille equation: $v = -\frac{1}{4\eta}\frac{\Delta P}{\Delta x}(R^2 - r^2)$ [42] (A-1)

where ΔP = Pressure drop between inlet and exit (Pa)

η = Dynamic viscosity (Pa*s)

Δx = Pipe length (m)

R = Internal pipe radius (m)

r = Location between pipe radius (m)

v = Velocity (m/s)

In this example where the fluid is water, the following values were chosen:

ΔP = P1 – P2 = 101325 Pa – 101324.8 Pa = 0.2 Pa

η = 0.001787 Pa*s Dynamic viscosity for water at T = 0° C

Δx = Pipe length = 2 m

R = Internal pipe radius = 0.05 m

Figure A-2 shows a comparison of the COMSOL solution vs. the analytical solution (from MS Excel and MATLAB). There is close agreement of the velocity values showing that the COMSOL simulation is accurate.

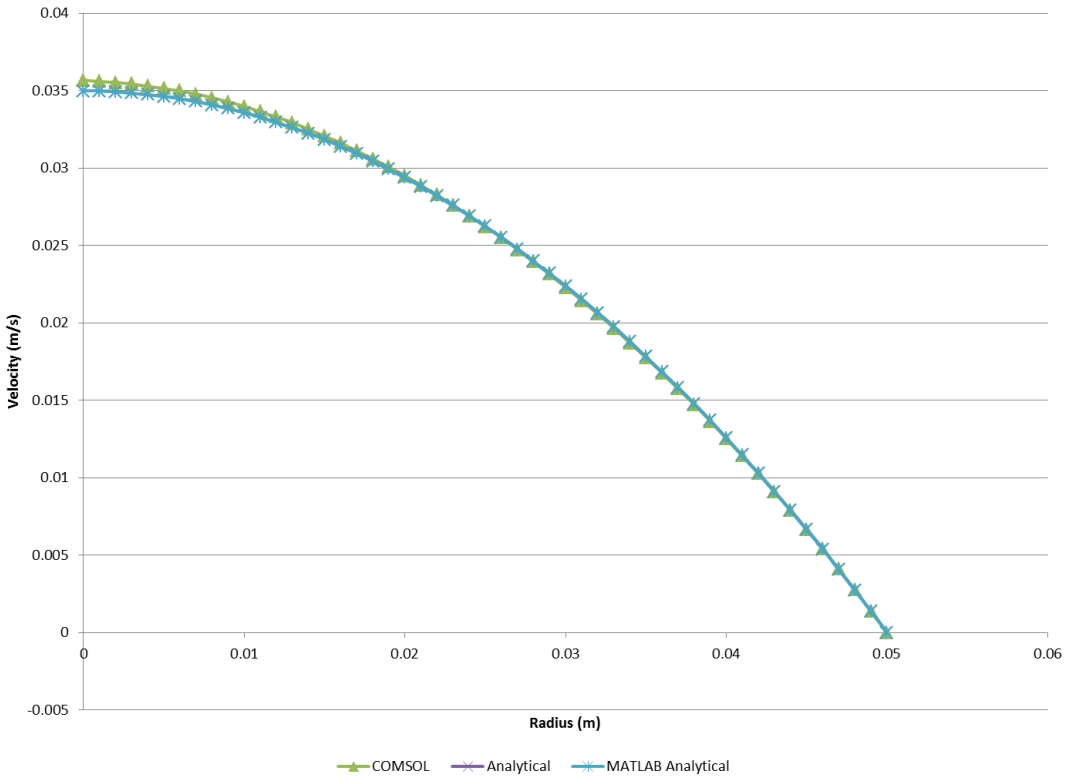

Figure A-2: Hagen-Poiseuille fully-developed flow of water with COMSOL solution vs. analytical solution for a 2 meter long pipe at $\dot{m}$ = 0.1373 kg/s

The mesh size was modified in the COMSOL simulation to determine which size gave the most accurate velocity values (see Figure A-3). As expected, the finer (smaller) the mesh size was, the smaller the error was, with Extremely Fine mesh providing an average error of 0.04% and a maximum average of 0.25%. Course and Normal mesh sizes caused considerable errors (maximum near 3% and 2%, respectively). Noticeably, error increases around the pipe wall (r = 0.05 m) where the velocity goes to zero using a no slip boundary condition. Due to these results, the COMSOL model of a

magnetoplasma spacecraft engine plume will use the smallest mesh size that is computationally feasible to reduce error to its smallest possible value.

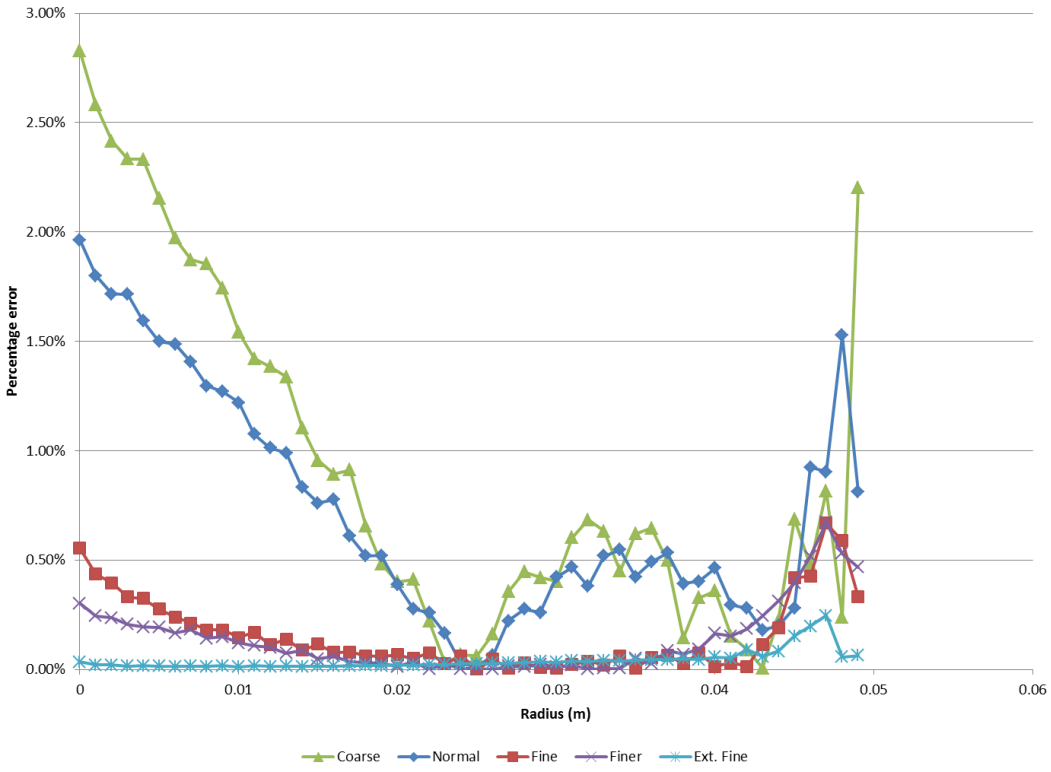

Figure A-3: Percentage error for COMSOL-derived velocity from analytical velocity at z = 2 m (exit) at $\dot{m}$ = 0.1373 kg/s

As the smallest model mesh size is desirable, it is expected that the Mechanical Engineering's computer clusters will be needed to handle the increased computational load. COMSOL Multiphysics® software is being installed on these clusters and will be available soon.

APPENDIX B

HARTMANN FLOW

Flow of an electrically conducting incompressible viscous fluid between two parallel plates is governed by the Hartmann equation, where there is a difference in pressure and a magnetic field.

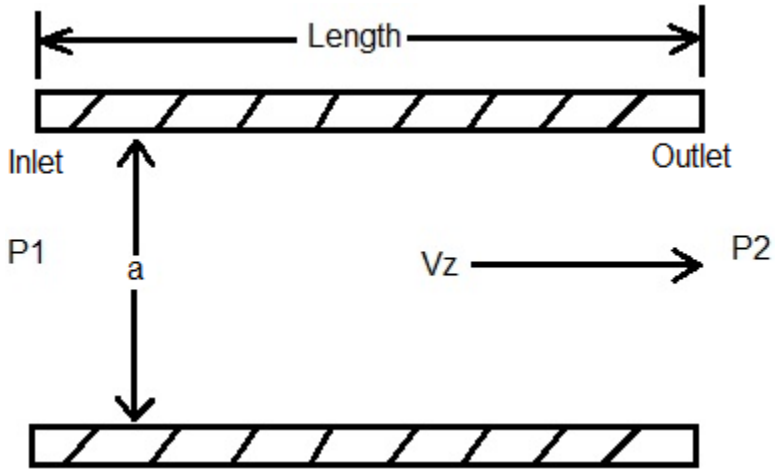

Figure B-1: Diagram of Hartmann flow of mercury between two parallel plates

The Hartmann constant: $\mathcal{H} = (\sigma B_o^2 a^2/\rho\nu)^{1/2}$ [43] (B-1)

The velocity at height = x is defined as:

$$V_z = [(P/\sigma B_0^2) - E/B_0] \cdot \left[1 - \frac{\cosh(\mathcal{H}x/a)}{\cosh \mathcal{H}}\right]$$ [43] (B-2)[42, 43]

where P = Difference in Pressure (Pa) per length of plates

E = Electrical field (V)

a = Height between two plates (m)

B_0 = Magnetic field (T)

In this example where the fluid is mercury, the following values were chosen:

Height = a = 0.2 m

Length = 10 m

ΔP = 101325 Pa – 101324.98 Pa = 0.02 Pa

P = ΔP / Length = 0.02 Pa / 10 m = 0.002 Pa/m

E = 0 V/m

$\mu = \rho * \nu$ = 0.0017 Pa*s Dynamic viscosity of mercury at T = 0° C

σ = 1 x 10^6 S/m Electrical conductivity

The average velocity was calculated using 200,000 nodes between the height of x = 0 m and x = 0.2 m. This average velocity was imputed into the COMSOL model and used as the input velocity. The COMSOL model was then run with the magnetic field, B_0, as 0.1 T, 0.01 T, and 0.001 T. The results were compared to the analytical result to determine how accurate COMSOL is. As you can see in the following graphs, the COMSOL results match the analytical results almost exactly.

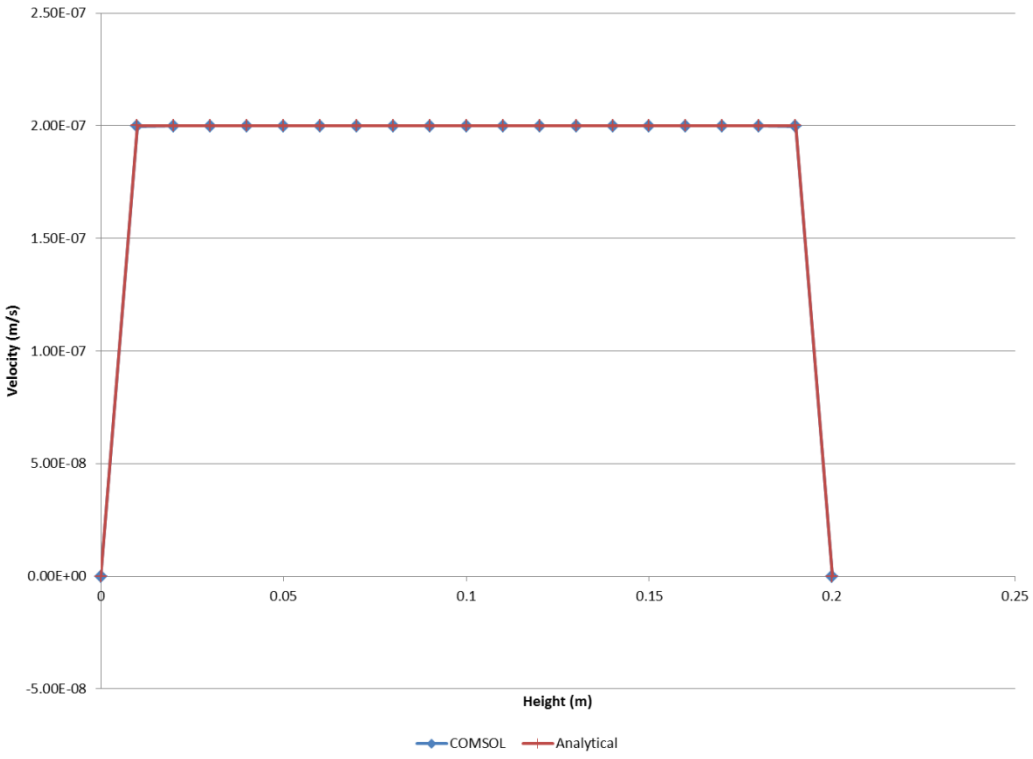

Figure B-2: Hartmann flow for B_0 = 0.1 T at z = 10 m (exit) for COMSOL derived and analytical solutions (with V_{avg} = 1.9918e-7 m/s)

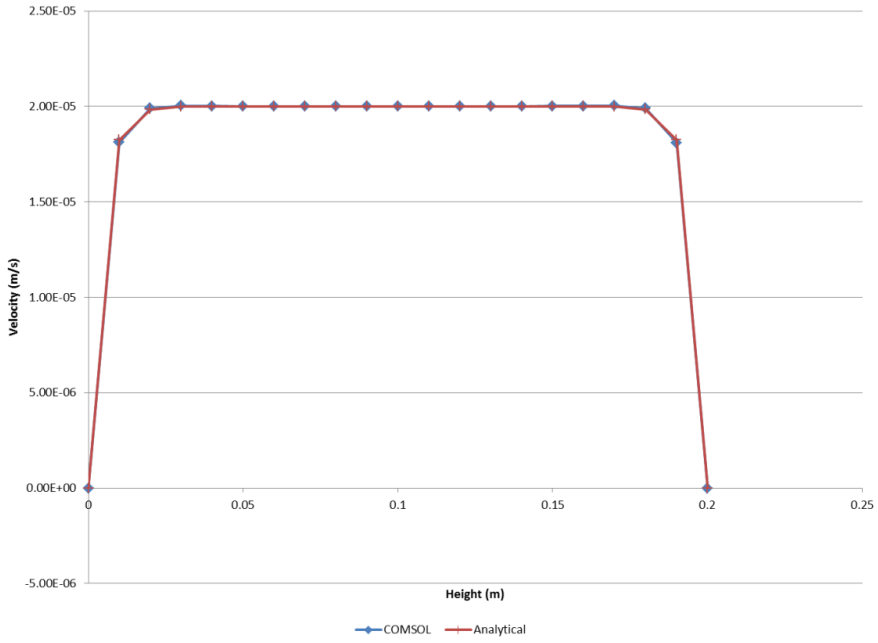

Figure B-3: Hartmann flow for B_0 = 0.01 T at z = 10 m (exit) for COMSOL derived and analytical solutions (with V_{avg} = 1.9178e-5 m/s)

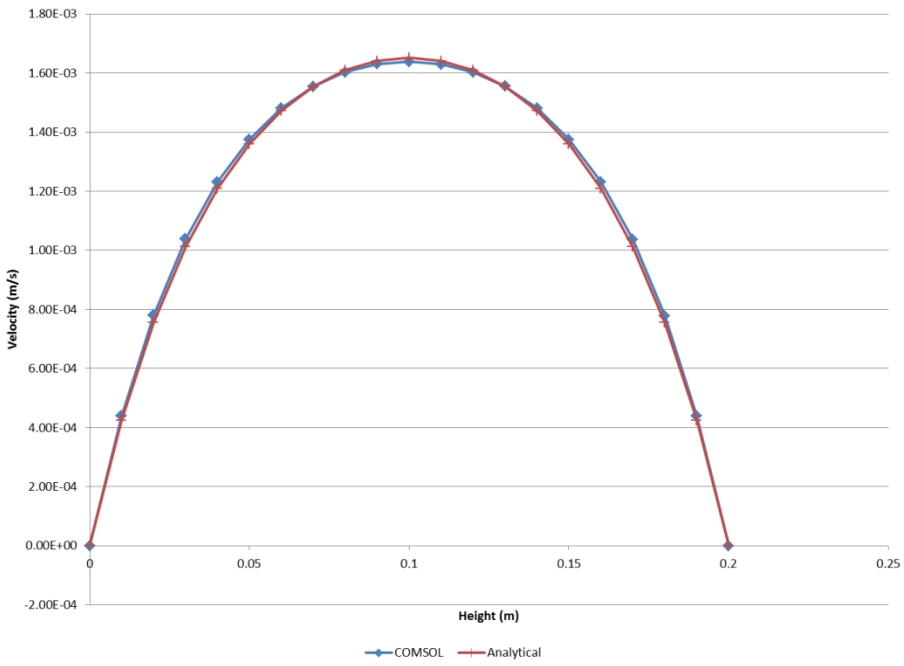

Figure B-4: Hartmann flow for B_0 = 0.001 T at z = 10 m (exit) for COMSOL derived and analytical solutions (with V_{avg} = 1.2e-3 m/s)

These results show that COMSOL Multiphysics® is accurate for modeling fluids in a magnetic field. The error associated with the Hartmann flow model is shown in Figure B-5 for Coarse, Normal, Fine, and Finer mesh sizes. As expected, the coarse mesh size gives the highest error. Normal, fine, and finer mesh sizes have about the same error values. Based on this information, a finer mesh was chosen for this research.

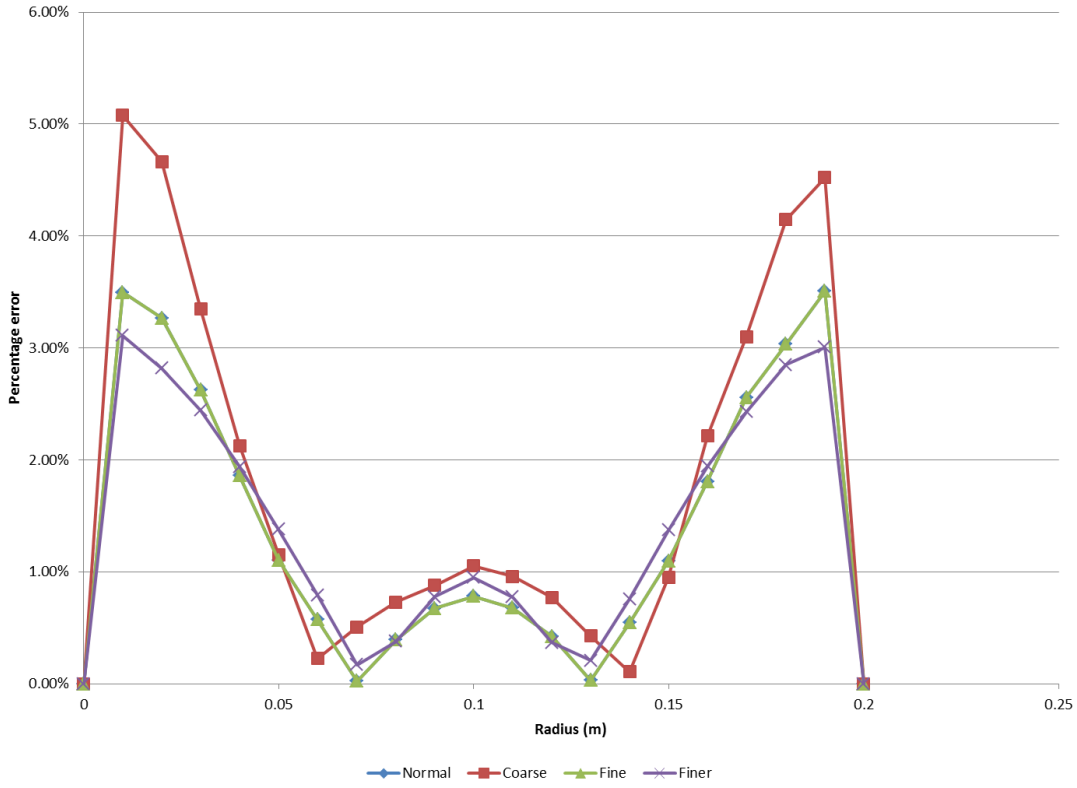

Figure B-5: Percentage error for COMSOL-derived velocity from analytical velocity at z = 10 m (exit) at V_{avg} = 1.2e-3 m/s

APPENDIX C

FUNCTIONAL DECOMPOSITION

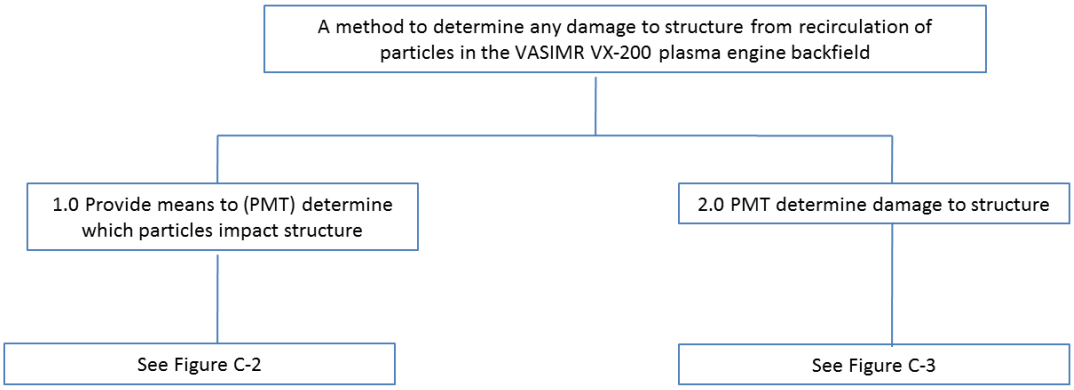

Figure C-1: Top-level functional decomposition of the magnetoplasma spacecraft engine recirculation research topic.

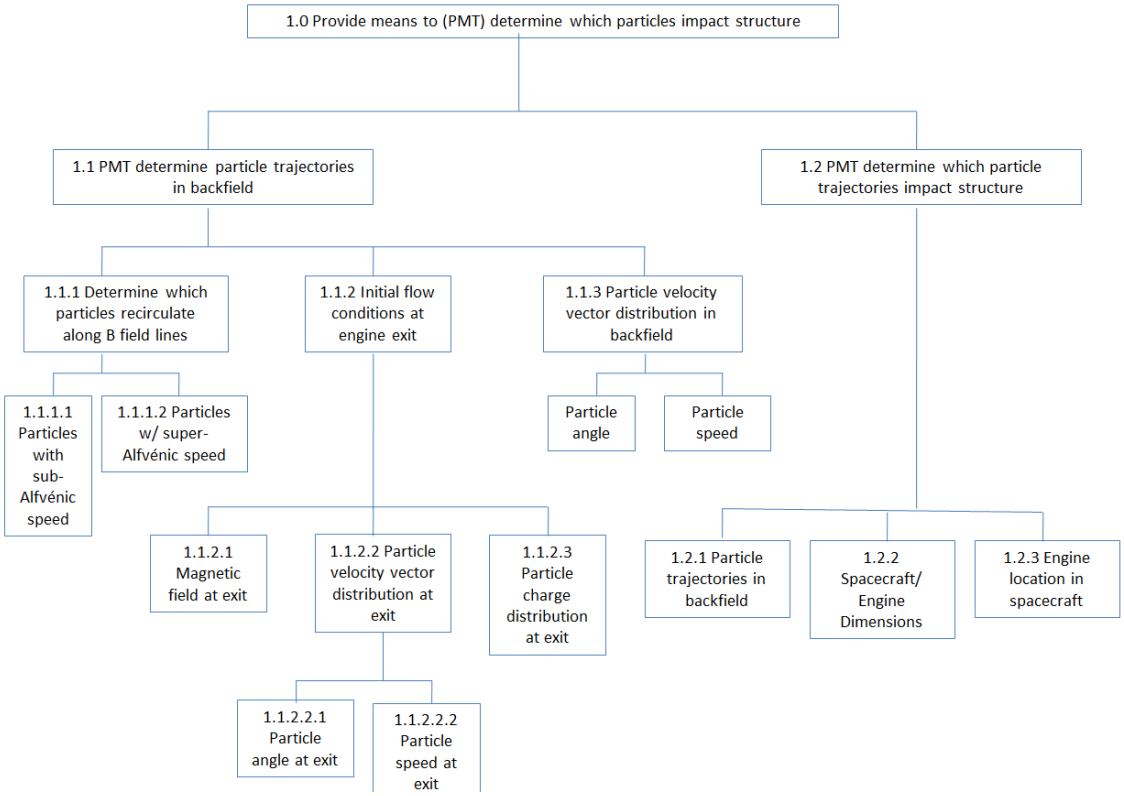

Figure C-2: Mid-level functional decomposition of the magnetoplasma spacecraft engine recirculation research topic

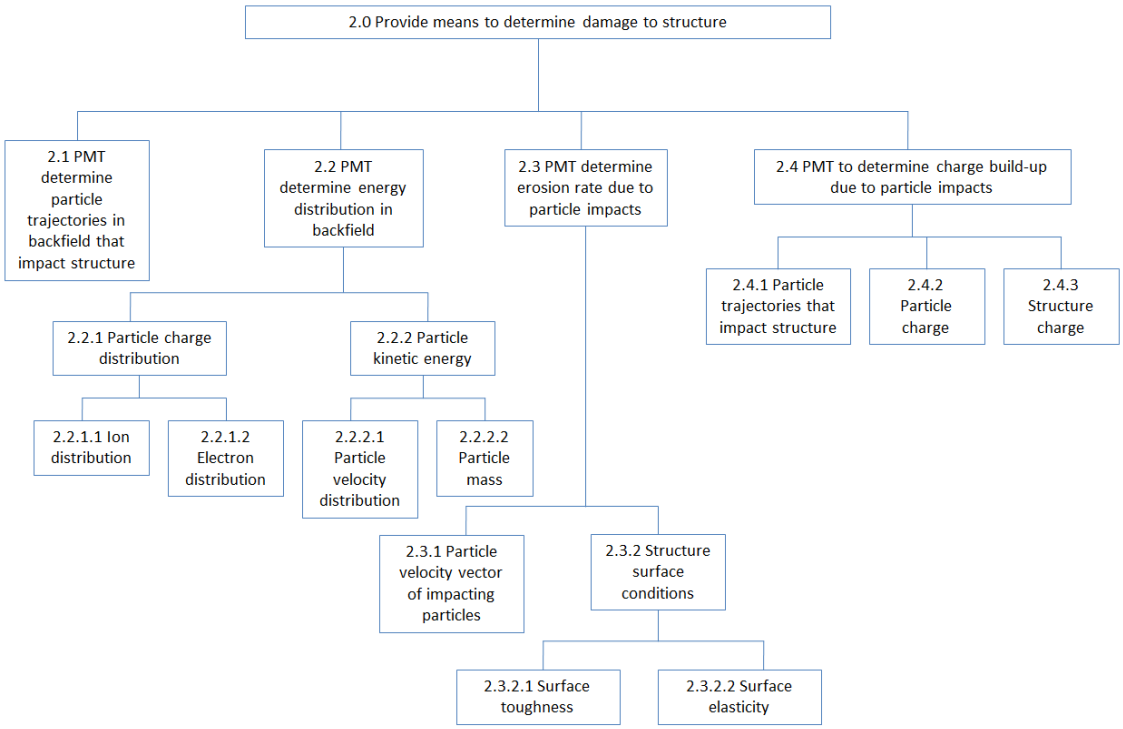

Figure C-3: Mid-level functional decomposition of the magnetoplasma spacecraft engine recirculation research topic.

APPENDIX D

BETA CALCULATIONS FOR PLASMA DOWNSTREAM OF MAGNETOPLASMA SPACECRAFT ENGINE NOZZLE

The Beta (β), a measure of dynamic pressure over magnetic pressure or a measure of plasma velocity over Alfvénic velocity, was calculated based on the flow velocity, temperature, and particle density provided by Figure 5 along the radius, where the data was recorded 1.6 meter downstream of the magnetic nozzle.

$$\beta = \frac{\rho u^2/2}{B^2/(2\mu_0)} = \left(\frac{u}{B/\sqrt{\mu_0 \rho}}\right)^2 = \left(\frac{u}{v_A}\right)^2 \quad (1)$$

where $v_A = \frac{B}{\sqrt{\mu_0 \rho}}$ is the Alfvénic velocity. (2)

Assuming that the plasma particle velocities stay constant as they travel downstream (neglecting the plasma's own electric field or the effect of the magnetic nozzle), then a calculation can be done for various magnetic fields to determine at what point the particles will attain super-Alfvénic velocity and are expected to detach. Figure D-1 shows that as the magnetic field decreases to around 5 Gauss, the plasma particles (taken along the centerline, where flow velocity is high) become super-Alfvénic (red line indicates where β = 1).

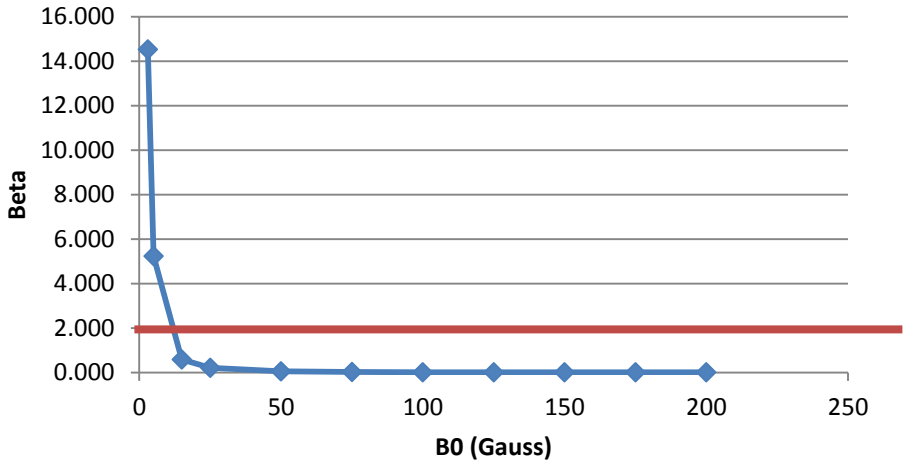

Figure D-1: Beta as a function of various magnetic fields for plasma near centerline (r = 0.2 m)

Figure D-2 shows that for the plasma particles along the plume's edge (r = -0.4 m) the particles are all traveling at a sub-Alfvénic velocity unless the magnetic field drops below 1 Gauss which will happen far from the spacecraft (red line indicates where $\beta = 1$).

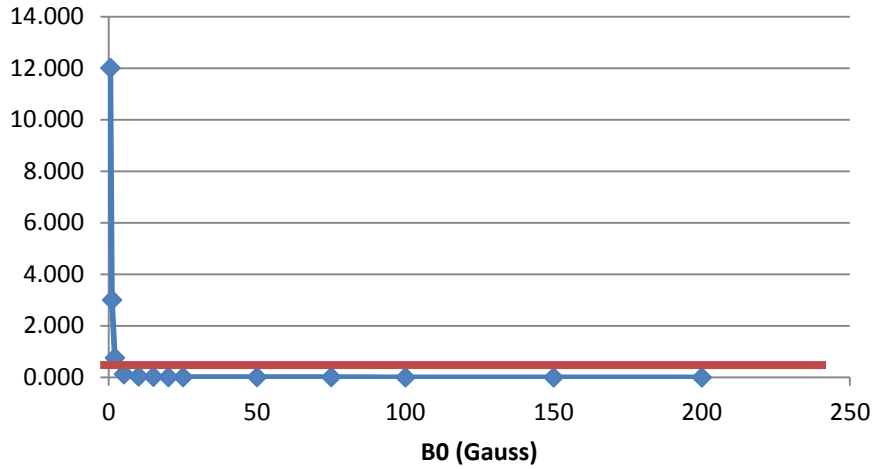

Figure D-2: Beta as a function of various magnetic fields for plasma at the edge of the plume (r =-0.4 m)

APPENDIX E

CORRECTED GRAPHS

According to the Ad Astra Rocket Company, there was an error with the location of the centerline or horizontal axis of which the plume should be axisymmetric. After discussing this with the Dr. Jared Squire, of the Ad Astra Rocket company, the centerline was erroneously placed at r = 0.0 m when it should have been at r = 0.178 m. I have recreated the flow velocity, density, and temperature graphs with the centerline corrected to r = 0.0 m.

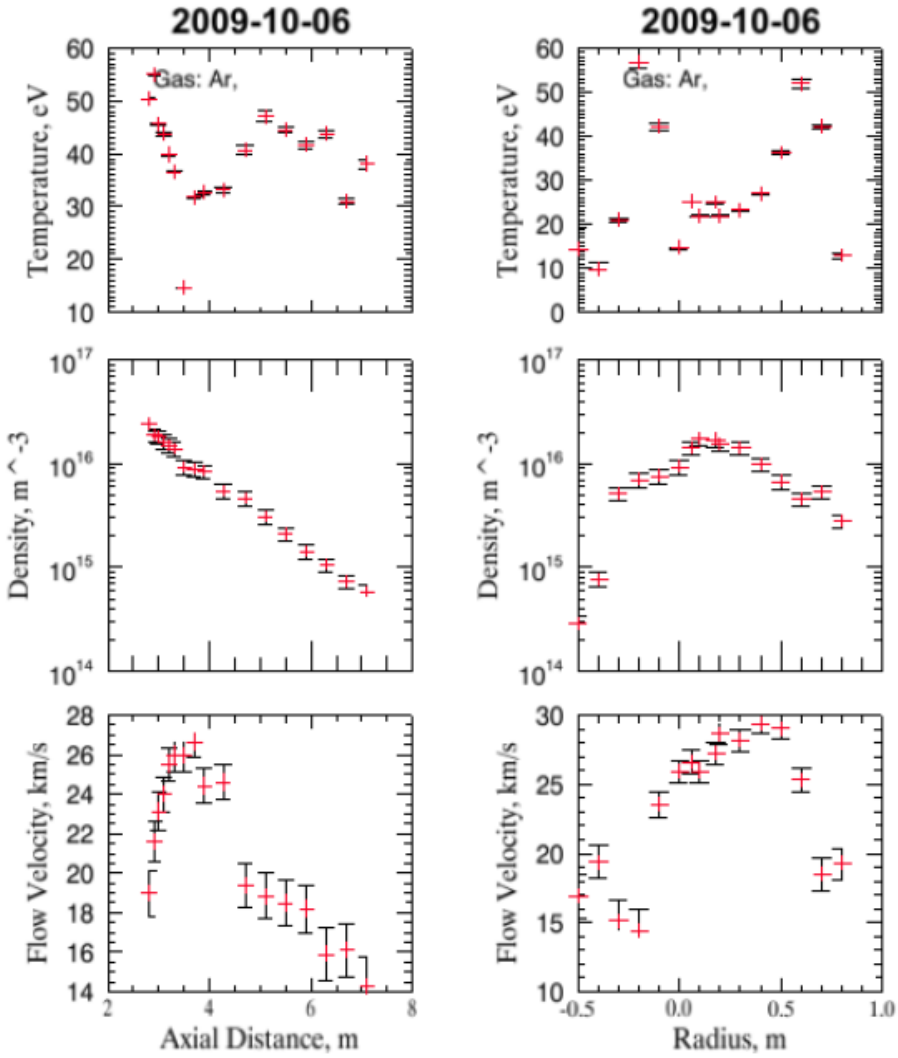
2009-10-06
Gas: Ar,
Temperature, eV
Density, m ^-3
Flow Velocity, km/s
Axial Distance, m
2009-10-06
Gas: Ar,
Temperature, eV
Density, m ^-3
Flow Velocity, km/s
Radius, m

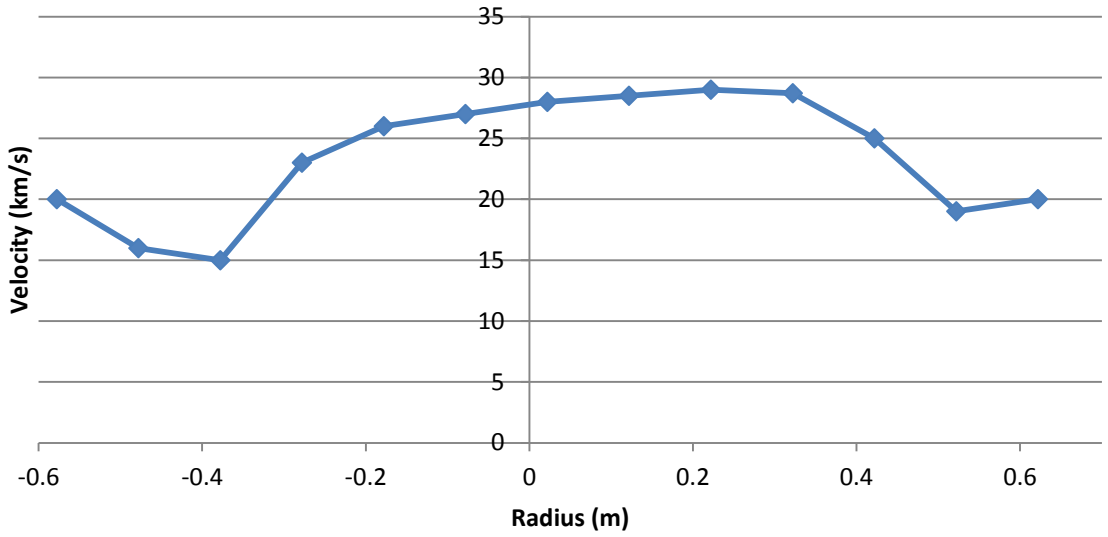

Figure E-1: Corrected flow velocity graph from Figure 5 as a function of radius.

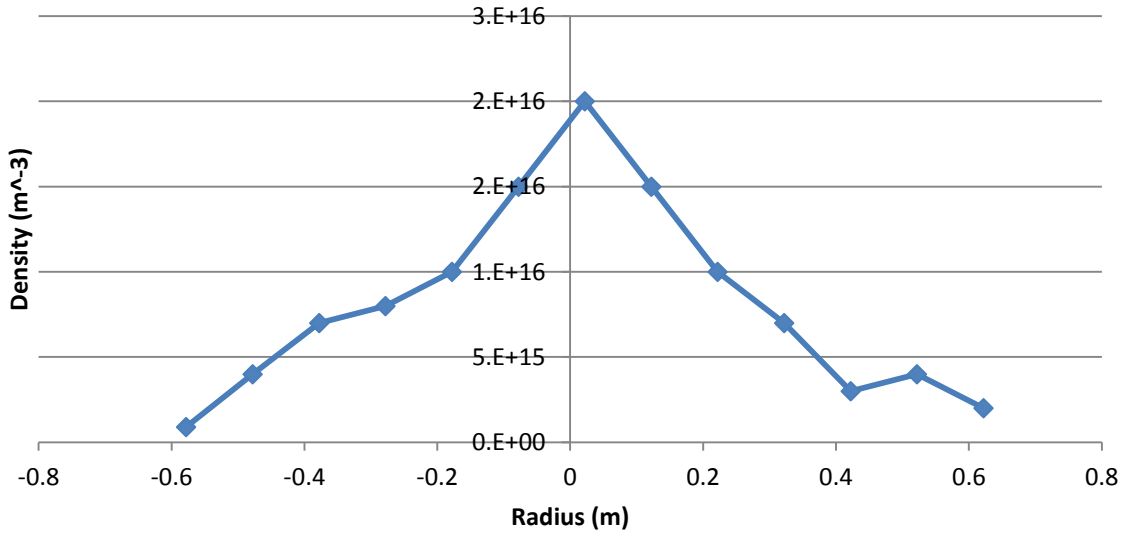

Figure E-2: Corrected density graph from Figure 5 as a function of radius.

As you can see the plasma density is essentially axisymmetric around the centerline, but the flow velocity is still slightly skewed to the right. Dr. Jared Squire believes that the skewing is due to the location of the Retarding Potential Analyzer

(RPA) which is used to measure the flow velocity. He believes that the RPA is in the shadow of the force impact measuring device along the negative radius.

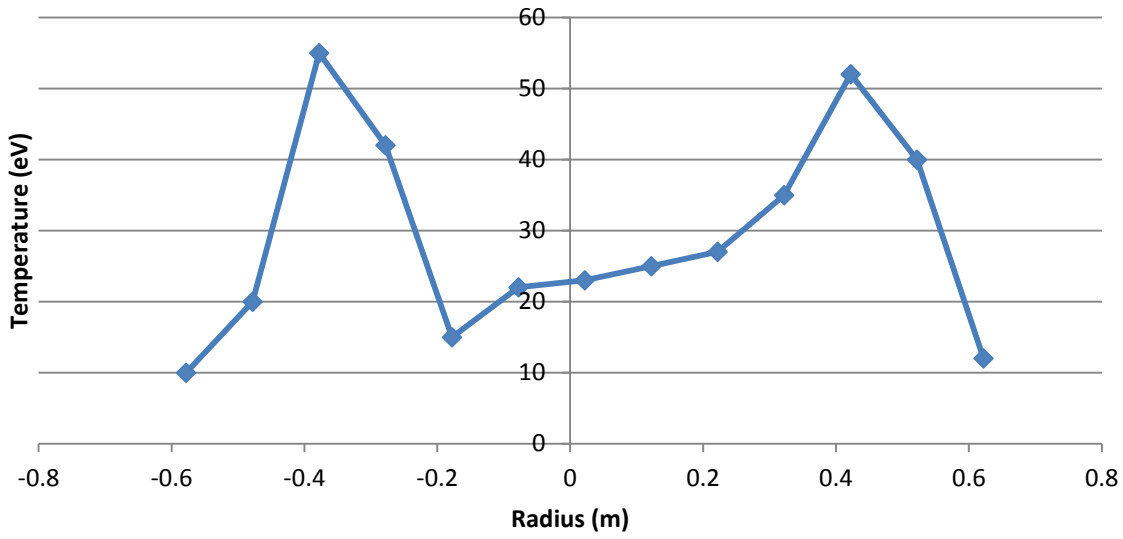

Figure E-3: Corrected temperature graph from Figure 5 as a function of radius

APPENDIX F

MAGNETIC FIELD COMPARISON

The magnetic field simulated in my COMSOL model was compared to the experimental magnetic field data from the VX-200. The following are graphs showing the COMSOL generated magnetic field strength (blue solid line) and the magnetic field strength experimentally measured from the VX-200 (red dashed line) by the Ad Astra Rocket Company.

The average error between the COMSOL model and experimental data was 7.64% for the B_r values and 3.83% for the B_z values from $0 < z < 4$ m. This is very good considering that the variables: number of coil turns, coil width, coil outer diameter, coil inner diameter, electrical current, and coil location were all unknown. It was assumed that all three magnetic coils used were of equal width for simplicity.

The magnetic field in the Z direction (B_z) at r = 0 m, plume centerline:

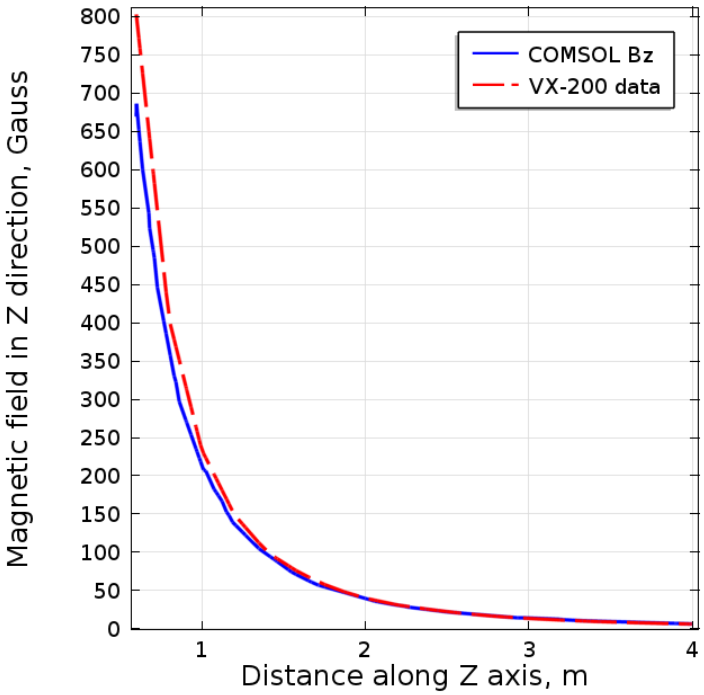

The magnetic field in the Z direction (Bz) at r = 0.1 m:

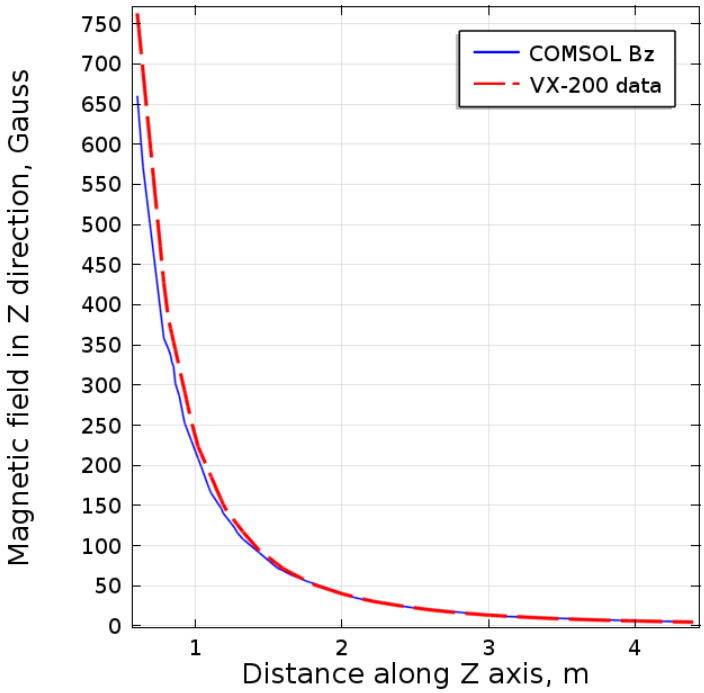

The magnetic field in the R direction (Br) at r = 0.1 m:

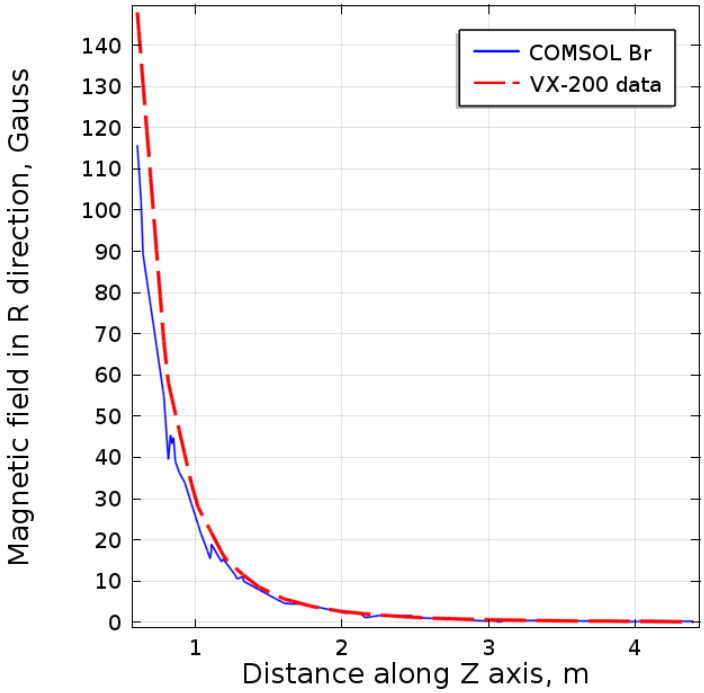

The magnetic field in the Z direction (Bz) at r = 0.2 m:

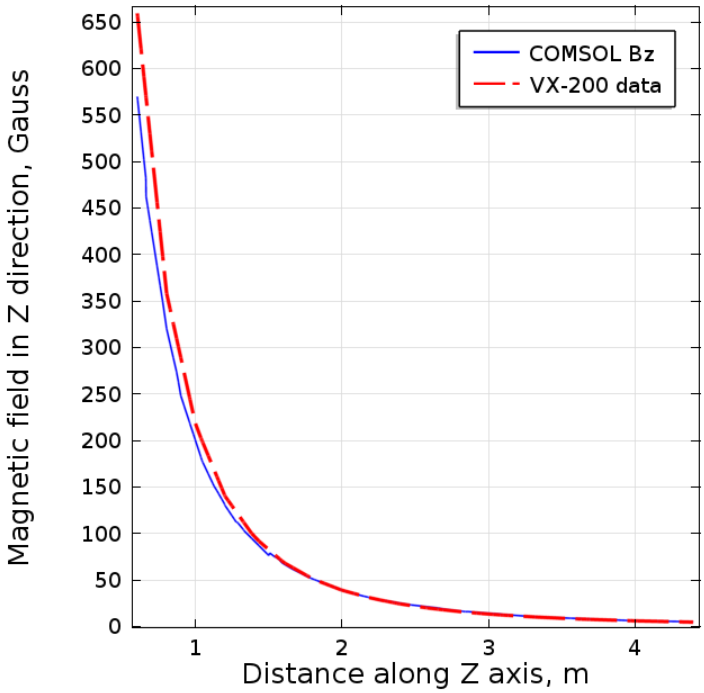

The magnetic field in the R direction (Br) at r = 0.2 m:

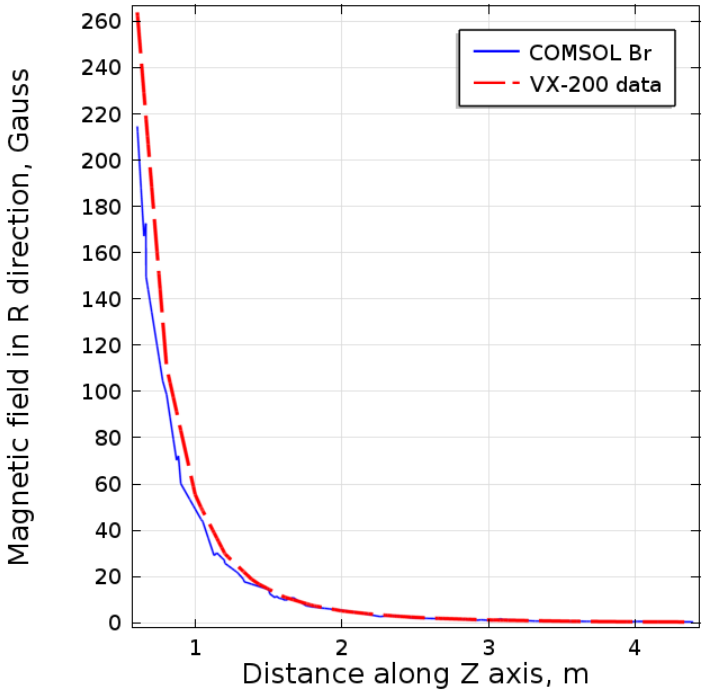

The magnetic field in the Z direction (Bz) at r = 0.3 m:

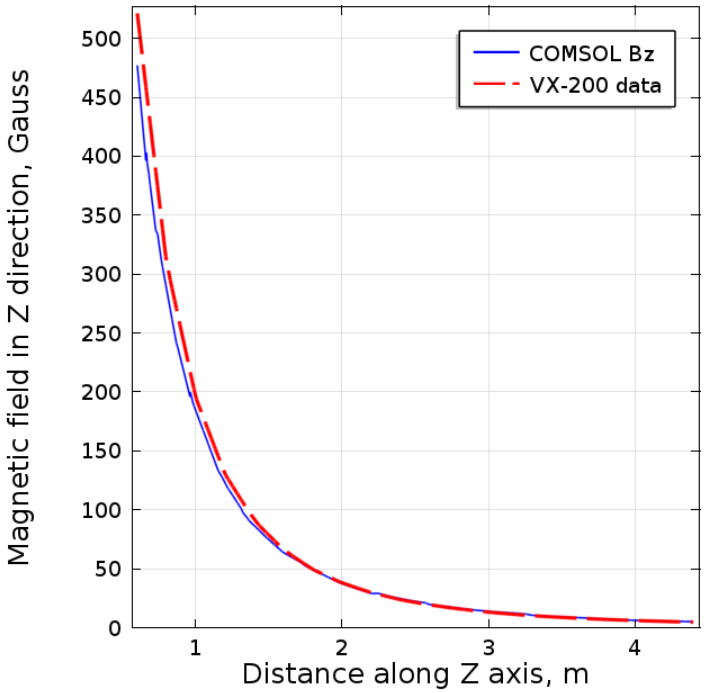

The magnetic field in the R direction (Br) at r = 0.3 m:

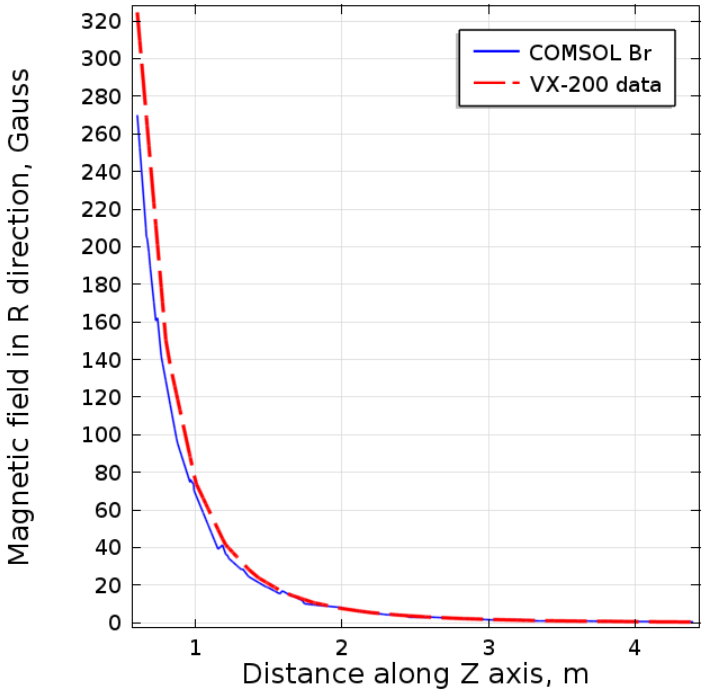

The magnetic field in the Z direction (Bz) at r = 0.4 m:

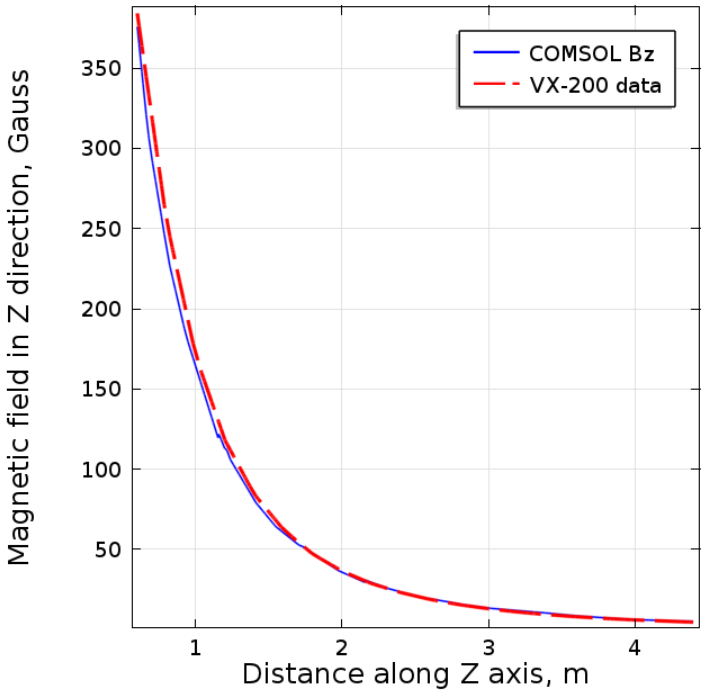

The magnetic field in the R direction (Br) at r = 0.4 m:

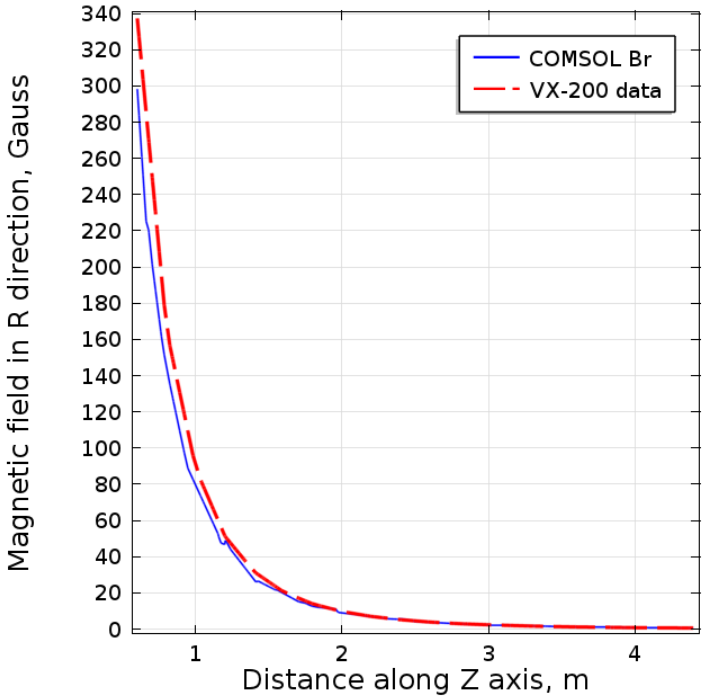

The magnetic field in the Z direction (Bz) at r = 0.5 m:

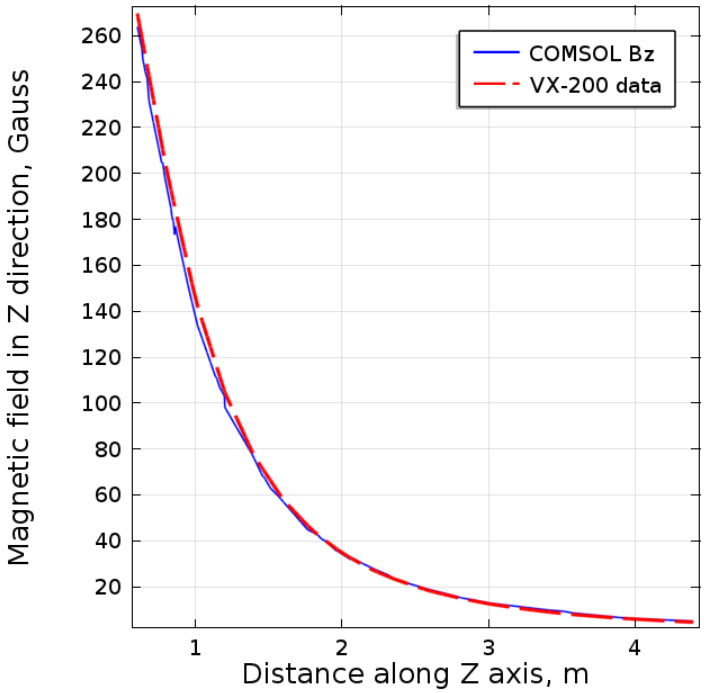

The magnetic field in the R direction (Br) at r = 0.5 m:

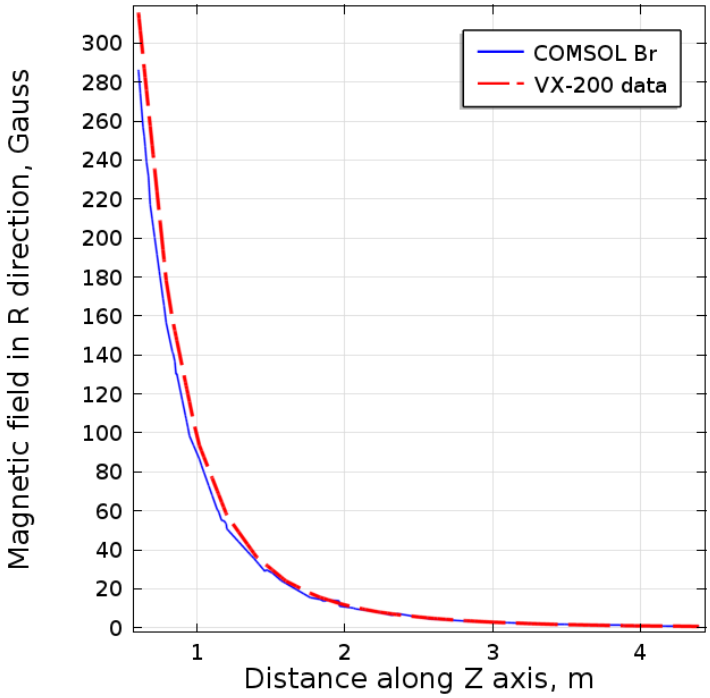

The magnetic field in the Z direction (Bz) at r = 0.6 m:

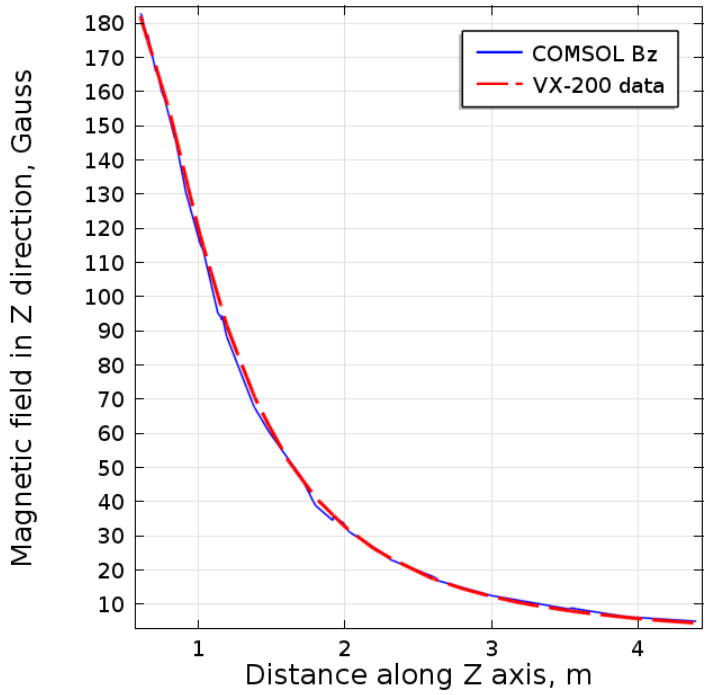

The magnetic field in the R direction (Br) at r = 0.6 m:

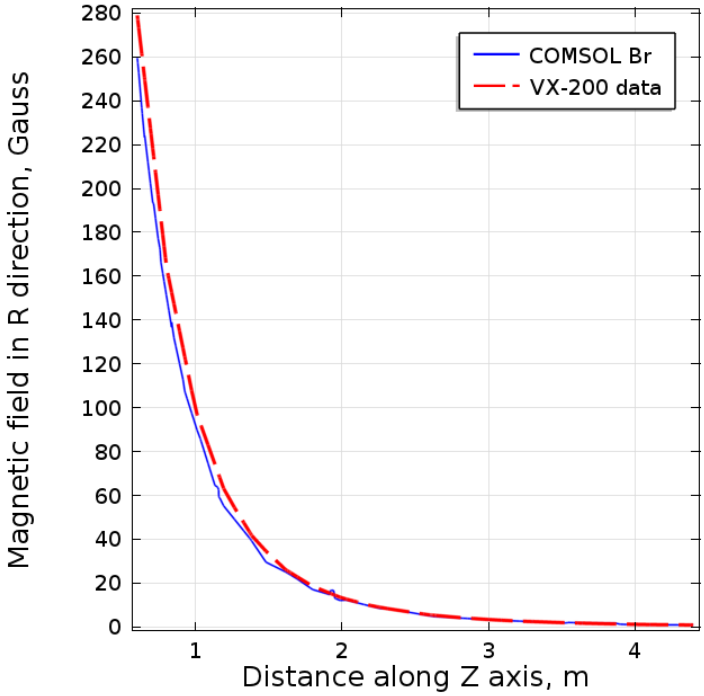

The magnetic field in the Z direction (Bz) at r = 0.7 m:

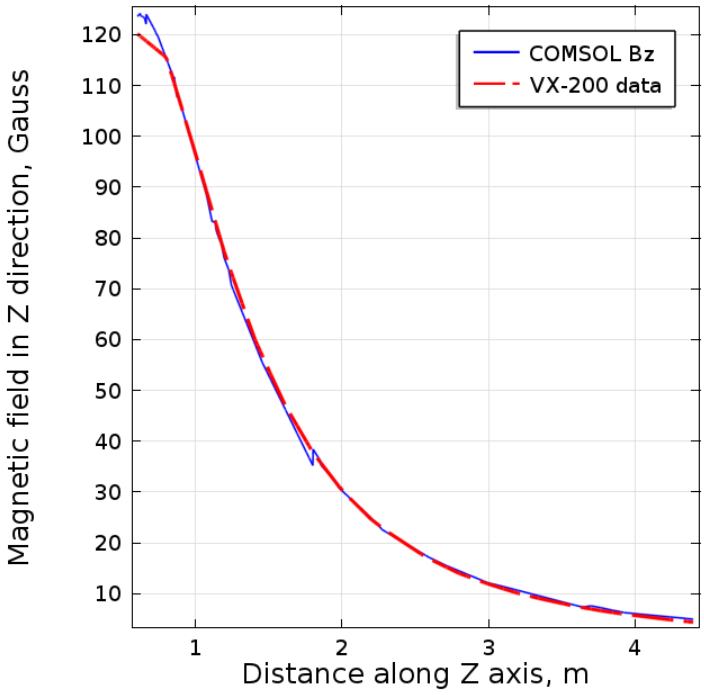

The magnetic field in the R direction (Br) at r = 0.7 m:

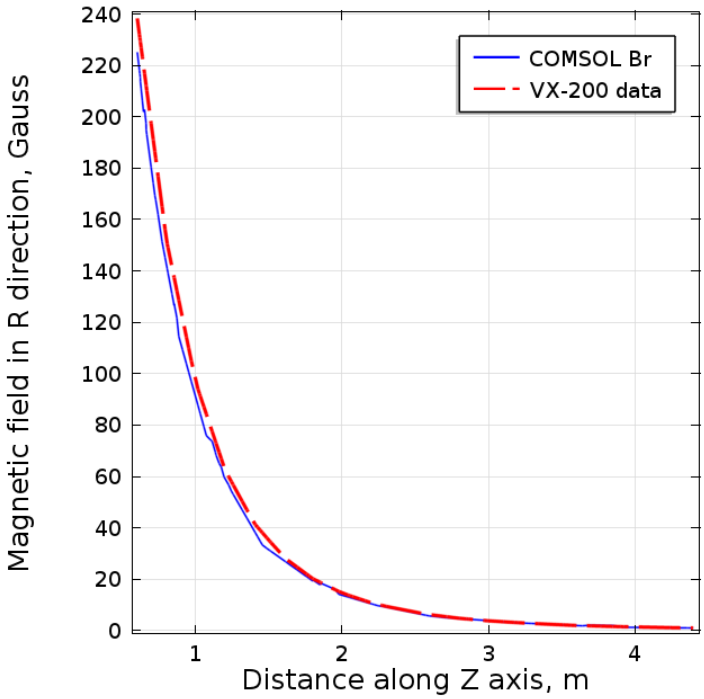

The magnetic field in the Z direction (Bz) at r = 0.8 m:

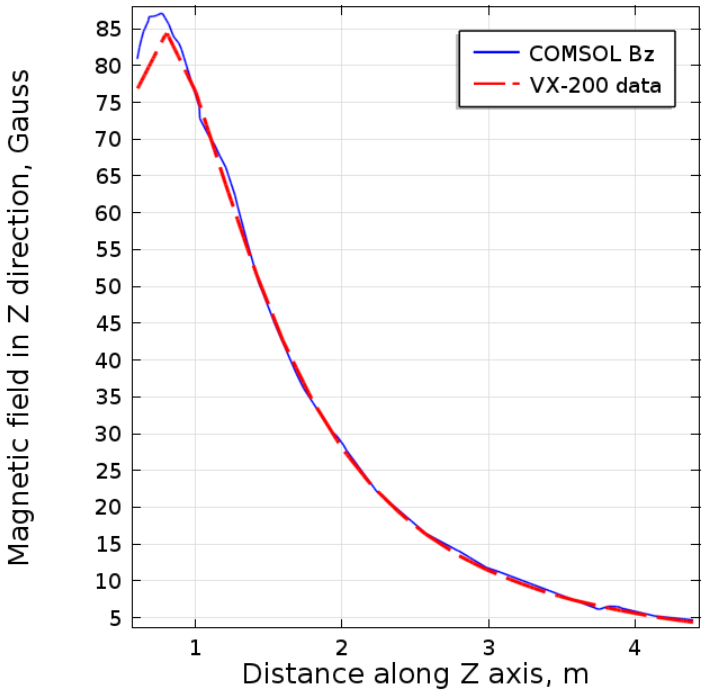

The magnetic field in the R direction (Br) at r = 0.8 m:

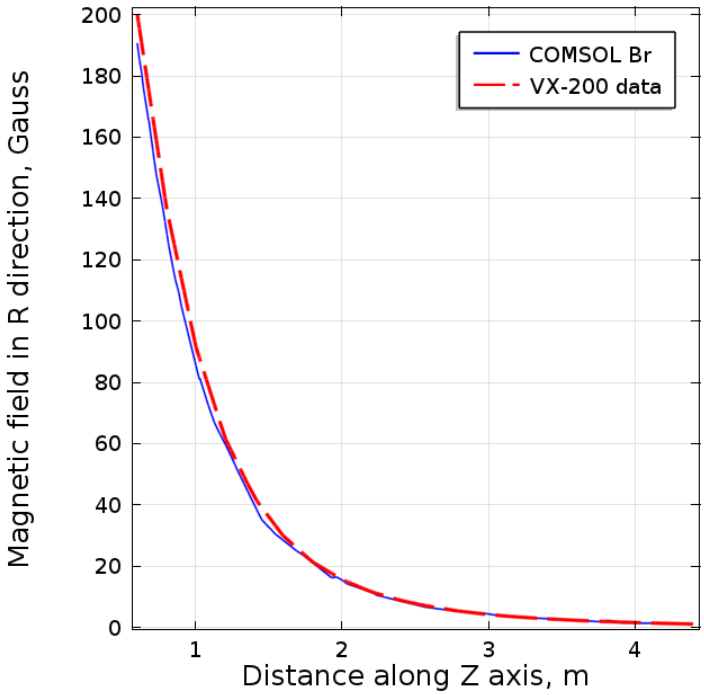

The magnetic field in the Z direction (Bz) at r = 0.9 m:

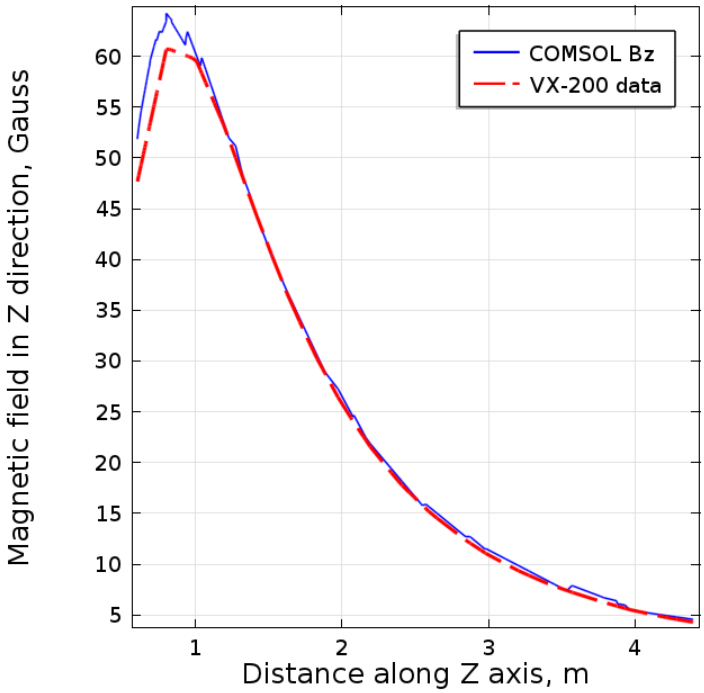

The magnetic field in the R direction (Br) at r = 0.9 m:

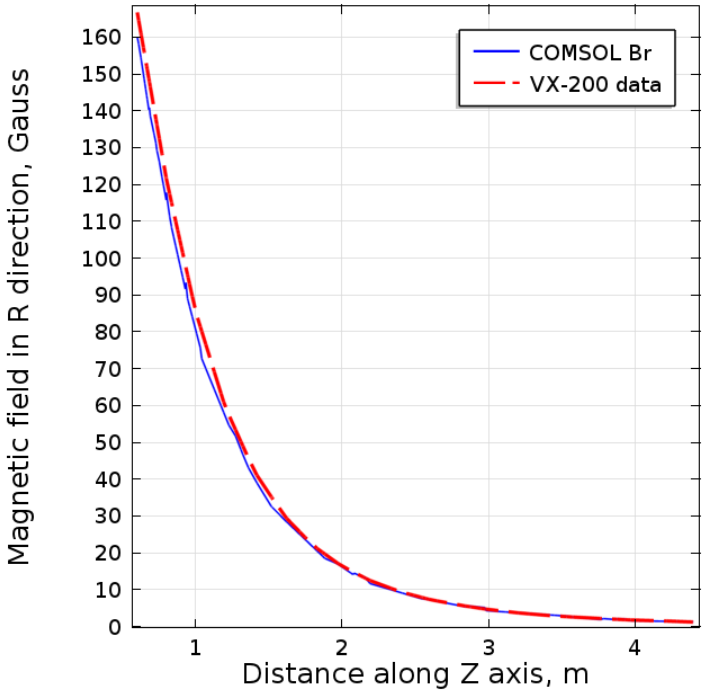

The magnetic field in the Z direction (Bz) at r = 1.0 m:

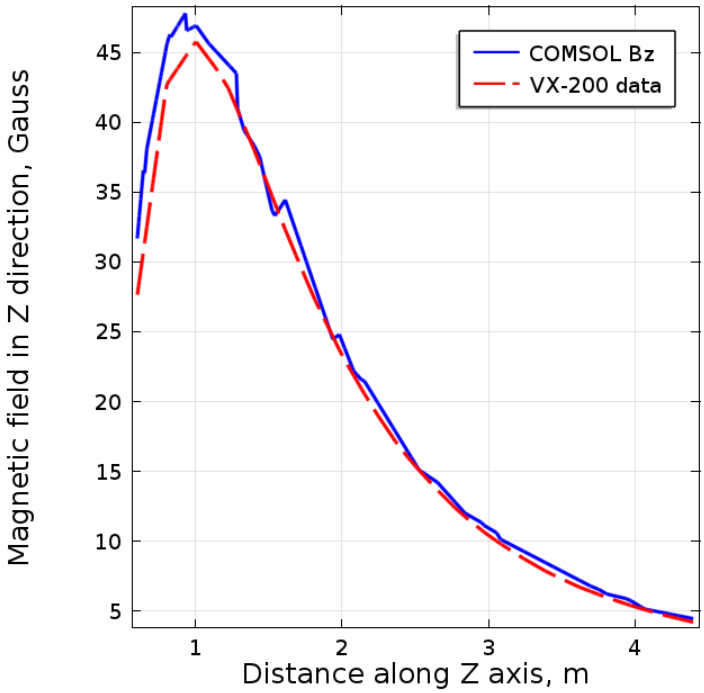

The magnetic field in the R direction (Br) at r = 1.0 m:

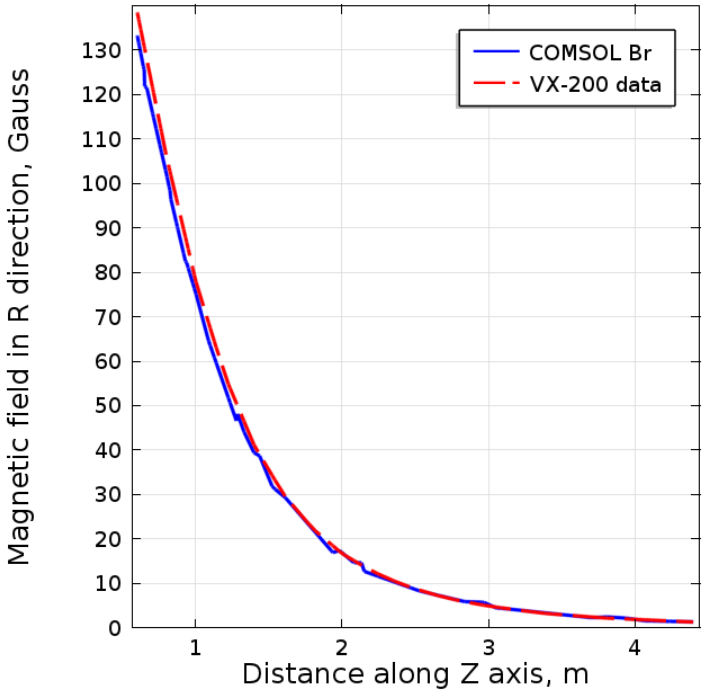

The magnetic field in the R direction (Br) as a function of radius:

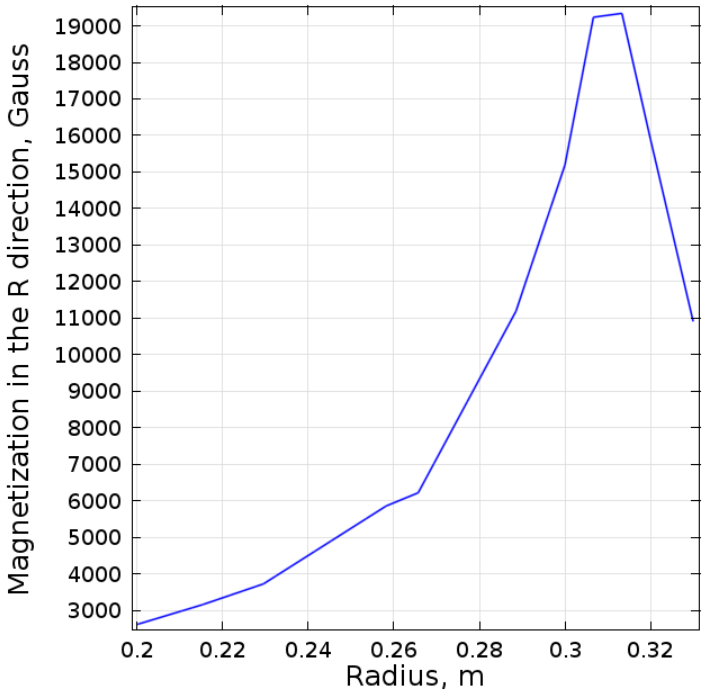

APPENDIX G

VALIDATION OF COMSOL MODEL WITH VX-200 EXPERIMENTAL DATA

1. Why did I choose a particle count of 1 million ions for my model?

One version of the ion model was run with 7 different numbers of particles (1000 to 5 million) to determine the effect that particle count has on the percentage of particles entering the backfield and of those impacting the engine/radiator panels. As can be seen in the table below, the particle count caused a great amount of variability in the percentages until 500,000 ions and greater were used. At higher particle counts, the percentages are virtually unchanged. However, the amount of time to run models became prohibitive the higher particle counts were. Therefore, a particle count of 1 million ions per model was chosen to provide the best results in the shortest amount of time.

Number of ions:	1000	10000	100000	500000	1000000	2000000	5000000
Escaping ions	99.70%	99.17%	99.05%	98.98%	98.99%	98.97%	98.98%
Entering backfield	0.30%	0.83%	0.96%	1.02%	1.01%	1.03%	1.02%
Impacting engine/radiators	0.00%	0.17%	0.18%	0.22%	0.22%	0.22%	0.22%
Time to run (hours):	0.20	0.40	0.50	1.00	1.50	5.50	17.00
Sensitivity:	100.00%	23.80%	17.97%	3.27%	0.00%	1.17%	1.52%

This relationship can be best illustrated in the following graph. The percentage of ions impacting the engine/radiator panels quickly settles around 0.22% when the particle count reaches 500,000 and higher.

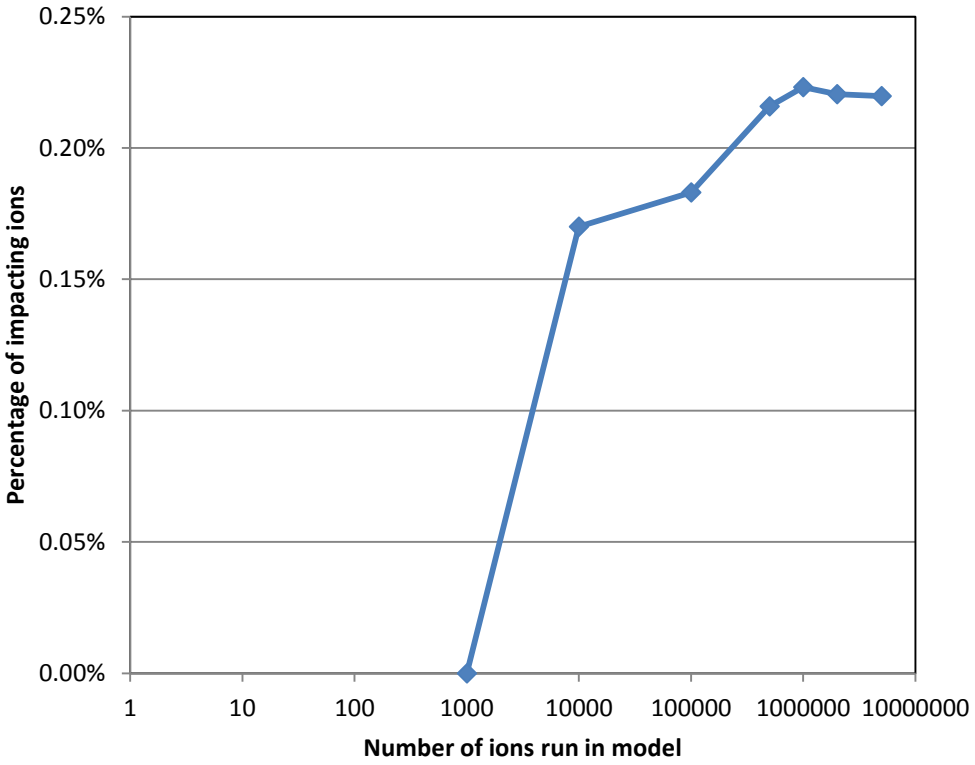

Figure G-1. Percentage of impacting ions as a function of particle count

2. Comparison to VX-200 experimental results: Velocity

The velocity from VX-200 experimental results was compared to the velocity derived from the numerical model and is shown in Figures G-2 and G-3. The difference between the two is very small when normalized.

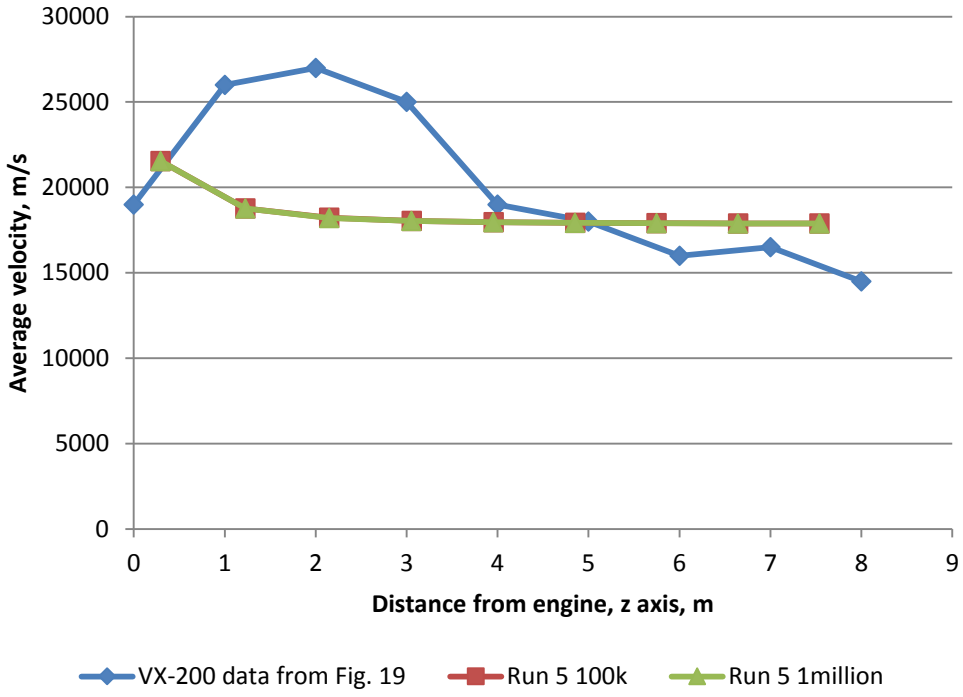

Figure G-2. Average velocity, m/s, as a function of Z distance from engine.

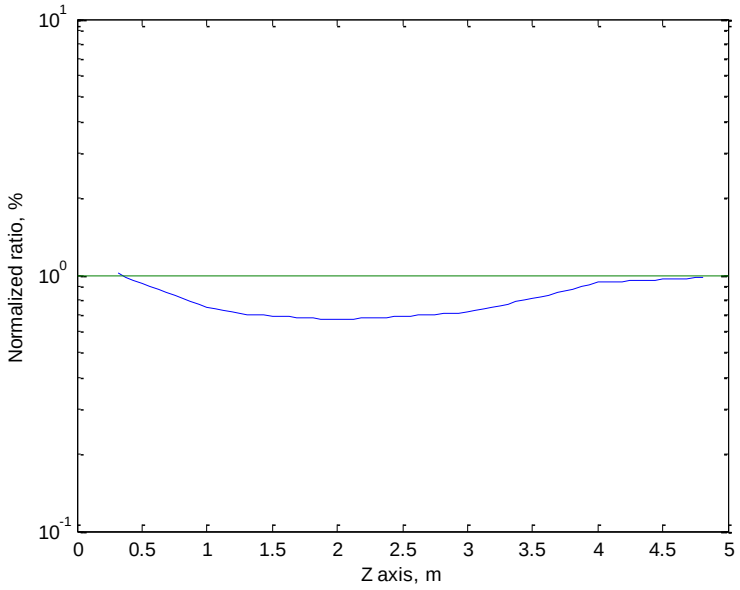

Figure G-3. Log normalization of COMSOL model's average velocity and VX-200 experimental velocity.

3. Comparison to VX-200 experimental results: Density

The density from VX-200 experimental results was compared to the density derived from the numerical model and is shown in Figure G-4. The difference between the two is very small when normalized.

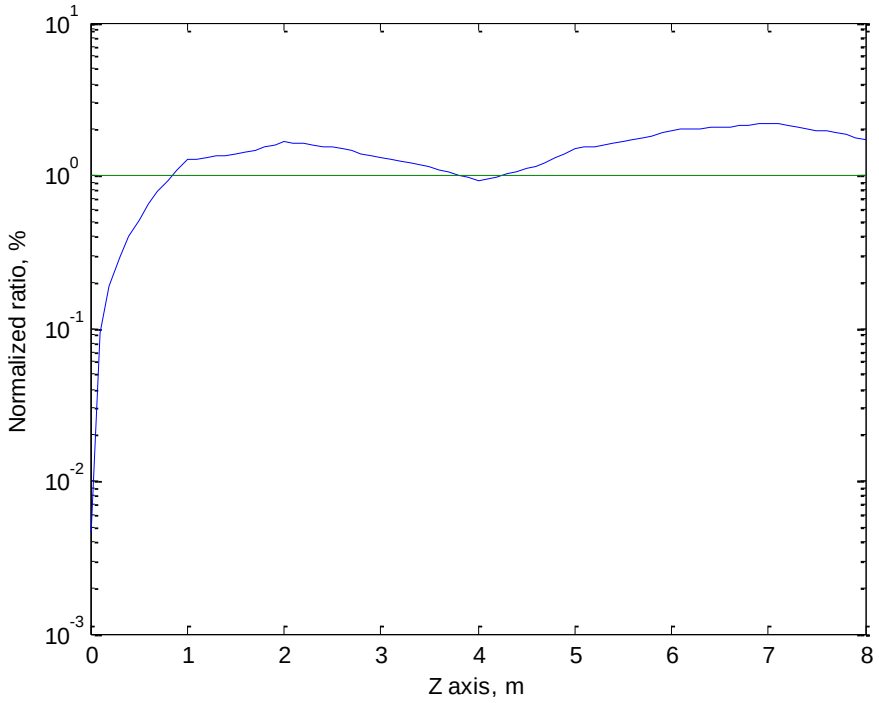

Figure G-4. Log scale of normalization for COMSOL model's density and VX-200 experimental density.

The change in V_r, V_z, and V_{mag} were all compared to verify that although V_r and V_z change in relation to each other over time, V_{mag} remains constant so that energy is conserved. This comparison is shown in Figure G-5.

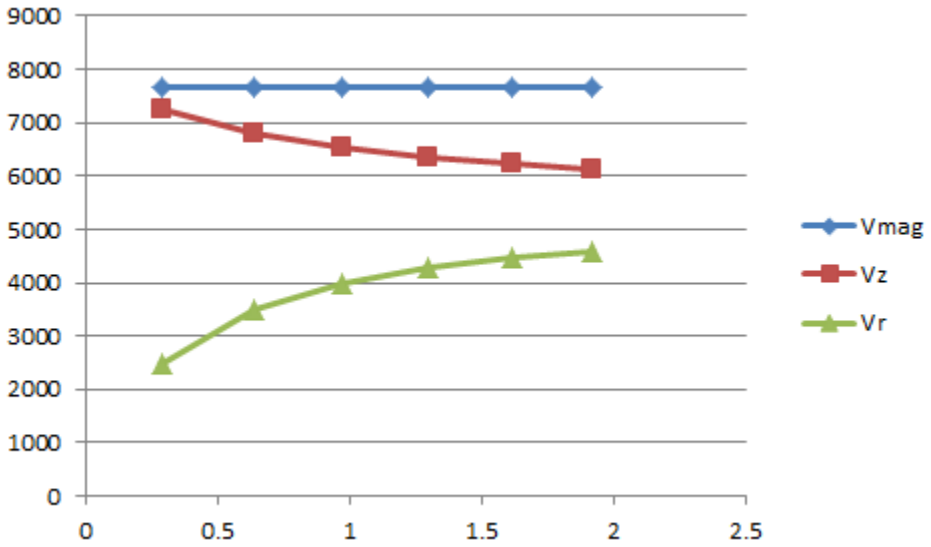

Figure G-5. Comparison of V_r, V_z, and V_{mag} to verify that energy is conserved.

APPENDIX H

KNUDSEN NUMBER

A particle approach was chosen to simulate the VX-200 because the Knudsen number at z = 0.3 m, where the experimental data was taken, is much higher than 1 and, therefore, continuum physics is not applicable.

With Ion Temperature

Helicon Only

Along r=0 m of Plume structure graph from AGU_2011_Gar._r.pdf

Current Density (A/m^2)	Axial distance (m)	Mean free path (m)	Knudsen Number	Δx
3.8	2.8	2.64E+02		
3.4	3	2.64E+02	155.4118	0.2
3	3.2	2.64E+02	176.1333	0.2
2.8	3.4	2.64E+02	94.35714	0.2
2.5	3.6	2.64E+02	158.52	0.2
2.3	3.8	2.64E+02	114.8696	0.2
2	4	2.64E+02	198.15	0.2
1.8	4.2	2.64E+02	146.7778	0.2
1.6	4.4	2.64E+02	165.125	0.2
1.5	4.6	2.64E+02	88.06667	0.2
1.4	4.8	2.64E+02	94.35714	0.2
1.3	5	2.64E+02	101.6154	0.2

	Average		135.7622
	Mean		146.7778

For ICH full power

Current Density (A/m^2)	Axial distance (m)	Mean free path (m)	Knudsen Number	Δx
3.8	2.8	2.64E+02		
3.6	3	2.64E+02	73.38889	
3.2	3.2	2.64E+02	165.125	0.2
3	3.4	2.64E+02	88.06667	0.2
2.7	3.6	2.64E+02	146.7778	0.2
2.5	3.8	2.64E+02	105.68	0.2
2.3	4	2.64E+02	114.8696	0.2
2.2	4.2	2.64E+02	60.04545	0.2
2	4.4	2.64E+02	132.1	0.2
1.8	4.6	2.64E+02	146.7778	0.2
1.6	4.8	2.64E+02	165.125	0.2
1.5	5	2.64E+02	88.06667	0.2
	Average		116.9112	
	Mean		114.8696	

With Electron Temperature

Helicon Only

Along r=0 m of Plume structure graph from AGU_2011_Gar_r.pdf

Current Density (A/m^2)	Axial distance (m)	Mean free path (m)	Knudsen Number	Δx
3.8	2.8	7.399		
3.4	3	7.399	4.352353	0.2
3	3.2	7.399	4.932667	0.2
2.8	3.4	7.399	2.6425	0.2
2.5	3.6	7.399	4.4394	0.2
2.3	3.8	7.399	3.216957	0.2
2	4	7.399	5.54925	0.2
1.8	4.2	7.399	4.110556	0.2
1.6	4.4	7.399	4.624375	0.2
1.5	4.6	7.399	2.466333	0.2
1.4	4.8	7.399	2.6425	0.2
1.3	5	7.399	2.845769	0.2
	Average		3.80206	
	Mean		4.110556	

For ICH full power

Current Density (A/m^2)	Axial distance (m)	Mean free path (m)	Knudsen Number	Δx
3.8	2.8	7.399		
3.6	3	7.399	2.055278	0.2
3.2	3.2	7.399	4.624375	0.2
3	3.4	7.399	2.466333	0.2
2.7	3.6	7.399	4.110556	0.2
2.5	3.8	7.399	2.9596	0.2
2.3	4	7.399	3.216957	0.2
2.2	4.2	7.399	1.681591	0.2
2	4.4	7.399	3.6995	0.2
1.8	4.6	7.399	4.110556	0.2
1.6	4.8	7.399	4.624375	0.2
1.5	5	7.399	2.466333	0.2
	Average		3.274132	
	Mean		3.216957	

APPENDIX I

IMPACT ANGLE CALCULATION

The effect of impact angle on sputter yield was determined by using equation 6 from Behrisch et al.[30]:

$$\frac{Y(E_0,\theta_0)}{Y(E_0,0)} = \left\{cos\left[\left(\frac{\theta_0}{\theta_0^*}\frac{\pi}{2}\right)^c\right]\right\}^{-f} exp\left(b\left\{1-1/cos\left[\left(\frac{\theta_0}{\theta_0^*}\frac{\pi}{2}\right)^c\right]\right\}\right)$$

The fitting values are from Table 15 (Behrisch) for argon impacts on aluminum surfaces.

E_0(eV)	f	b	c	$Y(E_0, 0)$	θ_0*	θ_0m
100	14.76	8.547	0.6703	1.17E-01	90	53.34
500	6.7055	3.4612	0.8024	9.10E-01	90	59.33

So if E_0, θ_0 = 100 eV, 23.91° (the average impact angle in my model), then

$$\frac{Y(100\ eV, 23.91°)}{Y(E_0,0)} = 1.00029\ \approx 1$$

$$\frac{Y(500\ eV, 23.91°)}{Y(E_0,0)} = 1.00012\ \approx 1$$

Therefore, because the ratios of sputter yield at angle and sputter yield at 90° are unity, there is no need to take impact angle into consideration when calculating erosion rates.

APPENDIX J

DATA ANALYSIS

Table J-1. Results sorted by percentage of ions impacting (high to low).

Run	A	B	C	Enter backfield	Impact	Impact <KE> eV	<Erosion> nm/month AL6061	<Erosion> nm/month Silicon
7	-1	1	-1	0.58%	0.0172%	26.99	1.129	0.471
5	-1	1	1	0.21%	0.0119%	31.22	1.386	0.611
1	-1	-1	-1	0.22%	0.0059%	18.78	0.050	0.000
3	1	1	-1	0.24%	0.0043%	41.76	0.853	0.357
6	-1	-1	1	0.09%	0.0037%	19.49	0.037	0.000
4	1	1	1	0.10%	0.0035%	41.78	0.700	0.294
2	1	-1	-1	0.07%	0.0002%	38.96	0.023	0.006
8	1	-1	1	0.04%	0.0001%	38.89	0.011	0.003

Table J-2. Results sorted by average kinetic energy of impacting ions (high to low).

Run	A	B	C	Enter backfield	Impact	Impact <KE> eV	<Erosion> nm/month AL6061	<Erosion> nm/month Silicon	AxB	BxC	AxC
4	1	1	1	0.10%	0.0035%	41.78	0.700	0.294	1	1	1
3	1	1	-1	0.24%	0.0043%	41.76	0.853	0.357	1	-1	-1
2	1	-1	-1	0.07%	0.0002%	38.96	0.023	0.006	-1	1	-1
8	1	-1	1	0.04%	0.0001%	38.89	0.011	0.003	-1	-1	1
5	-1	1	1	0.21%	0.0119%	31.22	1.386	0.611	-1	1	-1
7	-1	1	-1	0.58%	0.0172%	26.99	1.129	0.471	-1	-1	1
6	-1	-1	1	0.09%	0.0037%	19.49	0.037	0.000	1	-1	-1
1	-1	-1	-1	0.22%	0.0059%	18.78	0.050	0.000	1	1	1

Table J-3. Results sorted by erosion rate on an AL plate due to ions impacting (high to low).

Run	A	B	C	Enter backfield	Impact	Impact <KE> eV	<Erosion> nm/month AL6061	<Erosion> nm/month Silicon	AxB	BxC	AxC
5	-1	1	1	0.21%	0.0119%	31.22	1.386	0.611	-1	1	-1
7	-1	1	-1	0.58%	0.0172%	26.99	1.129	0.471	-1	-1	1
3	1	1	-1	0.24%	0.0043%	41.76	0.853	0.357	1	-1	-1
4	1	1	1	0.10%	0.0035%	41.78	0.700	0.294	1	1	1
1	-1	-1	-1	0.22%	0.0059%	18.78	0.050	0.000	1	1	1
6	-1	-1	1	0.09%	0.0037%	19.49	0.037	0.000	1	-1	-1
2	1	-1	-1	0.07%	0.0002%	38.96	0.023	0.006	-1	1	-1
8	1	-1	1	0.04%	0.0001%	38.89	0.011	0.003	-1	-1	1

APPENDIX K

MATLAB CODE USED

1. Postprocessing.m

This MATLAB program reads in the individual ion properties (location and kinetic energy), excludes non-impacting ions, finds the average kinetic energy of all impacting ions in this run, and then calculates an estimated erosion rate for aluminum and silicon using equations derived from the graphs presented in Section 2.8.2.

```
clear
clc
close all

% Read in the data
a = csvread('Run 5 Staack EP.csv',9,0);
KE = a(:,9);
x =  a(:,13);
y =  a(:,14);
z =  a(:,15);

%Initialize variables
counter = 0;
icounter = 0;
total = size(z,1);
ke_sum = 0;
kcount = 1;
mass_flow_rate = 2.2612e21;
Kb = 1.38e-23; % J/K
q = -1.602e-19; % C
Me = 9.109e-31; % kg
Mi = 6.633e-26; % kg
Na = 6.022141e23;       % particles/mol
AL_density = 2700;      % kg/m^3
SI_density = 2330;      % kg/m^3
AL_Molar = 0.0269815/Na;% kg/particles
SI_Molar = 0.06008/Na;  % kg/particles
Area = 23.9; % m^3
Impact_KE = 0;
SI_Yield = 32.84; % sputter energy threshold
AL_Yield = 21.5;  % sputter energy threshold
```

```
AL_atom_to_meters = AL_Molar/(AL_density*Area); %
converts # of atoms to meters eroded
SI_atom_to_meters = SI_Molar/(SI_density*Area); %
converts # of atoms to meters eroded
Time = 60*60*24*30; % converts seconds to months
Scale_up = mass_flow_rate/total; % scales simulated
ions to total mass flow rate

% Determine what the radius is from x and y
for g=1:total
    if x(g)>=0 && y(g)>=0
        rc(g) = sqrt(x(g)^2+y(g)^2);
    else
        rc(g) = -1*sqrt(x(g)^2+y(g)^2);
    end
end

r = rc(:);

% Binning
for i=1:total
    if z(i)<=1e-5
        counter = counter+1;
        if abs(rc(i))<=5
            icounter = icounter + 1;
            Impact_KE(icounter) = KE(i)/1.602176E-19;
        else
            icounter = icounter;
        end
    else
        counter = counter;
    end
end

for j=1:icounter
    Ve(j) = sqrt(2*(Impact_KE(icounter)/6.24e18)/Me);
    Te(j) = 1/3*(Me*(Ve(j).^2)/Kb);
    VBohm = sqrt(Kb*Te(j)/Mi);
    Potential(j)=-
Mi/q*((2*Impact_KE(icounter)/(6.24e18*Mi))-VBohm^2);
    Ji(j)=(icounter/25.4)*VBohm;
end

backfield = (counter/size(z,1))*100
```

```
impact = (icounter/size(z,1))*100

for k=1:size(Impact_KE',1)
    if Impact_KE(k)<=21.5497
        YieldAL2(k)=0;
    else
        YieldAL2(k)= 2.7E-7*(Impact_KE(k)^3)-1.57E-
5*(Impact_KE(k)^2)+0.00035*Impact_KE(k)-0.003;
    end
end

for k=1:size(Impact_KE',1)
    if Impact_KE(k)<=32.838
        YieldSI2(k)=0;
    else
        YieldSI2(k)= -6.44e-9*(Impact_KE(k)^4)+1.03e-
6*(Impact_KE(k)^3)-5.5e-
5*Impact_KE(k)^2+0.00121*Impact_KE(k)-0.00945;
    end
end

Total_AL_Erosion = sum(YieldAL2); % in # of AL atoms
eroded
Total_SI_Erosion = sum(YieldSI2); % in # of SI atoms
eroded

Total_erosionAL = 1e9 * Time * Total_AL_Erosion *
Scale_up * AL_atom_to_meters % nm/mo
Total_erosionSI = 1e9 * Time * Total_SI_Erosion *
Scale_up * SI_atom_to_meters % nm/mo

mean(YieldAL2)
```

2. Multiple_Bursts_Beta.m

This MATLAB program reads in the kinetic energy and location of all simulated ions in a run (here, Run 5) as well as the magnetic field strength at the location for 9 sequential time steps to transform from a Euler space to a Lagrangian space, as discussed in Section 5.5.3 Individual Run Results and Figure 51. This program then adds the ions into one large array for KE, B, X, Y, and Z. This array is sorted so that only a thin slice (-0.05 m < x < 0.05 m, y, z) remains to reduce CPU time. With this slice, the Velocity, Alfvénic Velocity, and Beta is calculated for each ion and displayed in a graph that became Figure 51.

```
clear
clc
close all

% Read in the kinetic energy and position of ions and
the magnetic field
% strength at their location
[KE0 B0 x0 y0 z0]=reads('Run 5 Magnetic0e-4.csv');
[KE1 B1 x1 y1 z1]=reads('Run 5 Magnetic1e-4.csv');
[KE2 B2 x2 y2 z2]=reads('Run 5 Magnetic2e-4.csv');
[KE3 B3 x3 y3 z3]=reads('Run 5 Magnetic3e-4.csv');
[KE4 B4 x4 y4 z4]=reads('Run 5 Magnetic4e-4.csv');
[KE5 B5 x5 y5 z5]=reads('Run 5 Magnetic5e-4.csv');
[KE6 B6 x6 y6 z6]=reads('Run 5 Magnetic6e-4.csv');
[KE7 B7 x7 y7 z7]=reads('Run 5 Magnetic7e-4.csv');
[KE8 B8 x8 y8 z8]=reads('Run 5 Magnetic8e-4.csv');
[KE9 B9 x9 y9 z9]=reads('Run 5 Magnetic9e-4.csv');
%[KE10 B10 x10 y10 z10]=reads('Run 5 Magnetic10e-
4.csv');

% Add all variables into a long vector to simulate a
continuous flow
% instead of one burst.
Total_KE =
[KE0',KE0',KE0',KE0',KE0',KE0',KE0',KE0',KE0',KE1
',KE1',KE1',KE1',KE1',KE1',KE1',KE1',KE1',KE2',KE2',KE
2',KE2',KE2',KE2',KE2',KE2',KE3',KE3',KE3',KE3',KE3',K
E3',KE3',KE4',KE4',KE4',KE4',KE4',KE4',KE5',KE5',KE5',
KE5',KE5',KE6',KE6',KE6',KE6',KE7',KE7',KE7',KE8',KE8'
,KE9'];
Total_KE = Total_KE';
Total_B =
[B0',B0',B0',B0',B0',B0',B0',B0',B0',B0',B1',B1',B1',B
1',B1',B1',B1',B1',B1',B2',B2',B2',B2',B2',B2',B2',B2'
,B3',B3',B3',B3',B3',B3',B3',B4',B4',B4',B4',B4',B4',B
5',B5',B5',B5',B5',B6',B6',B6',B6',B7',B7',B7',B8',B8'
,B9'];
Total_B = Total_B';
Total_X =
[x0',x0',x0',x0',x0',x0',x0',x0',x0',x0',x1',x1',x1',x
1',x1',x1',x1',x1',x1',x2',x2',x2',x2',x2',x2',x2',x2'
,x3',x3',x3',x3',x3',x3',x3',x4',x4',x4',x4',x4',x4',x
```

```
5',x5',x5',x5',x5',x6',x6',x6',x6',x7',x7',x7',x8',x8'
,x9'];
Total_X = Total_X';
Total_Y =
[y0',y0',y0',y0',y0',y0',y0',y0',y0',y0',y1',y1',y1',y
1',y1',y1',y1',y1',y1',y2',y2',y2',y2',y2',y2',y2',y2'
,y3',y3',y3',y3',y3',y3',y3',y4',y4',y4',y4',y4',y4',y
5',y5',y5',y5',y5',y6',y6',y6',y6',y7',y7',y7',y8',y8'
,y9'];
Total_Y = Total_Y';
Total_Z =
[z0',z0',z0',z0',z0',z0',z0',z0',z0',z0',z1',z1',z1',z
1',z1',z1',z1',z1',z1',z2',z2',z2',z2',z2',z2',z2',z2'
,z3',z3',z3',z3',z3',z3',z3',z4',z4',z4',z4',z4',z4',z
5',z5',z5',z5',z5',z6',z6',z6',z6',z7',z7',z7',z8',z8'
,z9'];
Total_Z = Total_Z';

% Declare the needed variables.
counter = 0;
total = size(Total_X,1);
Zspacing = 0.25; % spacing for the Z direction, m
Rspacing = 0.25; % spacing for the Radial direction, m
halfZ = Zspacing/2;
halfR = Rspacing/2;
R_total = 60/Rspacing+2;
[Z,R] = meshgrid(-30:Zspacing:30.25,-
30:Rspacing:30.25);
B_avg = zeros(R_total,R_total);
V_avg = zeros(R_total,R_total);
V_Alfven = zeros(R_total,R_total);
Beta = zeros(R_total,R_total);
Density = zeros(R_total,R_total);
Log_Amp = zeros(R_total,R_total);
Density_kg = zeros(R_total,R_total);
Volume =(Rspacing*Zspacing*0.1);
Z2 = linspace(-30,30,R_total);
scale = 2.2612e21/size(Total_X,1);

% Step 1: Cut a slice out of the 30 m sphere.
for i=1:total
    if Total_X(i)<=0.05 && Total_X(i)>=-0.05 &&
Total_Y(i)<29.9% slice is -0.05m < x < 0.05m
        counter = counter+1;
```

```
        SliceR(counter)  = Total_Y(i);
        SliceZ(counter)  = Total_Z(i);
        SliceB(counter)  = Total_B(i);
        SliceKE(counter) = Total_KE(i);
    end
end

SliceV = sqrt(2*SliceKE/6.633e-26); % Determine
velocity magnitude from KE.

% Step 2: Bin the sliced ions into Z x R bins
for i=1:R_total
    Rindex = -31 + i*Rspacing;
    for j=1:R_total
       Zindex = -31 + j*Zspacing;
       number = 0;
       Bsum = 0;
       Vsum = 0;
        for k=1:counter
            if SliceR(k)<=(Rindex+halfR) &&
SliceZ(k)<=(Zindex+halfZ) && SliceR(k)>(Rindex-halfR)
&& SliceZ(k)>(Zindex-halfZ)
                number = number + 1;
                Bsum = Bsum + SliceB(k);
                Vsum = Vsum + SliceV(k);
            end
        end
       Density(i,j)= number*scale/Volume; % # of
ions/m^3 x a scaling factor

       Density_kg(i,j)=Density(i,j)*(150e-
6/2.2612e21);% kg/m^3

       if number > 0
            B_avg(i,j)= Bsum/number; % Average B in
this square
            V_avg(i,j)= Vsum/number; % Average V in
this square
       end
       Total(i,j)=number;
    end
end
```

```
Count = sum(sum(Total,1)); % check to make sure total
number of ions was counted.

for l=1:R_total
    for m=1:R_total
        if Density_kg(l,m)>0
            V_Alfven(l,m) =
(B_avg(l,m))/sqrt((1.25664e-6)*Density_kg(l,m));
            Beta(l,m) = (V_avg(l,m)/V_Alfven(l,m))^2;
        end
    end
end

for l=1:R_total
    for m=1:R_total
        if Beta(l,m)>0
          Log_Beta(l,m)=log10(Beta(l,m));
        else Log_Beta(l,m)=-3;
        end
    end
end

% Interpolate to get a smoother graph.
INT_Log_Beta = interp2(Log_Beta,2);
INT_Density = interp2(Density,2);
INT_VAlfven = interp2(V_Alfven,2);
[Zi,Ri] = meshgrid(-30.25:Zspacing/4:30,-
30.25:Rspacing/4:30);

figure
contourf(R,Z,Density,50,'LineColor','none')
%axis([2.8 5 -0.7 0])
xlabel('Axial distance, m')
ylabel('Radius, m')
colorbar
%caxis([0 5])

figure
contourf(R,Z,log10(Density'/6.241e18),'LineColor','non
e')
%axis([0.2 10 -0.7 0])
xlabel('Axial distance, m')
ylabel('Radius, m')
colorbar
```

```
caxis([0 4])

figure
contourf(Ri,Zi,INT_Log_Beta',50,'LineColor','none')
%axis([-1 29 -30 30])
axis([0.2 2.4 -0.7 0])
xlabel('Axial distance, m')
ylabel('Radial Distance, m')
caxis([-2 0])
colorbar

figure
contourf(R,Z,Log_Beta',10)
%axis([2.8 5 -0.7 0])
caxis([0 4])
xlabel('Axial distance, m')
ylabel('Radius, m')
colorbar

figure
h = bar3(Z2,Log_Beta);
colormap jet
axis([0 R_total -30 30 -Inf Inf])
ylabel('Axial distance, m')
xlabel('Radius, m')
title('Beta')
set(gca,'XTickLabel',{'-30';'-20';'-
10';'0';'10';'20';'30'})
colorbar
caxis([-2 5])
for i = 1:length(h)
    zdata = get(h(i),'ZData');
    set(h(i),'CData',zdata) % Add back edge color
removed by interpolating shading
    set(h,'EdgeColor','k')
end
```

3. Contour_plot.m

```
clc
clear
close all

% Read in the data
```

```
a = csvread('Run 2 trunc.csv',9,0);
Vx =  a(:,3);
Vy =  a(:,4);
Vz =  a(:,5);
x1 =  a(:,6);
y1 =  a(:,7);
z1 =  a(:,8);
x2 =  a(:,13);
y2 =  a(:,14);
z2 =  a(:,15);

%Initialize variables
counter = 0;
bcounter = 0;
total = size(z1,1);
vspacing = 2000; % spacing for velocity, m/s
rspacing = 0.025; % spacing for radius, m
halfv = vspacing/2;
halfr = rspacing/2;
r_total = 0.7/rspacing+2;
v_total = 50000/vspacing + 1;
impact = zeros(r_total,v_total);
backfield = zeros(r_total,v_total);
[V,R] = meshgrid(0:vspacing/1000:50,0:rspacing:0.7);
New_V = 0;
New_R = 0;
New_X2 = 0;
New_Y2 = 0;

% Determine what the radius is from x and y
for g=1:total
    if x1(g)>=0 && y1(g)>=0
        r1(g) = sqrt(x1(g)^2+y1(g)^2);
    else
        r1(g) = -1*sqrt(x1(g)^2+y1(g)^2);
    end
    if x2(g)>=0 && y2(g)>=0
        r2(g) = sqrt(x2(g)^2+y2(g)^2);
    else
        r2(g) = -1*sqrt(x2(g)^2+y2(g)^2);
    end
end

r1 = r1(:);
```

```
r2 = r2(:);

% Binning
for i=1:total
    if z2(i)<=1e-3
        bcounter = bcounter + 1;
        BV(bcounter)=sqrt(Vx(i)^2+Vy(i)^2+Vz(i)^2);
        BR(bcounter)=abs(r1(i));
        if abs(r2(i))<=5
            counter = counter + 1;

New_V(counter)=sqrt(Vx(i)^2+Vy(i)^2+Vz(i)^2);
            New_R(counter)=abs(r1(i));
            New_X2(counter)=x2(i);
            New_Y2(counter)=y2(i);
        end
    end
end

% Separate into cells by initial radius and velocity
for i=1:r_total
    ra = i*rspacing - rspacing;
    for j=1:v_total
       va = j*vspacing - vspacing;
       counter = 0;
       bcounter = 0;
        for k=1:size(New_V(:),1)
            if New_R(k)<=(ra+halfr) &&
New_V(k)<=(va+halfv) && New_R(k)>(ra-halfr) &&
New_V(k)>(va-halfv)
                counter = counter + 1;
                impact(i,j)=100*counter/total;
            end
        end
        for m=1:size(BV(:),1)
             if BR(m)<=(ra+halfr) && BV(m)<=(va+halfv)
&& BR(m)>(ra-halfr) && BV(m)>(va-halfv)
                bcounter = bcounter + 1;
                backfield(i,j)=100*bcounter/total;
            end
        end
    end
end
```

```
Bp = sum(backfield);
Ip = sum(impact);
Bp2 = sum(backfield');
Ip2 = sum(impact');

avg_V = mean(New_V)
avg_R = mean(New_R)

% Percentage of ions entering backfield.
figure
contourf(R,V,backfield,30,'LineColor','none')
xlabel('Initial radial position at z=0.3 m,
m','fontsize',14,'fontweight','b')
ylabel('Initial velocity,
km/s','fontsize',14,'fontweight','b')
set(gca,'fontsize',14,'fontweight','b')
%caxis([0 0.01])
colorbar

% Percentage of ions impacting.
figure
contourf(R,V,impact,30,'LineColor','none')
xlabel('Initial radial position at z=0.3 m,
m','fontsize',14,'fontweight','b')
ylabel('Initial velocity,
km/s','fontsize',14,'fontweight','b')
set(gca,'fontsize',14,'fontweight','b')
colorbar

figure
plot(V,Bp,V,Ip)
axis([0 50 0 0.23 0 50 0 0.23])
xlabel('Initial velocity,
km/s','fontsize',14,'fontweight','b')
ylabel('Percentage of
ions','fontsize',14,'fontweight','b')
set(gca,'fontsize',14,'fontweight','b')
legend('Entering backfield','Impacting')

figure
plot(R,Bp2,R,Ip2)
axis([0 0.7 0 0.11 0 0.7 0 0.11])
xlabel('Initial radial position at z = 0.3 m,
m','fontsize',14,'fontweight','b')
```

```
ylabel('Percentage of
ions','fontsize',14,'fontweight','b')
set(gca,'fontsize',14,'fontweight','b')
legend('Entering
backfield','Impacting','Location','NorthWest')

figure
scatter(New_X2,New_Y2,'.')
axis([-3 3 -4 4])
xlabel('X direction,
m','fontsize',14,'fontweight','b')
ylabel('Y direction,
m','fontsize',14,'fontweight','b')
set(gca,'fontsize',14,'fontweight','b')
rectangle('Position', [-3 -2 2 4]) % side radiator
rectangle('Position', [1 -2 2 4]) % side radiator
rectangle('Position', [-0.75 -0.5 1.5 1]) % engine
housing
rectangle('Position', [-0.75 -3.8 1.5 3.3]) % bottom
radiator
rectangle('Position', [-0.75 0.5 1.5 3.3]) % top
radiator
```

4. DensityProfile.m

To generate the 20% wider and 20% narrower density profiles, I used the VX-200 density profile from VASIMR® literature. The code was developed to interpolate from this density profile in the ± 20% direction and is below:

```
clear
clc
close all

Rad1 = [-0.70
-0.65
-0.60
-0.55
-0.50
-0.45
-0.40
-0.35
-0.30
-0.25
```

```
-0.20
-0.15
-0.10
-0.05
0.00
0.05
0.10
0.15
0.20
0.25
0.30
0.35
0.40
0.45
0.50
0.55
0.60
0.65
0.70];

Den1 = [3.10E+15
6.18006E+15
6.44305E+15
8.35184E+15
1.01129E+16
1.76554E+16
3.64E+16
2.79E+17
1.59E+18
3.88E+18
6.67E+18
7.35E+18
8.36E+18
1.00E+19
1.25E+19
1.00E+19
8.36E+18
7.35E+18
6.67E+18
3.88E+18
1.59E+18
2.79E+17
3.64E+16
1.76554E+16
```

```
1.01129E+16
8.35184E+15
6.44305E+15
6.18006E+15
3.1012E+15];

sum1 = sum(Den1);

factor = 0.2;
Rad2 = Rad1*(1+factor);
Den2 = interp1(Rad2,Den1,Rad1);
sum2 = sum(Den2);
Den2s = Den2*sum1/sum2;

Percent1 = Den1/(sum(Den1));
Percent2 = Den2s/(sum(Den2));

subplot(3,1,1)
semilogy(Rad1,Den1,'o-', Rad1,Den2s,'x-')
subplot(3,1,2)
plot(Rad1,Den1,'o-', Rad1,Den2s,'x-')
subplot(3,1,3)
plot(Rad1,Percent1,'o-',Rad1,Percent2,'x-')

M = [Rad1;Percent1;Rad1;Percent2];
dlmwrite('DenProfiles.csv',M)
```

These 4 MATLAB files are also included electronically with this document and may be modified for another specific plume example. Other MATLAB programs may have been used for very specific situations such as in creating a particular graph and are not presented here.

APPENDIX L

TIME STEPS

The time steps used in the baseline Run 5 are presented below and were outputted by the COMSOL Multiphysics® program. The maximum time step was 1.92 x 10^{-4} seconds and the minimum time step was 1.88 x 10^{-7} seconds.

Time-dependent solver (Generalized-alpha)

Number of degrees of freedom solved for: 2999997

Step	Time	Stepsize	Res	Jac	Sol	Order	Tfail	LinIt	LinErr	LinRes
0	0	out	2	3	2	0	0	4	2.00E-06	4.60E-09
1	1.88E-07	1.88E-07	5	6	5	2	2	19	7.20E-08	1.80E-10
2	5.63E-07	3.75E-07	6	7	6	2	2	22	6.70E-06	1.70E-08
3	9.38E-07	3.75E-07	7	8	7	2	2	25	5.50E-06	1.40E-08
4	1.31E-06	3.75E-07	8	9	8	2	2	28	4.40E-06	1.10E-08
5	1.69E-06	3.75E-07	9	10	9	2	2	31	3.60E-06	9.00E-09
6	2.06E-06	3.75E-07	10	11	10	2	2	34	2.90E-06	7.30E-09
7	2.44E-06	3.75E-07	11	12	11	2	2	37	2.40E-06	6.00E-09
8	2.81E-06	3.75E-07	12	13	12	2	2	40	2.00E-06	4.90E-09
9	3.19E-06	3.75E-07	13	14	13	2	2	43	1.60E-06	4.10E-09
10	3.56E-06	3.75E-07	14	15	14	2	2	46	1.40E-06	3.50E-09
11	3.94E-06	3.75E-07	15	16	15	2	2	49	1.20E-06	3.00E-09
12	4.31E-06	3.75E-07	16	17	16	2	2	52	1.00E-06	2.50E-09
13	4.69E-06	3.75E-07	17	18	17	2	2	55	8.90E-07	2.20E-09
14	5.06E-06	3.75E-07	18	19	18	2	2	58	7.80E-07	1.90E-09
15	5.44E-06	3.75E-07	19	20	19	2	2	61	6.90E-07	1.70E-09
16	5.81E-06	3.75E-07	20	21	20	2	2	64	6.20E-07	1.50E-09
17	6.19E-06	3.75E-07	21	22	21	2	2	67	5.60E-07	1.40E-09
18	6.56E-06	3.75E-07	22	23	22	2	2	70	5.00E-07	1.20E-09
19	6.94E-06	3.75E-07	23	24	23	2	2	73	4.60E-07	1.10E-09
20	7.31E-06	3.75E-07	24	25	24	2	2	76	4.20E-07	1.00E-09
21	7.69E-06	3.75E-07	25	26	25	2	2	79	3.80E-07	9.30E-10

22	8.06E-06	3.75E-07	26	27	26	2	2	82	3.50E-07	8.50E-10
23	8.44E-06	3.75E-07	27	28	27	2	2	85	3.10E-07	7.70E-10
24	8.81E-06	3.75E-07	28	29	28	2	2	88	2.90E-07	7.10E-10
25	9.19E-06	3.75E-07	29	30	29	2	2	91	2.60E-07	6.40E-10
26	9.56E-06	3.75E-07	30	31	30	2	2	94	2.40E-07	5.80E-10
27	9.94E-06	3.75E-07	31	32	31	2	2	97	2.20E-07	5.30E-10
28	1.03E-05	3.75E-07	32	33	32	2	2	100	2.00E-07	4.80E-10
29	1.07E-05	3.75E-07	33	34	33	2	2	103	1.80E-07	4.40E-10
30	1.11E-05	3.75E-07	34	35	34	2	2	106	1.60E-07	4.00E-10
31	1.14E-05	3.75E-07	35	36	35	2	2	109	1.50E-07	3.60E-10
32	1.18E-05	3.75E-07	36	37	36	2	2	112	1.30E-07	3.20E-10
33	1.22E-05	3.75E-07	37	38	37	2	2	115	1.20E-07	2.90E-10
34	1.26E-05	3.75E-07	38	39	38	2	2	118	1.10E-07	2.60E-10
35	1.29E-05	3.75E-07	39	40	39	2	2	121	9.70E-08	2.40E-10
36	1.33E-05	3.75E-07	40	41	40	2	2	124	8.70E-08	2.10E-10
37	1.37E-05	3.75E-07	41	42	41	2	2	127	7.90E-08	1.90E-10
38	1.41E-05	3.75E-07	42	43	42	2	2	130	7.20E-08	1.80E-10
39	1.44E-05	3.75E-07	43	44	43	2	2	133	6.60E-08	1.60E-10
40	1.48E-05	3.75E-07	44	45	44	2	2	136	6.00E-08	1.50E-10
41	1.52E-05	3.75E-07	45	46	45	2	2	139	5.60E-08	1.40E-10
42	1.56E-05	3.75E-07	46	47	46	2	2	142	5.20E-08	1.30E-10
43	1.59E-05	3.75E-07	47	48	47	2	2	145	4.90E-08	1.20E-10
44	1.63E-05	3.75E-07	48	49	48	2	2	148	4.60E-08	1.10E-10
45	1.67E-05	3.75E-07	49	50	49	2	2	151	4.30E-08	1.10E-10
46	1.71E-05	3.75E-07	50	51	50	2	2	154	4.10E-08	1.00E-10
47	1.74E-05	3.75E-07	51	52	51	2	2	157	3.90E-08	9.60E-11
48	1.78E-05	3.75E-07	52	53	52	2	2	160	3.80E-08	9.20E-11
49	1.82E-05	3.75E-07	53	54	53	2	2	163	3.60E-08	8.70E-11
50	1.86E-05	3.75E-07	54	55	54	2	2	166	3.40E-08	8.30E-11
51	1.89E-05	3.75E-07	55	56	55	2	2	169	3.20E-08	7.90E-11
52	1.93E-05	3.75E-07	56	57	56	2	2	172	3.00E-08	7.50E-11
53	1.97E-05	3.75E-07	57	58	57	2	2	175	2.90E-08	7.00E-11
54	2.01E-05	3.75E-07	58	59	58	2	2	178	2.70E-08	6.60E-11
55	2.04E-05	3.75E-07	59	60	59	2	2	181	2.60E-08	6.30E-11
56	2.08E-05	3.75E-07	60	61	60	2	2	184	2.40E-08	5.90E-11
57	2.12E-05	3.75E-07	61	62	61	2	2	187	2.30E-08	5.60E-11
58	2.16E-05	3.75E-07	62	63	62	2	2	190	2.10E-08	5.20E-11
59	2.19E-05	3.75E-07	63	64	63	2	2	193	2.00E-08	4.90E-11
60	2.23E-05	3.75E-07	64	65	64	2	2	196	1.90E-08	4.70E-11
61	2.27E-05	3.75E-07	65	66	65	2	2	199	1.80E-08	4.40E-11

62	2.31E-05	3.75E-07	66	67	66	2	2	202	1.70E-08	4.10E-11
63	2.34E-05	3.75E-07	67	68	67	2	2	205	1.60E-08	3.90E-11
64	2.38E-05	3.75E-07	68	69	68	2	2	208	1.50E-08	3.70E-11
65	2.42E-05	3.75E-07	69	70	69	2	2	211	1.40E-08	3.50E-11
66	2.46E-05	3.75E-07	70	71	70	2	2	214	1.30E-08	3.30E-11
67	2.49E-05	3.75E-07	71	72	71	2	2	217	1.30E-08	3.10E-11
68	2.53E-05	3.75E-07	72	73	72	2	2	220	1.20E-08	2.90E-11
69	2.57E-05	3.75E-07	73	74	73	2	2	223	1.10E-08	2.70E-11
70	2.61E-05	3.75E-07	74	75	74	2	2	226	1.00E-08	2.60E-11
71	2.64E-05	3.75E-07	75	76	75	2	2	229	9.80E-09	2.40E-11
72	2.68E-05	3.75E-07	76	77	76	2	2	232	9.20E-09	2.20E-11
73	2.72E-05	3.75E-07	77	78	77	2	2	235	8.60E-09	2.10E-11
74	2.76E-05	3.75E-07	78	79	78	2	2	238	8.00E-09	2.00E-11
75	2.79E-05	3.75E-07	79	80	79	2	2	241	7.50E-09	1.90E-11
76	2.83E-05	3.75E-07	80	81	80	2	2	244	7.00E-09	1.70E-11
77	2.91E-05	7.50E-07	81	82	81	2	2	247	4.00E-07	9.80E-10
78	2.98E-05	7.50E-07	82	83	82	2	2	250	3.50E-07	8.60E-10
79	3.06E-05	7.50E-07	83	84	83	2	2	253	3.10E-07	7.50E-10
80	3.13E-05	7.50E-07	84	85	84	2	2	256	2.70E-07	6.60E-10
81	3.21E-05	7.50E-07	85	86	85	2	2	259	2.30E-07	5.60E-10
82	3.28E-05	7.50E-07	86	87	86	2	2	262	2.00E-07	4.90E-10
83	3.36E-05	7.50E-07	87	88	87	2	2	265	1.70E-07	4.20E-10
84	3.43E-05	7.50E-07	88	89	88	2	2	268	1.50E-07	3.70E-10
85	3.51E-05	7.50E-07	89	90	89	2	2	271	1.30E-07	3.20E-10
86	3.58E-05	7.50E-07	90	91	90	2	2	274	1.20E-07	2.80E-10
87	3.66E-05	7.50E-07	91	92	91	2	2	277	1.00E-07	2.50E-10
88	3.73E-05	7.50E-07	92	93	92	2	2	280	9.10E-08	2.20E-10
89	3.81E-05	7.50E-07	93	94	93	2	2	283	7.90E-08	1.90E-10
90	3.88E-05	7.50E-07	94	95	94	2	2	286	6.90E-08	1.70E-10
91	3.96E-05	7.50E-07	95	96	95	2	2	289	6.10E-08	1.50E-10
92	4.03E-05	7.50E-07	96	97	96	2	2	292	5.40E-08	1.30E-10
93	4.11E-05	7.50E-07	97	98	97	2	2	295	4.80E-08	1.20E-10
94	4.18E-05	7.50E-07	98	99	98	2	2	298	4.20E-08	1.00E-10
95	4.26E-05	7.50E-07	99	100	99	2	2	301	3.70E-08	8.90E-11
96	4.33E-05	7.50E-07	100	101	100	2	2	304	3.20E-08	7.80E-11
97	4.41E-05	7.50E-07	101	102	101	2	2	307	2.80E-08	6.90E-11
98	4.48E-05	7.50E-07	102	103	102	2	2	310	2.50E-08	6.10E-11
99	4.56E-05	7.50E-07	103	104	103	2	2	313	2.20E-08	5.40E-11
100	4.63E-05	7.50E-07	104	105	104	2	2	316	1.90E-08	4.80E-11
101	4.71E-05	7.50E-07	105	106	105	2	2	319	1.70E-08	4.20E-11

102	4.78E-05	7.50E-07	106	107	106	2	2	322	1.50E-08	3.80E-11
103	4.86E-05	7.50E-07	107	108	107	2	2	325	1.40E-08	3.30E-11
104	4.93E-05	7.50E-07	108	109	108	2	2	328	1.20E-08	3.00E-11
105	5.01E-05	7.50E-07	109	110	109	2	2	331	1.10E-08	2.60E-11
106	5.08E-05	7.50E-07	110	111	110	2	2	334	9.60E-09	2.40E-11
107	5.16E-05	7.50E-07	111	112	111	2	2	337	8.50E-09	2.10E-11
108	5.23E-05	7.50E-07	112	113	112	2	2	340	7.60E-09	1.90E-11
109	5.31E-05	7.50E-07	113	114	113	2	2	343	6.70E-09	1.70E-11
110	5.38E-05	7.50E-07	114	115	114	2	2	346	6.00E-09	1.50E-11
111	5.46E-05	7.50E-07	115	116	115	2	2	349	5.40E-09	1.30E-11
112	5.53E-05	7.50E-07	116	117	116	2	2	352	4.90E-09	1.20E-11
113	5.61E-05	7.50E-07	117	118	117	2	2	355	4.30E-09	1.10E-11
114	5.68E-05	7.50E-07	118	119	118	2	2	358	3.80E-09	9.40E-12
115	5.76E-05	7.50E-07	119	120	119	2	2	361	3.40E-09	8.40E-12
116	5.83E-05	7.50E-07	120	121	120	2	2	364	3.10E-09	7.50E-12
117	5.91E-05	7.50E-07	121	122	121	2	2	367	2.70E-09	6.70E-12
118	5.98E-05	7.50E-07	122	123	122	2	2	370	2.50E-09	6.00E-12
119	6.06E-05	7.50E-07	123	124	123	2	2	372	9.80E-06	2.40E-08
120	6.13E-05	7.50E-07	124	125	124	2	2	374	9.20E-06	2.30E-08
121	6.21E-05	7.50E-07	125	126	125	2	2	376	8.60E-06	2.10E-08
122	6.28E-05	7.50E-07	126	127	126	2	2	378	8.10E-06	2.00E-08
123	6.36E-05	7.50E-07	127	128	127	2	2	380	7.60E-06	1.90E-08
124	6.43E-05	7.50E-07	128	129	128	2	2	382	7.10E-06	1.70E-08
125	6.51E-05	7.50E-07	129	130	129	2	2	384	6.60E-06	1.60E-08
126	6.58E-05	7.50E-07	130	131	130	2	2	386	6.20E-06	1.50E-08
127	6.66E-05	7.50E-07	131	132	131	2	2	388	5.80E-06	1.40E-08
128	6.73E-05	7.50E-07	132	133	132	2	2	390	5.40E-06	1.30E-08
129	6.81E-05	7.50E-07	133	134	133	2	2	392	5.10E-06	1.30E-08
130	6.88E-05	7.50E-07	134	135	134	2	2	394	4.80E-06	1.20E-08
131	6.96E-05	7.50E-07	135	136	135	2	2	396	4.40E-06	1.10E-08
132	7.11E-05	1.50E-06	136	137	136	2	2	399	3.50E-08	8.40E-11
133	7.26E-05	1.50E-06	137	138	137	2	2	402	2.80E-08	6.90E-11
134	7.41E-05	1.50E-06	138	139	138	2	2	405	2.30E-08	5.60E-11
135	7.56E-05	1.50E-06	139	140	139	2	2	408	1.90E-08	4.60E-11
136	7.71E-05	1.50E-06	140	141	140	2	2	411	1.60E-08	3.80E-11
137	7.86E-05	1.50E-06	141	142	141	2	2	414	1.30E-08	3.10E-11
138	8.01E-05	1.50E-06	142	143	142	2	2	417	1.10E-08	2.60E-11
139	8.16E-05	1.50E-06	143	144	143	2	2	420	8.70E-09	2.10E-11
140	8.31E-05	1.50E-06	144	145	144	2	2	423	7.20E-09	1.80E-11
141	8.46E-05	1.50E-06	145	146	145	2	2	426	6.00E-09	1.50E-11

142	8.61E-05	1.50E-06	146	147	146	2	2	429	5.10E-09	1.20E-11
143	8.76E-05	1.50E-06	147	148	147	2	2	432	4.30E-09	1.00E-11
144	8.91E-05	1.50E-06	148	149	148	2	2	435	3.60E-09	8.90E-12
145	9.06E-05	1.50E-06	149	150	149	2	2	438	3.10E-09	7.50E-12
146	9.21E-05	1.50E-06	150	151	150	2	2	441	2.60E-09	6.40E-12
147	9.36E-05	1.50E-06	151	152	151	2	2	444	2.30E-09	5.60E-12
148	9.51E-05	1.50E-06	152	153	152	2	2	446	9.30E-06	2.30E-08
149	9.66E-05	1.50E-06	153	154	153	2	2	448	8.40E-06	2.10E-08
150	9.81E-05	1.50E-06	154	155	154	2	2	450	7.50E-06	1.80E-08
151	9.96E-05	1.50E-06	155	156	155	2	2	452	6.60E-06	1.60E-08
152	0.000101	1.50E-06	156	157	156	2	2	454	5.80E-06	1.40E-08
153	0.000103	1.50E-06	157	158	157	2	2	456	5.20E-06	1.30E-08
154	0.000104	1.50E-06	158	159	158	2	2	458	4.70E-06	1.20E-08
155	0.000106	1.50E-06	159	160	159	2	2	460	4.20E-06	1.00E-08
156	0.000107	1.50E-06	160	161	160	2	2	462	3.70E-06	9.30E-09
157	0.000109	1.50E-06	161	162	161	2	2	464	3.40E-06	8.30E-09
158	0.00011	1.50E-06	162	163	162	2	2	466	3.00E-06	7.50E-09
159	0.000112	1.50E-06	163	164	163	2	2	468	2.80E-06	6.80E-09
160	0.000113	1.50E-06	164	165	164	2	2	470	2.50E-06	6.20E-09
161	0.000115	1.50E-06	165	166	165	2	2	472	2.30E-06	5.60E-09
162	0.000116	1.50E-06	166	167	166	2	2	474	2.10E-06	5.10E-09
163	0.000118	1.50E-06	167	168	167	2	2	476	1.90E-06	4.70E-09
164	0.000119	1.50E-06	168	169	168	2	2	478	1.70E-06	4.20E-09
165	0.000121	1.50E-06	169	170	169	2	2	480	1.60E-06	3.90E-09
166	0.000122	1.50E-06	170	171	170	2	2	482	1.40E-06	3.50E-09
167	0.000124	1.50E-06	171	172	171	2	2	484	1.30E-06	3.20E-09
168	0.000125	1.50E-06	172	173	172	2	2	486	1.20E-06	2.90E-09
169	0.000127	1.50E-06	173	174	173	2	2	488	1.10E-06	2.70E-09
170	0.000128	1.50E-06	174	175	174	2	2	490	9.90E-07	2.40E-09
171	0.00013	1.50E-06	175	176	175	2	2	492	9.00E-07	2.20E-09
172	0.000131	1.50E-06	176	177	176	2	2	494	8.20E-07	2.00E-09
173	0.000133	1.50E-06	177	178	177	2	2	496	7.50E-07	1.90E-09
174	0.000136	3.00E-06	178	179	178	2	2	499	2.40E-09	5.80E-12
175	0.000139	3.00E-06	179	180	179	2	2	501	8.90E-06	2.20E-08
176	0.000142	3.00E-06	180	181	180	2	2	503	7.40E-06	1.80E-08
177	0.000145	3.00E-06	181	182	181	2	2	505	6.20E-06	1.50E-08
178	0.000148	3.00E-06	182	183	182	2	2	507	5.20E-06	1.30E-08
179	0.000151	3.00E-06	183	184	183	2	2	509	4.40E-06	1.10E-08
180	0.000154	3.00E-06	184	185	184	2	2	511	3.80E-06	9.30E-09
181	0.000157	3.00E-06	185	186	185	2	2	513	3.20E-06	7.90E-09

182	0.00016	3.00E-06	187	187	187	2	2	517	1.40E-06	3.40E-09
183	0.000163	3.00E-06	189	188	189	2	2	521	3.00E-06	7.40E-09
184	0.000166	3.00E-06	190	189	190	2	2	523	2.00E-06	5.00E-09
185	0.000169	3.00E-06	192	190	192	2	2	527	1.50E-06	3.80E-09
186	0.000172	3.00E-06	194	191	194	2	2	531	2.20E-06	5.60E-09
187	0.000175	3.00E-06	196	192	196	2	2	535	1.90E-06	4.70E-09
188	0.000178	3.00E-06	198	193	198	2	2	539	4.70E-07	1.20E-09
189	0.000181	3.00E-06	200	194	200	2	2	543	1.30E-06	3.20E-09
190	0.000184	3.00E-06	202	195	202	2	2	547	9.40E-07	2.40E-09
191	0.000187	3.00E-06	204	196	204	2	2	551	4.00E-07	1.00E-09
192	0.00019	3.00E-06	205	197	205	2	2	553	6.50E-07	1.60E-09
193	0.000193	3.00E-06	206	198	206	2	2	555	5.60E-07	1.40E-09
194	0.000196	3.00E-06	207	199	207	2	2	557	4.90E-07	1.20E-09
195	0.000199	3.00E-06	209	200	209	2	2	561	4.30E-07	1.10E-09
196	0.000202	3.00E-06	211	201	211	2	2	565	7.00E-07	1.80E-09
197	0.000205	3.00E-06	212	202	212	2	2	567	3.30E-07	8.20E-10
198	0.000208	3.00E-06	214	203	214	2	2	571	3.30E-07	8.30E-10
199	0.000211	3.00E-06	215	204	215	2	2	573	2.50E-07	6.30E-10
200	0.000214	3.00E-06	216	205	216	2	2	575	2.30E-07	5.60E-10
201	0.000217	3.00E-06	217	206	217	2	2	577	2.00E-07	5.00E-10
202	0.00022	3.00E-06	218	207	218	2	2	579	1.80E-07	4.40E-10
203	0.000223	3.00E-06	219	208	219	2	2	581	1.60E-07	3.90E-10
204	0.000226	3.00E-06	220	209	220	2	2	583	1.40E-07	3.50E-10
205	0.000229	3.00E-06	221	210	221	2	2	585	1.20E-07	3.10E-10
206	0.000232	3.00E-06	222	211	222	2	2	587	1.10E-07	2.70E-10
207	0.000238	6.00E-06	224	212	224	2	2	591	4.90E-06	1.20E-08
208	0.000244	6.00E-06	226	213	226	2	2	595	4.70E-06	1.20E-08
209	0.00025	6.00E-06	228	214	228	2	2	599	5.50E-06	1.40E-08
210	0.000256	6.00E-06	230	215	230	2	2	603	7.30E-06	1.80E-08
211	0.000262	6.00E-06	231	216	231	2	2	605	6.00E-07	1.50E-09
212	0.000268	6.00E-06	233	217	233	2	2	609	7.60E-06	1.90E-08
213	0.000274	6.00E-06	235	218	235	2	2	613	6.60E-06	1.70E-08
214	0.00028	6.00E-06	236	219	236	2	2	615	3.20E-07	7.90E-10
215	0.000286	6.00E-06	238	220	238	2	2	619	8.10E-06	2.00E-08
216	0.000292	6.00E-06	240	221	240	2	2	623	8.10E-06	2.00E-08
217	0.000298	6.00E-06	241	222	241	2	2	625	1.80E-07	4.50E-10
218	0.000304	6.00E-06	242	223	242	2	2	627	1.50E-07	3.70E-10
219	0.00031	6.00E-06	243	224	243	2	2	629	1.30E-07	3.20E-10
220	0.000316	6.00E-06	244	225	244	2	2	631	1.10E-07	2.70E-10
221	0.000322	6.00E-06	245	226	245	2	2	633	9.50E-08	2.40E-10

222	0.000328	6.00E-06	246	227	246	2	2	635	8.50E-08	2.10E-10
223	0.000334	6.00E-06	247	228	247	2	2	637	7.70E-08	1.90E-10
224	0.00034	6.00E-06	248	229	248	2	2	639	7.30E-08	1.80E-10
225	0.000346	6.00E-06	249	230	249	2	2	641	7.00E-08	1.70E-10
226	0.000352	6.00E-06	250	231	250	2	2	643	6.80E-08	1.70E-10
227	0.000358	6.00E-06	251	232	251	2	2	645	6.80E-08	1.70E-10
228	0.000364	6.00E-06	253	233	253	2	2	649	8.60E-06	2.10E-08
229	0.00037	6.00E-06	254	234	254	2	2	651	7.00E-08	1.70E-10
230	0.000376	6.00E-06	255	235	255	2	2	653	7.20E-08	1.80E-10
231	0.000382	6.00E-06	256	236	256	2	2	655	7.40E-08	1.80E-10
232	0.000388	6.00E-06	257	237	257	2	2	657	7.70E-08	1.90E-10
233	0.000394	6.00E-06	258	238	258	2	2	659	8.00E-08	2.00E-10
234	0.000406	1.20E-05	259	239	259	2	2	661	1.30E-06	3.20E-09
235	0.000418	1.20E-05	260	240	260	2	2	663	1.40E-06	3.50E-09
236	0.00043	1.20E-05	261	241	261	2	2	665	1.50E-06	3.70E-09
237	0.000442	1.20E-05	262	242	262	2	2	667	1.70E-06	3.90E-09
238	0.000454	1.20E-05	263	243	263	2	2	669	1.80E-06	4.20E-09
239	0.000466	1.20E-05	264	244	264	2	2	671	1.90E-06	4.40E-09
240	0.000478	1.20E-05	265	245	265	2	2	673	2.00E-06	4.70E-09
241	0.00049	1.20E-05	266	246	266	2	2	675	2.10E-06	5.00E-09
242	0.000502	1.20E-05	267	247	267	2	2	677	2.20E-06	5.20E-09
243	0.000514	1.20E-05	268	248	268	2	2	679	2.20E-06	5.40E-09
244	0.000526	1.20E-05	269	249	269	2	2	681	2.30E-06	5.50E-09
245	0.000538	1.20E-05	270	250	270	2	2	683	2.30E-06	5.60E-09
246	0.00055	1.20E-05	271	251	271	2	2	685	2.40E-06	5.70E-09
247	0.000562	1.20E-05	272	252	272	2	2	687	2.30E-06	5.70E-09
248	0.000574	1.20E-05	273	253	273	2	2	689	2.30E-06	5.60E-09
249	0.000586	1.20E-05	274	254	274	2	2	691	2.30E-06	5.50E-09
250	0.000598	1.20E-05	275	255	275	2	2	693	2.20E-06	5.30E-09
251	0.00061	1.20E-05	276	256	276	2	2	695	2.10E-06	5.20E-09
252	0.000622	1.20E-05	277	257	277	2	2	697	2.00E-06	5.00E-09
253	0.000634	1.20E-05	278	258	278	2	2	699	1.90E-06	4.80E-09
254	0.000658	2.40E-05	279	259	279	2	2	702	6.40E-08	1.50E-10
255	0.000682	2.40E-05	280	260	280	2	2	705	6.60E-08	1.50E-10
256	0.000706	2.40E-05	281	261	281	2	2	708	6.80E-08	1.60E-10
257	0.00073	2.40E-05	283	262	283	2	2	714	6.10E-06	1.50E-08
258	0.000754	2.40E-05	285	263	285	2	2	720	6.10E-06	1.50E-08
259	0.000778	2.40E-05	287	264	287	2	2	726	6.00E-06	1.50E-08
260	0.000802	2.40E-05	289	265	289	2	2	732	6.00E-06	1.50E-08
261	0.000826	2.40E-05	291	266	291	2	2	738	6.00E-06	1.50E-08

262	0.00085	2.40E-05	293	267	293	2	2	744	6.00E-06	1.50E-08
263	0.000874	2.40E-05	294	268	294	2	2	747	9.00E-08	2.10E-10
264	0.000898	2.40E-05	295	269	295	2	2	750	9.60E-08	2.20E-10
265	0.000922	2.40E-05	297	270	297	2	2	756	6.10E-06	1.50E-08
266	0.000946	2.40E-05	298	271	298	2	2	759	1.10E-07	2.60E-10
267	0.00097	2.40E-05	299	272	299	2	2	762	1.20E-07	2.70E-10
268	0.000994	2.40E-05	300	273	300	2	2	765	1.30E-07	2.90E-10
269	0.001018	2.40E-05	301	274	301	2	2	768	1.40E-07	3.10E-10
270	0.001066	4.80E-05	303	275	303	2	2	775	3.10E-06	7.50E-09
271	0.001114	4.80E-05	304	276	304	2	2	779	7.90E-08	1.70E-10
272	0.001162	4.80E-05	306	277	306	2	2	787	2.90E-06	7.00E-09
273	0.00121	4.80E-05	308	278	308	2	2	795	2.90E-06	7.00E-09
274	0.001258	4.80E-05	309	279	309	2	2	799	1.20E-07	2.50E-10
275	0.001306	4.80E-05	311	280	311	2	2	807	2.90E-06	7.00E-09
276	0.001354	4.80E-05	312	281	312	2	2	811	1.50E-07	3.30E-10
277	0.001402	4.80E-05	313	282	313	2	2	815	1.60E-07	3.60E-10
278	0.00145	4.80E-05	315	283	315	2	2	823	2.90E-06	6.90E-09
279	0.001498	4.80E-05	316	284	316	2	2	827	2.10E-07	4.60E-10
280	0.001546	4.80E-05	317	285	317	2	2	831	2.30E-07	5.00E-10
281	0.001642	9.60E-05	319	286	319	2	2	842	4.60E-07	1.00E-09
282	0.001738	9.60E-05	320	287	320	2	2	847	2.10E-06	4.30E-09
283	0.001834	9.60E-05	321	288	321	2	2	852	2.40E-06	5.00E-09
284	0.00193	9.60E-05	323	289	323	2	2	863	4.60E-07	1.00E-09
285	0.002026	9.60E-05	324	290	324	2	2	868	3.70E-06	7.60E-09
286	0.002122	9.60E-05	325	291	325	2	2	873	4.20E-06	8.60E-09
287	0.002218	9.60E-05	326	292	326	2	2	878	4.70E-06	9.70E-09
288	0.00241	0.000192	328	293	328	2	2	894	6.50E-06	1.30E-08
289	0.002602	0.000192	329	294	329	2	2	902	3.10E-06	5.00E-09
290	0.002794	0.000192	330	295	330	2	2	910	3.60E-06	5.90E-09
291	0.002986	0.000192	331	296	331	2	2	918	4.10E-06	6.90E-09
292	0.003178	0.000192	333	297	333	2	2	934	6.50E-06	1.30E-08

APPENDIX M

ALTERNATIVE ELECTRICAL CHARGING CALCULATIONS

While the Electric Potential was calculated using the equations in Section 4.3.3, there was an alternative method to determine the current densities, or fluxes, for ions and electrons. This alternative method comes from Appendix G in NASA JPL's "Guide to Mitigating Spacecraft Charging Effects"[44] and the equations are listed below:

Assuming V < 0:

$$J_E = J_{E0}\, exp\left(\frac{qV}{kT_E}\right) \tag{M-1}$$

$$J_I = J_{I0}\left(1 - \frac{qV}{kT_I}\right) \tag{M-2}$$

where

$$J_{E0} = \frac{qN_E}{2}\left(\frac{2kT_E}{\pi m_E}\right)^{1/2} \tag{M-3}$$

$$J_{I0} = \frac{qN_I}{2}\left(\frac{2kT_I}{\pi m_I}\right)^{1/2} \tag{M-4}$$

V = spacecraft potential relative to the space plasma = ϕ in Volts

N_E = density of electrons (#/cm^3)

N_I = density of ions (#/cm^3)

m_E = mass of electrons (9.11 x 10^{-31} kg)

m_I = mass of argon ion (6.63×10^{-26} kg)

q = magnitude of the electronic charge (1.602×10^{-19} C)

k = Boltzmann's constant (1.38×10^{-23} J/K)

T_E = temperature of electrons (K)

T_I = temperature of ions (K)

These equations can be used because the plasma potential measured experimentally was positive relative to ground so the engine surface potential would be negative. Instead of converting the average ion kinetic energy into the ion temperature, the kinetic energy was converted from eV to Joules and used wherever k T_I was called for.

The ion density was determined by use of a binning program in MATLAB® with individual ion locations and a scaling factor to match the mass flow rate of argon used experimentally. This program provided both an average density and a maximum density. The maximum density was used for the sheath potential calculation to determine the maximum potential. The charging is a surface charge and not an internal charge because a.) the highest ion kinetic energy (and thus temperature) out of all 8 runs was 41.78 eV, and b.) temperature ranges of 0 to 50 keV usually correlate to surface charging[35].

If the electron current density and ion current density are equal, thus allowing for a quasi-equilibrium plasma to exist, then the sheath potential can be determined.

$$J_E = J_I \tag{M-5}$$

$$J_{E0}\, exp\left(\frac{q\phi}{kT_E}\right) = J_{I0}\left(1 - \frac{q\phi}{kT_I}\right) \tag{M-6}$$

Substituting for J_{EO} and J_{IO} and letting kT_I = the average impacting ion kinetic energy yields:

$$\frac{qN_E}{2}\sqrt{\frac{2kT_E}{\pi m_E}}exp\left(\frac{q\phi}{kT_E}\right) = \frac{qN_I}{2}\sqrt{\frac{2<KE>_I}{\pi m_I}}\left(1-\frac{q\phi}{<KE>_I}\right) \quad \text{(M-7)}$$

Assuming that the plasma is quasi-neutral ($N_E = N_I$), then the densities cancel out to create:

$$\sqrt{\frac{2kT_E}{\pi m_E}}exp\left(\frac{-q\phi}{kT_E}\right) = \sqrt{\frac{2<KE>_I}{\pi m_I}}\left(1-\frac{q\phi}{<KE>_I}\right) \quad \text{(M-8)}$$

Assuming that the plasma near the surface is in thermal equilibrium ($T_E = T_I$), which is accurate once the engine reaches steady state operation, then the above equation can be reduced to:

$$\sqrt{\frac{2<KE>_I}{\pi m_E}}exp\left(\frac{-q\phi}{<KE>_I}\right) = \sqrt{\frac{2<KE>_I}{\pi m_I}}\left(1-\frac{q\phi}{<KE>_I}\right) \quad \text{(M-9)}$$

It is important to note that with these assumptions, the potential is now only a function of the impacting ions average kinetic energy and the masses of the argon ions and electrons.

As the sheath potential, ϕ, cannot be easily isolated and solved for in equation 4-22, a MS Excel® spreadsheet was used with all of the values for average impacting ion kinetic energy for each run. The spreadsheet then solved for ϕ when the difference between J_E and J_I roughly equaled zero (J_E - J_I column). The results are presented below:

Table 11. Spacecraft potential when the plasma is assumed to be quasi-neutral and isothermal *

Run #	$\langle KE \rangle_i$ (eV)	$\langle KE \rangle_i$ (J)	Ni max (#/m^3)	J_{e0} (A/m^2)	J_{i0} (A/m^2)	Potential, ϕ (V)	J_E (A/m^2)	J_I (A/m^2)	$J_E - J_I$	J (A/m^2 s)
1	18.78	3.00889E-18	5.25E+15	6.10E+02	2.26E+00	-74.94	11.28	11.28	0.000	8.02
2	38.96	6.24208E-18	1.78E+14	2.98E+01	1.10E-01	-155.46	0.55	0.55	0.000	0.39
3	41.76	6.69069E-18	3.83E+15	6.63E+02	2.46E+00	-166.64	12.26	12.26	0.000	8.71
4	41.78	6.69389E-18	3.12E+15	5.40E+02	2.00E+00	-166.72	9.98	9.98	0.000	7.09
5	31.22	5.00199E-18	1.06E+16	1.59E+03	5.88E+00	-124.58	29.34	29.34	0.000	20.84
6	19.49	3.12264E-18	3.29E+15	3.90E+02	1.44E+00	-77.77	7.21	7.21	0.000	5.12
7	26.99	4.32427E-18	1.53E+16	2.13E+03	7.90E+00	-107.70	39.44	39.44	0.000	28.01
8	38.89	6.23086E-18	8.90E+13	1.49E+01	5.51E-02	-155.18	0.28	0.28	0.000	0.20

The electric potentials calculated using this method are much higher than ones found with the method in Section 5.4. However, the highest value (-166.72 V) is still close to the potentials that current plasma contactor units mitigate on the ISS. Therefore, operating the engine by itself alone could lead to sizable charging and discharging damage, but using a plasma contactor unit simultaneously may reduce or eliminate this damage. More testing in an actual space environment is needed to determine conclusively.